

Elemental and charge-state composition inside Magnetic Clouds determined with ACE/SWICS

Dissertation
zur Erlangung des Doktorgrades
der Mathematisch-Naturwissenschaftlichen-Fakultät
der Christian-Albrechts-Universität
zu Kiel

vorgelegt von
Dipl.-Phys. Roland Rodde

Kiel im Mai 2009

Referent/in : _____

Korreferent/in : _____

Tag der mündlichen Prüfung : _____

Zum Druck genehmigt : _____

Der Dekan

Zusammenfassung

Koronale Massenauswürfe (CMEs) sind die explosionsartige Freisetzung großer Plasmawolken auf der Sonne. Bis heute sind die Mechanismen, die zur Auslösung dieser Auswürfe führen, nicht bekannt. Die interplanetaren Gegenstücke zu den CMEs werden ICMEs (Interplanetare CMEs) genannt. Bei einem Abstand von 1 AU von der Sonne zeigt ungefähr ein Drittel aller ICMEs eine gleichmäßige Rotation des magnetischen Feldstärkevektors (oftmals zusammen mit erhöhter Magnetfeldstärke). Diese Strukturen werden magnetische Wolken (MCs) genannt. Aufgrund der klaren Strukturierung kann das magnetische Feld modelliert werden. Nimmt man eine bestimmte Strukturierung des Magnetfeldes an und passt diese an gemessene Daten an, kann die Flugbahn einer Sonde innerhalb der MC rekonstruiert werden. Als erstes wurden 67 MCs, die im Zeitraum von 2001 bis 2007 auf ACE (Advanced Composition Explorer) trafen, anhand von Plasma- und Magnetfeldsignaturen identifiziert. In einem zweiten Schritt wurden drei Modelle an die Magnetfelddaten angepasst. Diese Modelle decken unterschiedliche Feldtypen (kräftefrei und nicht kräftefrei) und Geometrien (kreisförmige und elliptische Grundflächen) ab. Als erstes verglichen wir die Resultate der Modellanpassungen für die drei Modelle.

Unterschiede in der Element- und Ladungszusammensetzung von MCs in Bezug auf normalen Sonnenwind sind seit längerem bekannt (z. B. erhöhte Eisenladungszustände, erhöhtes O^{7+} zu O^{6+} Verhältnis und erhöhtes Verhältnis von Alphateilchen zu Protonen). Wir stellen uns jetzt die Frage, ob diese Unterschiede aus Durchflügen durch unterschiedliche Teile der MCs oder aus unterschiedlichen Entstehungsgeschichten resultieren. Unter Verwendung der Modellanpassungen und von mit SWICS (Solar Wind Ion Composition Spectrometer) gemessenen Kompositionsdaten mit einer Zeitauflösung von 1h können wir positionsabhängige Ladungs- und Elementzusammensetzungen bestimmen. Die grosse Variabilität entlang ähnlicher Flugbahnen deutet auf unterschiedliche Entstehungen der MCs hin. Wir konzentrieren uns auf den Einfluss von Flare-Assoziationen. Flare-Assoziationen führen zu erhöhten Ladungszuständen. Wir haben eine Abhängigkeit der Elementzusammensetzung vom mittleren Eisenladungszustand gefunden. Bei höherem Ladungszustand sind Elemente mit kleinem und hohem FIP (Erste Ionisationsenergie) angereichert. Als letztes betrachten wir die Symmetrie der Zeitreihen der mittleren Ladungszustände und stellen die Frage, ob sich das MC Plasma auf dem Weg von der Sonne zur Erde komplett durchmischt.

Abstract

Coronal Mass Ejections (CMEs) are violent releases of large plasma clouds at the sun. Up to now the mechanisms leading to the initiation of these ejections are not known. The interplanetary counterparts of CMEs are called ICMEs (Interplanetary CMEs). Approximately one third of all ICMEs detected in-situ at one AU distance from the sun show smooth rotation of the magnetic field vector (often accompanied by an enhanced magnetic field strength). These structures are called Magnetic Clouds (MCs). Their well ordered magnetic field makes them accessible to magnetic field modelling. Assuming a specific field topology and fitting models to the observed magnetic field data allows reconstruction of a spacecraft trajectory inside a MC. First we identified 67 MCs passing ACE (Advanced Composition Explorer) from 2001 to 2007 by looking for MC specific plasma and magnetic field signatures. In a second step the magnetic field data was fitted with three different models. These models cover different field types (force-free and non force-free) and different geometries (circular and elliptic cross sections). As a first result we make a comparison between the fit results of the three models.

Differences in elemental and charge state composition between MCs and ambient solar wind are well known (e. g. enhanced iron charge states, enhanced O⁷⁺ to O⁶⁺ ratios, and enhanced alpha to proton ratios). Now, we address the question, if these differences result from spacecraft trajectories through varying parts of the MC or from the MCs' diverse history of origins. By applying the magnetic field fit results and compositional data with a time resolution of 1h measured by SWICS (Solar Wind Ion Composition Spectrometer) position-dependent charge-state and elemental composition is calculated. The large inhomogeneity at similar trajectories indicates different origins of MCs. We concentrate on the influence of flare associations. Flare associations lead to mean charge states enhancements. We found a dependence of the elemental composition on the iron mean charge state, with an increase of low and high FIP (First Ionisation Potential) elements toward a higher mean charge state. In a last step we look for symmetries in the mean charge-states time series and address the question if the MC plasma does completely mix along the way from sun to Earth.

Contents

1. Introduction	1
1.1. Motivation of Addressed Topic	1
1.2. Inner Structure of the sun	3
1.3. Solar Magnetic Field	4
1.4. The Solar Corona	6
1.5. Coronal Disturbances	11
1.5.1. Flares	11
1.5.2. Coronal Mass Ejections	13
1.6. Interplanetary Coronal Mass Ejections and Magnetic clouds	16
2. Data Description	18
2.1. The ACE Mission	18
2.2. Instrumentation	19
2.2.1. SWICS	20
2.2.2. SWEPAM	20
2.2.3. MAG	21
2.2.4. EPAM	21
3. MC selection	22
3.1. Selection criteria	22
3.2. Overview of selected time intervals and signatures	25
3.3. Examples	28
4. Data Analysis	32
4.1. Magnetic Field Theoretical Background	32
4.2. MC modelling	34
4.2.1. Force-free Circular Model	34
4.2.2. Non Force-free Circular Model	35
4.2.3. Force-free Elliptic Model	36
4.2.4. Other Methods	38

Contents

4.3. Spacecraft position and free parameters	40
4.4. Minimum Variance Analysis (MVA)	42
4.5. The χ^2 -Fit	44
4.6. Determination of MCs Final Properties	46
4.7. Fit result errors	47
4.8. Calculation of ion count rates determined from SWICS	52
4.9. Determination of physical quantities from SWICS count rates	54
5. Results	56
5.1. Magnetic cloud fit results	56
5.2. Discussion of fit results	60
5.2.1. Velocity profiles from force-free elliptic model	64
5.3. Global MC model	64
5.4. Charge states	67
5.4.1. Iron charge states	67
5.4.2. Flare associations of MCs	69
5.4.3. Variability of Charge states	71
5.4.4. Oxygen and Iron freezing-in temperatures	75
5.4.5. Energetics of flare related MCs	78
5.5. Elemental Composition	78
5.5.1. Connection between elemental abundances and iron mean charge state	80
5.5.2. Solar cycle dependence of elemental composition	80
5.6. Differential Streaming in MCs	85
6. Discussion	88
6.1. Formation of MCs	88
6.2. Elemental variation with solar cycle	90
6.3. Mixing of plasma inside MCs	90
7. Summary and Conclusions	95
A. ICME detections with Solar Orbiter and Sentinels	98
A.1. Introduction	98
A.2. The model	100
A.2.1. CME generation	100
A.2.2. Evolution of ICMEs in the inner heliosphere	102
A.3. Results	103
A.3.1. Histograms	104

A.3.2. Time series	108
A.3.3. Systematic errors	109
B. Neutron detections with Solar Orbiter	114
B.1. Neutron production processes	114
B.2. Ion interactions with the magnetic field	116
B.3. Relativistic neutrons equations	117
B.4. Number of neutrons produced in solar flares	118
B.5. Number of solar flares	120
B.6. Modelling solar flare neutrons	121
B.7. Results for neutron detections with Solar Orbiter	121
B.8. Systematical error estimation	123
C. MC modelling fit results	126
C.1. Force-free cylindrical model	126
C.2. Non force-free cylindrical model	128
C.3. Force-free elliptical model	129
C.4. Literature values from different models	131
D. List of MC and solar wind interval plasma properties	134
D.1. MCs with flare association	135
D.2. MCs without flare association	137
D.3. Fast solar wind intervals	138
D.4. Slow solar wind intervals	139
E. List of MCs from 2001 to mid 2007 and their specific signatures	140

List of Tables

3.1. ICME in-situ signatures	23
4.1. Overview of magnetic field models	42
5.1. Elemental abundances in dependence of iron mean charge state	81
A.1. Spacecraft distances from the sun	103
A.2. ICME detection rates	105
A.3. Parameter distributions	107
B.1. Elements in neutron production processes	115
B.2. Neutron detections with neutron monitors	119
B.3. Influence of different neutron spectra	125
C.1. Fit results from force-free cylindrical model	126
C.2. Fit results from non force-free cylindrical model	128
C.3. Fit results from force-free elliptical model	129
C.4. Published fit results	131
D.1. Plasma properties of flare associated MCs	136
D.2. Plasma properties of MCs without flare association	137
D.3. Plasma properties of the fast solar wind intervals	138
D.4. Plasma properties of the slow solar wind intervals	139

List of Figures

1.1.	Principal structure of the sun	4
1.2.	Solar magnetic field at maximum and minimum	5
1.3.	Corona during solar eclipse	6
1.4.	EIT photograph of the sun	7
1.5.	Coronal magnetic field loops filled with plasma	8
1.6.	Electron density in the solar corona	9
1.7.	Ulysses solar wind measurements	10
1.8.	EIT photograph of a solar flare	12
1.9.	LASCO C2 image of a CME	13
1.10.	EIT photograph of a prominence	15
2.1.	ACE instrumentation and scientific goals	19
3.1.	Correlation between magnetic field variance and plasma β	25
3.2.	The MC from DoY 254.25-255.25, 2005	27
3.3.	The MC from DoY 119.02-119.57, 2001	29
3.4.	The MC from DoY 78.80-80.67, 2001	31
4.2.	Cylindric MC geometry	34
4.1.	Cylindrical, force-free MC field	34
4.3.	Cylindrical, non-force free MC field	35
4.4.	Elliptical, force-free MC field	37
4.5.	Elliptical MC expansion	38
4.6.	MC coordinate system	40
4.7.	GSE coordinate system	40
4.8.	Deviations from MVA direction	43
4.9.	MAG measurement uncertainties	46
4.10.	Magnetic field difference between models and data	48
4.11.	Fit for the MC on DoY 302, 2003	49
4.12.	Operating mode of the SWICS instrument	52

List of Figures

4.13. Example of an ET-Matrix at fixed E/q-ratio	53
5.1. Magnetic field model fits for the MC at DoY 119, 2001	57
5.2. Magnetic field model fits for the MC at DoY 94, 2001	58
5.3. Three different fit solutions for the MC at DoY 313, 2004	59
5.4. Comparison of fit results for angles θ, φ	61
5.5. Comparison of fit results for the shortest approach distance d_0 and for magnetic field strength at MC's centre B_0	62
5.6. Comparison of fit results for MC radius	63
5.7. Velocity profiles calculated from the force-free elliptic cross section model	65
5.8. Sketch of the relevance of different fit result in context of global MC structure	66
5.9. Iron mean charge state sorted by MC axis orientation	68
5.10. Comparison of average iron mean charge state to oxygen mean charge state	69
5.11. Iron charge-state distribution for two MCs	70
5.12. Variation of the iron mean charge state in dependence of solar wind speed	72
5.13. Determination of average charge-state distribution symmetry via ACF	73
5.14. Results from the ACF for the iron and oxygen mean charge state	74
5.15. Oxygen and iron freezing-in temperatures for the MC from DoY 304.07-304.50, 2003 . .	76
5.16. Comparison between GOES X-ray class, CME speed, and average iron mean charge state	77
5.17. Comparison of different elemental abundances to oxygen abundance	79
5.18. Temporal development of the Mg/Ne ratio in MCs and the solar wind	82
5.19. Temporal development of the Si/CNO ratio in MCs and the solar wind	83
5.20. Temporal development of the Mg/He ratio in MCs and the solar wind	84
5.21. Differential He streaming in MCs compared to the solar wind	86
6.1. Dependence of Mg/Ne ratio from AR age	89
6.2. Proton temperatures and thermal velocities at different distances	93
6.3. Dependence of MC plasma mixing on model parameters	94
A.1. Sentinel and SO orbits	99
A.2. Applied CME model	99
A.4. Radial ICME dimensions	100
A.3. CME occurrence parameter	101
A.5. CME parameter distributions	102
A.6. Alternative CME parameter distributions	104
A.7. ICME detection rates	106
A.8. Influence of different model parameters	107
A.9. Sunspot and ICME occurrence	109

List of Figures

A.10. Simulated ICME detections	110
A.11. Simulated ICME detections, part 2	111
B.1. Applied neutron spectrum	115
B.2. Angular distribution of escaping solar neutrons	116
B.3. Number of solar flares	120
B.4. Neutrons at SO and Earth	122

1. Introduction

The sun is a typical G2 main sequence star, which formed about five billion years ago. The source material had been processed by former generations of stars, creating a so called “metal rich” (elements heavier than helium) or population I star. The elemental abundance of the sun is about 90 % hydrogen and 10 % helium, with the heavier elements having a joint contribution of less than 1%. The most abundant heavy elements are oxygen and carbon, with oxygen being 1000 times rarer than hydrogen. The sun has an angular width of roughly 32 arcmin and therefore is the only star, where the disk can be spatially resolved by telescopes. Our immediate neighbour α -Centauri has a distance of 1.34 parsec from Earth, which is about $2 \cdot 10^5$ times the distance of sun to Earth, giving a angular extent of only 0.01 arcsec. Additionally the sun fills the solar system with its magnetic field and its plasma, the solar wind, making it the only star from which these properties can be measured in-situ by spacecraft.

In this section a short overview of the solar structure (sections 1.2, 1.4), the solar magnetic field (section 1.3), and CMEs (Coronal Mass Ejections) (section 1.5.2) or flares (section 1.5.1) as a result of solar activity is given. A summary of in-situ ICME (Interplanetary Coronal Mass Ejection) properties at varying distances from the sun (section 1.6) and the motivation for this work completes the chapter (section 1.1).

1.1. Motivation of Addressed Topic

Systematic observation of CMEs started with the beginning of the space age and, therefore, is a young field of scientific research. A Coronal Mass Ejection (CME) is “...an observable change in coronal structure that (1) occurs on a time scale of a few minutes and several hours and (2) involves the appearance and outward motion of a new, discrete, bright, white-light feature in coronagraph field of view” (citation from *Hudson et al. [2006]*). This phenomenological description of specific observations gets along without knowledge of the underlying physical processes. To this day, coronagraph observations remain an important source in the field of CME research. The large number of CMEs imaged by coronagraphs makes this data very suitable for statistical studies (e. g. LASCO onboard SOHO imaged thousands of CMEs since its launch in the mid 90s). From these images conclusions on CME structure and physical quantities such as total masses, velocities, and accelerations can be drawn. Remote observations in other wavelength regimes (EUV for thermal conditions in the corona, radio from electron emission at the local plasma frequency, X-rays from accelerated electrons), photospheric magnetic fields and in-situ

1. Introduction

measurements of energetic particles are additional sources of information for studying CME evolution. Nevertheless, many aspects concerning CME structure, CME initiation, and CME propagation are unsolved. One of the reasons are the limitations of the applied observation techniques. E. g. coronagraph images provide line-of-sight projections of the three-dimensional CME structure and their field of view starts at roughly one solar radius distance above the solar limb, making it impossible to image the early phases of CME evolution.

The knowledge of CME initiation and propagation is not just a question of academic interest. The energetic particles accelerated at CME shock fronts in the corona arrive at Earth only 10-15 minutes later. This radiation exposure is a severe danger to astronauts and can destroy satellite electronics. A better understanding of CME initiation will make longer advance warning times possible. After leaving the sun CMEs become ICMEs that can cause geomagnetic storms when they encounter the Earth's magnetosphere. These storms lead to a strong restructuring of Earth's magnetic field that can cause large area power supply breakdowns by magnetic induction effects. For a reliable prediction of these events we have to know how geometrical structure, magnetic field, and propagation of the CME develop in interplanetary space.

If an ICME traverses a spacecraft in-situ measurements can be carried out. Magnetic fields can be determined inside these structures for the first time. Some ICMEs ($\approx 1/3$ at 1 AU) show smooth rotation of the magnetic field vector and enhanced magnetic field strength. They are called Magnetic Clouds (MCs). Their well-ordered magnetic field makes it possible to model them as fluxropes (see chapter 4). These models make different idealisations. By comparing them we can draw conclusions about the model uncertainties (see section 5.2). Another unsolved question is the formation of these fluxropes. Are they already present in the pre-CME corona or do they form as a result of CME initiation (see section 6.1)? Furthermore, in-situ measurements allow the determination of charge-state and elemental composition inside MCs. The charge-state composition is formed while the CME travels through the corona (on timescales of hours) giving indications about thermal conditions during the CME initiation process. The elemental composition gives insight in the pre-CME conditions because the fractionation processes act on timescales of days (see *Wimmer-Schweingruber et al. [2006]*). The large variability in charge-state and elemental composition brings up the question, if these differences occur in consequence of different classes of CMEs or from spacecraft trajectories through different parts of the MC. The in-situ measurements only provide data along the one-dimensional spacecraft trajectory. With the help of magnetic field models we can try to reconstruct the spacecraft trajectory inside a MC and attempt to answer this question (see chapter 4 and 5).

CMEs are often accompanied by flares or disappearing filaments. Flare-associated CMEs are accelerated to high velocities within short timescales in the inner corona (impulsive CMEs) and other CMEs show a persistent but weak acceleration to lower velocities (gradual CMEs) (see *Pick et al. [2006]*). Is there a difference in elemental and charge-state composition between these classes (see chapter 5)?

ACE determines the plasma composition of MCs at a distance of 1 AU from the sun. If we want to draw conclusions from these measurements we have to answer the question: If we have an inhomogeneous elemental or charge-state composition at CME release, how much of this inhomogeneity is destroyed at this distance by mixing of the plasma (see section 6.3)?

1.2. Inner Structure of the sun

Figure 1.1 shows a schematic view of the solar structure. As the solar interior is not accessible to direct measurements (except solar neutrinos), indirect methods have to be applied. One method is helioseismology. By measuring the Doppler shift of photospheric spectral lines a solar pressure wave mode spectrum can be obtained. From these spectra the solar interior can be calculated similarly to seismology.

In the core, ranging from 0 to 0.2 solar radii, the sun produces its energy by nuclear fission, merging Hydrogen to Helium. The dominant reaction mechanism with a fraction of 90 % is the proton-proton chain. The generated neutrinos directly escape from the core, as their cross section for interaction with matter is very small. The generated gamma rays are absorbed and emitted many times, thereby changing their wavelength. It takes the radiation about 10^5 years to get from the core to the solar surface. This radiation generates an outward directed pressure. The radiation pressure together with the much larger thermal gas pressure balances the inward directed gravitational pressure, which otherwise would lead to the collapse of the sun. This will be the fate of the sun in ≈ 5 billion years, when fission will stop, leaving the sun's remnants as a white dwarf.

The radiative zone ranges from 0.2- 0.7 solar radii. In this zone convection is not present, and it shows rigid rotation. When temperature gradients become strong enough to drive convection the radiative zone ends. In the convection zone the ascending and descending plasma produces the granulation pattern seen in the photosphere. The plasma in the convection zone rotates differentially, with the time of circulation being smaller at the solar equator than at the poles. The movement of the plasma combined with differential rotation generates the sun's magnetic field. When strong magnetic fields emerge from the convection zone sunspots can be seen in the photosphere. Sunspots are areas on the solar surface appearing dark, because the temperature is lower than in the surrounding photosphere due to perturbation of the convection by the magnetic field. In the photosphere the visible light of the sun emerges. As a first approximation the emitted radiation can be described by a black body spectrum with a temperature of 5800 K. Imprinted on this continuous spectrum are the absorption lines of different elements, the Fraunhofer lines. From the strength of these absorption lines the elemental abundances in the photosphere can be calculated. The magnetic field at the solar surface can be determined from Zeeman-splitting of spectral lines. The photosphere has a radial width of only some hundred kilometers.

The solar atmosphere consists of the chromosphere and the corona, which will be discussed in more detail in 1.4.

1. Introduction

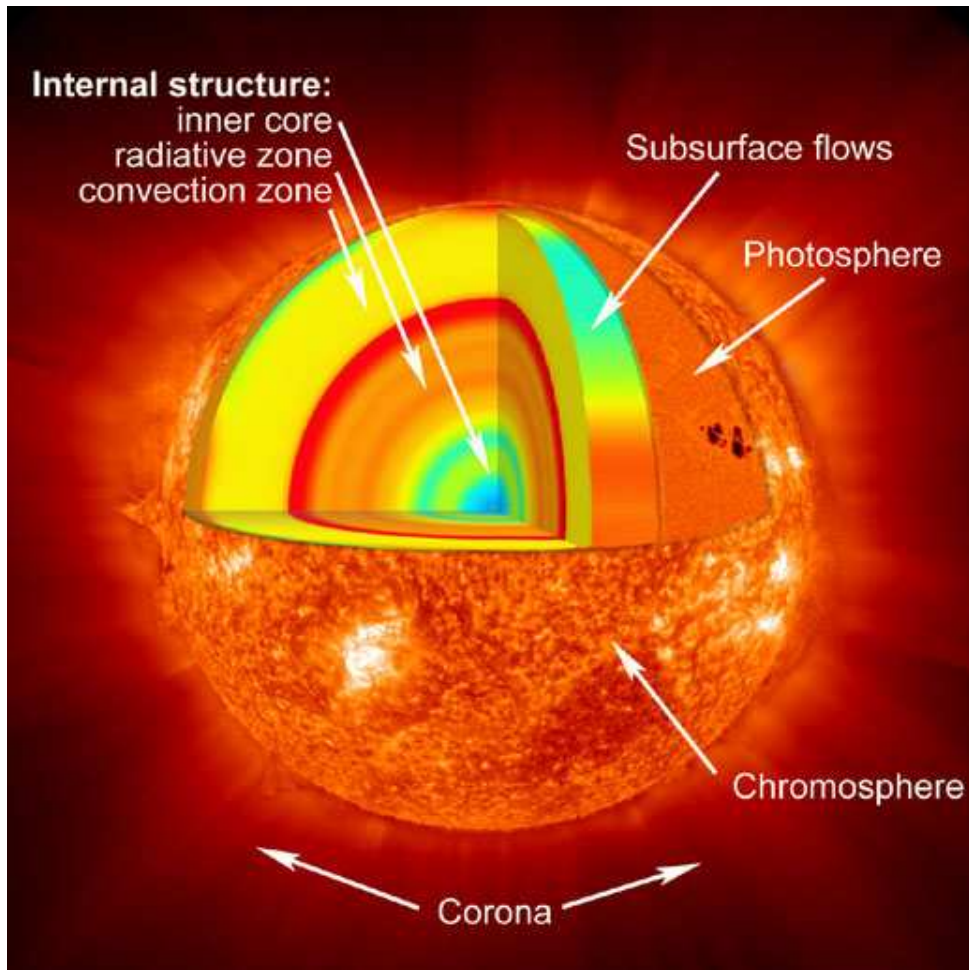


Figure 1.1.: The principal structure of the sun. The inner core generates the sun's energy by thermonuclear fusion processes at high temperatures ($\approx 10^7$ K) and densities (≈ 100 g/cm 3). Energy transport in the radiative zone is dominated by photon diffusion processes. In the convective zone energy is transported by hot plasma moving towards the solar surface and cold plasma sinking down again. The photosphere is the surface of the sun as seen in visible light ($T \approx 5800$ K). The adjacent chromosphere has its name from the red colour of the H α -emission. The solar corona consists of tenuous (10^9 - 10^7 particles cm $^{-3}$), hot plasma (some million K) only visible during solar eclipses. In this region the solar wind emanates. (taken from: http://www.nasa.gov/images/content/171925main_heliolayers_label_516.jpg)

1.3. Solar Magnetic Field

The solar magnetic field is generated in the convection zone by the moving plasma. The differential rotation as well as the convective motion of the plasma are necessary for field generation. A sufficient solar dynamo model has to explain the conversion of a poloidal to a toroidal field and back again, the rate of field emergence at the photosphere, the change in magnetic field complexity with the solar cycle,

1.3. Solar Magnetic Field

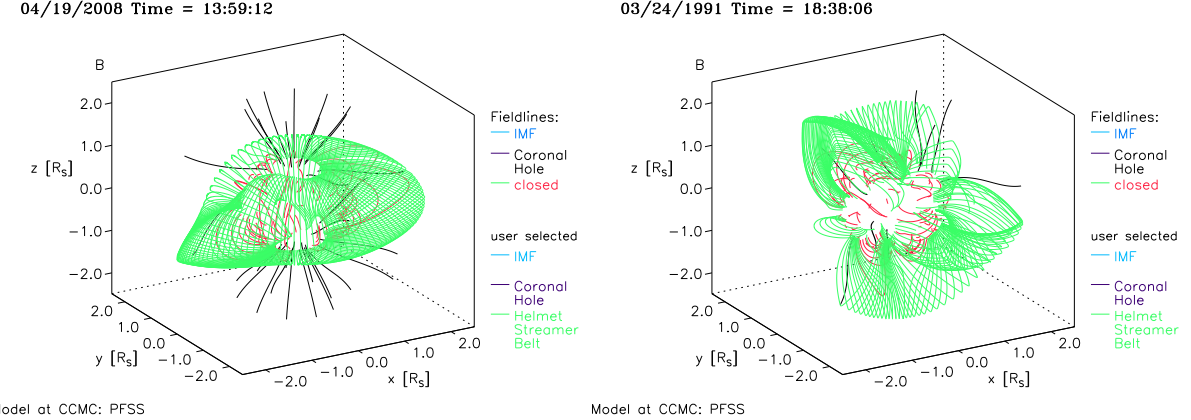


Figure 1.2.: Solar magnetic field at solar minimum conditions (left) and during solar maximum (right). At solar minimum the magnetic field is highly ordered, showing coronal holes near the poles and the streamer belt along the solar equator. At solar maximum regions of closed and open fields are mixed on smaller length scales, giving a more chaotic field alignment. The coronal magnetic fields are calculated from a PFSS (Potential Field Source Surface) model by Janet Luhmann using magnetograms, which exhibit the magnetic field in photospheric heights. (source: <http://ccmc.gsfc.nasa.gov/index.php>)

the polarity reversal after an eleven year solar cycle, the drift of the sunspots from large longitudes to small longitudes, the leading polarity in bipolar sunspot groups, and the axis tilt of sunspot groups with respect to the solar equator. A review on solar dynamo models can be found in Charbonneau [2005].

Figure 1.2 shows the variation of the coronal magnetic field with the solar cycle. The structuring of the magnetic field directly influences the corona. The plasma in the corona is bound to the magnetic field lines, as the plasma β is well below unity. Regions of closed field lines are filled with denser and hotter plasma. In these areas the slow solar wind emanates. Regions of open field lines have lower densities and cooler plasma, producing the fast solar wind. During solar minimum the global solar magnetic field can be well explained by a dipole field, while at solar maximum quadrupole and even octopole moments become important. During maximum the magnetic flux is enhanced, due to small scale dipole fields of the sunspot groups, giving rise to enhanced solar activity. This activity occurs when the magnetic field is reorganised by reconnection.

Coronal magnetic fields are often calculated with PFSS (Potential Field Source Surface) models. Assuming, that no currents are present (potential field) and that the magnetic field becomes radial at a source surface radius (normally chosen between 2-3 solar radii), as the solar wind plasma carries the frozen-in magnetic field away, the coronal fields are calculated from magnetograms, which measure the magnetic field in the photosphere. Outside of the source surface radius the field is described by heliospheric magnetic field models, such as the Parker-field.

1. Introduction



Figure 1.3.: Picture of a total solar eclipse. The photons from the photosphere are Thomson scattered by the plasma electrons in the corona. The larger the electron density is, the brighter the coronal features appear. As the intensity of scattered light is magnitudes below the intensity of photospheric light, the corona can only be seen during solar eclipses. (taken from: <http://www.mreclipse.com/SERphoto/TSE1999/image/T99comp2Bw.JPG>)

1.4. The Solar Corona

The first component of the solar atmosphere is the chromosphere. It extends from the photosphere up to a height of ≈ 2000 km. The emission is dominated by the red H_{α} -line, which gives the chromosphere its name. Unlike the expectation the temperature in the chromosphere raises from photospheric values to ≈ 20000 K. The chromosphere is separated from the corona by a thin transition region, in which the electron density declines very fast and the electron temperature rises to several hundred thousand K.

The corona can be seen with naked eye during the time of a total solar eclipse. Figure 1.3 shows an example. Since the beginning of space-based observations the corona can be permanently observed in white light with coronagraphs. These instruments shade the sun artificially with an aperture. The LASCO coronagraph onboard SOHO is capable of observing the corona from 1.1 to 30 solar radii distance for example. The total brightness of the white light corona varies with a factor of two between solar maximum and solar minimum, indicating a temporal variation of the total electron number in the corona.

Other instruments like TRACE (Transition Region and Coronal Explorer) or EIT (Extreme ultraviolet Imaging Telescope) image the emission of the hot coronal plasma ions in the extreme ultraviolet wavelength. From the ratio of two spectral lines of an element with different charge states present the

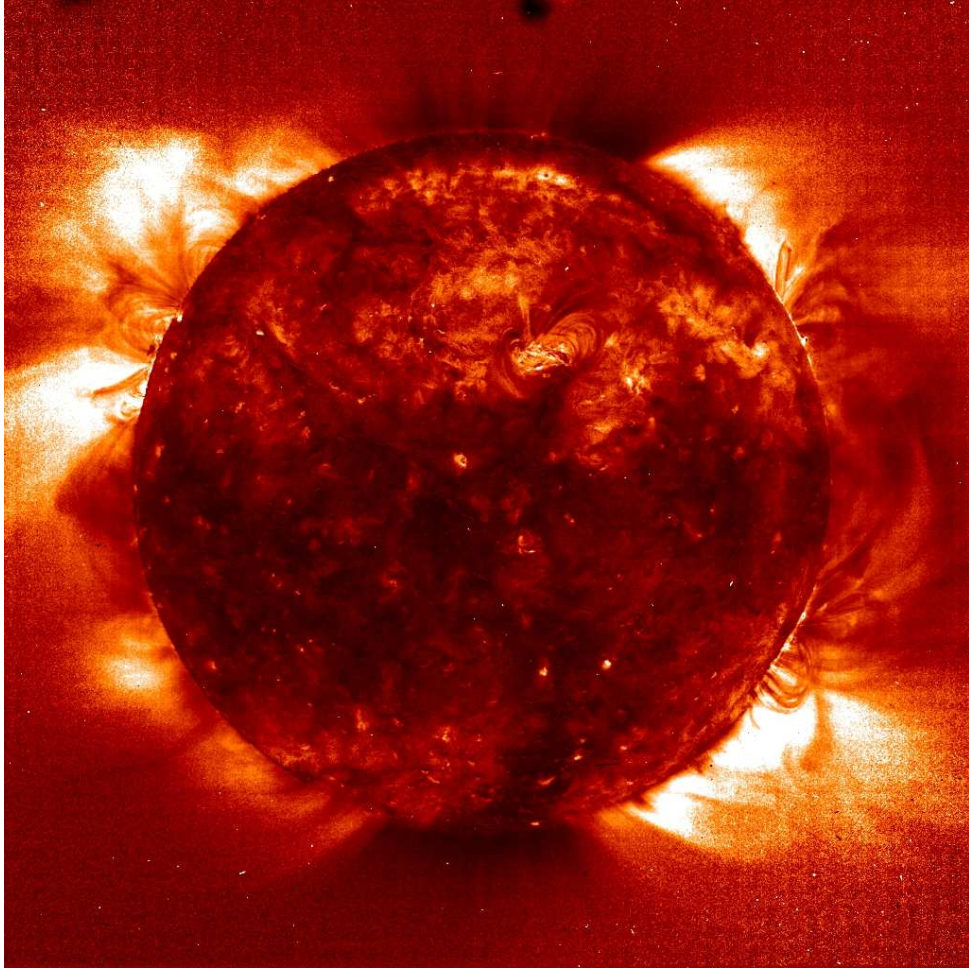


Figure 1.4.: A SOHO EIT full sun image recorded on 19 September 1997 at 01:00 UT. It shows the ratio of the Fe^{11+} line at 195 Å to the $\text{Fe}^{8+}/\text{Fe}^{9+}$ line at 171 Å. This line ratio is an indicator for the temperature distribution in the solar corona with dark areas being cooler and bright areas being hotter. Clearly visible are the coronal holes at the south and the north pole, which appear very cool. The numerous magnetic loops show highly varying temperatures. This shows how large the variation in coronal temperatures can be. (taken from: <http://sohowww.nascom.nasa.gov/gallery/SolarCorona/large/eit030.jpg>)

temperature of the plasma can be derived. Figure 1.4 shows an image for the ratio of a Fe^{11+} line to a $\text{Fe}^{8+}/\text{Fe}^{9+}$ line made with EIT. Brighter regions represent a stronger Fe^{11+} line, which means that the plasma is hotter in these regions. The image was taken during solar minimum and therefore two extended coronal holes are visible at the poles. Also visible are some very bright ARs (Active Regions) indicating the higher temperatures of the plasma in these regions. The temperature in coronal holes is lower than 1 MK, in closed-field regions 1-2 MK, and normally 2-6 MK for ARs. In the outer regions of the corona and the interplanetary medium the ion temperature decreases due to adiabatic cooling. At 1 AU distance from the sun protons typically show a temperature of roughly 0.05-0.1 MK. Note that dif-

1. Introduction

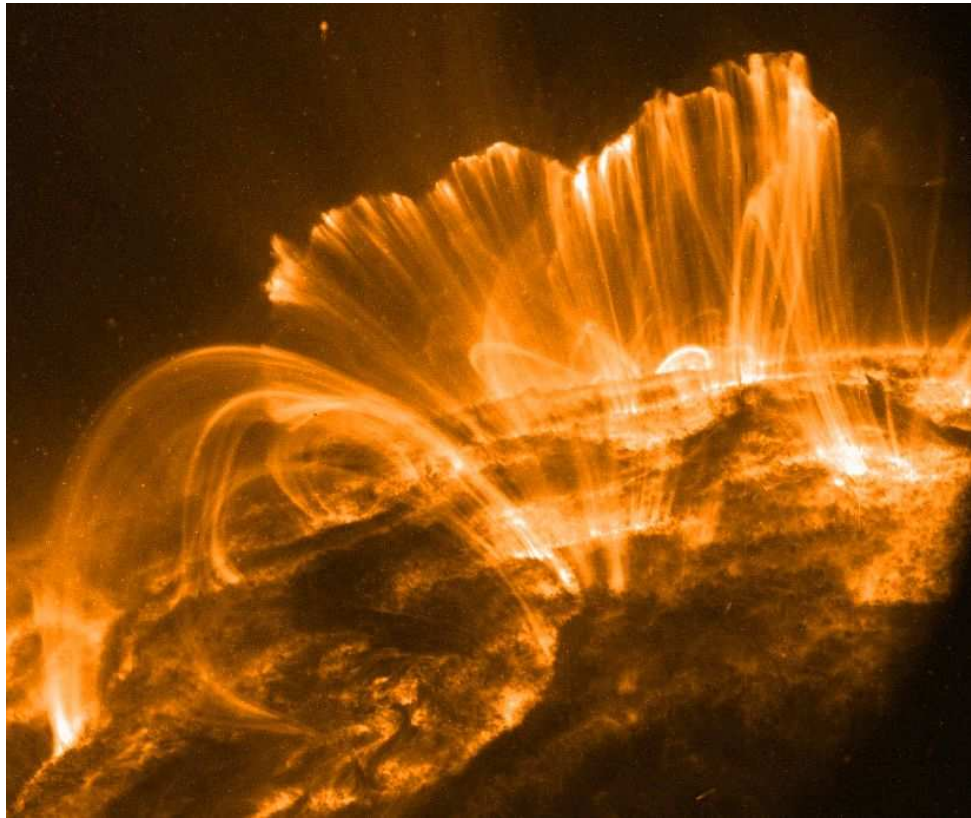


Figure 1.5.: This picture shows the coronal magnetic field in an active region anchored at the solar surface and filled with hot plasma after the occurrence of a M-class flare. The picture was made with the TRACE telescope at a wavelength of 195 Å (extreme ultraviolet light), observing a Fe^{11+} line, covering the temperature range of 0.5-2.0 MK. As the plasma cools down it will rain back to the solar surface, and the arches will become fainter and fainter. This flare was accompanied by the occurrence of solar energetic particles and an earthward directed CME, which caused a geomagnetic storm when arriving at Earth 31 hours later. (source: http://www.nasa.gov/images/content/113849main_trace2_lg.jpg)

ferent ion species have a different temperature at this distance as the different ion species are no longer in thermodynamic equilibrium and can be heated by wave-particle interactions. The general mechanism of coronal heating is still unknown. Possible explanations are wave energy dissipation or heating due to micro- and nanoflares.

As a result of low particle densities and relatively high magnetic field strengths (especially in ARs) the plasma β is below unity in the corona and the plasma is bound to the magnetic field lines. Figure 1.5 shows an image of magnetic field loops filled with hot plasma made with the TRACE telescope. The dense, hot plasma is captured at the field lines and illuminates them. As the plasma particles are bound to the field lines anchored in the photosphere, different loop system exist, that are nearly isolated, and loops filled with plasma of different temperatures can form. The electron density decreases from the

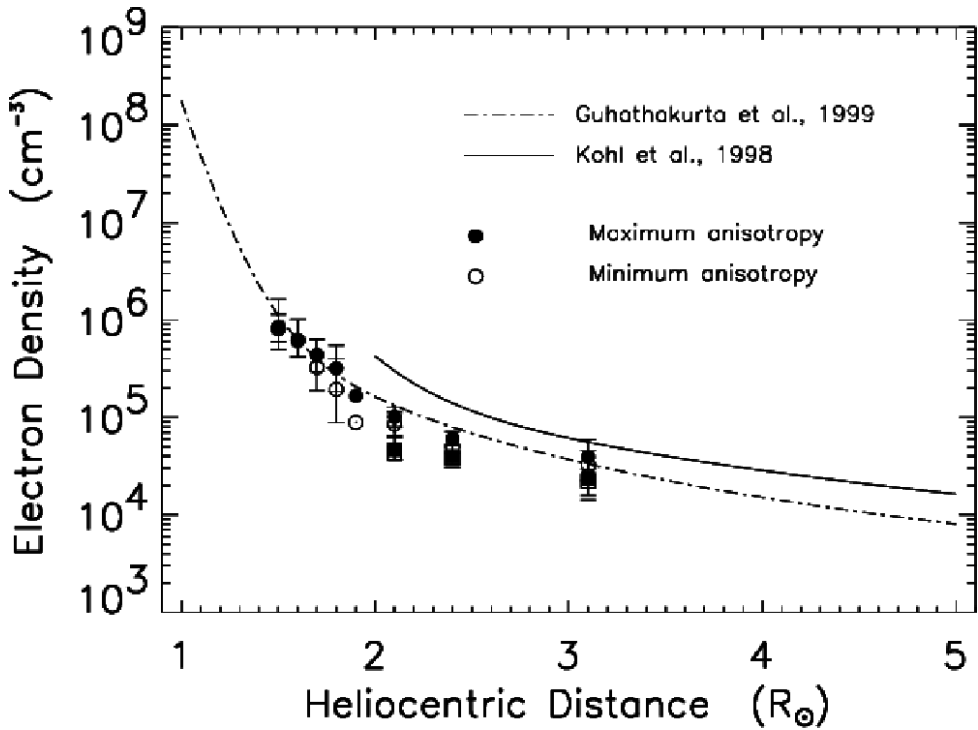


Figure 1.6.: This plot shows the electron density structure of the solar corona. The electron density is not constant over the whole sun. For example in coronal holes it is smaller than in ARs. As a result of dropping densities the charge states of different ions will freeze-in at specific distances. The figure is taken from Antonucci *et al.* [2004].

inner corona to the outer corona (see figure 1.6). Similar to the temperature the density depends on the magnetic field structure in a specific region. The density is lowest in open field regions, higher in closed field regions, and highest in ARs. As a result of decreasing electron densities and beginning of solar wind acceleration in the outer corona the charge states of ions freeze in. This means that at a distance specific for an ion pair the expansion timescale becomes smaller than the ionisation or recombination timescale. The elemental composition of the corona is not the same as in the photosphere. Fractionation processes modify the elemental composition. One of these effects is the First Ionisation Potential (FIP) effect, that leads to an enhancement of elements with low ionisation energies compared to elements with high ionisation energies.

As the photosphere the corona shows differential rotation, but only with a difference of roughly one day between polar and equatorial rotation periods.

The corona is the source region of the solar wind. The solar wind consists of coronal plasma, that is steadily accelerated from subalfvénic velocities to superalfvénic velocities in the outer corona. The radially outward moving solar wind sweeps the magnetic field away, which leads to the formation of the Parker-field. Two different types of solar wind are distinguishable. The slow solar wind is associated

1. Introduction

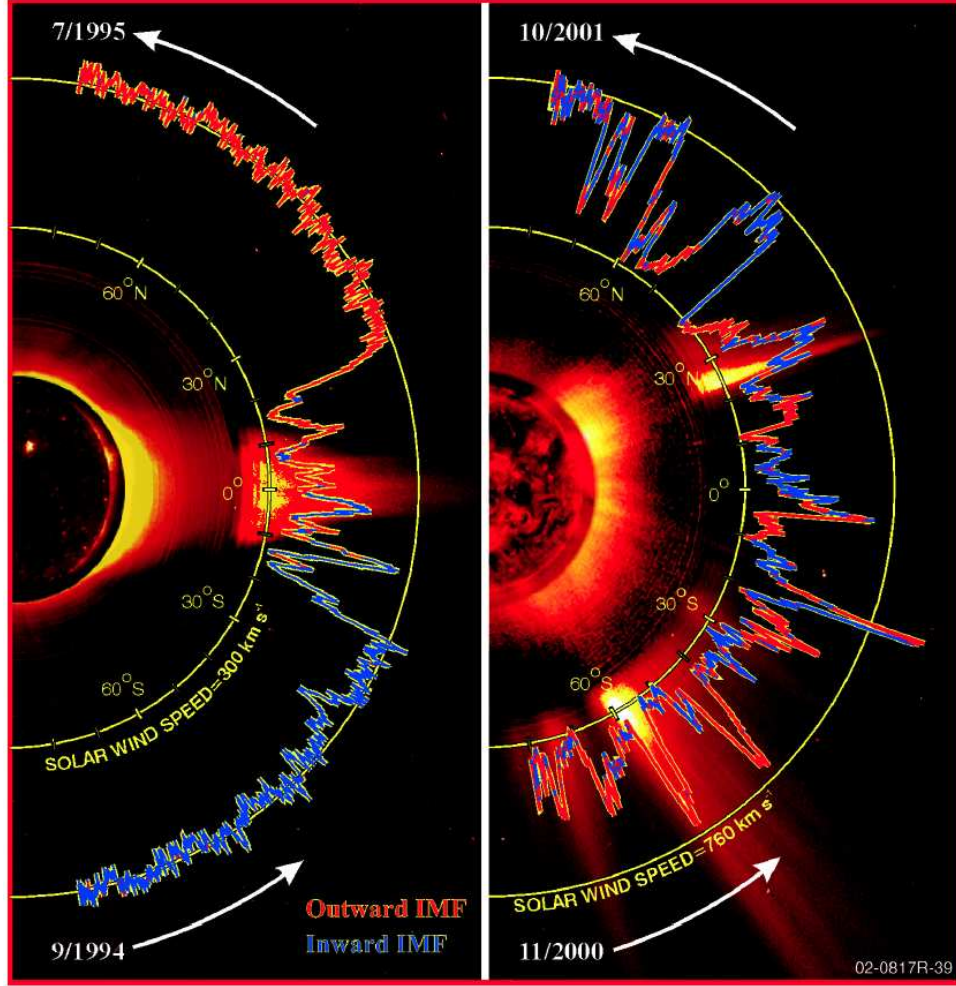


Figure 1.7.: Results from Ulysses solar wind velocity and magnetic field measurements. The left panel shows solar minimum conditions, with fast solar wind emanating from the coronal holes at the poles and slow solar wind originating from the streamer belt at the solar equator. During solar maximum coronal holes and streamers mix on the full solar surface, leading to a small scale variation between regions emanating fast and slow solar wind. As seen in figure 1.2 the magnetic field polarity is dipole-like during minimum and chaotic during maximum. (taken from: <http://solarprobe.gsfc.nasa.gov/solarwind.jpg>)

with regions possessing a closed magnetic field configuration. It reaches proton velocities of about 400 km/s, proton densities of 10 cm^{-3} , and proton temperatures of 0.05 MK at 1 AU distance from the sun. The fast solar wind has its origin in the coronal holes. It is much less variable than the slow solar wind and shows a proton velocity of 700 km/s, a proton density of 3 cm^{-3} , and proton temperatures of 0.1 MK at 1 AU distance from the sun. Surprisingly, the fast solar wind shows higher temperatures than the slow solar wind in interplanetary space, although it originates from cooler coronal regions. Figure 1.7 shows the variation between slow and fast solar wind streams at solar maximum and minimum determined by Ulysses. For further informations about the solar corona see *Schwenn and Marsch [1990]* or *Aschwanden*

[2004] for example.

1.5. Coronal Disturbances

Especially during times of solar maximum the corona releases large amounts of energy within short timescales. The energy results from reconfigurations of the magnetic fields that take place from time to time. These reconfigurations are associated with a variety of observable phenomena like particle acceleration, electromagnetic radiation at different wavelengths, and local changes in the coronal structure. Flares are local brightenings lasting for some minutes to half an hour (see section 1.5.1). CMEs are large clouds of plasma blasted away from the sun (see section 1.5.2). These clouds can be observed in-situ by spacecraft in interplanetary space and are called ICMEs (see section 1.6).

1.5.1. Flares

When the magnetic field configuration in ARs becomes unstable, reconfiguration of the field via reconnection takes place. The reconnection changes the magnetic field from non-potential state back to potential state, leading to a release of energy. A requirement for fast magnetic reconnection is anomalous resistivity in the current sheet, where reconnection takes place. The processes leading to the rapid onset of magnetic reconnection in flare regions are not fully understood up to now. Different driver mechanisms have been suggested, including a rising prominence above the neutral line (CSKHP model), the emergence of new magnetic flux from the photosphere (Emerging Flux Model), the footpoint motion of magnetic field lines toward the neutral line (Equilibrium Loss Model) or footpoint motion parallel to the neutral line in an initially quadrupolar magnetic field configuration (Magnetic Breakout model). For further details see *Aschwanden* [2004]. After reconnection is triggered, the occurring currents lead to primary plasma heating and particles are accelerated by wave-particle interactions and at the developing shocks.

In a second step the accelerated particles and thermal conduction fronts propagate downward to the chromosphere, heating the dense, cool chromospheric plasma. This leads to the emission of hard X-rays from bremsstrahlung of energetic electrons. The chromospheric plasma is heated to temperatures of 5-35 MK during this step leading to an expansion into the coronal flare loops due to the resulting overpressure. The high temperatures result in emission of soft X-rays from the plasma filled flare loops. When the heating rate becomes smaller than radiative and conductive losses, the flare loop plasma temperature starts to decrease. Therefore, the wavelength of the maximum emission is shifted towards longer wavelengths with time. It only takes a few minutes to shift the emission maximum from hard X-rays to EUV (Extreme Ultra Violet). A picture of a large flare taken at a EUV wavelength is shown in figure 1.8.

Another aspect is neutron production within flare loops. Shock accelerated protons are mirrored between magnetic field footpoints of the flare loops and can produce energetic neutrons (MeV to GeV range)

1. Introduction

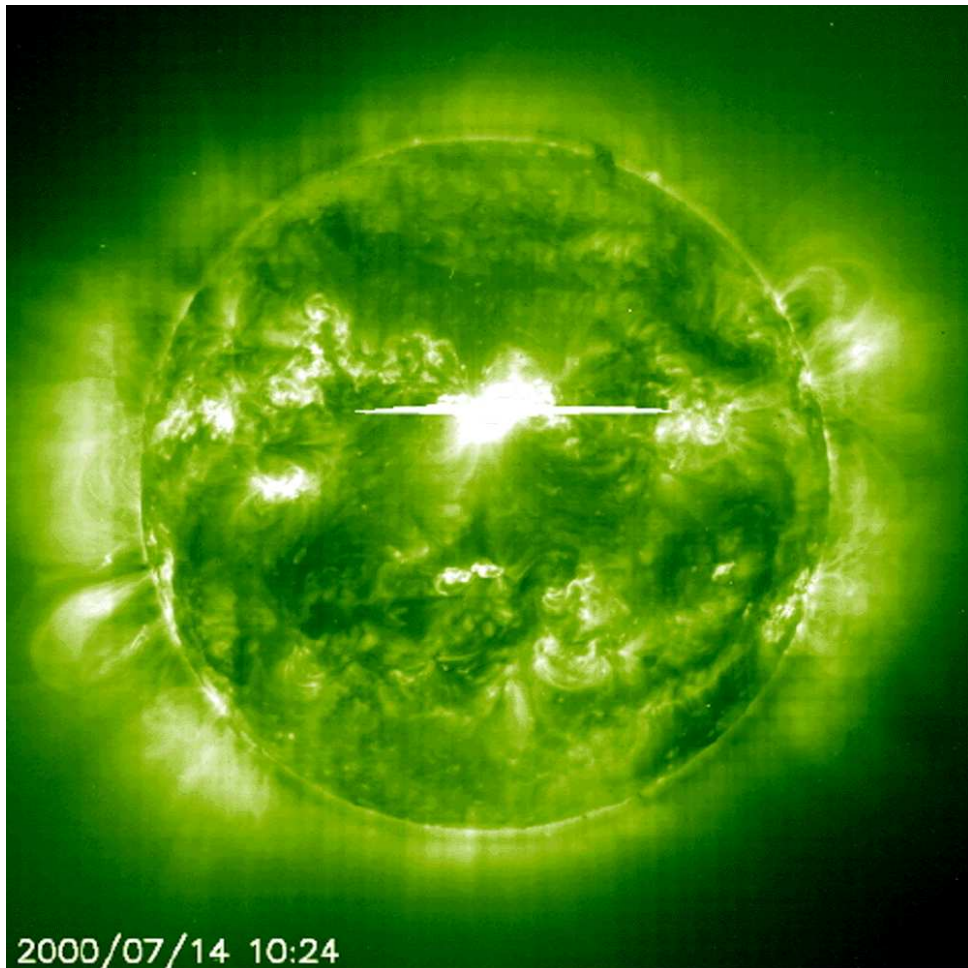


Figure 1.8.: This SOHO EIT image of a X-class solar flare was made at a wavelength of 195 Å. The flare region shows a short extreme brightening. The large energy release by magnetic reconnection heats the plasma at the flare site to more than 10^7 K and occurring shocks accelerate particles from MeV to GeV energies. If magnetically connected, these particles arrive at Earth within about 10 to 15 minutes. Flares often are accompanied by CMEs. (source: http://www.radiohc.org/Distributions/Dxers/july14/flare_eit195_big.gif)

when hitting heavier nuclei in the chromosphere. The relativistic neutrons are able to reach Earth, before they decay (see appendix B).

Flare strength is often quantified by the peak flux in the 1-8 Å range determined with the GOES satellites. The strongest flares are called X-class flares with a peak flux exceeding 10^{-4} W m $^{-2}$, M-class flares exceed 10^{-5} W m $^{-2}$ and C-class flares exceeding 10^{-6} W m $^{-2}$. Smaller flares are called B-class flares (peak flux $> 10^{-7}$ W m $^{-2}$) and A-class flares (peak flux $> 10^{-8}$ W m $^{-2}$). A-class flares can only be identified during times of low background flux. X-class flares are about 10 times less frequent than M-class flares, while M-class flares are ≈ 10 times less frequent than C-class flares. The solar flare rate

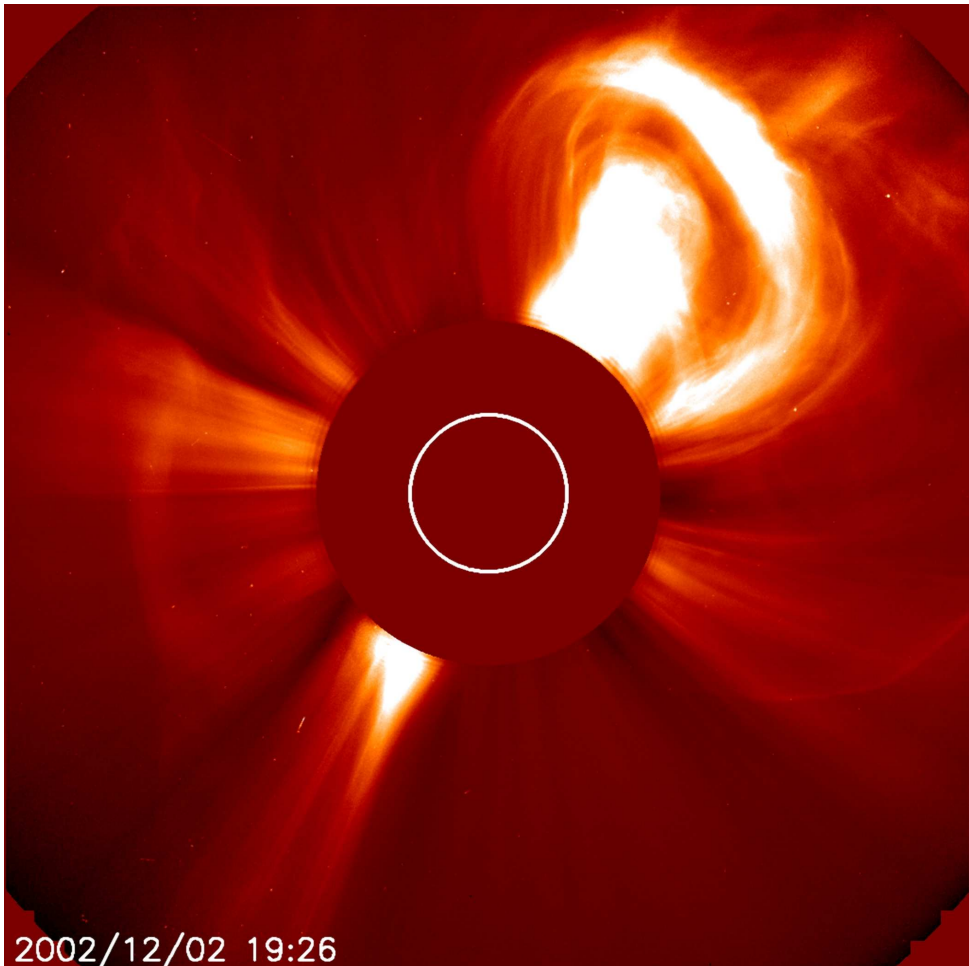


Figure 1.9.: This LASCO C2 image shows a large CME blasting off into space on December 2nd, 2002. It presents the classic three part structure of a CME. A bright leading edge, consisting of compressed plasma, a dark cavity, which sometimes can be identified as the MC plasma measured at 1 AU, and a bright core, which is made up of the erupting prominence/filament remnants. The speed of a CME near the sun typically varies between 100-2000 km/s. (source: <http://sohowww.nascom.nasa.gov/gallery/images/20021202c2cme.html>)

varies with a factor of roughly 20 between solar minimum and maximum. Furthermore, the flare number shows much higher fluctuation than the sunspot number.

Most flares can be directly associated with areas of sunspots at the solar surface (Active Regions), occurring between 30 degrees northern and southern latitude.

1.5.2. Coronal Mass Ejections

While normal solar wind is a steady stream of plasma leaving the sun, CME plasma is released in explosive events. They are often closely associated with flares. This is no one-to-one correlation, as 40 % of

1. Introduction

all flares exceeding M-class level do not show an associated CME, and not all CMEs can be related to a flare. The average mass carried away by a CME is in the range of 10^{11} to 10^{13} kg. As the flare occurrence rate, CME frequency varies with solar cycle. At solar maximum the number of CMEs is almost 4-5 per day and a factor of about 10 smaller at solar minimum (*Schwenn et al. [2006]*). Therefore CMEs account only for solar wind mass loss of a few percent compared with normal solar wind. The initial velocity of CMEs near the sun typically is in the range of 100-2000 km/s.

CMEs are remotely imaged by coronagraphs, showing the electron density structure of the CME (see section 1.4). Many different geometrical shapes can be distinguished, including bubbles, semi-shells and helical structures. Figure 1.9 shows an image of a three-part structured CME with the bright leading edge, the dark cavity, and a bright core, which is a quite often observed CME geometry. CMEs originating from central latitudes and longitudes are often observed around the whole solar disk and are called halo CMEs. With high probability they are directed earthward or anti-earthward. As coronagraph images give just integrated line of sight density information, projection effects play an important role in geometric appearance and determination of CME speeds. Only CMEs originating from the solar limb are seen with their true velocities and angular extent, while CMEs arising near the solar centre show lower projected velocities and larger angular extent (see appendix A.2.1).

Measured accelerations of CMEs give direct evidence for forces acting on them. Most of the acceleration occurs within a few solar radii. Acceleration profiles of CMEs can be very different. The so called gradual events show persistently weak acceleration, while impulsive CMEs show large accelerations (up to 5 km/s^2) lasting for tens of minutes. This behaviour indicates different release and acceleration mechanisms (*Schwenn et al. [2006]*).

Several CME initiation models exist. Early models suggested sudden plasma heating and subsequent expansion due to thermal pressure as triggering mechanism. Most of todays models assume a slow build up of magnetic energy until a critical point is reached and magnetic energy is released within short timescales. As coronal magnetic fields cannot be observed directly, the suggested mechanisms for the theoretical models are quite different. One general problem of the storage and release model is the Aly-Sturrock energy limit. A fully opened force-free magnetic field is the most energetic configuration. This would make CME initiation just by magnetic field reorganisation impossible. Ways around this energy limit are a non force-free corona, an only partial opening of the field lines, or non-ideal MHD processes as reconnection.

In the magnetic flux cancellation model, a fluxrope is formed by subsequent flux cancellation along the neutral line, near the base of a helmet streamer. These fluxropes are able to support cool, dense chromospheric plasma in the corona. When seen above the solar limb these structures are called prominences, when located on the solar disk they are called filaments. Figure 1.10 shows an example of a prominence, taken at a He+ emission line. Under normal circumstances He is fully ionised at these heights. Filaments are oriented almost parallel to neutral lines and CMEs show an association of 40-50 % with disappear-

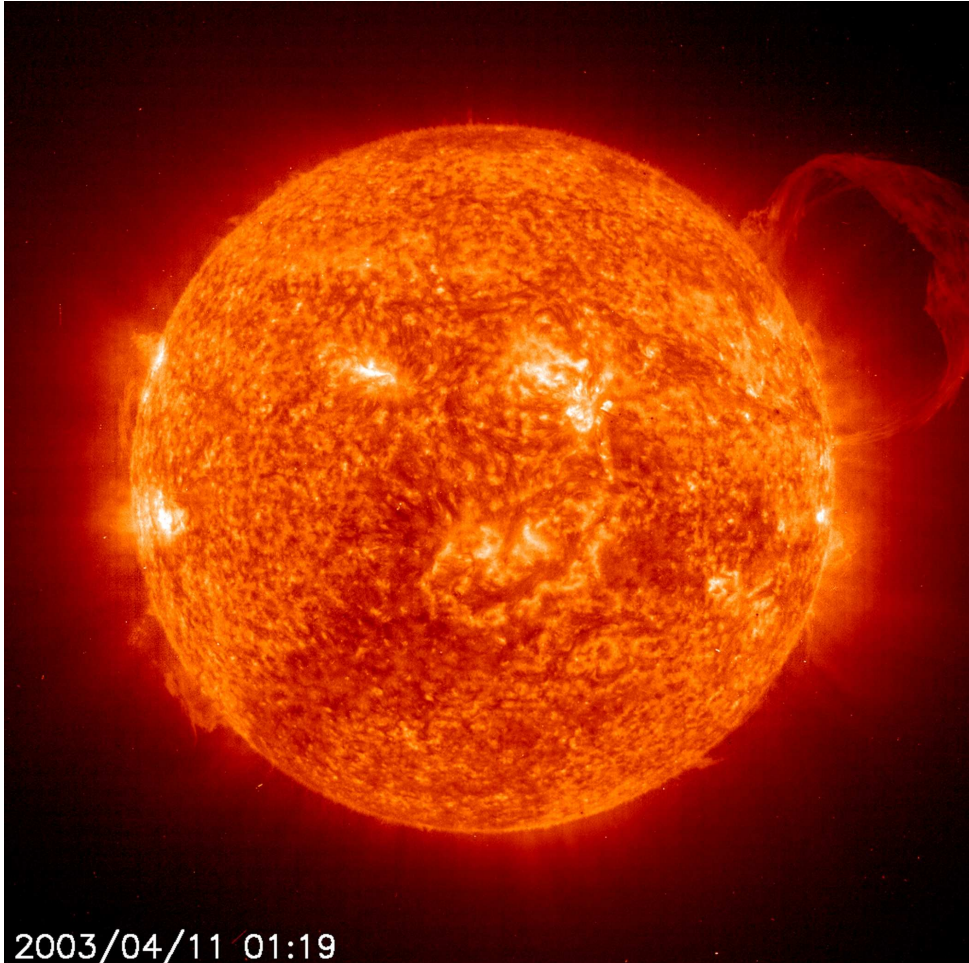


Figure 1.10.: A picture of a prominence taken by the SOHO EIT instrument on April 11th, 2003. The image shows He⁺ emission at a wavelength of 304 Å. The prominence consists of cool, dense plasma, kept in shape by coronal magnetic fields. These structures can be stable for some weeks before disappearing. When the magnetic field becomes unstable the prominence is emitted as part of a CME. The same structure located in front of the solar disk instead of being located at the limb, is called a filament. Filaments appear dark against the solar disk due to absorption. (taken from: <http://sohowww.nascom.nasa.gov/gallery/images/large/304arch.jpg>)

ing filaments (*Alexander* [2006]). As the fluxrope magnetic field becomes stronger by continuous flux cancellation of the overlying field an upward pressure evolves pushing the fluxrope to a higher equilibrium position. When reaching a point, where no nearby equilibrium position is accessible, the fluxrope erupts as a CME. Significant magnetic energy release could result from reconnection at the current sheet developing between fluxrope and sun. This model needs just a dipolar field configuration.

A model with a quadrupolar magnetic field configuration is the magnetic breakout model. The basic configuration is an initial potential field containing four flux systems and one coronal null point (needed for

1. Introduction

reconnection). By introducing a sheared arcade or a fluxrope, a magnetic field component parallel to the neutral line emerges (formation of a filament channel). An upward pressure develops which compresses the overlying potential field. Expanding the potential field increases the downward tension keeping the system in equilibrium. Additionally, the coronal null point evolves toward a current sheet. When the current sheet becomes thin enough, reconnection starts, removing the overlying magnetic flux from the central arcade to the neighbouring ones and reducing the downward tension at the central arcade. This leads to further expansion of the sheared field, triggering faster reconnection of the overlying field. The result is the explosive release of the filament channel as a CME. As further consequence a current sheet forms between sun and erupting CME, activating normal flare reconnection.

Another possible mechanism is CME initiation due to the kink instability. Starting with a fluxrope and an overlying arcade, the footpoints of the fluxrope are rotated. This rotation winds up the field lines of the fluxrope. The magnetic pressure at the lower boundary of the fluxrope exceeds the pressure at the higher boundary. When the twist of the magnetic field lines exceeds a critical amount, the overlying field is pushed aside and the fluxrope lifts off as a CME, possibly starting reconnection behind it. See *Aschwanden [2004]*, *Aschwanden et al. [2008]*, *Forbes et al. [2006]* for more information about CME initiation.

Fast CMEs are able to drive shocks near the sun. These shocks accelerate ions (up to GeV/nuc) and electrons (up to MeV) to high energies (gradual SEP (Solar Energetic Particle Event)), which leave the sun along open magnetic field lines. While the shock moves through the corona, radio emission at the local plasma frequency and its first harmonic occurs (Type II radio burst). As the coronal density decreases with larger distances, the wavelength of the radio emission increases with time. After a CME release the corona often shows dimming in EUV and soft X-rays. This behaviour can be interpreted as rarefaction of the CME launch site and can persist for some days. Dimming is strongest for plasma with temperatures of ≈ 1 MK, indicating that the ejected material was located at coronal heights.

1.6. Interplanetary Coronal Mass Ejections and Magnetic clouds

When a CME has left the sun and is travelling through the heliosphere, it can be detected by in-situ measurements as an ICME. Magnetic Clouds (MCs) are a subclass of ICMEs (about 30 %), showing smooth rotation of the magnetic field vector, combined with a low variance of the field, and often enhanced magnetic field strength. Therefore the magnetic field can be modelled with analytical functions (see section 4). Up to now it is not clear if MCs are an own class of ICMEs, or if they are part of each ICME but missed by the observing spacecraft in most cases. Chapter 3 describes the determination of MC timeframes by means of different in-situ properties compared to normal solar wind.

The Helios spacecraft made in-situ determinations of solar wind properties within the inner heliosphere (0.3-1 AU). ACE, WIND and the two STEREO spacecrafts are located at a distance of 1 AU from the sun within the ecliptic plane. Ulysses has an polar orbit with distances varying roughly between 1.5 to

1.6. Interplanetary Coronal Mass Ejections and Magnetic clouds

5.5 AU. Measurements in the outer heliosphere were carried out by the Voyager 2 spacecraft. In the last years the SMEI mission imaged ICMEs in white light at large solar distances (exceeding 1 AU) possible. It is an ongoing debate, if the commonly seen three part structure of a CME near the sun (see figure 1.9) can be identified in the in-situ data. The bright front could be compressed ambient solar wind plasma, the dark cavity the MC plasma itself, and the bright core could be filament remnants. Therefore one would expect low charge-state plasma trailing the MC. This behaviour is observed only in rare cases.

As the ICME travels in the ambient solar wind, interactions between these two streams take place. In the inner heliosphere (below 1 AU) ICMEs expand to an average radial size of 0.25 AU at 1 AU, what often can be observed as linear velocity decrease between leading and trailing edge at 1 AU. This expansion leads to a density decrease faster than R^{-2} . SMEI observations indicate no significant variation of angular extent to 1 AU (see *Howard et al.* [2007], *Webb et al.* [2006]). The ICME speed does not change significantly between 0.3-1 AU. Comparison between CME and ICME speed shows that fast CMEs decelerate on their way to 1 AU, while slow CMEs are accelerated due to the interactions with the solar wind. Magnetic field strength and proton temperature show a smaller decrease with distance than the normal solar wind. This contradicts the expectation of a faster temperature decrease compared to normal solar wind in the case of adiabatic cooling, indicating additional heating of ICME plasma.

An often observed feature in ICMEs is the presence of bidirectional suprathermal electrons. This indicates, that the footpoints of the magnetic field are still anchored at the sun, when the ICME has reached 1 AU, and electrons are mirrored in this magnetic bottle.

Fast ICMEs drive shocks in the interplanetary medium. These shocks accelerate particles, cause radio emission, and precede the ICME leading edge by a few hours. The compressed sheath plasma directly following the shock is dense, hot and has a large magnetic field strength, showing high directional fluctuation. When the magnetic field in the sheath region has a large negative B_z component, it interacts with Earth's magnetosphere leading to the formation of geomagnetic storms. These storms can cause severe damage to satellites or lead to the breakdown of electrical power supply.

Observations beyond 1 AU indicate further increase to a final radial size of about 2 AU at 10-15 AU distance. The speed itself changes very slowly with increasing distance. Ulysses found signatures of ICME overexpansion in high latitude observations (see *Balogh et al.* [2001]), with a rarefaction region developing at the ICME centre. As the ICMEs move outward they catch up with each other or with CIRs (Corotating Interaction Regions) to form Merged Interaction Regions (MIRs) or GMIRs (Global MIRs), surrounding Earth and sun as a quasi-spherical shell. These GMIRs act as diffusive barriers for galactic cosmic rays, leading to a Forbush decrease (Fast reduction of galactic cosmic ray flux > 5%). See *Forsyth et al.* [2006] and *Gazis et al.* [2006] for further information about ICMEs.

2. Data Description

In this chapter a short summary of the ACE mission and the instruments used for the determination of MC properties is given. In section 2.1 general facts about the mission, instrumentation, and the scientific goals are described. In section 2.2 the mode of operation for all instruments, which have been used in the context of this work, are discussed in more detail.

2.1. The ACE Mission

ACE was proposed in 1986 as a part of the Explorer Concept Study Program. To cut down the budget of the project some of the instruments onboard are flight spares of other missions (for example SWICS is the flight spare from the Ulysses mission and MAG the flight spare from the WIND mission). The ACE spacecraft was launched on August 25, 1997 by a Delta II rocket. The final orbit is around the L1 libration point, which is located 1.5 million km sunward of the Earth. The major semi-axis of the orbit is about 150000 km, while the minor axis is about 75000 km. One orbiting period lasts ≈ 180 days. The spacecraft spins with 5 rpm and the spin axis generally is pointing toward the sun (within an angle of 20°). Thus positioned outside earths magnetosphere, undisturbed observations of the different particle species present in interplanetary space are possible.

The scientific payload of ACE consists of nine instruments: CRIS (Cosmic Ray Isotope Spectrometer), SIS (Solar Isotope Spectrometer), ULEIS (Ultra Low Energy Isotope Spectrometer), SEPICA (Solar Energetic Particle Ionic Charge Analyser), EPAM (Electron, Proton and Alpha Monitor), SWIMS (Solar Wind Ion Mass Spectrometer), SWICS (Solar Wind Ion Composition Spectrometer), SWEPAM (Solar Wind Electron, Proton and Alpha Monitor), and MAG (Magnetometer). In figure 2.1 the energy ranges of the instruments are shown together with the energy range of different particle species. As seen from the instrumentation the attention lies on in-situ particle measurements. The main scientific goals are:

- Elemental and isotopic composition of the different source populations (solar composition, composition of the local interstellar medium, ...).
- Origin of the elements and the subsequent evolution (solar system evolution, galactic evolution, nucleosynthetic processes, ...).
- Formation of the solar corona and solar wind acceleration (fractionation processes, variability of coronal conditions , ...).

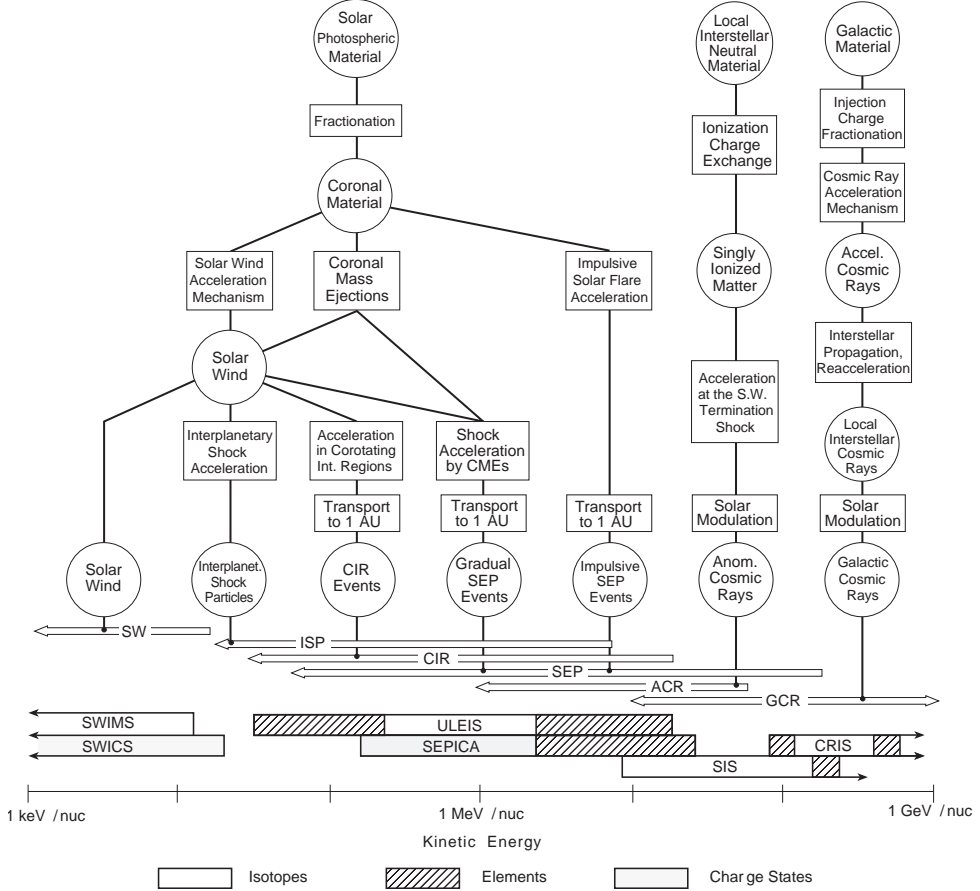


Figure 2.1.: This diagram shows the various particle components present in interplanetary space, their origin, the distinct mechanisms acting on them, and the energy ranges covered by the different instruments onboard ACE (Taken from *Stone et al.* [1998]).

- Particle acceleration and particle transport (fractionation during SEPs and interplanetary acceleration, constraints on acceleration models, ...)

Due to its position between sun and earth the spacecraft can be used for space weather forecasting, giving an advance warning time of about 1h before the appearance of a geomagnetic storm, caused by the interaction of the interplanetary magnetic field and Earth's magnetosphere. For more details about the whole mission see *Stone et al.* [1998].

2.2. Instrumentation

Results from EPAM, SWEPAM, and MAG have been used for MC boundary determination (see chapter 3). Additionally, the MAG data was used for MC fitting (section 4.2). SWEPAM results give the basic plasma properties, such as proton density, speed and temperature. Calculation of elemental and charge-state composition for minor ions (all ions except H, He) is done with SWICS. From SWICS Level 1 data

2. Data Description

is applied, which has to be processed before physical quantities are obtained (see sections 4.8, 4.9). For the other instruments Level 2 data was used, which is available at the ACE science centre¹. The principle mode of operation for these four instruments is shortly discussed, to get an idea of the their capabilities.

2.2.1. SWICS

Ions enter SWICS through a collimator, that selects the entrance trajectories of the particles. Next they enter an electrostatic deflection system, which selects particles of a defined E/q -ratio. The instrument has two channels: One for H and He ions (Auxiliary Channel) and the main channel for all ions except H. The deflection voltage for the main channel can be varied from 46 – 6300 V. There are 60 logarithmically spaced voltage steps during a measurement cycle of 12 min. After leaving the deflection system the ions are post-accelerated to lift their energy above the threshold of the solid-state detector (SSD) (\approx 25–35 keV). The post-acceleration voltage is in the range of 15 to 30 kV. The ions fly through a thin carbon foil (\approx 1.5 $\mu\text{g cm}^{-2}$), emitting secondary electrons, which are measured by a micro-channel plate. This triggers the start signal for the ToF (Time of Flight) determination. After a distance of 10 cm the ion enters one of the three solid state detectors (auxiliary channel only one SSD). Again emitting secondary electrons, these electrons trigger the stop signal for the ToF measurement. In the SSD the total energy of the ion is determined. From these measurements the incident energy, the charge state, and the mass of the ion can be calculated.

The instrument is capable of measuring ions with an energy of 0.49–100 keV/charge (0.16–15.05 keV/charge in the auxiliary channel). The ADC (Analog to Digital Converter) works with a 256 channel energy resolution and a 1024 channel ToF resolution. For further information about SWICS see *Gloeckler et al.* [1998].

2.2.2. SWEPPAM

The SWEPPAM instrument consists of two parts. SWEPPAM-I makes 3-d measurements of protons and alpha particles, SWEPPAM-E makes 3-d measurements of electrons. Both parts have a similar construction. The particles enter the instrument through a fan-shaped entrance aperture and then are deflected by a spherical section electrostatic analyser (ESA). Particles having an E/q and angle of incidence to pass the ESA are detected by channel electron multipliers (CEMs). SWEPPAM-I has a total of 16 CEMs with an angular separation of 5 degrees, SWEPPAM-E has 7 CEMs with an angular separation of 21 degrees. Depending on which of the CEMs detects the particle the polar angle of incidence is determined. As the spacecraft spins, the entrance aperture rotates selecting particles with different azimuthal angles. Thus, the CEM number, the spin phase, and the ESA step level permit 3-d measurements. SWEPPAM-I covers an energy range of 260 eV/q–36 keV/q with 200 possible ESA voltages, while SWEPPAM-E measures electrons from 1.6 eV to 1.35 keV with 32 voltage levels. The time resolution of the instrument is 64

¹<http://www.srl.caltech.edu/ACE/ASC/index.html>

seconds. In normal solar wind operation modus one SWEPAM-I cycle covers 40 E/q levels, adjusted to solar wind bulk speed, and 61 azimuthal angles. In search mode the 40 E/q steps are fixed with a range of 0.500-35.2 keV/q. SWEPAM-E measures in 20 E/q steps and 30 azimuthal angles during one cycle in normal solar wind mode. In STEA (Suprathermal Electron Angle Scan) mode only the 10 highest voltage levels are used and the azimuthal angle is determined in 60 steps. For further information about SWEPAM look at *McComas et al.* [1998].

2.2.3. MAG

The MAG instrument consists of two identical triaxial fluxgate magnetometers. The sensors are mounted at the outer edges of two titanium booms in a distance of 4.19 m from the centre of the spacecraft. The static magnetic field from the ACE spacecraft is estimated to be < 0.35 nT at this position. In absence of an external field the fluxgate sensors are balanced and no signal appears at the output terminals. When an external field is applied the sensor balance is disturbed. Now a current proportional to the external field is created to null the effective field seen by the sensor. The associated voltage is the measured quantity. Three orthogonal single axis sensors determine the three components of the magnetic field vector. The instrument has eight dynamic ranges, starting with ± 4 nT and ending with ± 65536 nT. The digital resolution is 12 bit in each range. The RMS sensor noise level is < 0.006 nT over the 0-10 Hz band. As a result of the full redundancy of both magnetometers the MAG instrument has a very good data coverage. The internal sampling rate is 24 magnetic field vectors per second. The transmitted data stream is 6 vectors/s divided between both magnetometers depending on the telemetry mode. For a detailed description of MAG see *Smith et al.* [1998].

2.2.4. EPAM

The EPAM instrument consists of two particle telescopes measuring ions with energies of 46-4800 keV, and electrons with energies of 40-350 keV. Each telescope has a LEMS (Low-Energy Magnetic Spectrometer) part measuring ions and a LEFS (Low-Energy Foil Spectrometer) part measuring ions and electrons. Depending on the orientation with respect to the spacecraft spin axis the instruments are denoted with this angle. The two LEMS sensors are oriented 30° and 120° from the spin axis, while the angles are 60° and 150° for the two LEFS sensors. The LEFS150/LEMS30 telescope has an additional instrument the CA60 (Composition aperture), which measures ion composition. A magnet in front of the LEMS particle detectors sweeps out electrons with energies below 500 keV. The deflected electrons from the LEMS30 are detected in the CA60 and therefore called DE30 (Deflected Electrons). In front of the LEFS detectors ions with energies below 350 keV are absorbed by an aluminised Parylene foil. The passing particles are detected by segmented totally depleted surface barrier Si detectors. The Si detectors in the LEFS150/LEMS30 telescope have four segments, while the detectors in the LEFS60/LEMS120 have eight sectors, giving the possibility to search for anisotropies. To discriminate between high energy electrons and ions the LEMS and LEFS Si detectors in each telescope work in anti-coincidence. More details about this instrument can be found in *Gold et al.* [1998].

3. MC selection

In a first step, timeframes of MC occurrence have to be identified. A lot of in-situ signatures exist, that discriminate between the presence of normal solar wind plasma and the presence of ICME/MC plasma at the site of the spacecraft (see section 3.1). A proper determination of the MCs' start and end times is very fundamental, because the results of MC fitting described in chapter 4 are very sensitive to the chosen MC boundaries. The number of MCs is strongly correlated with the solar cycle, reaching its peak occurrence at solar maximum. All 67 MCs identified appeared during the timeframe from 2001 to the beginning of 2007 (see section 3.2). For a complete list of the determined MCs see appendix E. In section 3.3 the difficulty of MC boundary determination is discussed in detail for some examples.

3.1. Selection criteria

In table 3.1 signatures for the presence of ICME/MC plasma are listed. The left column gives a qualitative description of the signatures, while the right column gives a quantitative description, if such a description exists. The different signatures are grouped in five classes: B denoting magnetic field signatures, P general plasma signatures, C compositional signatures, W plasma wave signatures, and S suprathermal particle signatures. The expected proton temperature mentioned in signature P3 is defined from a empirical correlation between solar wind speed and proton temperature for near-Earth spacecraft (see *Richardson and Cane [1995]*). T_{exp} in K is calculated from

$$T_{\text{exp}} = 1000(0.031V_{\text{sw}} - 5.1)^2 \quad \text{for } V_{\text{sw}} < 500 \text{ km/s}, \quad (3.1)$$

$$T_{\text{exp}} = 510V_{\text{sw}} - 142000 \quad \text{for } V_{\text{sw}} \geq 500 \text{ km/s}. \quad (3.2)$$

ICMEs and MCs share most of the listed signatures. The only major difference occurs in the behaviour of the magnetic field. The signatures defining a MC are listed in B6, with B1 being the most important.

For determination of MC timeframes only a part of the set of signatures was used. Signatures B1-B4 were checked on the basis of MAG data, for signatures P1-P3 and C1 SWEPAM data was used, and the presence of signature S1 was determined by means of 272 eV electrons STEA (Suprathermal Electron Angle Scan) pitch angle distributions. The 272 eV electrons are chosen, because they lie well outside the core population. The break between the thermal core population and the suprathermal population typically occurs at energies of ≈ 70 eV at 1 AU, depending on solar wind conditions. On the other hand the count rates at this energy are high enough to provide good statistical significance and artifacts in the

3.1. Selection criteria

Signature	Description
B1: Rotation in \vec{B} -field	Rotation $\gg 30^\circ$, smooth
B2: Enhancement of magnetic field	$ \vec{B} > 10 \text{ nT}$
B3: Variance decrease of \vec{B}	
B4: Discontinuity at ICME boundaries	
B5: Field line draping around ICME	
B6: Magnetic clouds	Signatures B1, B2, plasma $\beta < 1$
P1: Declining velocity profile/expansion	Monotonic decrease
P2: Extreme density decrease	Density $\leq 1 \text{ cm}^{-3}$
P3: Proton temperature decrease	$T_p < 0.5 T_{\exp}$
P4: Electron temperature decrease	$T_e < 6 \times 10^4 \text{ K}$
P5: Electron temperature increase	$T_e \gg T_p$
P6: Upstream forward shock/”Bow wave”	Rankine-Hugoniot relations
C1: Enhanced α/proton ratio	$\text{He}^{2+}/\text{H}^+ > 8\%$
C2: Elevated oxygen charge states	$\text{O}^{7+}/\text{O}^{6+} > 1$
C3: Unusually high Fe charge states	$\langle Q \rangle_{\text{Fe}} > 12, Q_{\text{Fe}}^{15+} > 0.01$
C4: Occurrence of He^+	$\text{He}^+/\text{He}^{2+} > 0.01$
C5: Enhancements of Fe/O	$\frac{(\text{Fe}/\text{O})_{\text{ICME}}}{(\text{Fe}/\text{O})_{\text{photosphere}}} > 5$
C6: Unusually high ${}^3\text{He}/{}^4\text{He}$	$\frac{({}^3\text{He}/{}^4\text{He})_{\text{ICME}}}{({}^3\text{He}/{}^4\text{He})_{\text{photosphere}}} > 2$
W1: Ion acoustic waves	
S1: Bidirectional electron strahl	
S2: Bidirectional $\sim \text{MeV}$ ions	2nd harmonic $>$ 1st harmonic
S3: Cosmic ray depletions	Few % at $\sim 1 \text{ GeV}$
S4: Bidirectional cosmic rays	2nd harmonic $>$ 1st harmonic

Table 3.1.: In-situ signatures of ICMEs in magnetic field, plasma dynamics, composition, plasma waves, suprathermal particles, and energetic particles at $\approx 1 \text{ AU}$ heliospheric distance (Taken from Zurbuchen and Richardson [2006]).

3. MC selection

data (for example sunlight contamination) play only a minor role. Additionally, LEMS120 1.9-4.8 MeV ion data and DE30 electron data from EPAM was taken into account. Usually SEPs show peak intensities in ≈ 1 MeV protons near the passage of the shock and a subsequent decrease at the leading edge of the ICME with a recovery of intensities after passage of the trailing edge. Another possible signature is a change in the electron and ion intensity decay rate during the passage of an ICME. An example of using SEP observations for ICME boundary determinations is given in *Malandraki et al.* [2005]. Minor ion signatures were not used in determining MC timeframes, because this would introduce a bias for charge-state and elemental composition studies.

Two derived quantities are computed: the plasma β and the specific proton entropy. The plasma β is calculated from the magnetic field strength, the proton temperature and proton density using: $\beta = 4\mu_0 n_p k_B T_p / B^2$. Usage of this equation will underestimate the plasma β , if signature P5 is present. Since electron temperature and density are not available from the ACE Science Center¹, this is the best approach possible to determine the plasma β .

The specific proton entropy is proportional to: $\ln(T_p/n_p^{\gamma-1})$, with the adiabatic index γ being 1.5 (see *Pagel et al.* [2004]).

Several existing MC lists were taken as sources for starting the MC boundary determination. Continuous updated lists are available for the ACE² and the Wind³ spacecraft (For other references see section C). In most cases the deduced start and end times for different signatures do not show a precise agreement or signatures are not present at all. For this case a priority scheme for the different signatures has to be applied. Another problem is the data coverage of the SWEPAM instrument, in particular the proton density, temperature, and the α /proton-ratio. Most important are smooth magnetic field rotation, reduced magnetic field strength variance, and enhanced magnetic field strength, followed by bidirectional suprathermal electron flows, proton temperature, and velocity decrease. If the MC is a part of a multiple ICME structure, only the magnetic field signatures are reliable boundary indicators. Structures composed of two MC, directly following each other, are hard to distinguish from a single MC structure, if no clear magnetic field discontinuity is present. Single signatures are not unique ICME identifiers, like density decrease in corotating interaction regions, or proton temperature decrease in heliospheric plasma sheet crossings. In the case of other missing and weakly pronounced signatures this might lead to misidentification of MCs. Therefore identifying MCs and choosing the boundaries stays subjective to a certain degree. MC with durations of less than 6 hours are excluded from further analysis. For a typical MC the uncertainty in boundary determination should be within about 2-3 hours.

3.2. Overview of selected time intervals and signatures

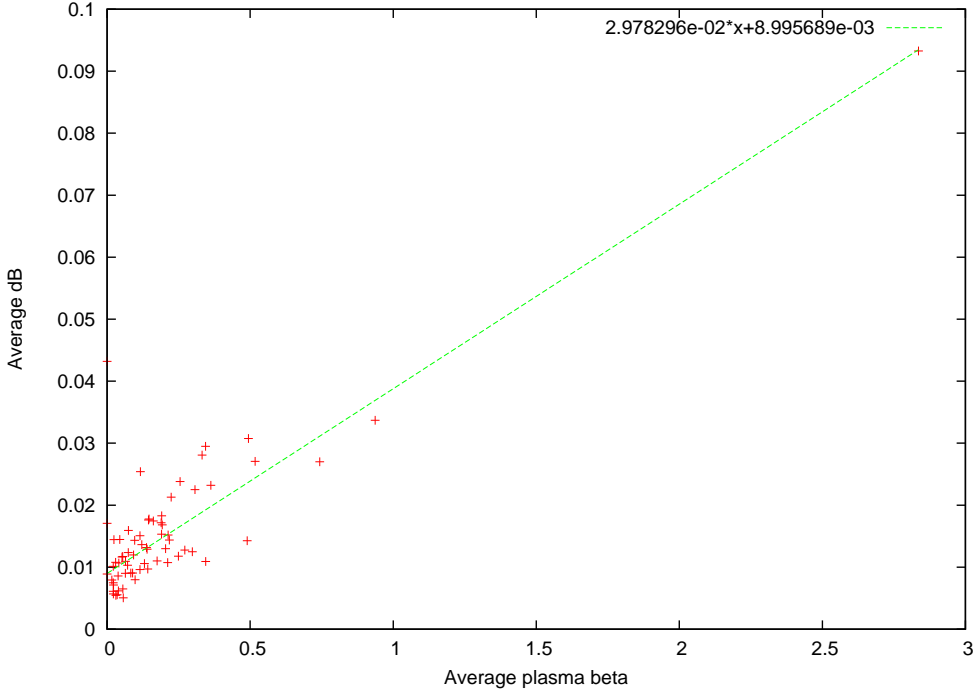


Figure 3.1.: This figure shows the average plasma β for each MC as calculated in section 3.1 and the magnetic field variance dB calculated from 16s MAG data (see equation 3.3). The green line shows a linear fit to the data. The correlation coefficient is 0.93.

3.2. Overview of selected time intervals and signatures

In principle the number of MCs at 1 AU should vary like the number of CMEs ejected at the sun. The ratio of CMEs at solar maximum to CMEs at solar minimum is about 0.2. In 2001 (at solar maximum) a total number of 17 MCs was identified, while in 2006 (at solar minimum) 9 MCs were identified. The calculated probability for getting 9 or more MCs at solar minimum by chance is $\approx 1\%$. There are three possible arguments explaining this behaviour. At solar maximum the distribution of CMEs apparent latitude is much broader than at solar minimum (see *Ivanov et al. [1999]*). Therefore it is expected that a smaller fraction of all ejected CMEs is directed earthwards. Another argument is that the ratio of MCs/ICMEs could change with the solar cycle (*Richardson and Cane [2004b]*). They argue that at solar maximum the complexity of coronal magnetic fields reduces the probability for MC structure formation. The ratio of MCs/ICMEs found at solar minimum was $\approx 70\%$, while it was only $\approx 20\%$ at solar maximum.

The MCs observed often show a “grouped” occurrence, with two or three MCs passing the spacecraft within a few days. In our sample of 67 MCs we find 10 time intervals with two MC identifications within

¹<http://www.srl.caltech.edu/ACE/ASC/index.html>

²Near-Earth Interplanetary Coronal Mass Ejections in 1996-2007, <http://www.ssg.sr.unh.edu/mag/ace/ACElists/ICMTable.html>

³Magnetic Clouds, http://lepmfi.gsfc.nasa.gov/mfi/mag_cloud_pub1.html

3. MC selection

five days and two time intervals with three MC identifications within 5 days (the time intervals with two MC identifications do not include the time intervals with three MC identifications). The AR associated with CME activity act like the ray of a lighthouse. If the AR points towards Earth the generated CMEs are likely seen as ICMEs some days later, while they are not seen if the AR is near the solar limb or on the far side of the sun. Large active regions can be stable for several solar rotations. Therefore the MCs are not independent of each other. For example, if on average three of the observed MCs have their origin in the same active region the by-chance probability for observing 9 MCs rises to 11 %.

The SWEPAM data coverage during MC passage is very much dependent on the observed quantity. The proton velocity has the highest coverage with an average of 97.2 % during all MC passages. For all MCs except one at least one proton velocity measurement was available. Proton density and proton temperature have a data coverage of 87.9 % respectively 90.0 % for the selected time intervals. As the α/proton -ratio is calculated from two measured quantities, its data coverage is worst (79.5 %). Usage of the combined SWICS-SWEPAM proton data⁴ significantly increases the data coverage to 99.6 % for the proton velocity, 99.4 % for the proton temperature, 99.1 % for the proton density, while the α/proton -ratio coverage stays the same.

What about the occurrence of different signatures according to table 3.1? The magnetic field variance dB/B is calculated from MAG data in 16 seconds resolution for a binning time of 16 minutes using equation:

$$\frac{dB}{B} = \frac{\sqrt{\overline{(|\vec{B}| - \overline{|\vec{B}|})^2}}}{\overline{|\vec{B}|}} \quad (3.3)$$

The correlation coefficient of $|\vec{B}|$ and dB/B calculated from all MCs is -0.06. This shows, that dB/B in MCs is nearly independent of magnetic field magnitude. Figure 3.1 shows a plot of the plasma β and dB/B . The lower the plasma β , the lower the magnetic field variance. The magnetic field tries to relax to force-free state and the lower the plasma β the better this state can be reached. Calculating annual averages for dB/B from the whole MAG dataset results in 0.032-0.058. In this case the magnetic field strength and magnetic field variance are highly correlated. At solar maximum, when the average magnetic field strength is high, dB/B is low. 95 % of the MCs have a dB/B that is smaller than the lower value.

76 % of the MCs show an average magnetic field strength exceeding 10 nT. All of the selected time intervals except four show smooth rotation of the magnetic field vector larger than 30° and the plasma β is smaller than unity for 97.7 % of the data points. As these are the primary signatures for MC selection, the high probabilities are not remarkable.

Especially the general plasma signatures are not present in many cases. Proton velocity decrease is present in 85 % of the MCs, 57 % of the data shows reduced proton temperature, an α/proton -ratio larger than 0.08 is found in 27 % of all cases, and the proton density is lower than 1 cm⁻³ for only 10 % of the

⁴http://www.srl.caltech.edu/ACE/ASC/level2/lvl2DATA_SWEPAM-SWICS.html

3.2. Overview of selected time intervals and signatures

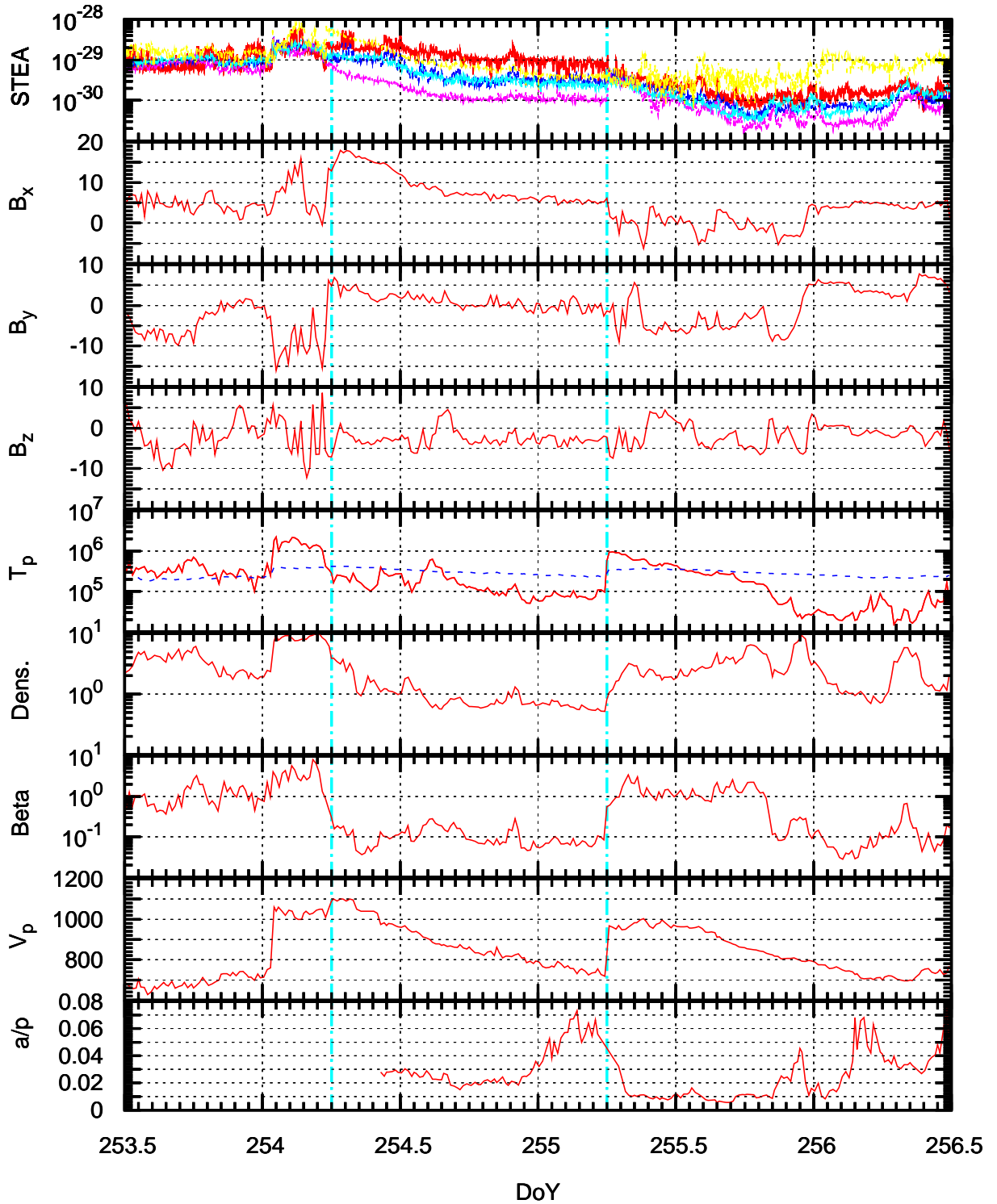


Figure 3.2.: ACE data for the MC from DoY 254.25-255.25 in 2005. From top to bottom the following data is shown: 272 eV electron STEA pitch angle distributions (red=0°-36°, blue=36°-72°, pink=72°-108°, light blue=108°-144°, and yellow=144°-180°) in electrons s³ cm⁻⁶, magnetic field components in nT, proton temperature in K, proton density in cm⁻³, the plasma β (calculated as described in section 3.1), the proton velocity in km/s, and the α /proton ratio. Vertical light blue lines indicate the determined MC boundaries.

3. MC selection

data points. The proton density averages show no difference between annual solar wind and MC data. Bidirectional suprathermal electrons are present in most of the MCs for at least some time. The EPAM measurements show no variation in the proton and electron intensities for roughly 50 % of the MCs.

3.3. Examples

To get a feeling for the data that has been used, and for the difficulties occurring during boundary determination, we show some examples of MCs. These MCs are chosen to represent different classes of plasma environments. Three cases of MCs will be discussed:

- A MC, in which the different signatures show temporal agreement and are clearly visible (see figure 3.2). This case is rather unlikely, as only $\approx 10\%$ of all MCs show good temporal agreement in most of the signatures. In these cases the accuracy of boundary times should be approximately 1 hour.
- A MC embedded in a larger ICME structure (see figure 3.3). In this quite common case boundary determination can become very uncertain, because the boundaries are based on magnetic field data alone.
- A MC structure that possibly consists of two separate MCs (see figure 3.4). The discrimination between the one MC case or the two MC cases is one of the most difficult problems occurring. In the full dataset only two structures consisting of two MCs have been identified.

Figure 3.2 shows a MC passing over ACE from DoY 254.25 to 255.25, 2005. After crossing the leading edge the proton temperature decreases very fast, all three magnetic field components show clear discontinuities, and the proton velocity shows an almost linear decrease in the whole timeframe. As result of the decreased proton temperature and proton density the plasma β is low for the whole event. Bidirectional suprathermal 272 eV electron signatures are present all the way from leading to trailing edge. In this case the trailing edge of the MC can be determined very well, because the plasma following the MC is faster than the MC itself, preventing the formation of a rarefaction region. Instead a shock forms at the trailing edge, leading to a fast proton temperature increase and strong magnetic field variation. The α/proton -ratio stays low within the MC (even below normal solar wind ratio), except for a short timeframe near the trailing edge. The average magnetic field strength is 10 nT for this MC, and the magnetic field components show only a small amount of rotation.

In figure 3.3 the MC from DoY 119.02-119.57, 2001 is plotted. In this MC the different MC signatures show temporal disagreement for the leading edge and some signatures continue after the trailing edge. The proton temperature decrease, which indicates the entrance into the ICME plasma, starts at \approx DoY 118.60. The proton velocity decrease starts at DoY 118.90, α/proton ratio begins to increase at DoY 118.95, and bidirectional suprathermal electrons are present at DoY 119.0. Without the strong variation

3.3. Examples

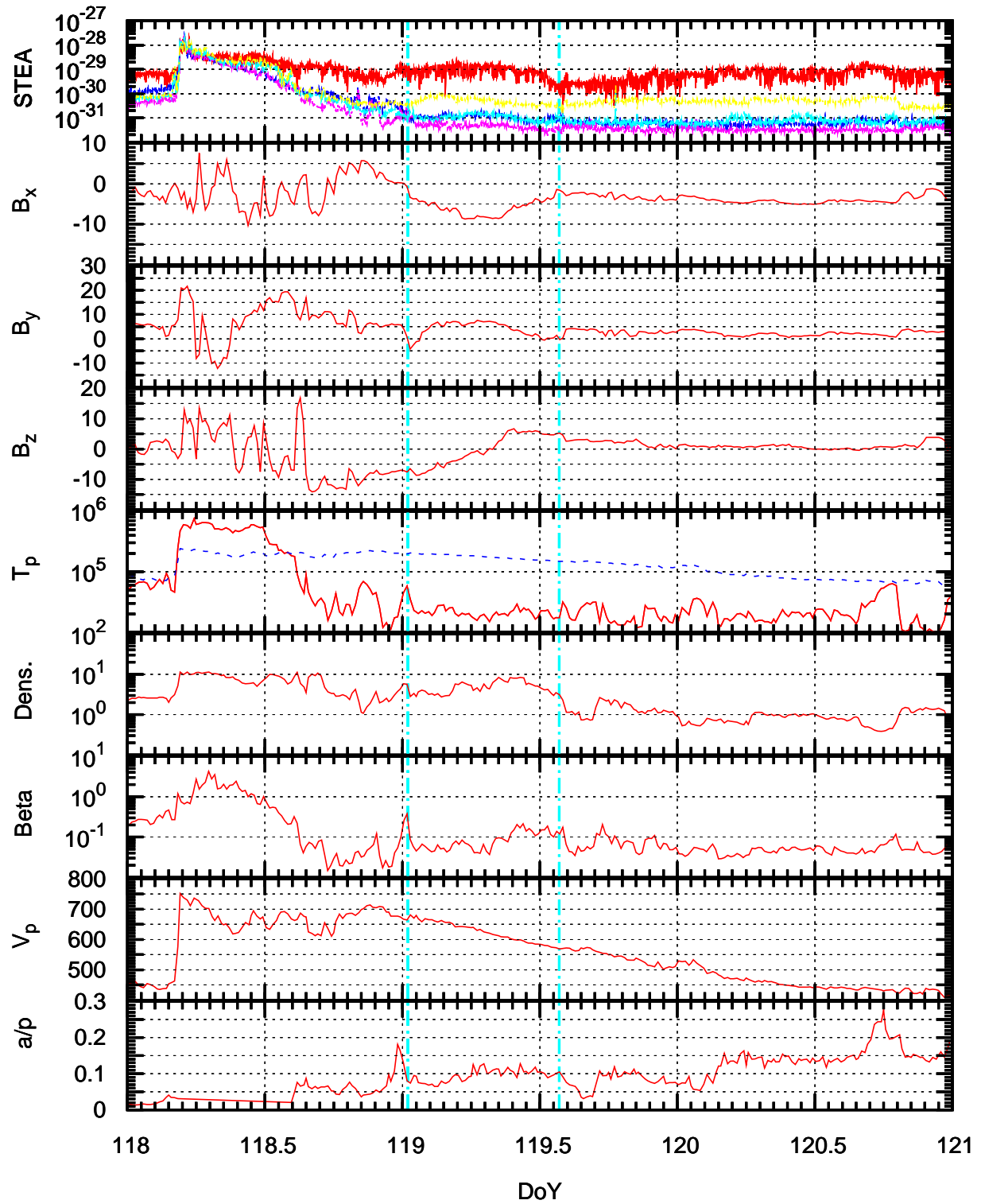


Figure 3.3.: ACE data for the MC from DoY 119.02-119.57 in 2001. The legend can be found in figure 3.2.

3. MC selection

in B_y the start of smooth magnetic field rotation would be DoY 118.85. After passage of the trailing edge the proton temperature stays low, the proton velocity shows further decrease, and bidirectional suprathermal electrons are still present. Therefore the end time is determined from the vanishing magnetic field rotation alone. Another indication might be the additional decrease in proton density. The average magnetic field strength was low (9.4 nT) during this MC, but the plasma β was well below unity (0.090).

The MC shown in figure 3.4 ranged from DoY 78.80 to DoY 80.67, 2001. It has an average magnetic field strength of 15.7 nT and a very low magnetic field variance dB/B of 0.006. The start time is determined by the end of variation in the B_y component and by the end of the proton density enhancement. Proton velocity trend and proton temperature indicate a start time of DoY 78.72. The determination of the trailing edge is difficult, because none of the signatures shows a rapid change. The rotation of the magnetic field slowly disappears as well as the proton velocity decrease, and the proton temperature rises very slowly, while the density keeps its level just like the bidirectional suprathermal electrons. This MC was identified as a single MC by some authors (*Feng et al.* [2007]; *Lynch et al.* [2003]) and as a double MC-structure by others (*Hidalgo* [2003]; *Nieves-Chinchilla et al.* [2005]). As there are no large variations in the magnetic field components, the magnetic field strength, the decrease of the proton velocity, and in the suprathermal electron pitch angle distribution and the reductions in the proton density and α/proton -ratio are within the normal fluctuations, it is not possible to decide whether this is a single MC structure or a double MC structure from the applied signatures. It was treated as a single MC for further analysis. Of course the reconstruction of MC geometry (see chapter 4) will be quite different for both cases.

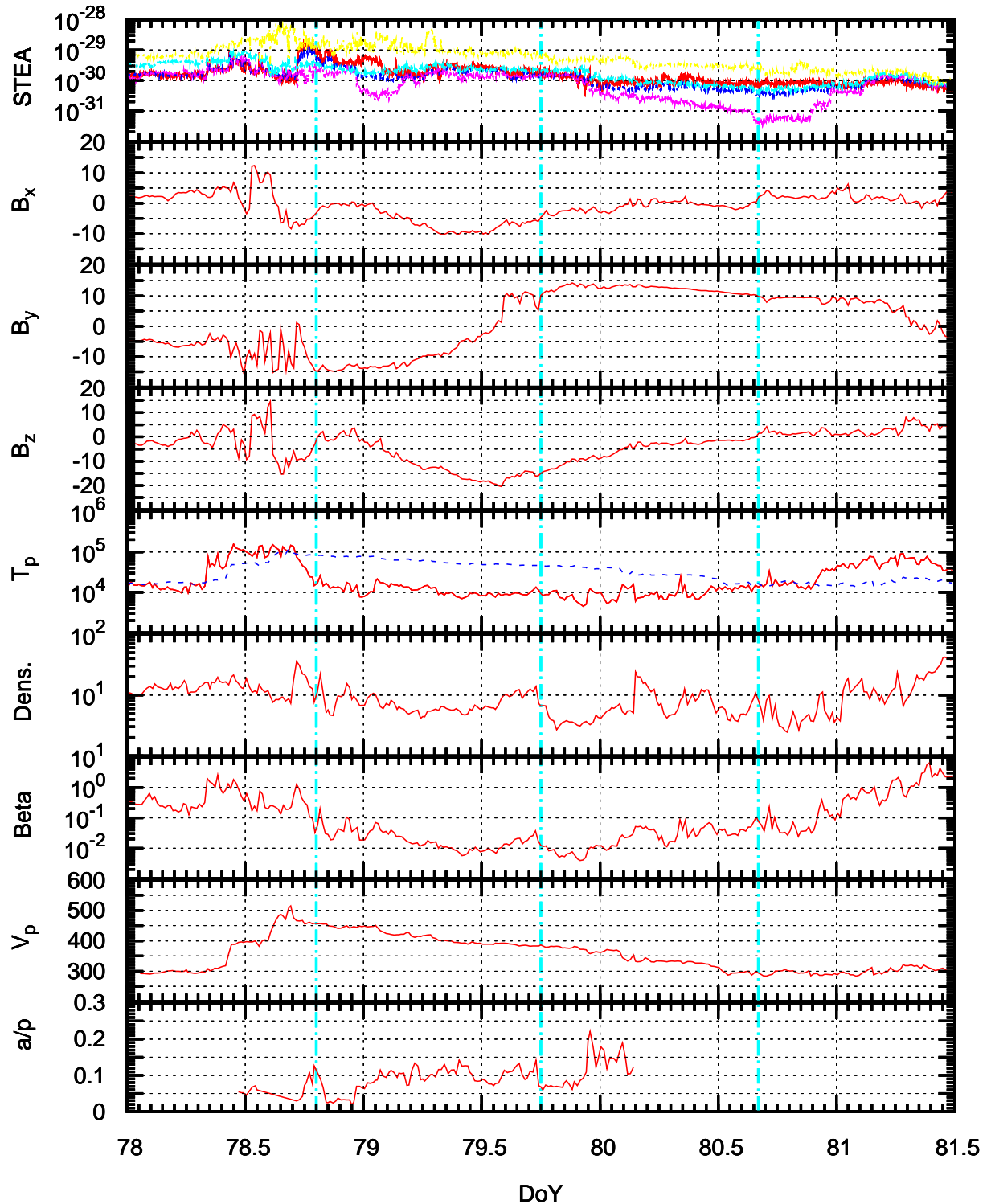


Figure 3.4.: ACE data for the MC from DoY 78.80-80.67 in 2001. The legend can be found in figure 3.2. The vertical light blue line at DoY 79.75 is the start time of the second MC given in the Lepping MC list (http://lepmfi.gsfc.nasa.gov/mfi/mag_cloud_pub1.html).

4. Data Analysis

In this chapter the different possibilities for modelling MCs will be discussed after a short introduction of the underlying basic electromagnetic equations. Three different magnetic field models are introduced, which describe the local structure of a MC as a cylindrical fluxrope with different cross sections. Two of them share a circular cross section. The first model assumes a force-free magnetic field, while the second describes a non force-free field. The third model assumes an elliptic cross section and is a generalisation of the first model. MC expansion is considered in this model, while the MC is static in the other models. In this section the methods that fit the model parameters to the magnetic field data from MAG onboard ACE and how they allow a reconstruction of the MCs geometry and the trajectory of the spacecraft through the MC are presented. This is followed by a review of the uncertainties in the obtained results and a comparison with other authors. A short description of the methods used to calculate ion fluxes and densities from the SWICS instrument data completes the chapter.

4.1. Magnetic Field Theoretical Background

The basic formulae of electrodynamics are Maxwell's equations

$$\vec{\nabla} \cdot \vec{E} = \frac{\rho_E}{\epsilon_0}, \quad (4.1)$$

$$\vec{\nabla} \cdot \vec{B} = 0, \quad (4.2)$$

$$\vec{\nabla} \times \vec{E} = -\frac{\partial \vec{B}}{\partial t}, \quad (4.3)$$

$$\vec{\nabla} \times \vec{B} = \frac{1}{c^2} \frac{\partial \vec{E}}{\partial t} + \mu_0 \vec{j}. \quad (4.4)$$

In these equations \vec{j} describes the electric current density, ρ_E is the electric charge density, \vec{E} denotes the electric field, and \vec{B} indicates the magnetic induction (also called magnetic field in this context instead of $\vec{H} = \frac{\vec{B}}{\mu_0}$, which normally is called magnetic field¹). All equations are in rationalised metric units. Another important equation is Ohm's Law, which describes the connection between the electric current density and the electric field (in this case the presence of a magnetic field \vec{B} is assumed).

$$\vec{j} = \sigma (\vec{E} + \vec{v} \times \vec{B}), \quad (4.5)$$

¹We will follow the modern literature e. g. *Demtröder* [2009] in this respect

4.1. Magnetic Field Theoretical Background

where σ is the electric conductivity constant.

A particle with charge q moving with speed \vec{v} in a magnetic field \vec{B} experiences the Lorentz force

$$\vec{F} = q(\vec{v} \times \vec{B}). \quad (4.6)$$

If the Lorentz force acts not only on a single particle but on a current density $\vec{j} = \rho q \vec{v}$, (ρ denotes the particle density, q is the average particle charge) the Lorentz force becomes

$$\vec{F} = \vec{j} \times \vec{B}. \quad (4.7)$$

A magnetic field configuration is called force-free when the Lorentz force is zero, which means that \vec{j} and \vec{B} are parallel. For vanishing displacement current equation 4.4 simplifies to $\vec{\nabla} \times \vec{B} = \mu_0 \vec{j}$, known as Ampère's law. Applying this equation and equation 4.7 leads to

$$(\vec{\nabla} \times \vec{B}) \times \vec{B} = 0. \quad (4.8)$$

This is the basic equation of force-free fields. It is a homogeneous, non-linear differential equation and, therefore, the calculation of force-free fields is non-trivial. A subset of solutions is given by linear force-free fields that satisfy the condition

$$(\vec{\nabla} \times \vec{B}) = \mu_0 \vec{j} = \alpha(\vec{r}) \vec{B}. \quad (4.9)$$

$\alpha(\vec{r})$ is a scalar function of position. Applying the vector relation $\vec{\nabla} \cdot (\vec{\nabla} \times \vec{B}) = 0$ and equation 4.2 lead to

$$\alpha(\vec{\nabla} \cdot \vec{B}) + \vec{B} \cdot \vec{\nabla} \alpha = \vec{B} \cdot \vec{\nabla} \alpha = 0,$$

which is only valid (assuming a non-zero magnetic field) if $\alpha(\vec{r})$ is constant along the direction of \vec{B} . Therefore $\alpha(\vec{r})$ does not vary along any field line of \vec{B} ! In the easiest case $\alpha(\vec{r})$ has the same value for every field line and becomes a simple constant. Keeping this in mind and making use of the vector identity $\vec{\nabla} \times (\vec{\nabla} \times \vec{B}) = \vec{\nabla}(\vec{\nabla} \cdot \vec{B}) - \vec{\nabla}^2 \vec{B}$, equation 4.2, and equation 4.9 we derive the Helmholtz equation

$$\vec{\nabla} \times (\vec{\nabla} \times \vec{B}) = -\vec{\nabla}^2 \vec{B} = \alpha^2 \vec{B}. \quad (4.10)$$

The importance of force-free magnetic fields for MC modelling results from the low plasma β inside these structures (typical values are in the range of 0.1) where the magnetic pressure dominates the thermal pressure of the plasma particles. For stationary conditions it becomes $\vec{j} \times \vec{B} = \vec{\nabla} p$, if no other forces (e. g. gravity) are acting on the plasma, as is the case in interplanetary space. Neglecting the pressure gradient (low plasma β) leads to the force-free situation.

For further details about the discussed topics look into *Wimmer-Schweingruber* [2002-04], *Stroth* [2002], or *Aschwanden* [2004].

4. Data Analysis

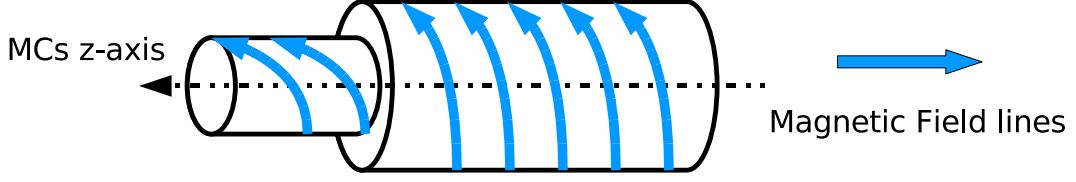


Figure 4.2.: A sketch of the MC's geometry. Magnetic field lines become more and more azimuthal toward the edge of the MC.

4.2. MC modelling

In this section we will discuss how the geometric properties of a MC can be obtained from a time series of magnetic field measurements taken along a trajectory inside of it. All models assume a locally cylindric geometry with different cross sections and all models are not really three dimensional because the magnetic field is considered to be independent of the length z inside the modelled structure (see figure 4.2). Therefore the magnetic field is the same at any length.

4.2.1. Force-free Circular Model

The easiest coordinate system in which equation 4.10 can be solved are cylindrical coordinates. Assuming cylindrical symmetry (the components of the magnetic field depend only on r) together with equation 4.9 leads to

$$\alpha B_r = \frac{1}{r} \frac{\partial B_z}{\partial \varphi} - \frac{\partial B_\varphi}{\partial z} = 0.$$

For the two remaining components of the magnetic field B_φ , and B_z we obtain from equation 4.10

$$\frac{1}{r} \frac{\partial}{\partial r} \left(r \frac{\partial B_z}{\partial r} \right) + \alpha^2 B_z = 0, \quad (4.11)$$

$$\frac{1}{r} \frac{\partial}{\partial r} \left(r \frac{\partial B_\varphi}{\partial r} \right) + \alpha^2 B_\varphi = 0, \quad (4.12)$$

and from equation 4.9

$$B_\varphi = -\frac{1}{\alpha} \frac{\partial B_z}{\partial r}, \quad (4.13)$$

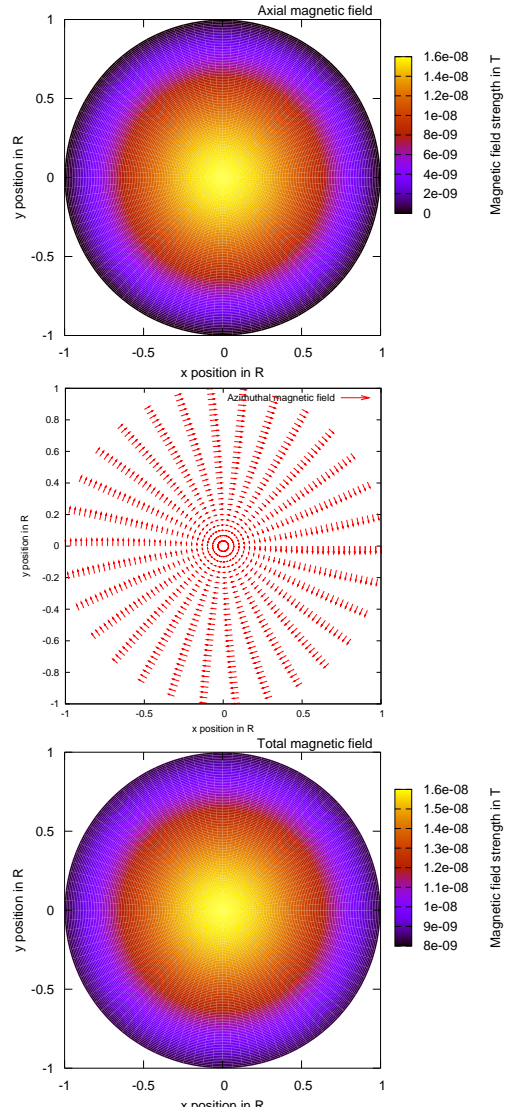


Figure 4.1.: Magnetic field inside a force-free MC with circular cross section.

4.2. MC modelling

because all other terms cancel. Substituting r with $r' = \alpha r$ in equation 4.11 and dividing by α^2 results in

$$\frac{\partial^2 B_z}{\partial r'^2} + \frac{1}{r'} \frac{\partial B_z}{\partial r'} + B_z = 0. \quad (4.14)$$

Equation 4.14 is the Bessel equation with the solution (found by *Lundquist* [1950] in 1950)

$$B_z = B_0 J_0(\alpha r). \quad (4.15)$$

For the azimuthal component of the magnetic field equations 4.12 and 4.13 lead to

$$B_\varphi = B_0 H J_1(\alpha r). \quad (4.16)$$

J_0 and J_1 are the zeroth and first order Bessel functions, B_0 scales the strength of the magnetic field, and H , the sign of the helicity, is the direction of rotation in the azimuthal component (right-handed ($H = 1$) or left-handed ($H = -1$) rotation). The first square root of J_0 is at 2.405. This is the point where the magnetic field becomes fully azimuthal and therefore determines the boundary of the cloud. Knowing the clouds radius R we can determine $\alpha = \frac{2.405}{R}$. In figure 4.1 the different magnetic field components and magnetic field magnitude are shown. The only quantity that can be varied to achieve another magnetic field configuration is the magnetic field strength B_0 (B_0 is 16 nT in figure 4.1) in this model, while the ratio of axial to azimuthal magnetic field is fixed at every point inside the MC. This model is common e. g. in MC modelling and has been and is used by several authors (*Lepping et al.* [1990]; *Lynch et al.* [2003]; *Feng et al.* [2007]).

4.2.2. Non Force-free Circular Model

When the assumption of a force-free plasma is not valid we have to go back to the Maxwell equations (4.1-4.4) to find a solution. *Cid et al.* [2002] introduces cylindric geometry with circular cross section, a static behaviour of the MC, and a current density $\vec{j} = (0, j_\varphi, j_z)$, where j_z is constant and $j_\varphi = \alpha r$ (α being a constant) as boundary

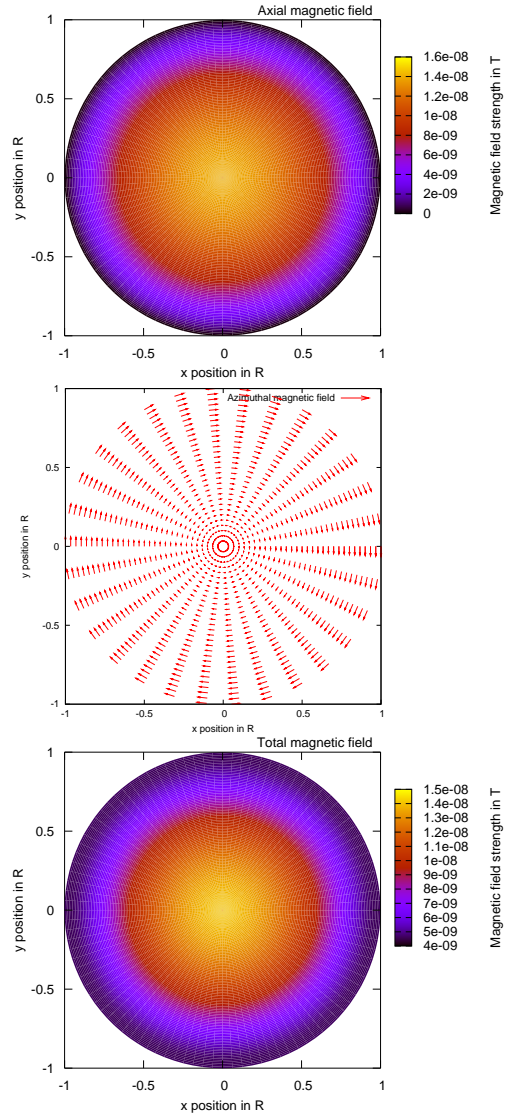


Figure 4.3.: Magnetic field inside the non force-free MC with circular cross section.

4. Data Analysis

conditions. With $B_r = 0$ (magnetic field lines lie on closed cylinder surfaces) equation 4.4 determines the magnetic field

$$B_r = 0 \quad (4.17)$$

$$-\frac{\partial B_z}{\partial r} = \mu_0 \alpha r \quad (4.18)$$

$$\frac{1}{r} \frac{\partial (r B_\varphi)}{\partial r} = \mu_0 j_z \quad (4.19)$$

Obviously the magnetic field will be cylindrically symmetric as in the force-free model discussed in the previous section. Demanding a strictly azimuthal field at the MC boundary the solutions are

$$B_\varphi = \frac{\mu_0}{2} j_z r, \quad (4.20)$$

$$B_z = \frac{\mu_0}{2} \alpha (R^2 - r^2), \quad (4.21)$$

where R denotes the MC's radius. Unlike the force-free model the ratio of the azimuthal and the axial component is not fixed at a specific point inside the MC but depends on the chosen j_z and α . Figure 4.3 shows the magnetic field components for $R = 0.1$ AU, $\alpha = 1.0 \cdot 10^{-22} \frac{\text{C}}{\text{m}^3\text{s}}$, and $j_z = 0.5 \cdot 10^{-12} \frac{\text{C}}{\text{m}^2\text{s}}$. Choosing this set of parameters leads to a characteristic magnetic field for a MC at 1 AU. The helicity of the cloud depends on the sign of j_z . The Lorentz force (equation 4.7) inside the cloud is: $\vec{F}_l = \left(\frac{\mu_0}{2} r (\alpha^2 (R^2 - r^2) - j_z^2), 0, 0 \right)$. This radial force shows the non force-free character of the model and has to be balanced by a pressure gradient to keep the cloud static. In the model the pressure gradient develops from inhomogeneities of electron density or temperature across the MC. For further details of the model look into *Cid et al.* [2002].

4.2.3. Force-free Elliptic Model

The third applied model is a force-free, “cylindric” model with elliptic cross section, and self-similar expansion (the cross section shape is not changed by the expansion). To solve equation 4.9 we use elliptic cylindrical coordinates. Elliptic cylindrical coordinates are defined by:

$$x = c \cosh u \cos v, \quad (4.22)$$

$$y = c \sinh u \sin v, \quad (4.23)$$

$$z = z, \quad (4.24)$$

Contours of constant u are ellipses with different ratios of the minor semi-axis b to major semi-axis a . The larger u gets, the more these ellipses become circular. Therefore, a maximum value of u , called u_0 , is chosen, which describes the ellipticity of the MC (called generating ellipse). From transformation equations 4.22, 4.23, and 4.24 we can determine $\vec{\nabla}$ (see *Bronstein et al.* [2001] for example) in this curvilinear coordinate system. Assuming \vec{B} is independent of z , and introducing $h_u \doteq c \sqrt{\cosh^2 u - \cos^2 v}$

4.2. MC modelling

we can solve equation 4.9 in elliptic coordinates

$$\frac{1}{h_u} \frac{\partial B_z}{\partial v} = \alpha B_u \quad (4.25)$$

$$\frac{1}{h_u} \frac{\partial B_z}{\partial u} = \alpha B_v \quad (4.26)$$

$$\frac{1}{h_u^2} \left(\frac{\partial}{\partial u} (h_u B_v) - \frac{\partial}{\partial v} (h_u B_u) \right) = \alpha B_z \quad (4.27)$$

From this equations we see that B_u and B_v are derivatives of B_z and, therefore, the problem is solved with the knowledge of B_z . Substituting equations 4.25 and 4.26 into 4.27 leads to an equation only depending on B_z

$$\frac{\partial^2 B_z}{\partial u^2} + \frac{\partial^2 B_z}{\partial v^2} = -\alpha^2 c^2 (\cosh^2 u - \cos^2 v) B_z.$$

After solving this equation the solutions for the magnetic field components are (see *Vandas and Romashets [2003]*)

$$B_u = \frac{1}{\alpha c \sqrt{\cosh^2 u - \cos^2 v}} \frac{\partial B_z}{\partial v}, \quad (4.28)$$

$$B_v = \frac{1}{\alpha c \sqrt{\cosh^2 u - \cos^2 v}} \frac{\partial B_z}{\partial u}, \quad (4.29)$$

$$B_z = B_0 \frac{\text{ceh}_0(u, -\varepsilon/32) \text{ce}_0(v, -\varepsilon/32)}{\text{ce}_0^2(0, -\varepsilon/32)} \quad (4.30)$$

In this equations ε is $(\alpha c)^2$, ce_0 and ceh_0 are ordinary and modified Mathieu functions of zeroth order (see *The Group “Numerical Analysis” at Delft University of Technology [1973]* for additional numerical implications). As in the previous models, B_z is zero at the MC’s boundary. In this model, α does not only depend on the MC’s radius but also on its oblateness. B_0 as in the circular force-free model determines the field strength at the centre of the cloud. Figure 4.4 shows the magnetic field of this model for a ratio of the major to the minor axis of 3 and $B_0 = 16$ nT.

The expansion of the MC’s cross section is assumed to be self-similar (see figure 4.5) and therefore the expan-

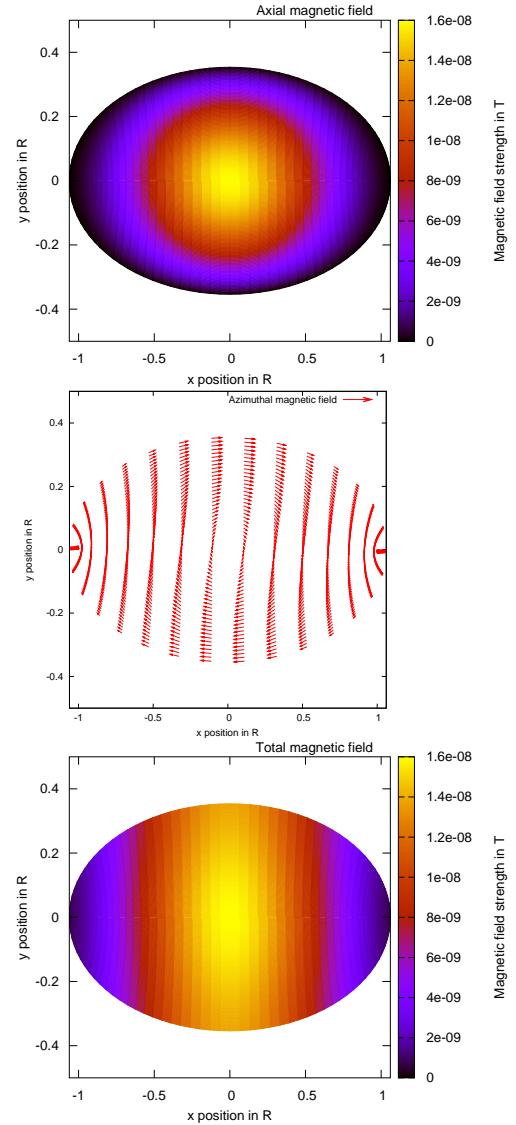


Figure 4.4.: Magnetic field inside the force-free MC with elliptic cross section and a ratio $\frac{a}{b} = 3$.

4. Data Analysis

sion law is $\vec{v}_r = \frac{\vec{r}}{t + t_0}$. B_0 and α in equations 4.28-4.30 become time dependent

$$\alpha \rightarrow \frac{\alpha}{1 + \frac{t}{t_0}}, \quad (4.31)$$

$$B_0 \rightarrow \frac{B_0}{\left(1 + \frac{t}{t_0}\right)^2}. \quad (4.32)$$

t_0 is a constant determining the expansion behaviour of the cloud. Small values of t_0 mean fast expansion, while large values imply slow expansion of the MC's cross section.

Due to its large number of free parameters and its asymmetric magnetic field many different magnetic field characteristics can be explained by this model. For example magnetic field data with large rotation in the magnetic field vector and a almost constant magnetic field strength, as well as data with the highest magnetic field strength near the borders, or the typical MC data with the highest magnetic field strength at the centre can be fit by this model.

This model is described in detail by *Vandas and Romashets* [2003, 2002]; *Vandas et al.* [2005, 2006].

4.2.4. Other Methods

There are many other approaches in MC modelling. A short summary of the basic ideas behind the different models is given together with some references to literature.

1. Cylindrical model with non constant alpha:

This is a force-free model with cylindrical geometry. The only difference to the model explained in section 4.2.1 is the assumption that α is no longer a constant, but has a radial dependence ($\alpha \sim r^\varepsilon$).

The resulting magnetic field components are more variable than in the constant α model depending

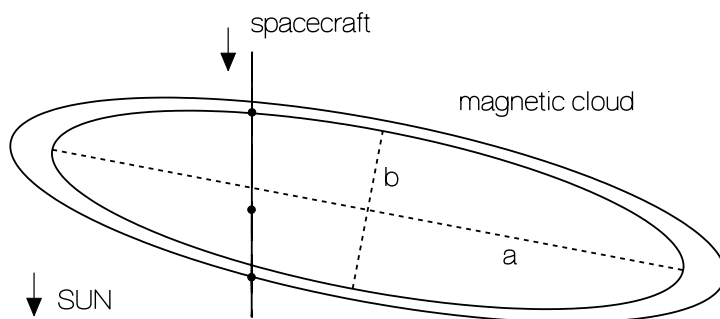


Figure 4.5.: The dashed lines show the semi-major and semi-minor axes at the first encounter of the spacecraft with the MC. The three points on the spacecraft trajectory denote the point of first encounter, the point of shortest approach to the MC's axis, and the point of the spacecraft's exit. The larger ellipse displays the cloud's cross section when the spacecraft leaves the MC. The size of the MC has increased during the traverse of the spacecraft (taken from *Vandas et al.* [2006]).

4.2. MC modelling

on the ε selected (see *Romashets and Vandas* [2002]). Choosing an ε makes different magnetic field configurations for B_φ and B_z possible.

2. Asymmetric cylindrical model:

This model uses bi-cylindrical coordinates to solve equation 4.10 in a cylindrical geometry. The model is force-free and the solution are also Bessel functions, but the position of the highest field magnitude can be shifted toward the edges of the MC. Therefore, asymmetric field distributions can be explained better with this model than with the model explained in section 4.2.1 (see *Romashets and Vandas* [2005]).

3. Non force-free elliptical models:

The geometry of the MC is the same as in the model described in section 4.2.3. Maxwell's equations (equations 4.1-4.4) and the continuity equation in stationary conditions are solved in the elliptical coordinate system to obtain the magnetic field inside the MC. Due to the non force-free conditions the obtained magnetic field has more free parameters than the model from section 4.2.3 (see *Hidalgo et al.* [2002]; *Hidalgo* [2003]; *Nieves-Chinchilla et al.* [2002, 2005]).

4. Kinetic evolution models:

An initially cylindrical MC configuration is assumed near the solar surface (few solar radii). The plasma of the MC is moving strictly radially outward leading to conservation of the angular extent and to distortion of the shape. An expansion of the MC in radial direction leads to enhancement of the initial diameter. Depending on the ratio of expansion to transit speed, different cross sections occur at 1 AU (see e. g. *Riley and Crooker* [2004]; *Owens et al.* [2006]).

5. Grad-Shafranov reconstruction:

The Grad-Shafranov equation can be used to reconstruct two dimensional structures that are time-coherent and magneto-hydrostatic. Because MCs are three-dimensional structures one has to find an invariant axis first. With help of different field line invariants and from knowing the vector potential \vec{A} along the spacecraft trajectory the cross section and the field of the MC can be determined (see *Sonnerup et al.* [2006]).

6. MHD-models:

From a set of MHD-equations the propagation and evolution of a MC is modelled. These models take into account the interaction of the MC with the ambient solar wind on the base of model assumptions. From this approach the geometric structure, the density, and the magnetic field inside the MC can be calculated at different distances from the sun (see e. g. *Vandas et al.* [2002]; *Odstrcil et al.* [2002]).

7. Other geometries:

Models with cylindrical geometry are the most common ones, but a number of models with other

4. Data Analysis

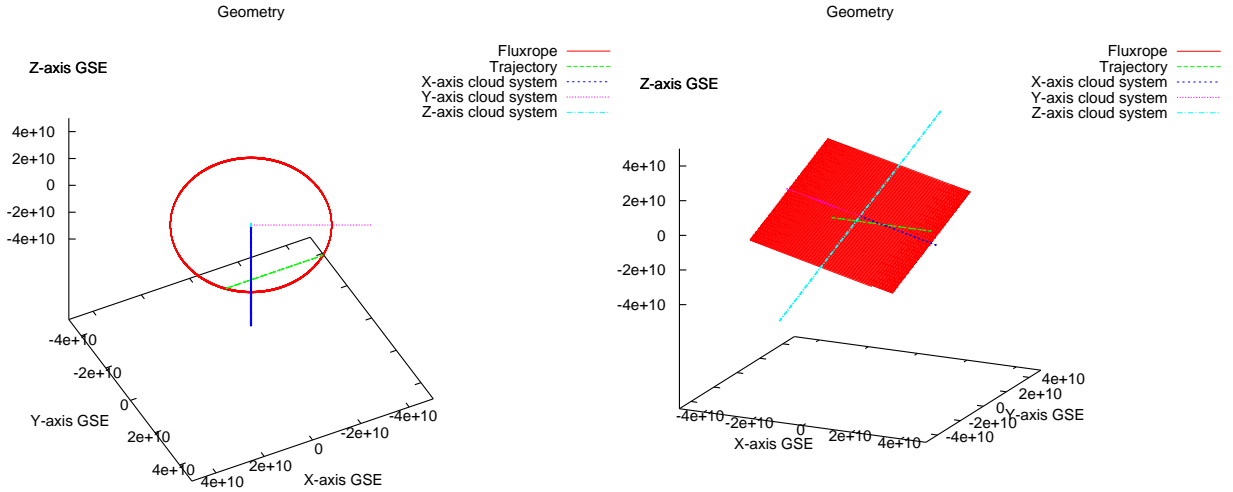


Figure 4.6.: The plots show the GSE coordinate axes, the coordinate axes of the MCs coordinate system, the MCs boundary, and the spacecraft trajectory, assuming that the MC is moving anti-parallel to the GSE x-axis. The left figure shows a view along the MCs z-axis, while the right figure shows a view perpendicular to it. The angle θ is 37° , the angle φ is 63° , and the shortest approach distance is 0.15 AU in this picture.

basic geometries do exist. For example, *Vandas et al.* [1993] applied a spheroidal geometry, while *Ivanov et al.* [1989] applied a toroidal configuration for MC modelling.

Table 4.1 gives an overview of the applied models.

4.3. Spacecraft position and free parameters

The magnetic field data measured by MAG used for the MC modelling is based on measurements in the GSE coordinate system. In the GSE coordinate system the x-axis points from the earth to the sun, the z-axis is perpendicular to the ecliptic plane, pointing to the north, and the y-axis completes a right-hand system (nearly anti-parallel with the direction of Earth's motion around the sun, see figure 4.7).

The length of the spacecraft trajectory inside the MC is determined by the solar wind speed (represented by the average proton speed during the MC encounter) times the MC duration. It is assumed that the MC is moving radially away from the sun and therefore anti-parallel to

GSE coordinate system as seen from 45° inclination

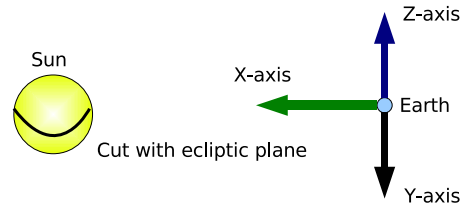


Figure 4.7.: Shown are the sun, Earth, and the three axes of the GSE coordinate system as seen from an angle of 45° to the ecliptic plane.

4.3. Spacecraft position and free parameters

the GSE x-axis. Apart from the small proper motion of the spacecraft, this gives the direction of the spacecraft trajectory. The spacecraft movement is neglected, because the velocity is small compared to the MCs velocity (≈ 30 km/s vs. 350 km/s or above).

The modelled magnetic field has to be transformed from the MC coordinate system (see figure 4.6) into the GSE system to make the measured magnetic field and the modelled magnetic field comparable. First the magnetic field components in the MC system have to be written in cartesian coordinates from the cylindrical coordinates:

$$B_x = -B_\varphi \sin \varphi \quad (4.33)$$

$$B_y = B_\varphi \cos \varphi \quad (4.34)$$

$$B_z = B_z \quad (4.35)$$

In elliptic coordinates the following relations have to be used:

$$B_x = \frac{-\cosh u \sin v B_v + \sinh u \cos v B_u}{\sqrt{(\cosh u \sin v)^2 + (\sinh u \cos v)^2}} \quad (4.36)$$

$$B_y = \frac{\sinh u \cos v B_v + \cosh u \sin v B_u}{\sqrt{(\cosh u \sin v)^2 + (\sinh u \cos v)^2}} \quad (4.37)$$

$$B_z = B_z \quad (4.38)$$

Then the orientation of the MC's z-axis with respect to the GSE coordinate system is given by the angles φ and θ . θ is the angle between the GSE z-axis and the MC's z-axis, φ denotes the angle between the GSE x-axis and the projection of the MC's z-axis onto the GSE xy-plane counted counterclockwise. With these angles a transformation matrix \mathbf{A} between the two coordinate systems can be defined:

$$\mathbf{A} = \begin{pmatrix} \cos(\varphi) \cos(\theta) & -\sin(\varphi) & \cos(\varphi) \sin(\theta) \\ \sin(\varphi) \cos(\theta) & \cos(\varphi) & \sin(\varphi) \sin(\theta) \\ -\sin(\theta) & 0 & \cos(\theta) \end{pmatrix} \quad (4.39)$$

\mathbf{A} is a rotation matrix and the angles are the usual Euler angles. The transformation is performed with the matrix multiplication $\vec{B}_{\text{GSE}} = \mathbf{A} \cdot \vec{B}_{\text{mod}}$.

The position of the spacecraft trajectory inside the MC is furthermore affected by the distance of shortest approach d_0 . It denotes the shortest distance between the points on the spacecraft trajectory and the clouds centre. In the models with circular cross section this point is reached after half of the MC duration. In the elliptical model the point in time of the shortest approach can even be located outside the MC boundaries. With a given length of the spacecraft trajectory and a given absolute value of the shortest approach distance there are always two possible solutions for the spacecraft trajectory, therefore, d_0 is signed.

In the models with circular cross sections, the angles φ , θ , and the shortest approach distance d_0 determine the geometrical properties of the cloud as free parameters. In the elliptical model there are the

4. Data Analysis

Model	Mag. field param.	Geometric param.	Field type	Cross section	Expansion
Model 4.2.1	B_0	d_0, θ, φ	Force-free	Cylindric	No
Model 4.2.2	α, j_z	d_0, θ, φ	Non force-free	Cylindric	No
Model 4.2.3	B_0	$d_0, \theta, \varphi, \psi, t_0, \mu_0$	Force-free	Elliptic	Yes

Table 4.1.: Summary of the different magnetic field model characteristics and their free parameters. The free parameters are separated by their importance for the MC's geometric appearance.

ellipticity of the generating ellipse μ_0 , the time constant of the MC's expansion t_0 , and the angle ψ (describing the orientation of the MC's cross section) as additional free parameters. Free parameters with no influence on the geometric appearance are the magnetic field constants α, j_z , and B_0 (see section 4.2). They can be directly determined from a fit to magnetic field magnitude data because this data is independent of the coordinate system. If these free parameters are known, the position of the spacecraft inside the MC and the magnetic field at this position in GSE coordinates can be calculated. These free parameters are identified with the help of a Levenberg-Marquardt fit.

To obtain the final set of parameters we perform the following procedure:

- The following sequence is applied 75 times:
 1. Random generated parameter initial values.
 2. Minimum variance analysis for the MC's z-axis orientation.
 3. Fit of the magnetic field parameters to the magnetic field strength.
 4. Fit of the remaining free parameters to the three magnetic field components.
- The final set of parameters is determined from the 75 runs on the basis of χ^2 .

The fundamental problem for this kind of modelling is the reconstruction of a 3-d structure from 1-d measurements taken along the spacecraft trajectory. This under-determination makes it inevitable to define a specific MC geometry. In fact, nobody knows the real 3-d structure of MCs at 1 AU. The reason for modelling a MC as a cylinder is motivated by coronagraph images, which show flux rope structures in some cases near the sun. Even in this case one has to be careful, as we have a 2-d projection of a 3-d structure.

4.4. Minimum Variance Analysis (MVA)

To get a first idea of the angles θ and φ a MVA is carried out. This method was used by *Sonnerup and Cahill* [1967] to determine the normal of the magnetopause current layer. The idea is to find the

4.4. Minimum Variance Analysis (MVA)

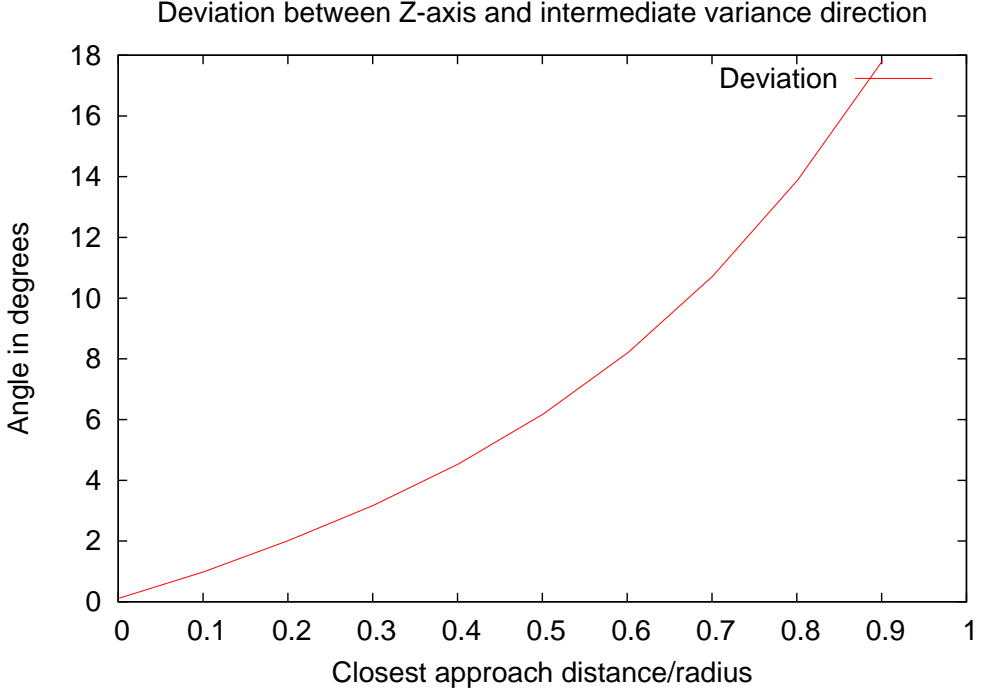


Figure 4.8.: This plot shows the angle between the z-axis of a modelled MC (with model 4.2.1) and the direction of medium variance in dependence of the shortest approach distance d_0 . The field was unit-normalised before applying the MVA.

eigenvalues and eigenvectors of the covariant matrix $\mathbf{M}_{\alpha\beta}$.

$$\mathbf{M}_{\alpha\beta} = (\overline{B_\alpha B_\beta} - \overline{B_\alpha} \overline{B_\beta}), \quad (4.40)$$

where α and β are $\in \{1, 2, 3\}$ for the different cartesian components of the magnetic field. The overhead bar denotes the average over all measurements during the MC passage ($\overline{B}_\alpha = \frac{1}{N} \sum_{i=1}^N B_{\alpha,i}$). The three eigenvalues and the corresponding eigenvectors define the three axes of the variance ellipsoid. These axes are called the direction of minimum, intermediate and maximum variance. If two of the eigenvalues are equal, the variance ellipsoid becomes degenerate and the three variance axes cannot be determined unambiguously. To ensure uniqueness of the variance axes *Sonnerup and Cahill* [1967] used only data where the ratio of the intermediate to the minimum eigenvalue exceeded 1.5.

According to *Lepping et al.* [1990] the MVA is normally carried out with unit normalised magnetic field vectors. Assuming a MC with the field configuration as in chapter 4.2.1 and a trajectory of the spacecraft passing through the centre of the MC ($d_0 = 0$) the meaning of the three variance directions becomes clear. If the MCs coordinate system (see figure 4.6) is not rotated with respect to the GSE coordinate system, the spacecraft will cross the MC from $(-1,0)$ to $(1,0)$ in the central picture of figure 4.1. The x-component of the magnetic field is 0 for all data points, therefore the x-axis is the direction of minimum variance. The z-component varies from 0 at the MCs boundaries to 1 (unit normalised field) at the

4. Data Analysis

clouds centre, determining the direction of medium variance. The y-component is -1 at one boundary of the MC, becomes 0 at the centre and 1 at the other boundary, identifying the direction of maximum variance. Thus θ and φ are determined by the direction of the eigenvector belonging to the intermediate eigenvalue.

When the spacecraft does not pass through the centre of the MC the intermediate variance direction and the z-axis of the MC no longer have the same direction. The larger d_0 gets, the larger the deviation between the two directions gets. Figure 4.8 shows the angle between the medium variance direction and the MC's z-axis in dependence of the shortest approach distance. To create figure 4.8 the magnetic field along the spacecraft trajectory for a given d_0 according to section 4.2.1 is calculated. The field is unit normalised and the direction of medium variance direction is computed. Now the difference between this direction and the known direction of the MC z-axis is calculated for 10 different values of d_0 .

4.5. The χ^2 -Fit

To find the set of free parameters that reproduces the data the best within the model restrictions a Levenberg-Marquardt fitting algorithm is applied. A short summary of the method is given in this section with respect to the special features associated with the problem at hand, for further details see *Press et al.* [1992].

Assume a set of data points y_i , that are independently normally (Gaussian) distributed around the “true” model $y(x)$. The expected standard deviation of each data point y_i is denoted by σ_i . The probability of the data set to be drawn from a model function $y(x)$, can be calculated from the product of the probability of each data point to be a representation of $y(x)$

$$P \propto \prod_{i=1}^N \exp \left(-\frac{1}{2} \left(\frac{y_i - y(x_i)}{\sigma_i} \right)^2 \right) \Delta y. \quad (4.41)$$

A Δy has to be chosen, to get finite probabilities from the probability density function. The higher P gets, the more likely the found solution gets. So maximising equation 4.41 results in the model with the highest probability. Taking the negative natural logarithm of equation 4.41 leads to

$$\left(\sum_{i=1}^N \frac{(y_i - y(x_i))^2}{2\sigma_i^2} \right) - N \ln \Delta y. \quad (4.42)$$

Maximising equation 4.41 is the same as minimising equation 4.42. The second term of equation 4.42 consists only of constants and therefore it can be neglected. The first term multiplied by 2 is just χ^2 , which has to be minimised by a properly chosen set of free parameters \vec{a} , to get the most probable model function $y(x; \vec{a})$

$$\chi^2 \equiv \sum_{i=1}^N \left(\frac{y_i - y(x_i; a_1 \dots a_M)}{\sigma_i} \right)^2. \quad (4.43)$$

4.5. The χ^2 -Fit

Now, the question is how to find the set of free parameters \vec{a} that minimises the χ^2 ? We expect that the χ^2 function is well approximated by a quadratic form near the minimum

$$\chi^2(\vec{a}) \approx \gamma - \vec{d} \cdot \vec{a} + \frac{1}{2} \vec{a} \cdot \mathbf{D} \cdot \vec{a}. \quad (4.44)$$

This equation arises from the Taylor expansion of χ^2 around a point \mathbf{P} . \vec{d} is the vector of the first partial derivatives of $\chi^2(\vec{a})$ at \mathbf{P} and \mathbf{D} is the Hessian matrix (second partial derivative matrix) of $\chi^2(\vec{a})$ at \mathbf{P} . Taking the negative gradient of equation 4.44 and considering the disappearance of the gradient at $\chi^2(\vec{a}_{\min})$ we can calculate \vec{a}_{\min} from \vec{a}_{cur} with the help of the following equation

$$\vec{a}_{\min} = \vec{a}_{\text{cur}} + \mathbf{D}^{-1} \cdot (-\chi^2(\vec{a}_{\text{cur}})). \quad (4.45)$$

If equation 4.44 is a poor local approximation to the shape of the function $\chi^2(\vec{a})$ at \vec{a}_{cur} , equation 4.46 has to be used instead of equation 4.45. \vec{a} is changed iteratively until equation 4.45 becomes applicable by stepping down the gradient (steepest descent method)

$$\vec{a}_{\text{next}} = \vec{a}_{\text{cur}} - \text{constant} \times \chi^2(\vec{a}_{\text{cur}}). \quad (4.46)$$

The constant should be small enough not to exhaust the downhill direction.

The Levenberg-Marquardt method combines equations 4.45 and 4.46 by introducing a value λ that switches between both methods. Depending on the behaviour of χ^2 , λ is scaled up or down by factors of ten. Large values for λ mean application of the steepest descent method, while small values for λ mean application of equation 4.45.

In the case of MC modelling the merit function χ^2 is not just a function of one set of data points y_i and one $y(x; \vec{a})$, but of the three magnetic field components $\vec{B}^{\text{obs}} = (B_x^{\text{obs}}(t), B_y^{\text{obs}}(t), B_z^{\text{obs}}(t))$ observed at time t and the three model functions $\vec{B}^{\text{mod}} = (B_x^{\text{mod}}(t, \vec{a}), B_y^{\text{mod}}(t, \vec{a}), B_z^{\text{mod}}(t, \vec{a}))$. According to equation 4.43 χ^2 in this case is calculated as

$$\chi^2 = \sum_{i=1}^N \left(\frac{B_{x,i}^{\text{obs}} - B_{x,i}^{\text{mod}}}{\sigma_{x,i}} \right)^2 + \left(\frac{B_{y,i}^{\text{obs}} - B_{y,i}^{\text{mod}}}{\sigma_{y,i}} \right)^2 + \left(\frac{B_{z,i}^{\text{obs}} - B_{z,i}^{\text{mod}}}{\sigma_{z,i}} \right)^2. \quad (4.47)$$

The quantity of χ^2 strongly depends on the chosen σ s. Too large values for the σ s result in too low quantities for χ^2 and too low magnitudes for the σ s result in a too large χ^2 . Another common definition of the χ^2 (also called sum of the squares (ssq)) in MC modelling (see *Lepping et al.* [2003, 2004] for example) is based on the relative deviation between the modelled and the observed magnetic field components

$$\chi^2 = \sum_{i=1}^N \left(\frac{B_{x,i}^{\text{obs}} - B_{x,i}^{\text{mod}}}{B_i^{\text{obs}}} \right)^2 + \left(\frac{B_{y,i}^{\text{obs}} - B_{y,i}^{\text{mod}}}{B_i^{\text{obs}}} \right)^2 + \left(\frac{B_{z,i}^{\text{obs}} - B_{z,i}^{\text{mod}}}{B_i^{\text{obs}}} \right)^2. \quad (4.48)$$

The magnetic field components of the observed and the modelled field are unit normalised separately. The field magnitude of the observed field is calculated with $B_i^{\text{obs}} = \sqrt{(B_{x,i}^{\text{obs}})^2 + (B_{y,i}^{\text{obs}})^2 + (B_{z,i}^{\text{obs}})^2}$,

4. Data Analysis

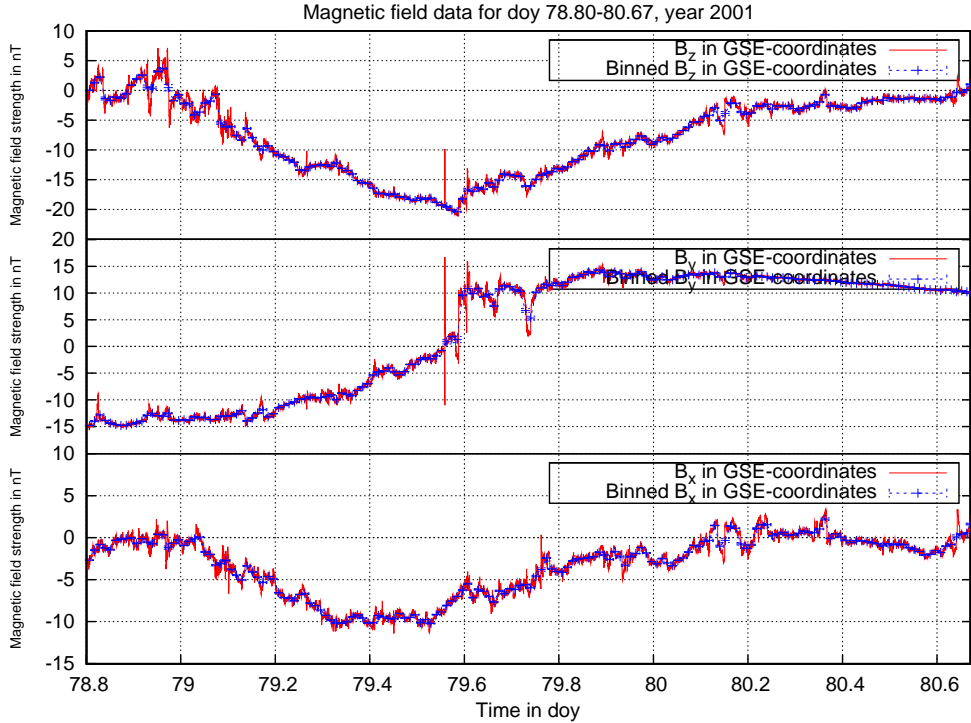


Figure 4.9.: MAG measurements are shown in 16 sec. resolution (red) together with the 16 min binned magnetic field components applied in MC fitting (blue) for a MC during March 2001. The error-bars are calculated from the variation in the 16 sec data within each bin. Typical values lie in the range of 0.01 to 0.5 nT.

and $B_i^{\text{mod}} = \sqrt{\left(B_{x,i}^{\text{mod}}\right)^2 + \left(B_{y,i}^{\text{mod}}\right)^2 + \left(B_{z,i}^{\text{mod}}\right)^2}$ is the quantity of the modelled field.

The χ^2 in equations 4.48, and 4.47 depends on the number of data points. The larger the number of data points, the larger χ^2 gets. To compensate this behaviour of χ^2 a reduced χ_R^2 is defined by

$$\chi_R^2 = \frac{\chi^2}{3N - f}. \quad (4.49)$$

$3N$ is the total number of data points assuming that each magnetic field component has N data points. f is the number of free parameters. For the models with cylindrical cross-sections f is 3 and f is 6 for the model with the elliptical cross-section. If the σ s in equation 4.47 have the correct dimension and the measured data results from the assumed model and the data points are normally distributed, the resulting χ_R^2 should be approximately 1.

4.6. Determination of MCs Final Properties

For this kind of non-linear fitting the final set of parameters often depends on the initially chosen parameters, as the fit converges toward a local minimum of the χ^2 -distribution. For each of the MCs a total

number of 75 fits was carried out with different initial values for the free parameters. Each fit results in a different set of final parameters and a different χ^2 . Depending on the magnitude of χ^2 and the relevance of χ^2 as a maximum likelihood estimator, the probability for the different solutions can be determined. χ_{\min}^2 is distributed as a χ^2 -distribution with $N - f$ degrees of freedom, where N is the number of data points and f is the number of free parameters. The expectation value of this distribution is $N - f$. While this is true only for $(0, 1)$ -normal distributed quantities, the knowledge of the standard deviation in each measured data point is necessary.

Calculating the variation of the magnetic field components from the 16 seconds MAG measurements shows that the resulting standard deviations are much too small, often resulting in a reduced χ_R^2 of several thousands (See figure 4.9 for an example). This shows that the main contribution to the standard deviation doesn't result from measurement uncertainties but from the limited complexity of the applied magnetic field models. Therefore the standard deviation for each magnetic field data point was chosen to be equal to the same arbitrary constant before fitting. Assuming that the parameter set with the lowest resulting χ_{\min}^2 explains the data set and the χ_{\min}^2 should be in the range $N - f \pm \sqrt{2(N - f)}$ each χ^2 is divided by $\frac{\chi_{\min}^2}{N - f}$. Of course this procedure requires normally distributed errors (See section 4.7).

Now the $\Delta\chi^2$ for the different fit solutions with respect to the best solution χ_{\min}^2 can be calculated: $\Delta\chi^2 \equiv \chi^2(\vec{a}_j) - \chi_{\min}^2(\vec{a}_0)$, with \vec{a}_j being the fitted parameters from the j 's fit and \vec{a}_0 being the fitted parameters from the best fit. The $\Delta\chi^2$ itself now is distributed as a χ^2 -distribution with f degrees of freedom (See Press *et al.* [1992]). From this distribution confidence levels in dependence of the $\Delta\chi^2$ can be determined by integrating the χ^2 -distribution from zero to $\Delta\chi^2$. For each fit result with a specific $\Delta\chi^2$ we now can give a probability for rejection of this solution.

The final fit parameters are determined by weighting the resulting fit parameter from each fit with the probability of not being rejected. In the same way standard deviations for the parameter are calculated. The final angles for MCs axis orientation and the B_0 in the models 4.2.1 and 4.2.2 are directly calculated from the fit results, while the radius and the shortest approach distance d_0 is calculated from logarithmic values. This is because the fit sometimes results in very large values for these quantities and even low probabilities have a huge influence on the results. For the same reason B_0 and the time constant t_0 in the model 4.2.3 are derived from logarithmic values.

4.7. Fit result errors

If the models described in the sections 4.2.1-4.2.3 really would explain the measured data, we would expect the measured data to be normal distributed around the modelled data. In figure 4.10 the difference distribution of the measured and the modelled magnetic field data is shown. To make MCs of different magnetic field strength comparable, the deviations in each MC were divided by the average magnetic field strength. A histogram was calculated from the deviations in the three magnetic field components and plotted as a probability density function. For both classes of applied magnetic field

4. Data Analysis

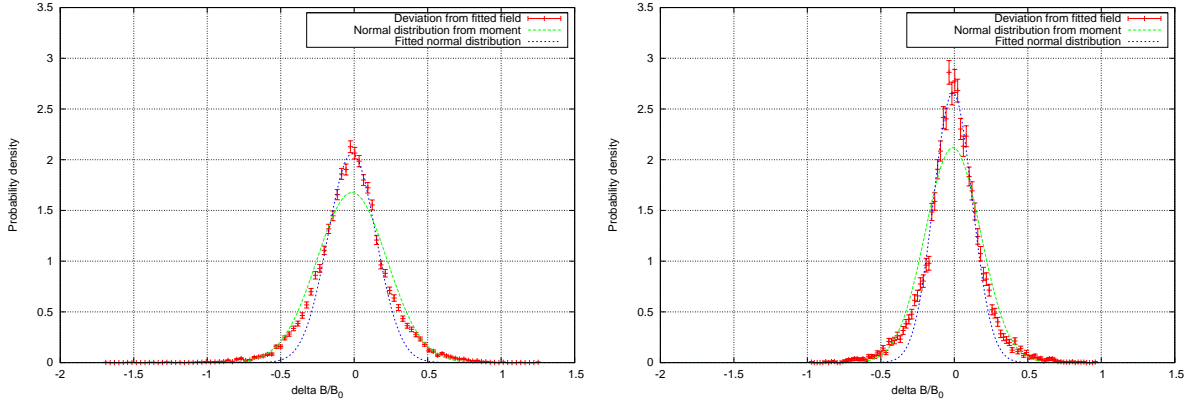


Figure 4.10.: Deviation of the measured magnetic field data from the modelled data for the case of the models with circular cross section (left) and for the case of the model with elliptical cross section (right). The distribution was determined from a total of 53 MC. For each MC the fit with the lowest χ^2 was taken for calculation. The blue line shows a normal distribution fitted to the core (in the range $-0.2, 0.2$) of the obtained distribution, while the green line shows a normal distribution with a σ calculated from the second moment of the obtained distribution.

models we see that the distributions are not normal. Of course the models are not able to explain strong variations of the magnetic field on short timescales as often seen in the MAG data (See figure 4.11 for an example). These variations result in groups of data points lying a long way off the fitted curves, producing the tails seen in the difference distributions. Nevertheless the cores of the distributions look Gaussian. Fitting a normal distribution to the core of the difference distribution gives us the fraction of data points that can be explained by a normal distribution. For the elliptic model 87.4 % of the data can be explained by a normal distribution, while for the circular models this number is 84.1 %. The σ s for these core distributions are 0.130 for the elliptical model and 0.161 for the circular models. As expected the elliptical model produces smaller deviations due to the larger number of free parameters and its flexibility in producing magnetic fields of different shape. Calculating a normal distribution from the second moments of the difference distributions results in a σ of 0.187 for the elliptical model and of 0.234 for the circular models. This shows that the distribution becomes narrower even for the points in the tails for the case of the elliptic model. Because large variations on short timescales cannot be explained by any of the models we would expect larger importance of the tails for the case of the elliptical model. The ratio of the σ from the distribution determined from the second moment to the σ of the core distribution is 1.44 for the case of the elliptical model and 1.45 for the circular models. This ratio is determined by the tails (in the case of no tails the ratio would be ≈ 1) and only 12.6% of all points lie in the tails for the elliptical model (compared to 15.9% for the circular models). Thus, the tails in fact have a larger importance in the elliptic model, because the ratio of the σ s stays the same.

Keeping these considerations in mind, we can calculate the formal standard errors in the fitted parameters

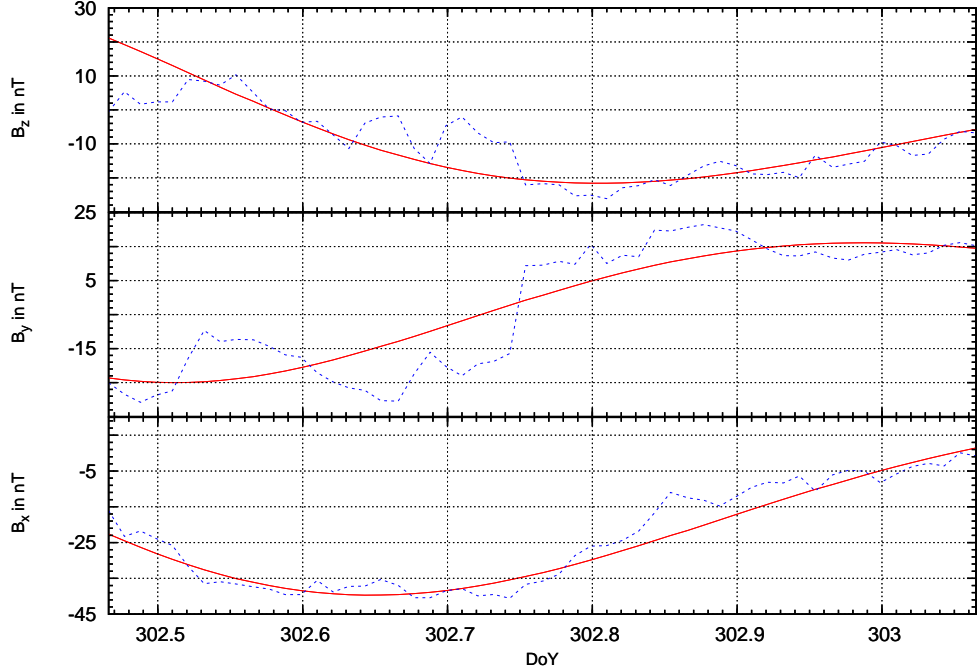


Figure 4.11.: The blue lines show the three magnetic field components measured in the GSE coordinate system during a MC at the end of October 2003. The red lines show the best fit with the elliptical model (see section 4.2.3). In particular the B_y and the B_z components show large variations within short timescales, leading to the formation of tails in the difference distributions. Another feature nearly seen in all MCs is the wave-like oscillation of the observed field around the fitted field with periods of some hours.

under the assumption of normal distributed errors (see *Press et al.* [1992]). Variation in one parameter will lead to a change in the χ^2 . Denoting the parameter set minimising the χ^2 with \vec{a}_0 and the parameter set varied in one component with \vec{a} , the difference in the χ^2 's is denoted by:

$$\Delta\chi^2 \equiv \chi^2(\vec{a}) - \chi^2(\vec{a}_0)$$

This quantity is distributed as a χ^2 -distribution with one degree of freedom.

Without loss of generality let us assume, that the first component of \vec{a}_0 is changed by a arbitrary, fixed δa_1 , while the remaining components of $\delta \vec{a}$ are chosen to minimise the χ^2 under these constraints. In the case of no correlation between the parameters the remaining components of $\delta \vec{a}$ would be zero. In general we can calculate these components from multiplying equation 4.45 with \mathbf{D} and replacing \mathbf{D} with $[\alpha] = 0.5\mathbf{D}$ ($[\alpha]$ is called curvature matrix). This results in a set of linear equations

$$[\alpha] \cdot \delta \vec{a} = \vec{\beta}. \quad (4.50)$$

4. Data Analysis

All of the β_k s are zero for $k > 1$, because the components of $\delta\vec{a}$ by definition are chosen to minimise the χ^2 and at the minimum the gradient vanishes. Multiplying equation 4.50 with $[\alpha]^{-1}$ results in

$$\delta\vec{a} = [\alpha]^{-1} \cdot \begin{pmatrix} c \\ 0 \\ \vdots \\ 0 \end{pmatrix} = [C] \cdot \begin{pmatrix} c \\ 0 \\ \vdots \\ 0 \end{pmatrix}. \quad (4.51)$$

$[C]$ is called covariance matrix and the c is determined by $c = \delta a_1 / C_{11}$. According to equation 4.44 the change of the χ^2 in the vicinity of \vec{a}_0 , where the gradient becomes zero, can be calculated by

$$\Delta\chi^2 = \delta\vec{a} \cdot [\alpha(\vec{a}_0)] \cdot \delta\vec{a}. \quad (4.52)$$

Inserting equation 4.51 in equation 4.52 and solving for δa_1 gives us the formal standard error for the first parameter

$$\delta a_1 = \pm \sqrt{C_{11}}.$$

The formal standard error for the remaining parameter can be calculated in a uniform manner.

As the set of final parameters minimises the χ^2 for the three magnetic field components at the same time, this set usually does not minimise χ^2 for each of the magnetic field components separately (Each of the magnetic field components has a different minimising parameter set). The covariance matrix is calculated for each of the magnetic field components separately, and thus the requirements for applying the method described above are no longer fulfilled. Calculating the formal standard error from the covariance matrix anyway overestimates the error by magnitudes.

Fitting a simulated dataset with known parameters is another possibility of uncertainty estimation. *Lepping et al.* [2003], and *Lepping et al.* [2004] determined the variation of the fit parameters in dependence of different input noise levels. In a first attempt they calculated the model magnetic field from their constant alpha force-free cylindrically symmetric model (see *Lepping et al.* [1990]). By adding a normal distributed random noise field \vec{B}_{RN} of different strength (σ of 0, 1, 2, 4, 8 nT) to the exact solution and fitting the resulting field, deviations from the initial parameter distribution can be obtained. In principle, this approach should lead to the same error estimates as the errors obtained from the covariant matrix.

This procedure results in a magnetic field that strongly varies on short timescales because every data point is independent of the ambient points. The noised up field is distributed in bands around the modelled magnetic field strength. The width of the bands is dependent on the input noise level. The higher the noise level, the higher the width of the band will be. The distribution of the measured magnetic field around the fitted field often shows relatively smooth, low frequency wave-like noise variation in MCs. *Lepping et al.* [2003] conclude: "...that legitimate uncertainty estimates of output fit parameters cannot be realistically accomplished with random noise."

In a second approach they calculated the difference between observed and modelled magnetic fields in

4.7. Fit result errors

19 MCs as a basis for more realistic noise profiles. The MCs were observed with the WIND spacecraft and only cases of good quality fits were considered. For each measured MC 25 noise data points were calculated for each of the three magnetic field components by linear extrapolation. Each noise profile was multiplied with a factor to achieve an average RMS (including all three magnetic field components) of 2.0 nT. To increase the number of available noise sets each set was temporally inverted (data point 1 becomes data point 25, data point 2 becomes data point 24, ...), and for further increase the resulting noise sets were multiplied with -1 to get a total number of 76 noise sets.

They calculated a set of 6 simulated MCs from two different cloud axis orientations (angle of 90° and 60° with respect to the GSE x-axis, MC's axis lies within the ecliptic plane for both cases) and three different closest approach distances ($\frac{d_0}{R_0} = 0.0, 0.3, 0.6$). Scaling the available noise sets with factors of 0.25, 1.0, 1.5, and 2.0 (to study the influence of different noise levels) and adding them to the simulated MC data gives a total number of $6 \cdot 76 \cdot 4 = 1824$ MCs. They fitted this set of magnetic clouds with the model described in *Lepping et al.* [1990] and averages, in dependence of MC's axis orientation, shortest approach distance and noise level were calculated. Additionally, the RMS of the parameter distributions were determined using the formula 4.53 and used as uncertainties in the parameters

$$\sigma_A = \sqrt{\frac{1}{N} \sum_{j=1}^N (P_j - \langle P \rangle)^2}, \quad \text{with } \langle P \rangle = \frac{1}{N} \sum_{j=1}^N P_j. \quad (4.53)$$

Briefly summarising their results gives an idea of different parameter influences and errors:

- As expected the uncertainty in the fitted parameters becomes larger with increasing noise level (corresponding to a higher χ^2 in the fit results).
- An increase in the closest approach distance d_0 leads to larger uncertainties in the magnetic field strength constant B_0 , and to a lesser extent in the angles θ and ϕ . Surprisingly the MCs axis cone angle error (which is calculated from the average of the angles between the fitted MCs axis orientations and the modelled axis orientation) doesn't show this behaviour.
- The uncertainties are larger for almost all parameters in the case of a 60° angle between MCs axis and the GSE x-axis.
- The MC's radius is well determined. Even for the highest noise level and the largest closest approach distance the deviations are in the order of 20 %.
- The shortest approach distance is hard to determine. Even at moderate noise levels the uncertainty reaches values of 0.2 times the MC's radius and exceeds 0.5 times the MC's radius at higher noise levels.
- The error in the magnetic field strength constant B_0 is smaller than 25% for all cases except one.

4. Data Analysis

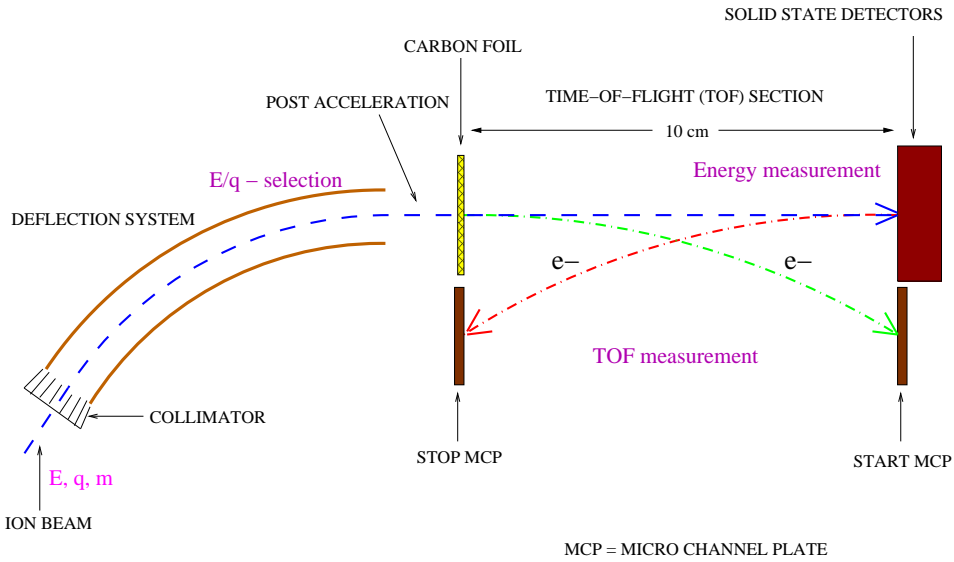


Figure 4.12.: Diagram of the SWICS instrument. Ions with appropriate E/q ratio enter the instrument via the deflection system, release secondary electrons from the carbon foil and hit a SSD, again releasing secondary electrons and triggering an energy measurement. The secondary electrons from the carbon foil and the SSD are used for the time of flight determination (Taken from *Kötén* [2009]).

- The uncertainty in the MC's axis orientation is in the order of 5° to 40° depending on the noise level.

Although the applied magnetic field models are not comparable one-to-one, the general trends listed above should be true in our case. In section 5.1 the influence of the different magnetic field models on the fitted parameter set is shown, which gives a hint on the uncertainty of the fitted parameters. In that section these results will be compared with the uncertainty from the Lepping approach.

4.8. Calculation of ion count rates determined from SWICS

A short introduction in the working principle of SWICS is given in section 2.2. Figure 4.12 shows a schematic view of SWICS, with the E/q preselection, the ToF measurement (τ), and the energy measurement (E_{tot}) highlighted in magenta. The post-acceleration voltage V_a (≈ -24 keV) and the length of the ToF section d (≈ 10 cm) are kept on constant values. From these measurements the mass m_i , charge q_i , and initial energy E_i of an ion in principle can be determined by

$$q_i = \frac{E_{\text{tot}}}{V_a + \frac{E}{q}} \quad (4.54)$$

$$m_i = \frac{2E_{\text{tot}}\tau^2}{d^2} \quad (4.55)$$

$$E_i = \frac{E q_i}{q} \quad (4.56)$$

4.8. Calculation of ion count rates determined from SWICS

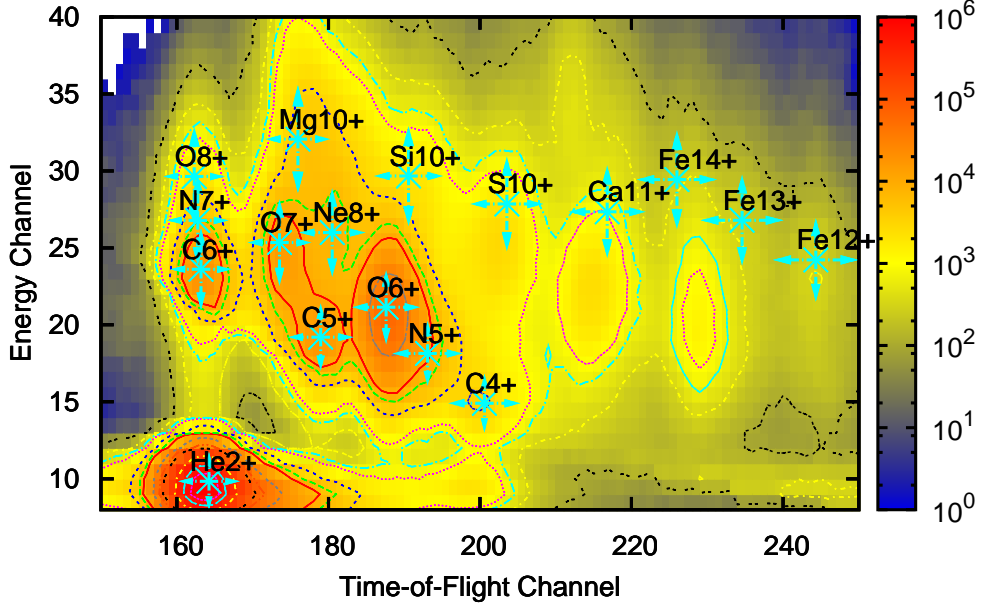


Figure 4.13.: The peak positions of different ions in the ET-matrix at E/q step 40 are shown. The blue arrows indicate the σ s of the ion distribution functions. At a specific E/q step the ions have fixed peak positions and σ s, making the peak height of an ion the sole unknown parameter. This plot was created from long term data including data from 2001-2007 (Taken from Berger [2008]).

The initial energy of an ion can also be expressed as an initial ion velocity v_i depending on the selected E/q ratio, ion mass, and ion charge

$$v_i = \sqrt{\frac{2Eq_i}{qm_i}}. \quad (4.57)$$

Therefore the Velocity Distribution Function (VDF) of a specific ion can be obtained by measuring at different E/q ratios. From this VDF physical properties, such as the ion density, the ion temperature, the ion bulk speed can be calculated.

When plotting the corresponding ToF and total energy measurements at a specific E/q ratio, figure 4.13 is obtained. Ions with different mass and charge have no sharp positions in this matrix, as we would expect from equations 4.54 and 4.55. Effects like the uncertainty in the E/q selection, interaction of the ions with the carbon foil, and pulse height defect of the SSD blur and shift the distribution function of ions. As the different ion distributions show strong overlap, a method has to be applied, which assigns a count correctly to an ion species. With the help of an Levenberg-Marquardt fit and a forward model by Kötten [2009], Berger [2008] determined the ion distribution functions on the basis of long term data in each E/q step. The distribution function of the i th ion can be described by a two-dimensional Gaussian

$$G_i(\tau, E_{\text{tot}}) = A_i \exp -\frac{(\tau - \tau_i)^2}{2(\sigma_{\tau,i})^2} - \frac{(E_{\text{tot}} - E_{\text{tot},i})^2}{2(\sigma_{E_{\text{tot},i}})^2}.$$

4. Data Analysis

As the shape and position of the ion distribution functions is constant, the solely unknown parameters are the peak heights A_i . The determination of the A_i s is done with a Levenberg-Marquardt fit algorithm. As the number of counts in the (τ, E_{tot}) -bins is low for most ions in high time resolution (12 min, 1h), the maximum likelihood estimator cannot be based on Gaussian statistics as in equation 4.41. Therefore, the maximum likelihood estimator is based on Poissonian statistics. After fitting of the A_i s the measured counts are assigned to the different ions by the probability calculated from the ion distribution functions.

4.9. Determination of physical quantities from SWICS count rates

Assigning the measured counts to the different ions is just the first step in determination of physical properties as ion temperatures, velocities, or densities. We assume that the phase space density of an ion s , $\rho_s(x, y, z, v_x, v_y, v_z, t)$, is constant in time and in x, y, z for the time of the measurement. Furthermore a measurement in an E/q step integrates the phase space density along the v_z and v_y component (see duty cycle). Therefore the phase space density of an ion s is related to the count rate in the i th E/q step by

$$\rho_{s,i}(v_x^{s,i}) = \frac{N_{s,i}}{v_{s,i}\tau g\eta_{s,i}\Delta v_{s,i}D(\alpha, \beta)}. \quad (4.58)$$

The different factors in equation 4.58 will be briefly discussed (for more information see *Berger* [2008], and *Köten* [2009]):

- The duty cycle $D(\alpha, \beta)$:

We assume a Maxwellian thermal distribution for all ions in velocity space. The integration along v_z and v_y does not cover the full range from $-\infty$ to ∞ due to instrumental properties. The duty cycle gives the fraction of the distribution, that is seen on average during the measurement. It depends on the angle α between the GSE x-axis and the field of view of the SWICS instrument, and on the Mach Angle β of the ion thermal distribution. The Mach angle is defined as the ratio of thermal velocity to bulk speed velocity ($\beta = \arctan\left(\frac{v_{\text{th}}}{v_{\text{sw}}}\right)$).

- Instrumental Efficiency $\eta_{s,i}$:

After passing the deflection system an ion has to trigger a ToF and an energy measurement. The interaction of the ion with the carbon foil leads to angular scattering, energy loss, and to the release of secondary electrons. These electrons have to hit the MCP for the start signal. The ion itself has to hit the active area of the SSD and has to overcome the energy threshold of the SSD. The secondary electrons from the SSD have to hit the second SSD for a stop signal. The combined probability for triggering all of these measurements is called instrumental efficiency $\eta_{s,i}$.

- Acceptance of the electrostatic analyser $\Delta v_{s,i}$:

As the electrostatic analyser has a finite width (see figure 4.12), also ions with lower speeds (larger

4.9. Determination of physical quantities from SWICS count rates

deflection than for the norm trajectory) and higher speeds (lower deflection compared to norm trajectory) can pass the deflection system. An uncertainty in the E/q selection of $\pm 3\%$ is assumed. From this value the acceptance for the speed interval $\Delta v_{s,i}$ is calculated.

- Spatial volume of the measurement $v_{s,i}\tau g$:

$v_{s,i}$ is the velocity of ion s in the i th E/q step. τ is the time of the measurement (typically 12 sec for one E/q step). The distance covered by an ion during the time of the measurement is given by $v_{s,i}\tau$. g is the active area of SWICS (0.0225 cm^2), called geometry factor. Multiplying the three factors gives the spatial volume from which ions can enter the instrument.

After calculating the differential phase space densities at different velocities v_x (the different E/q steps), the density of an ion is obtained by computing the zero order moment, the bulk velocity by computing the first order moment, and the temperature by computing the second order moment. Generally the uncertainty for the higher moment quantities is larger than for the low moment quantities.

5. Results

In this chapter the fit results from the different applied magnetic field models will be presented. Tables of the fit results for each model can be found in appendix C. The distribution of deviations between fitted and observed magnetic field components has been discussed in section 4.7. In section 5.1 some examples for fitted MCs will be shown and limitations of the fit process will be discussed. In section 5.2 the fit results from the different models are compared with each other and the errors from the Lepping approach (see section 4.7). The last section 5.3 describes the usage of fit results to link elemental and charge-state composition with spacecraft position.

5.1. Magnetic cloud fit results

The applied magnetic field models and their free parameters are described in the last chapter (section 4.2), as well as the fitting procedure (section 4.5). In figure 5.1 and 5.2 the fitted magnetic field for two MCs is shown. The best fit (with the lowest χ^2) achieved with each model was used to generate these plots. The ssq ($\text{ssq} = \sum_{i=1}^N \left(\frac{B_{x,i}^{\text{obs}}}{B_i^{\text{obs}}} - \frac{B_{x,i}^{\text{mod}}}{B_i^{\text{mod}}} \right)^2 + \left(\frac{B_{y,i}^{\text{obs}}}{B_i^{\text{obs}}} - \frac{B_{y,i}^{\text{mod}}}{B_i^{\text{mod}}} \right)^2 + \left(\frac{B_{z,i}^{\text{obs}}}{B_i^{\text{obs}}} - \frac{B_{z,i}^{\text{mod}}}{B_i^{\text{mod}}} \right)^2$, sum of squares, see section 4.5) of the fits is in the range of 0.004-0.170, with an average ssq of ≈ 0.04 . A total number of 67 MCs was fitted. For 14 of these MCs the helicity could not be determined unambiguously. In these cases the rotation of the magnetic field was very low (not exceeding 30-40°). For the remaining 53 MCs the fit parameters are listed in appendix C.

Keeping the start and end times of a MC as an additional free parameter was rejected after some tests. In most cases the fitted time period was shortened to get rid of short timescale magnetic field variations. In a manner of speaking the fit “smoothens” the magnetic field by taking fewer data points into account. As there are no physical reasons for this time period shortening, the start and end times are kept fixed. Usually the determined MC boundary times have an uncertainty of a few hours (see chapter 3), but exact boundaries have to be defined for the fit. This has an influence on the fit results. In particular for the circular cross section models, where the magnetic field strength is symmetric with respect to the centre, often either the left part of the time series or the right part is fitted well. Even a small displacement of the boundaries will change the probability of the different solutions and can completely change the final set of fit parameters.

Another limitation of the force-free circular cross section model is the ratio of the magnetic field strength

5.1. Magnetic cloud fit results

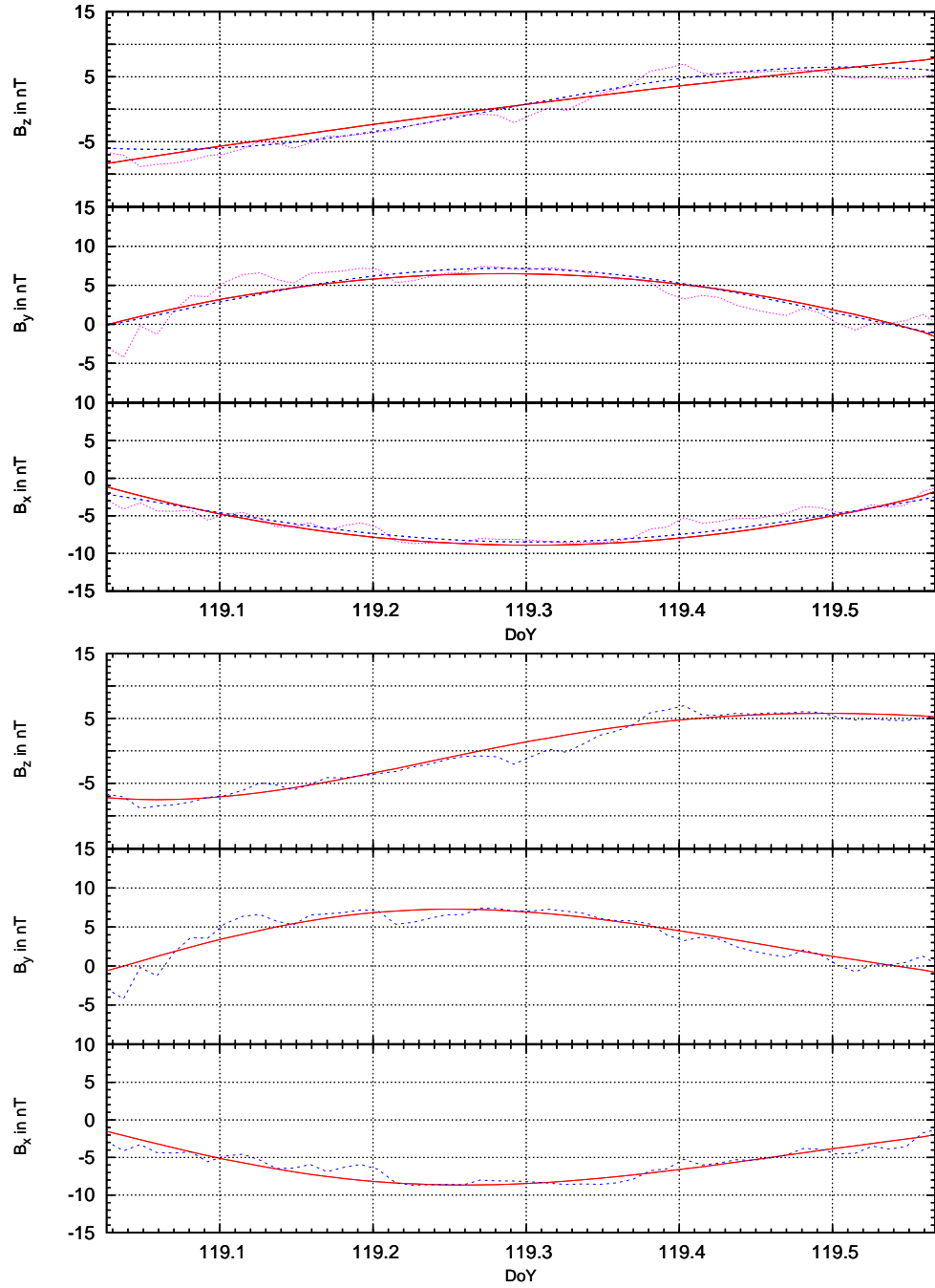


Figure 5.1.: Fits to the magnetic field of the MC passing ACE from DoY 119.02-119.56, 2001. In the upper plot the fit with the circular cross section non force-free model is shown in red, and the circular cross section force-free model in blue. Magnetic field data is plotted in pink. The ssq (see section 4.5) is 0.018 for the non-force free model and 0.012 for the force-free model, indicating a good fit to the data. The lower plot shows the fit with the force-free elliptical cross section model. Magnetic field data is plotted in blue, while the fit is plotted in red. In this case the ssq is 0.012 as for the force-free model with circular cross section (figure 5.1). The larger number of free parameter for the elliptical model does not improve the fit quality for this MC.

5. Results

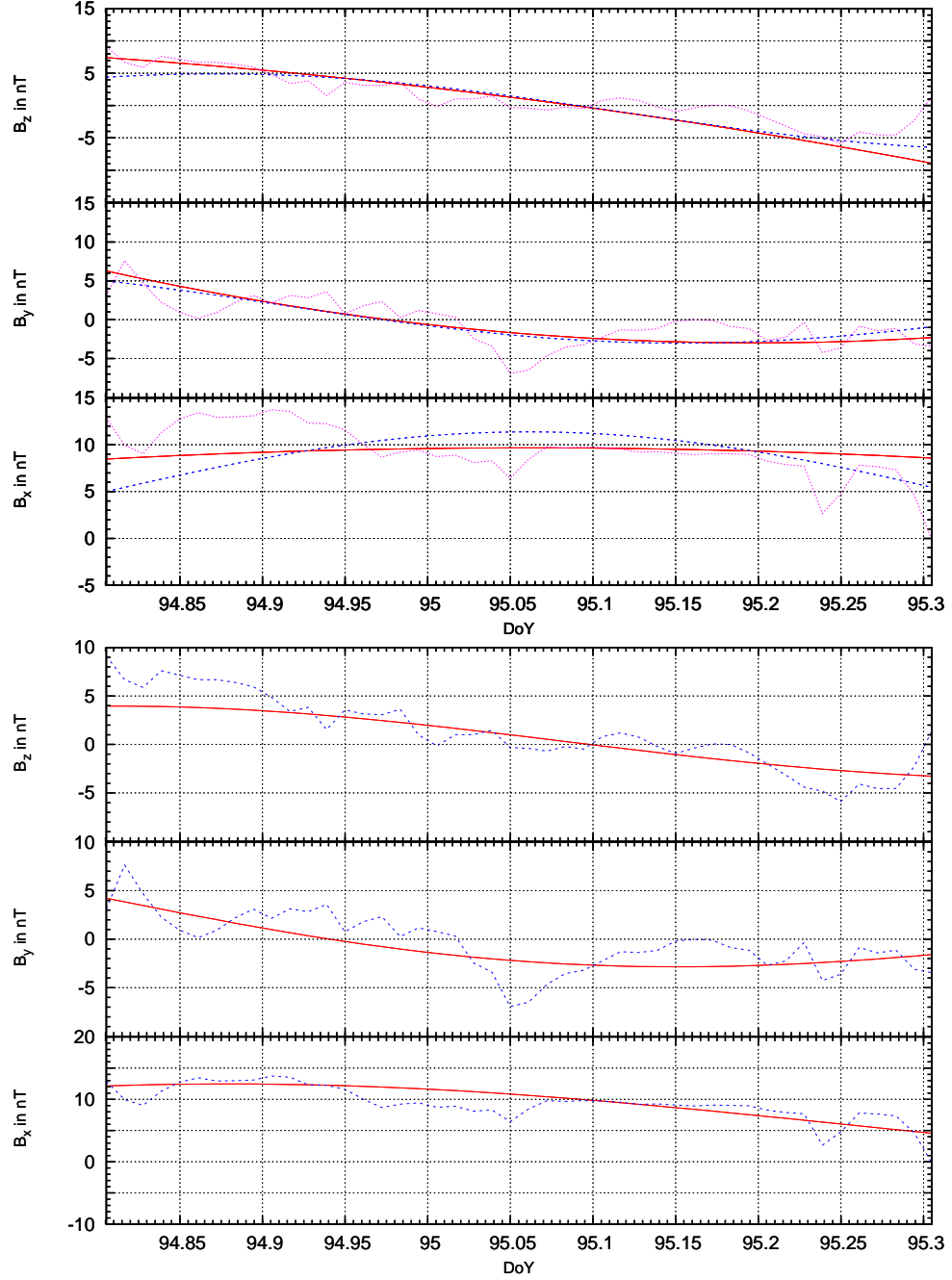


Figure 5.2.: Magnetic field fits for the MC at DoY 94.80-95.31, 2001. The arrangement of plots and the plotted quantities are the same as in figure 5.1. For this MC magnetic field variations with a period of roughly one hour are present, which cannot be generated with the applied models. Therefore the ssq is 0.037 for the circular cross section non force-free model and 0.042 for the circular cross section force-free model. The ssq for the elliptic cross section model fit is 0.041 and thus in the same dimension as for the circular cross section models. There is no general asymmetry in the magnetic field present, but variations on short timescale, which also cannot be explained with the elliptic model.

5.1. Magnetic cloud fit results

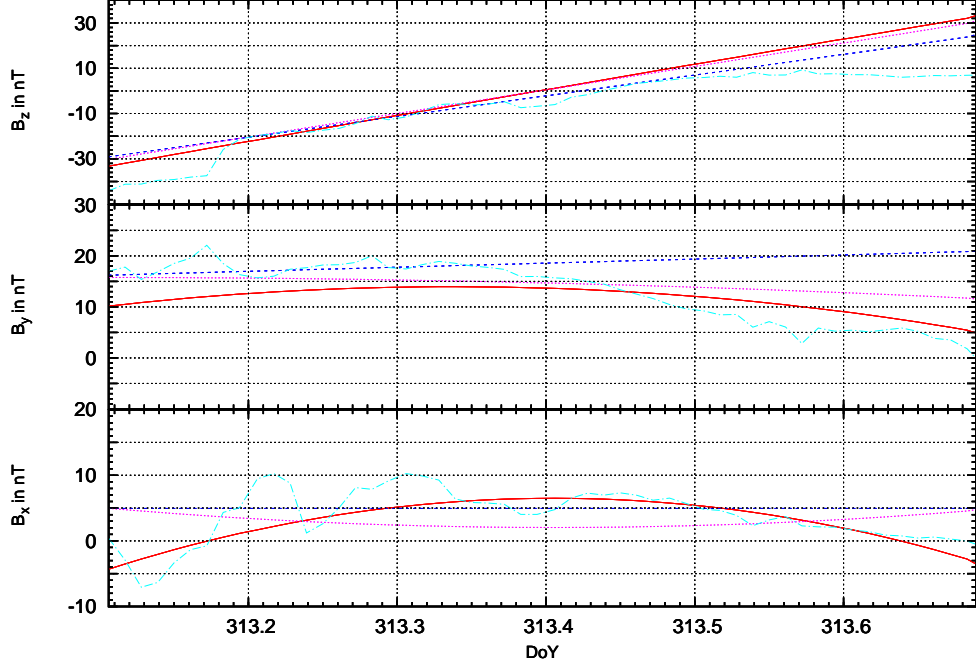


Figure 5.3.: Three fits with the circular cross section non force-free model for the MC at DoY 313.1-313.69, 2004. The red curve is the best fit with a ssq of 0.022, the dark blue curve fit has a ssq of 0.024 and the pink curve fit has a ssq of 0.025. The magnetic field data is plotted in light blue. The dark blue and pink fit have nearly the same set of parameter ($\theta = 1.3^\circ$ (-1.4° for pink), $\varphi = 165^\circ$ (160°), $d_0 = 3.1 \cdot 10^9$ m ($2.7 \cdot 10^9$ m)), the red fit has $\theta = -2.5^\circ$, $\varphi = 31^\circ$, and $d_0 = -2.2 \cdot 10^9$ m. The ambiguity of fit results can nicely be seen in the B_y component, were the leading part of the MC is best fitted by the dark blue curve and the trailing part is best fitted by the red curve.

near the MC's centre and at the limb. Even for a trajectory directly hitting the centre of the MC this ratio cannot exceed 1.72 and this model cannot explain a higher magnetic field strength at the limb than at the centre. The non force-free circular cross section model can only explain symmetric trends in magnetic field data, but the ratio of limb and centre field strength is not determined. The elliptic cross section force-free model can explain asymmetric field trends. The problem with the elliptic model is the increased number of free parameters. As the parameters are not really independent of each other, a magnetic field data set sometimes can be explained by different sets of fit parameters. None of the models can explain magnetic field variations on short timescales (within hours) (see figure 5.2). A fundamental problem of MC fitting is the fact that the results can not be checked independently with other observed quantities. The size and central magnetic field strength B_0 of a fitted MC can be compared to in-situ measured magnetic field strength and the dimension of MC intervals, but this comparison can only reject fit solutions which are completely implausible.

5. Results

5.2. Discussion of fit results

In some cases a fit with one set of parameters is only a good approximation for parts of the magnetic field data set. If another solution exists that fits the remaining parts of the data set better, the resulting χ^2 can have the same value, even though the set of parameters is completely different. The existence of different equally probable solutions results in large standard deviations for the parameters, when calculated from the 75 parameter sets according to section 4.5. Figure 5.3 shows an example of a MC, for which different solutions with nearly the same χ^2 exist. The difference in the χ^2 for the second best fit to the best fit is 0.33 % and 1.14 % for the third best fit to the best fit. When θ is $\approx 0^\circ$ and φ is $\approx 0^\circ$ or 180° the MC's z-axis is nearly parallel oriented to the spacecraft trajectory and small variations in the angles lead to large variation in the MC's radius (the length of the spacecraft trajectory inside the MC is fixed and given by solar wind speed and MC's passage time). The blue fit shown in figure 5.3 results in a MC radius of $5.3 \cdot 10^9$ m, while the MC radius is $6.4 \cdot 10^9$ m for the pink fit, even though the shortest approach distance d_0 is smaller for the pink fit.

To get an idea of the fit result variability determined with the different magnetic field models, the parameters are compared with each other. Of course, we can only compare parameters, which all models have in common. These are the magnetic field strength at the MC's centre B_0 , the orientation of MC's z-axis, expressed by the angles θ and φ , and the shortest approach distance of the spacecraft d_0 . The MC radius can be only compared between the two models with circular cross sections (The elliptic model has a large semi-axis and a small semi-axis). Now the difference in these parameter is calculated for each combination of models. As we have three different models we get three sets of differences. In figures 5.4 to 5.6 histograms of the differences between the various models are shown. Not unexpectedly the difference is smallest for the comparison of the models sharing the same geometry. From these difference distributions a standard deviation for the parameter was calculated using: $\sqrt{\frac{1}{N} \sum_{i=1}^N (\Delta x_i)^2}$, with Δx_i being the difference in parameter x between two models $x_i^{\text{model } 1} - x_i^{\text{model } 2}$. The calculated standard deviations are (see figure 5.4 for abbreviations):

- θ : 5.5° for NFC to FFC, 11.9° for NFC to FFE, 10.5° for FFC to FFE.
- ϕ : 15.1° for NFC to FFC, 48.4° for NFC to FFE, 46.4° for FFC to FFE.
- B_0 : 7.6 nT for NFC to FFC, 14.9 nT for NFC to FFE, 13.3 nT for FFC to FFE.
- d_0 : 0.0187 AU for NFC to FFC, 0.039 AU for NFC to FFE, 0.041 AU for FFC to FFE.
- Size: 0.025 AU for NFC to FFC.

Since the deviations between the circular cross section models are small, the deviations to the elliptic cross section model are nearly the same. Taking these standard deviations as the uncertainty of the

5.2. Discussion of fit results

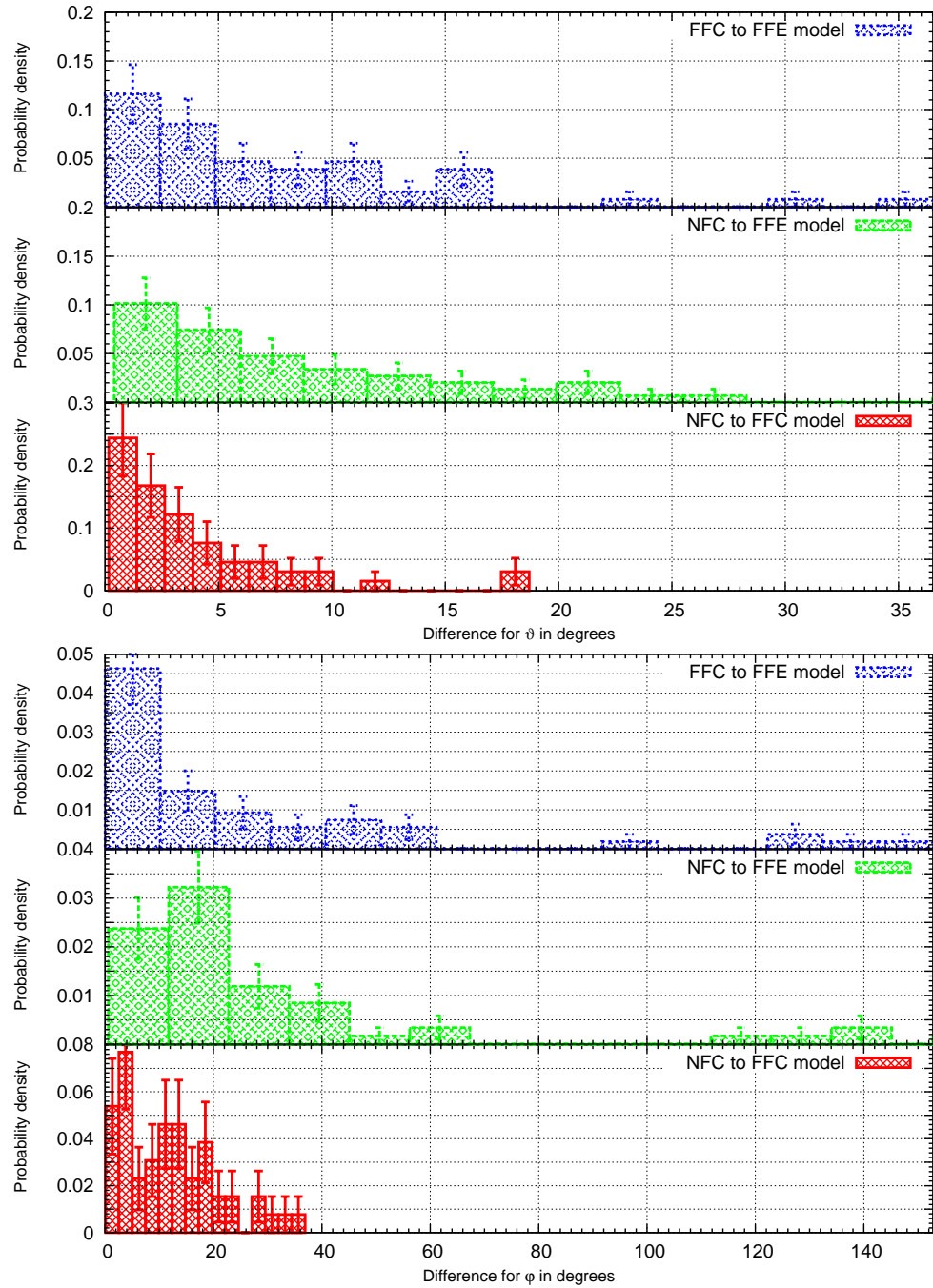


Figure 5.4.: The upper plot shows a histogram of the deviations between the different model fit results for the MC axis orientation parameter θ . NFC is the non force-free model with circular cross section, FFC the force-free model with circular cross section, and FFE the force-free model with elliptic cross section. Due to the same geometry deviations between the NFC and FFC model are smallest. Errors are calculated from the number of events in each bin. In the lower plot the Histogram of the deviations between the different model fit results for the MC axis orientation parameter ϕ is shown. Again the difference between the NFC and FFC model are smallest. Compared with θ , the angle ϕ shows much larger variation depending on the applied model (note the different scaling of the x-axis).

5. Results

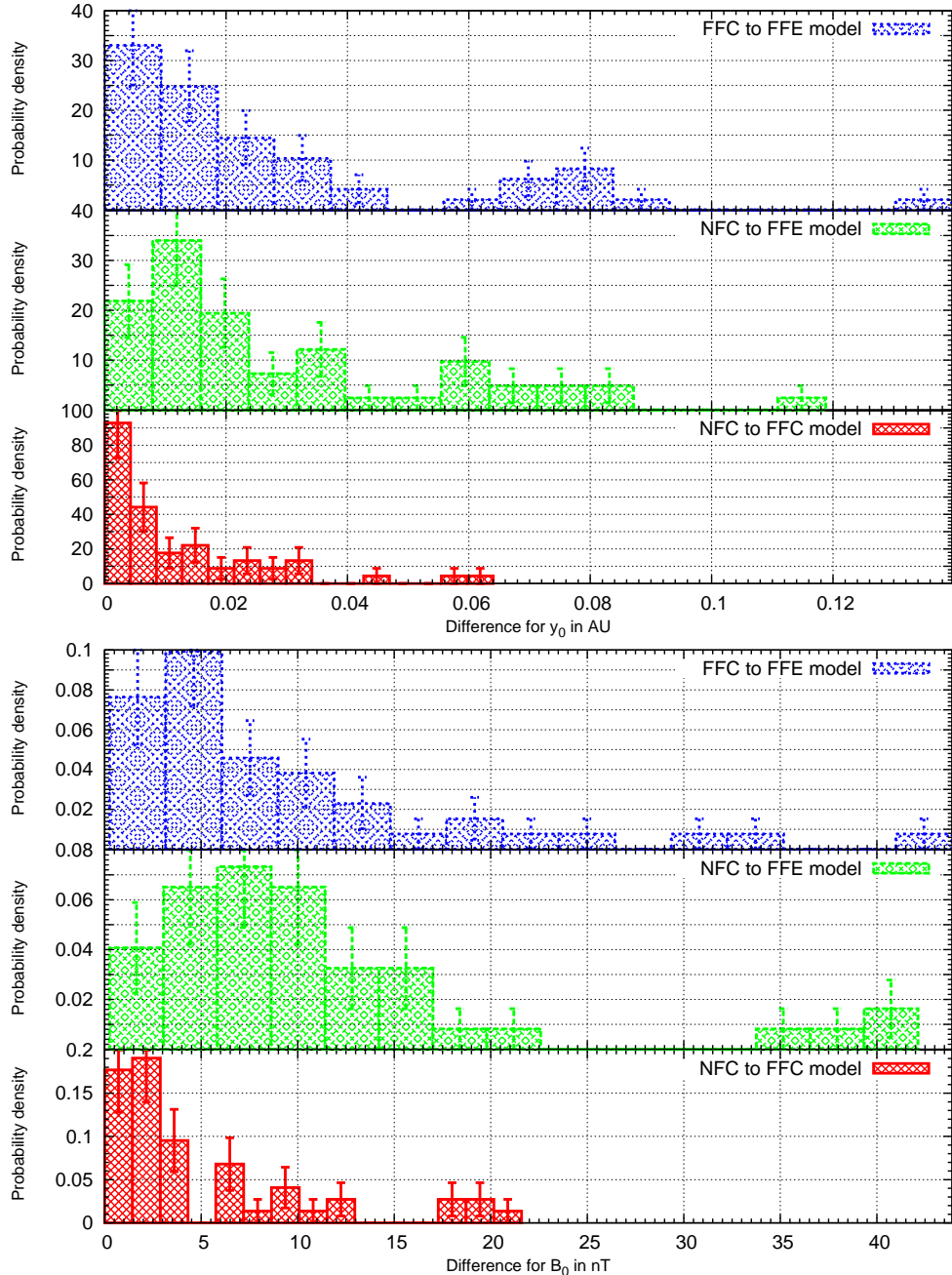


Figure 5.5.: The upper plot shows the histogram of the deviations between the different model fit results for the MC shortest approach distance d_0 . Abbreviations for the models are as in figure 5.4. The average radius for the circular non force-free model is 0.096 AU and 0.093 AU for the circular force-free model. One MC was discarded in the upper two panels, because the difference between the circular models and the elliptic model exceeded 0.25 AU. The lower plot shows the histogram of the deviations between the different model fit results for the MC central magnetic field strength B_0 . The non-force free model central magnetic field strength is poorly determined in the case of a glancing encounter with the MC. In some cases two encounters are possible for the elliptic model (see figure 4.4). One along the large semi-axis (with low central magnetic field strength), and one along the short semi-axis (with large central magnetic field strength). This explains the large deviations which sometimes occur.

5.2. Discussion of fit results

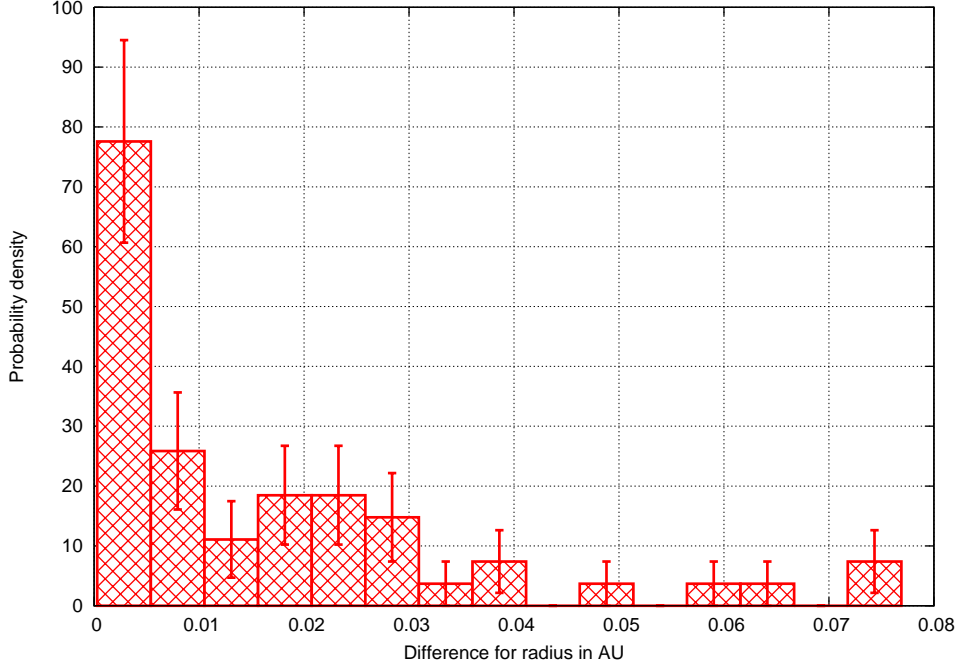


Figure 5.6.: Histogram of the deviations between the different circular model fit results for the MC radius. As there is no single radius in the elliptic model, only the circular models are compared. Abbreviations for the models are as in figure 5.4. The average radius for the circular non force-free model is 0.096 AU and 0.093 AU for the circular force-free model.

parameters we can compare them with the errors calculated with the Lepping approach (see section 4.7). Therefore, we use the tables of *Lepping et al.* [2003] to determine the uncertainties from average MC properties. The average ssq of the applied models is ≈ 0.04 . This corresponds to their very high noise level. The average angle between the GSE x-axis and the MC z-axis is 67.7° , which is between the two tabulated cases 60° and 90° . The average shortest approach distance is 50 % of the average MC radius, which is between the tabulated values of 30 % and 60 % times the MC radius. Linear interpolation was used to calculate the corresponding uncertainties for 67.7° and $d_0 = 0.5$ times the MC radius.

The uncertainties of the parameters calculated from their tables are: $\sigma_{B_0}=7.3$ nT, calculated with an average B_0 of 22.5 nT, $\sigma_\theta=21^\circ$, $\sigma_\varphi=66^\circ$, $\sigma_{d_0}=0.83$ times the MC radius, $\sigma_{\text{Radius}}=15$ % of the MC radius. The average MC radius is 0.096 AU for the circular cross section non force-free model and 0.093 AU for the circular cross section force-free model. Therefore the average uncertainty for the MC radius is roughly 0.015 AU, and 0.08 AU for d_0 .

The errors calculated from the model comparison and from the Lepping approach are comparable within a factor of two. A part of the deviations can be explained by the different models. d_0 for example can reach values larger than the MC radius in the Lepping model. Generally B_0 is overestimated in the elliptic magnetic field model (see figure 5.5), leading to the large deviations in B_0 . The remaining

5. Results

difference arises from the different approach. The Lepping approach examines how the fit results vary with different input fields, and our approach considers how the fit results vary with different magnetic field models and geometries. From this comparison we conclude:

- The angle θ is determined much more accurately than φ .
- The uncertainty in d_0 is at least 33 %.
- The uncertainty in MCs size is about 25 %.

Let's take a short look on the parameter distributions itself. The average MC dimension of ≈ 0.2 AU is in good agreement with the results of *Bothmer and Schwenn* [1998] (0.25 AU) and *Lynch et al.* [2003] (0.19 AU). The average angle θ is $\approx 0^\circ$ as in the Bothmer and Lynch paper, but the distribution is narrower in our case. The distributions for φ are different: While in both papers the probability for an angle of 0-40° is low, it is high in our cases. A possible explanation is a solar cycle dependence of the MC axis orientation. The sun is exceptionally inactive in the current solar minimum.

5.2.1. Velocity profiles from force-free elliptic model

A possibility to check the fit results for consistency is given in the elliptic cross section force-free model. The MC self-similar expansion is controlled by the parameter t_0 (see section 4.2.3). The lower t_0 the faster the expansion takes place. The expansion velocity is superimposed on the velocity of the whole MC. Now the total velocity at time t can be calculated from the position of the spacecraft inside the MC at time t . This calculated solar wind speed can be compared to the in-situ measured solar wind speed. Figure 5.7 shows an example of these two velocities inside a MC. Also shown is a histogram of the deviations between calculated and measured velocities. In most cases the deviations are quite small. Note that a decrease in MCs size is not included in the model and therefore speed profiles decreasing from the leading to the trailing edge cannot be modelled. The modelled solar wind speed was calculated to have the same average as the in-situ speed. Thus there is always an intersection between the two speed profiles. As most MCs show only small expansion speeds (between -50 to 50 km/s), their in-situ speed profile will always show relatively good agreement with the calculated speed profile, as long as t_0 is large enough (exceeding about 10 times the MC duration). Hence it is difficult to judge the relevance of the histogram shown in figure 5.7 for the trueness of the fitted parameter.

5.3. Global MC model

The trajectory of the spacecraft inside the local part of a MC is determined by the fit parameter (see figure 4.6) . Now the question is, where is this local part positioned with respect to the global structure of the MC? In figure 5.8 a sketch of a possible global MC structure is shown projected into the ecliptic

5.3. Global MC model

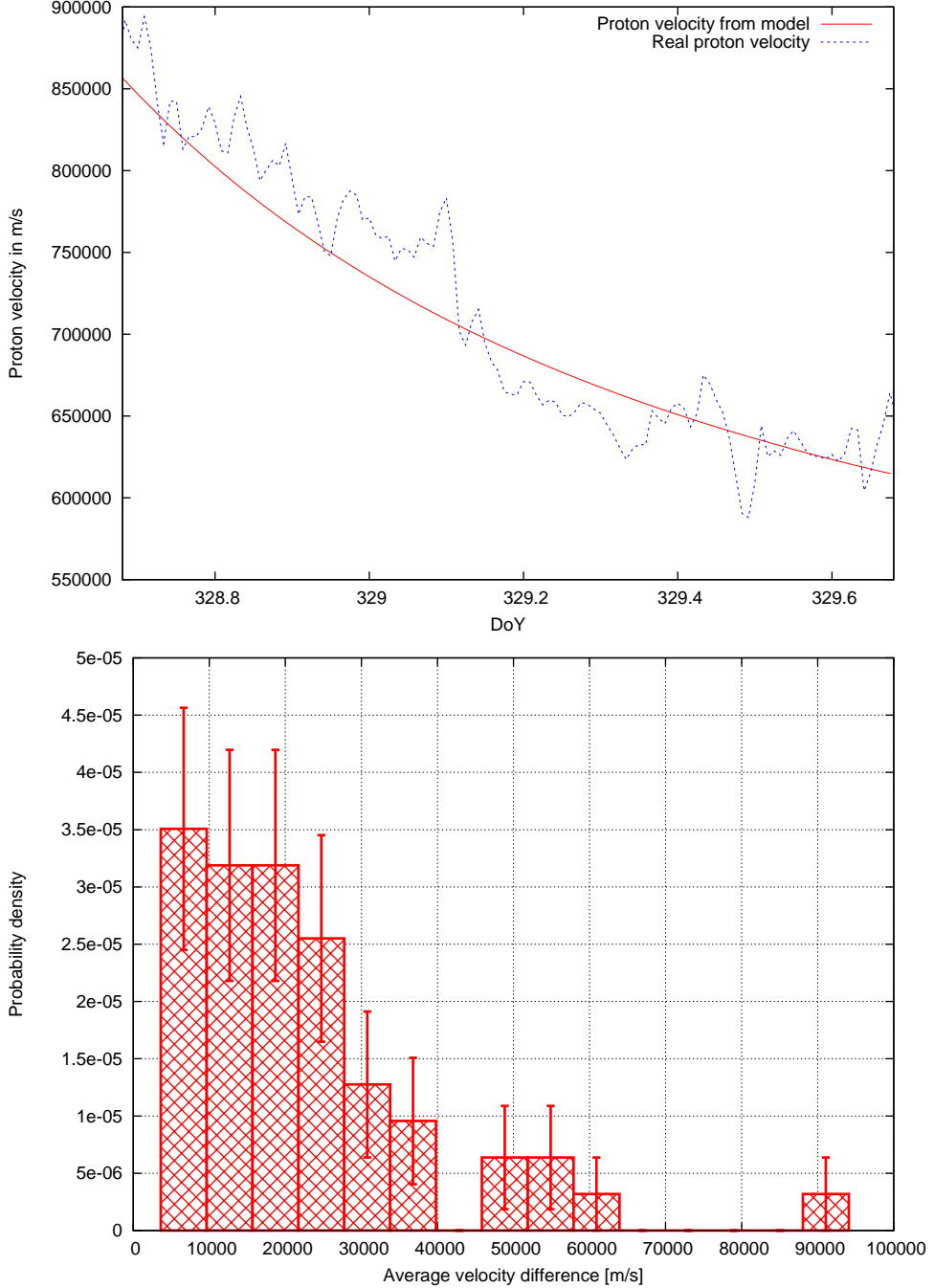


Figure 5.7.: The upper plot shows the proton velocity measured with SWEPAM (blue) and the proton speed calculated with the fit results of the force-free elliptic model for the MC from DoY 328.68-329.69, 2001. Measured and modelled data show good agreement. The average deviation between modelled and observed velocity is 25.7 km/s. The lower plot shows the histogram of the deviations between the measured proton speed and the calculated proton speed for the whole dataset of 53 MCs. The deviation was calculated using: $\sqrt{\sum_{i=1}^N (v_i^o - v_i^m)^2}/N$. v_i^o is the observed proton speed, v_i^m the modelled proton speed, and N the number of data points. An increase in proton speed from leading to trailing edge cannot be explained by the model and leads to large deviations.

5. Results

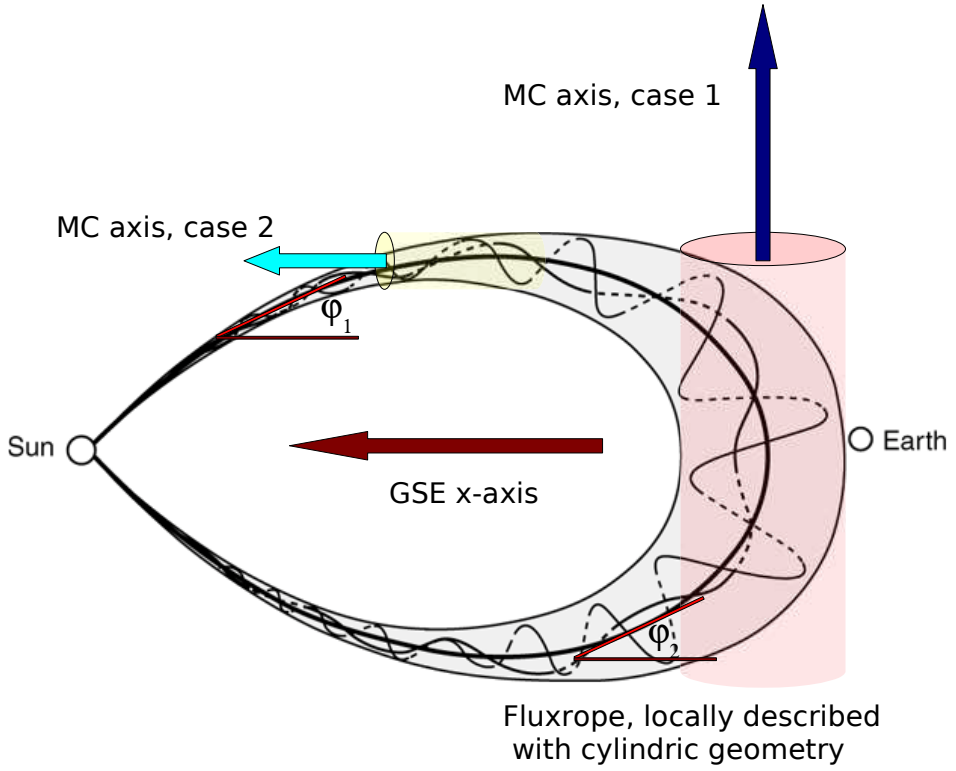


Figure 5.8.: Sketch of a MC in the ecliptic plane. The fit results for the axis orientation angle φ can be interpreted as encounter with different parts of the MC. Assuming that all MCs have the illustrated structure, a fitted angle $\varphi = 90^\circ$ means an encounter with the MC's centre (case 1), an angle $\varphi = 0^\circ$ represents an encounter with the MC's leg (case 2). The parts of the MC connecting the legs back to the sun are neglected ($\varphi_1 = \varphi_2$, but located at different parts of the MC). (Sketch of the MC taken from http://dawn.ucla.edu/personnel/russell/papers/true_dimen/fig3.gif)

plane. The angle φ gives the local orientation of the MC's z-axis. This axis has to be parallel to the thick black line in the sketch, where it represents the magnetic field line at the MC's centre (Only axial magnetic field). So we look for the position of the thick black line, where the field line angle with respect to the GSE x-axis is the same as φ , to determine the part of the MC that was hit by the spacecraft. As the direction of the z-axis is non-relevant for this treatment, angles φ larger than 180° are decreased by 180° . Additionally we make no difference between upper or lower leg and put: $\varphi_{\text{new}} = 180^\circ - \varphi_{\text{old}}$, if φ exceeds 90° . Since the determination of the MC part encountered would no longer be unique, the connection of the legs back to the sun are neglected (see figure 5.8). The angle φ from the circular cross section non-force model is used in the following context, as the deviations to the circular cross section force-free model are quite small and it is easier to handle (fewer free parameters) than the elliptic cross section model, although its average ssq is as good as for the elliptic model.

Indications supporting the applied MC geometry are coronagraph observations (three part CME, see

section 1.5.2), and the presence of bidirectional suprothermal electrons, which indicate magnetic field lines anchored at the sun's surface. But even if the global structure is comparable to the sketch, local distortions will lead to misidentification of the crossed MC part.

5.4. Charge states

The charge-state distributions of the elements are the imprints of the coronal temperature profile at different distances from the sun. Depending on ionisation and recombination cross sections the ratio $\frac{X_i}{X_{i+1}}$ (charge states X^{i+} and $X^{(i+1)+}$ of element X) becomes fixed, when the ionisation timescale exceeds the expansion timescale, as the electron density decreases with increasing distance from the sun (see section 1.4). After crossing this radius the ion charge state is denoted as frozen in. Iron charge states freeze in at distances of roughly 3-4 solar radii and oxygen charge states at distances of about 2 solar radii (see *Reinard et al. [2001]*).

5.4.1. Iron charge states

To visualise the effect of different spacecraft trajectories on the iron mean charge state inside a MC the method described in section 5.3 was applied to determine the encountered part of the MC. The distance of the spacecraft to the MCs centre at time t is computed from the fitted parameters of the circular cross section non force-free model. The iron mean charge state was calculated from SWICS data with a time resolution of one hour by $\langle Q_{\text{Fe}} \rangle = \sum_{i=7}^{24} \frac{n_i i}{n_{\text{ges}}}$, with the total iron density $n_{\text{ges}} = \sum_{i=7}^{24} n_i$. In figure 5.9 the iron mean charge state in dependence of φ (in-ecliptic orientation of MCs axis, see figure 5.9) and the distance to MCs centre is shown. There are no obvious trends visible in this figure. MCs with high average iron mean charge state alternate with low average mean charge state MCs at all axis orientations. Some of them show the highest iron mean charge state near the leading edge and others near the trailing edge. Only in a few cases the highest iron mean charge state is reached near the MCs centre and drops down toward the edges.

There are three possible explanations for this behaviour:

- The fit results for parameter φ are not accurate enough. The differences between the circular cross section models and the elliptic cross section model in fact indicate uncertainties of about 50° (see section 5.2).
- The global MC model described in section 5.3 is not valid in all observed cases. Missing signatures of bidirectional suprothermal electrons in some of the MCs indicate disconnection of magnetic field lines from the sun for example.
- There are different classes of MCs which are released during periods of varying coronal temperature environment.

5. Results

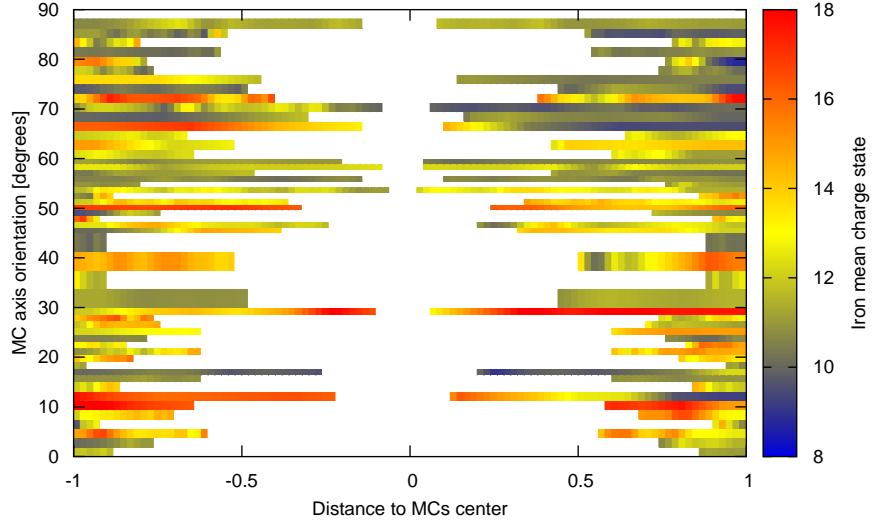


Figure 5.9.: The iron mean charge state is plotted for 52 MCs in dependence of the spacecraft distance to the MC's centre and MC's axis orientation (see section 5.3). A distance of 1 denotes the MC's leading edge, while -1 is the trailing edge of the MC. The (-1,1) interval was divided in 100 equidistant steps using linear interpolation for the iron mean charge state. An axis orientation of 90° describes an encounter with the central part of the MC, while an axis orientation of 0° is an encounter with the MC's leg. The white area results from the fact that the spacecraft never gets closer to the MC's centre than the closest approach distance d_0 . The width of the bars is calculated from 15° intervals. Each interval is divided by the number of MCs within this interval and the bars are arranged by the angle of axis orientation (the lowest angle is at the bottom in each interval, the highest angle is at the top, leading to small deviations ($< 15^\circ$) from the true axis orientation). The plot was calculated from iron data with a time resolution of one hour.

We will concentrate on the third explanation below. In the next section we will divide the MCs in two groups. One group is associated with flares and the other has no flare association.

Now we will look at the oxygen mean charge state and see if there are general differences in the thermal environment at different distances from the sun. In figure 5.10 the correlation between the iron and oxygen mean charge state is shown. The mean charge states were averaged over the duration of the MCs passage. Both quantities are well correlated with a correlation coefficient of 0.71. From the O^{7+}/O^{6+} ratio we can calculate the coronal temperature at the O^{7+}/O^{6+} ratio freezing-in distance under the assumption of thermodynamic equilibrium (see section 5.4.4). From this temperature and the tables by *Arnaud and Rothenflug* [1985] we can calculate a theoretical iron charge-state distribution and a theoretical mean iron charge state. These values are plotted green in figure 5.10.

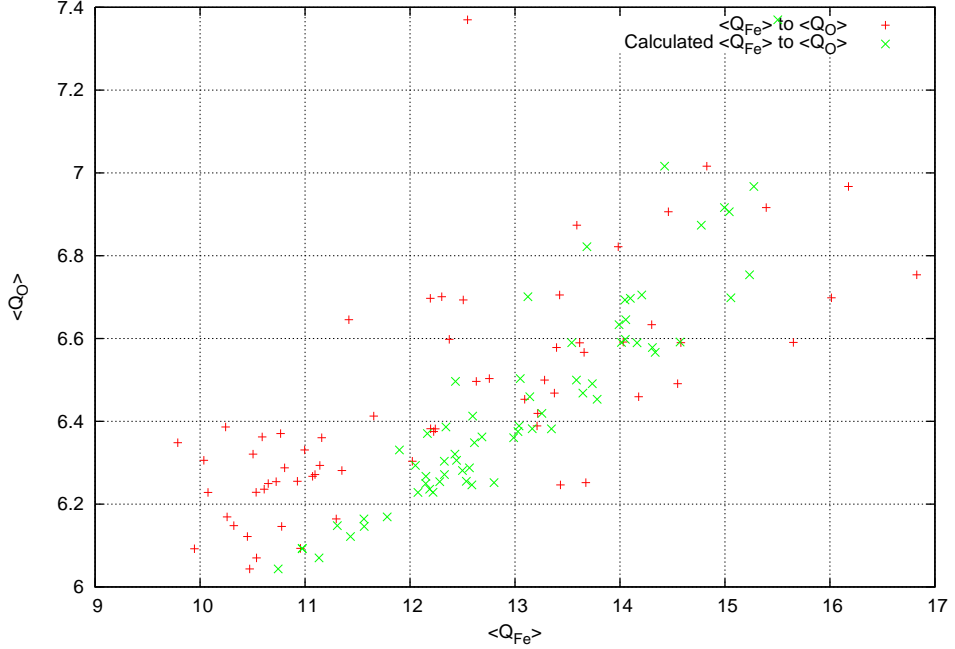


Figure 5.10.: The red symbols show the relation between the oxygen and iron mean charge state in 66 MCs. The green symbols show the theoretical iron mean charge state calculated from the O^{7+}/O^{6+} ratio under the assumption of thermodynamic equilibrium plotted versus the oxygen mean charge state.

Now we can compare the observed iron mean charge state with the theoretical iron mean charge state calculated from the O^{7+}/O^{6+} ratio. For low observed iron mean charge states the theoretical iron mean charge state is higher than the observed, indicating cooling of the corona from the O^{7+}/O^{6+} freezing-in radius to the larger radii, where the iron charge states freeze in. At high iron mean charge states the observed charge states are higher than the theoretical, suggesting higher temperatures at the iron charge state freezing-in distances than at the O^{7+}/O^{6+} freezing-in radius or deviations from the thermodynamic equilibrium assumption. In the model from *Aellig et al. [1997]* higher iron charge-state ratios freeze in closer to the sun, where the coronal temperatures are higher, but in a larger distance to the sun than the O^{7+}/O^{6+} ratio.

5.4.2. Flare associations of MCs

As we see from figure 5.9 the mean iron charge state is not just a matter of spacecraft trajectory inside the MC. We look for different coronal thermal conditions under which the MCs develop. Therefore, we searched for flare associations of the MCs. The MCs were identified in an ICME database¹. For roughly 60 % of the MCs the related CME could be identified (see sections 1.5.2 and 1.6). Comparing the time of first appearance of the CME in the C2 field of view of the LASCO coronagraph with the GOES X-ray

¹<http://www.ssg.sr.unh.edu/mag/ace/ACElists/ICMTable.html>

5. Results

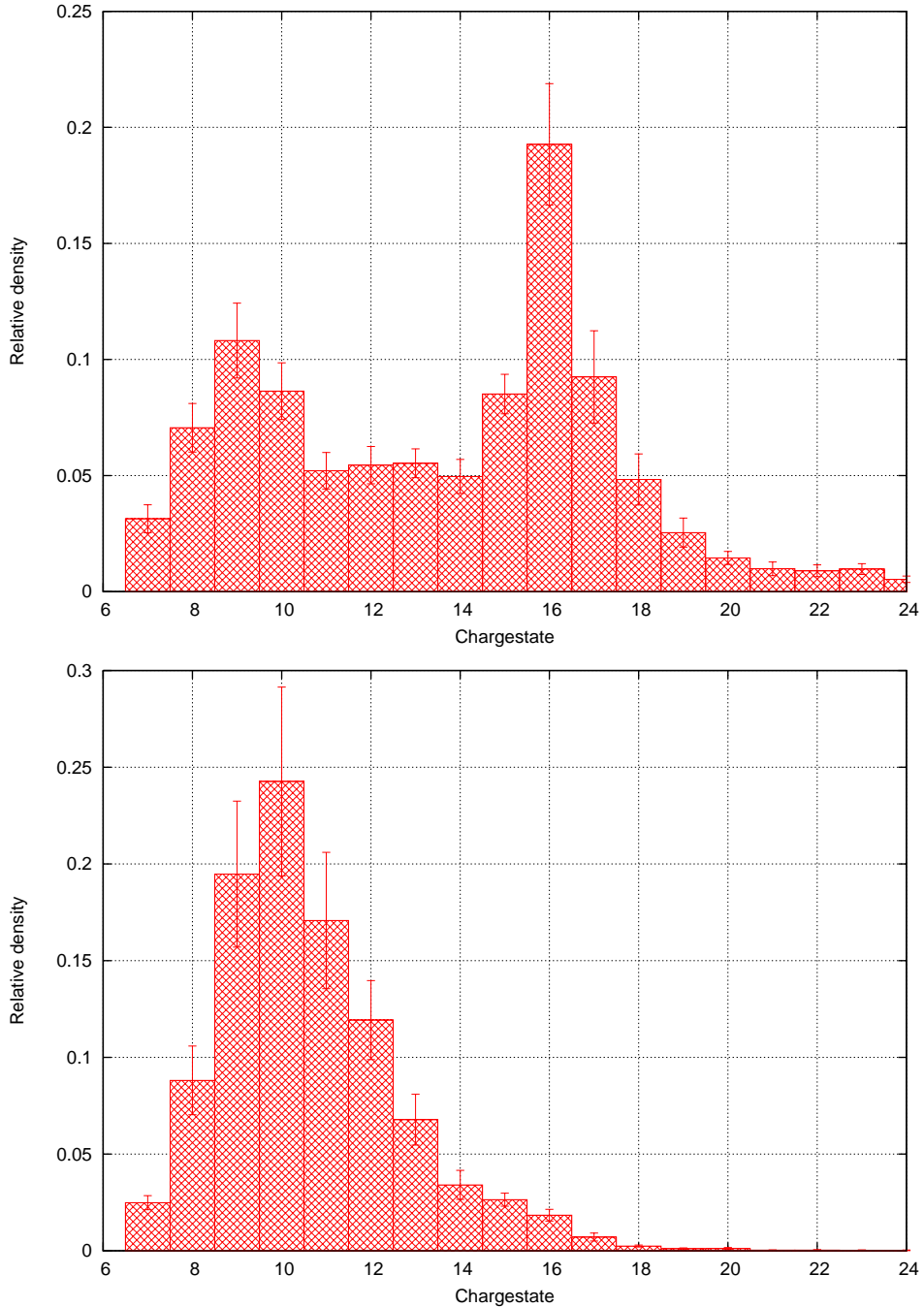


Figure 5.11.: The upper plot shows the iron charge-state distribution of a MC associated with a 1.0 M-class flare. The lower plot shows the iron charge-state distribution for a MC not associated with a flare. The ion densities were obtained by averaging the 1h data over the duration of the MC. The uncertainties are calculated from the density uncertainties of the single ion species provided by the count rate analysis (see section 4.8) by error propagation.

flux temporal associations between flares and CMEs were obtained. For 30 MCs a relation to a flare with a peak flux exceeding C-class strength could be determined. For the remaining MCs no CME associations could be identified. The reasons are ambiguities in the CME assignment during periods of high CME activity or data gaps in the LASCO measurements. The positions of the flares on the solar surface are compared with AR positions², to determine the AR emitting the CME.

Now we look into the iron charge-state distributions determined from each MC. Two different groups of MCs can be identified from the observed iron charge states. One group shows a large amount of Fe¹⁶⁺ and adjacent charge states, while these high charge states are not present in the other group. Figure 5.11 illustrates this issue. Now we compare the presence of these high charge states with the flare association of the MC. All MCs showing this high charge-state component are related with strong flares, but not all MCs associated with a strong flare reveal high iron charge states. MCs associated with flares located near the solar limb do not show the enhancement in iron charge states (see *Reinard* [2008]). Only 4 of our MCs are associated with limb flares (distance to solar disk centre > 40°).

Thus, we divide the MCs in two groups. Flare-associated MCs showing a high iron charge-state component and MCs without flare associations not showing this component. 38 of the MCs belong to the flare-associated group, 28 are not a member of this group. For comparison, the iron charge-state distribution of 21 fast solar wind periods and 21 periods slow solar wind (3 in each year) were calculated. None of these distributions shows an enhancement in the high charge states comparable to the flare-associated MC group.

5.4.3. Variability of Charge states

In this section we want to characterise the fluctuations in the mean charge states seen in figure 5.9 on a statistical basis. First we calculate the standard deviation of the iron mean charge state during the MCs passage from 1-h data to get an idea of the general temporal variation. In figure 5.12 the variation of the iron mean charge state is plotted towards the in-situ proton velocity. Faster MCs tend to show larger variation in the iron mean charge state. (The correlation coefficient is 0.482, calculated from $KOR(\vec{x}, \vec{y}) = \frac{1}{N\sigma_x\sigma_y} \sum_{i=1}^N (x_i - \bar{x})(y_i - \bar{y})$. \bar{x} and \bar{y} denote averages, while σ_x and σ_y represent the standard deviations, calculated from \vec{x} and \vec{y} . The significance level is 95.2 %.) Comparing this variation in the iron mean charge state to the variation in the oxygen mean charge state provides a correlation as good (correlation coefficient 0.70) as for the mean charge states themselves (see figure 5.10). A high level of fluctuation in the mean charge state can result from many short timescale variations or from a single change from leading to trailing edge of the MC.

Now, we look at the symmetry of the mean charge-state variations. MCs are low plasma β structures (see figure 3.1) and, therefore, the ions should primarily mix along the magnetic field lines. Assuming a locally cylindric structure of the MC as in the magnetic field models 4.2.1 and 4.2.2, the magnetic field

²<http://www.solar.ifa.hawaii.edu/ARMaps/archive.html>

5. Results

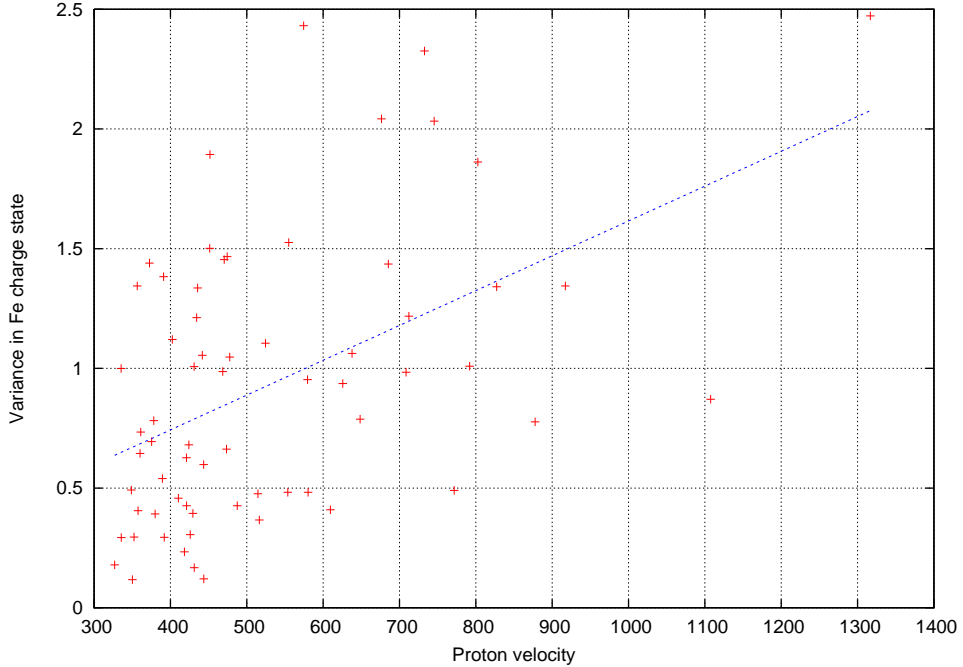


Figure 5.12.: Variation of the iron mean charge state in dependence of the solar wind speed for 66 MCs. The variation was determined from the standard deviation of the iron mean charge state 1h data over the duration of the MC. The blue line is obtained by linear regression.

lines form closed cylindrical surfaces because the magnetic field has no radial component. The gradient of the magnetic field strength is perpendicular to these surfaces and the occurring drifts do not remove the ions from the surface. When the spacecraft enters a MC it will be at the closest approach distance d_0 at $D/2$, with D being the duration of the MC passage. The spacecraft will intersect each cylindric surface within the MC, which has a radius larger than d_0 , twice. E. g. if it intersects the cylindric surface with radius R_1 at $t = 0.1D$ it will intersect this surface at $t = 0.9D$ for a second time. If the plasma on each magnetic surface is completely mixed, we would expect to see the same time sequence for the mean charge state in the first and second half of the MC, but mirrored in time for the second part of the MC. To quantify the self-similarity of the time series we calculate the autocorrelation function (ACF) for a time-shift of $0.5D$ and the second half of the time series mirrored. In figure 5.13 the procedure is shown for two hypothetical cases. The autocorrelation coefficient was calculated from the mirrored time series using,

$$\text{ACF}(0.5D) = \frac{\sum_{i=0}^{N-1} (x_i - \bar{x}) \left(x_{((i+\frac{N}{2}) \bmod N)} - \bar{x} \right)}{\sum_{i=0}^{N-1} (x_i - \bar{x})^2}. \quad (5.1)$$

A high self-similarity will lead to a autocorrelation coefficient of ≈ 1 , no temporal correlation in the time series will lead to a autocorrelation coefficient of 0, and a negative autocorrelation coefficient is

5.4. Charge states

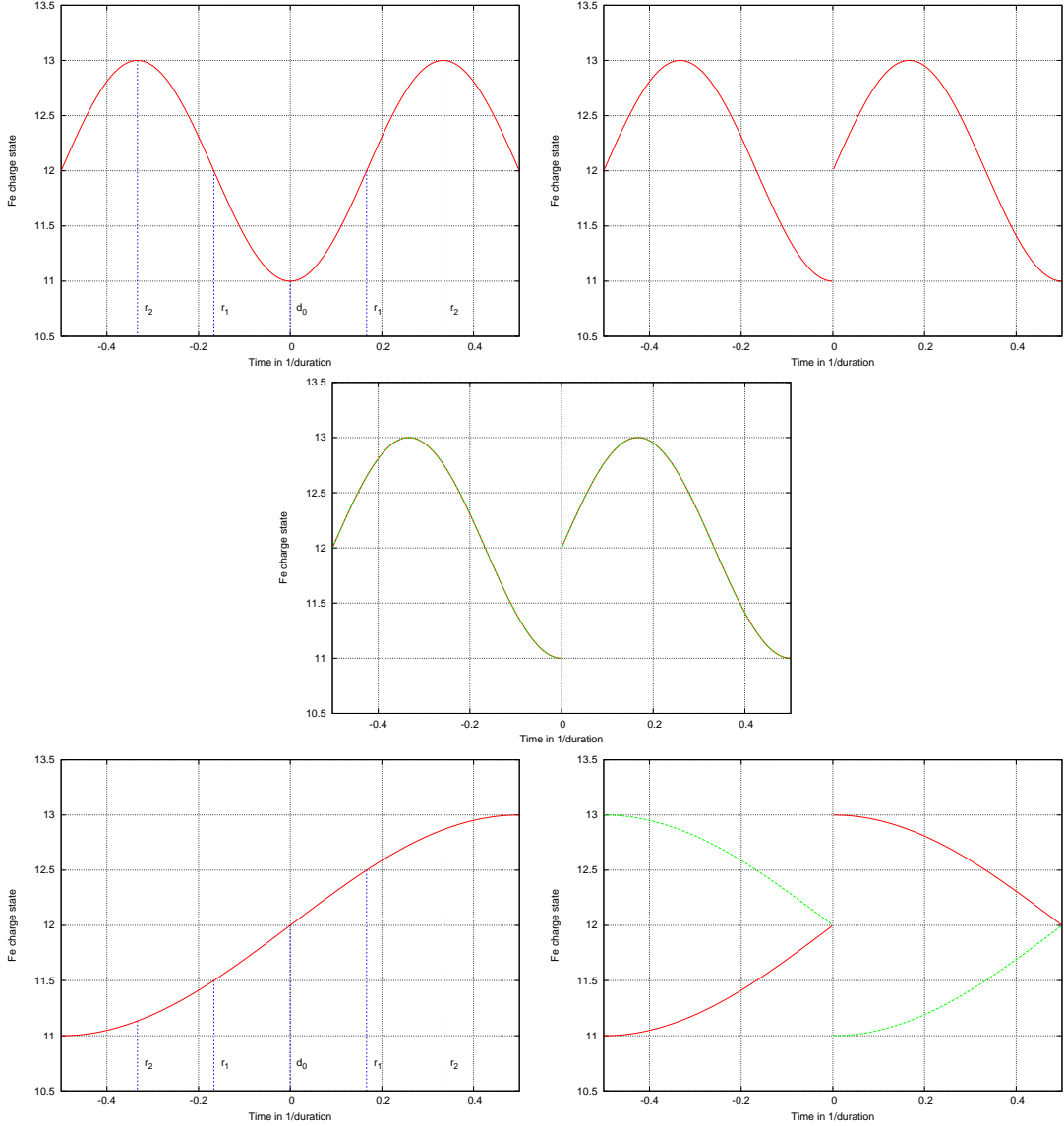


Figure 5.13.: The left plot in the upper row shows a schematic mean charge-state time series that would be obtained from a constant mean charge state on each cylindric surface. The right figure in the upper row shows the same time series, with the second half (after passage of d_0) mirrored in time. In the plot in the middle row one curve is the mirrored graph and the other the mirrored graph shifted by 0.5 times the duration of the spacecraft passage. In this case the autocorrelation coefficient ACF ($0.5 \times \text{duration}$) is 1. The left figure in the lower row shows a schematic mean charge-state time series with a high mean charge state near the trailing and a low mean charge state near the leading edge. In the right figure in the lower row the mirrored time series and the mirrored time series shifted by 0.5 times the duration are plotted. In that case the autocorrelation coefficient ACF ($0.5 \times \text{duration}$) is -0.99.

5. Results

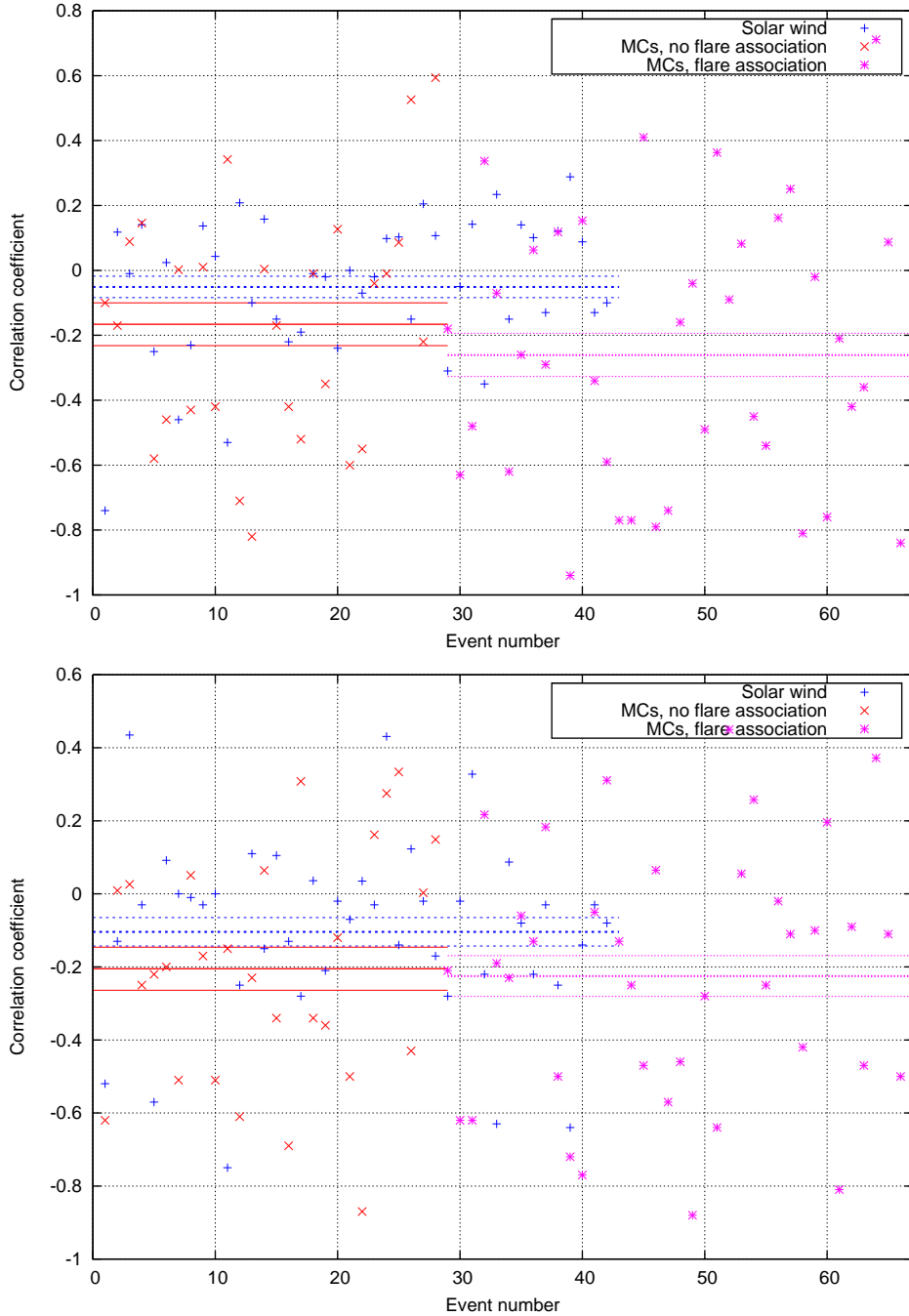


Figure 5.14.: Autocorrelation coefficients calculated with the procedure described in figure 5.13. The blue symbols show the 42 reference solar wind periods, red symbols show MCs with no flare association, and flare-associated MCs are plotted pink. The event number in each of the three groups is given from the time of occurrence. A thick bar denotes the average and the thin bars represent the standard deviation of the mean value. The upper plot was computed from the iron mean charge-state time series, the lower from the oxygen mean charge-state time series.

obtained, if the mirrored time series shows contrary behaviour in the first and second half.

In figure 5.14 the autocorrelation coefficients are shown for all 66 MCs divided in to a group with and without flare association and for 42 reference periods of fast and slow solar wind. The MCs with flare association tend to show lower autocorrelation coefficients than the ones without flare association for the case of the iron mean charge state. A Kolmogorov-Smirnov significance test (K-S test) gives a probability of 62 % that the measurements are drawn from the same distribution and, therefore, this difference is not significant. Looking at the iron mean charge state the MC autocorrelation coefficients are significantly lower than for the solar wind intervals (99.6 % significance level from K-S test). This suggests the presence of a high mean charge state in one half of the MC and of a low mean charge state in the other half for most of the MCs. For the oxygen mean charge state the same tendency is true but the significance level according to the K-S test is only 92.9 %.

We looked for general differences in the iron mean charge state between the first and second half of the MCs. For the MCs with flare association the iron mean charge state in the first half is 13.26 ± 0.27 and 13.68 ± 0.24 in the second half, which is in the overlap of the given errors. For the MCs without flare association this difference is even smaller.

5.4.4. Oxygen and Iron freezing-in temperatures

Freezing-in temperatures provide information about the electron temperatures at specific distances in the corona. *Arnaud and Rothenflug* [1985] calculated the expected charge-state composition for different temperatures in thermal equilibrium conditions (all particle species have the same temperature). We applied these tables to determine the freezing-in temperatures for the ion density ratio $X^{y+}/X^{(y+1)+}$, by looking for the temperature at which the observed ion density ratio is achieved. Within the resolution of the tabulated values we adapted linear interpolation to increase accuracy. Figure 5.15 shows the iron and oxygen freeze-in temperatures calculated from these tables. The considered MC (DoY 304.07-304.50, 2003) had the highest average iron mean charge state of the whole sample. The iron charge-state ratios for highly ionised iron indicate a freezing-in temperatures of ≈ 10 MK, which is much higher than the freezing-in temperature of the O^{6+}/O^{7+} ratio (≈ 3 MK). This indicates subsequent heating of the electrons after the plasma has passed the O^{6+}/O^{7+} ratio freezing-in radius. *Rakowski et al.* [2007] modelled the formation of charge-state distributions in ICMEs as a result of CME cavity and core (see section 1.5.2) plasma mixing. In this model the core plasma reaches the highest temperature at distances of 3-5 solar radii due to additional heating, which is in good agreement with the iron freeze-in distances. The successive mixing of the core and cavity plasma results in the formation of the frequently observed (see figure 5.11) low charge state (from the cavity) and high charge state (from the core) component.

5. Results

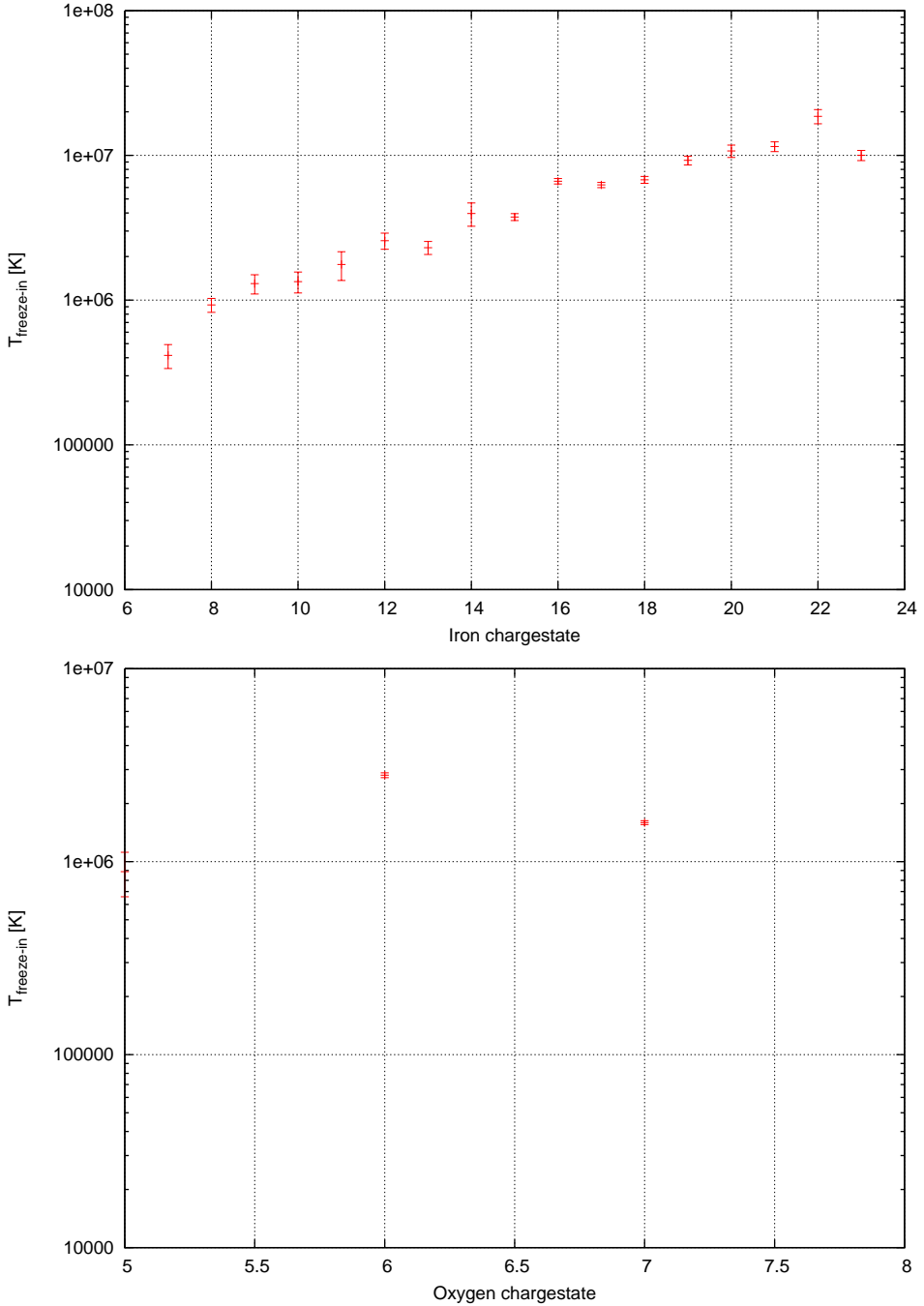


Figure 5.15.: Iron and Oxygen freeze-in temperatures for the MC from DoY 304.07-304.50, 2003 associated with a 11.0 X-class flare. The upper plot shows the iron freeze-in temperatures calculated from the ion density ratio $\text{Fe}^{x+}/\text{Fe}^{(x+1)+}$ utilising the tables from *Arnaud and Rothenflug* [1985]. E. g. at $x = 11$ the freeze-in temperature derived from the density ratio $\text{Fe}^{11+}/\text{Fe}^{12+}$ is plotted. Errors are computed from the density ratio $\text{Fe}^{x+}/\text{Fe}^{(x+1)+} + \Delta(\text{Fe}^{x+}/\text{Fe}^{(x+1)+})$. The lower figure shows the freezing-in temperatures obtained from the oxygen ion density ratios obtained by the same procedure.

5.4. Charge states

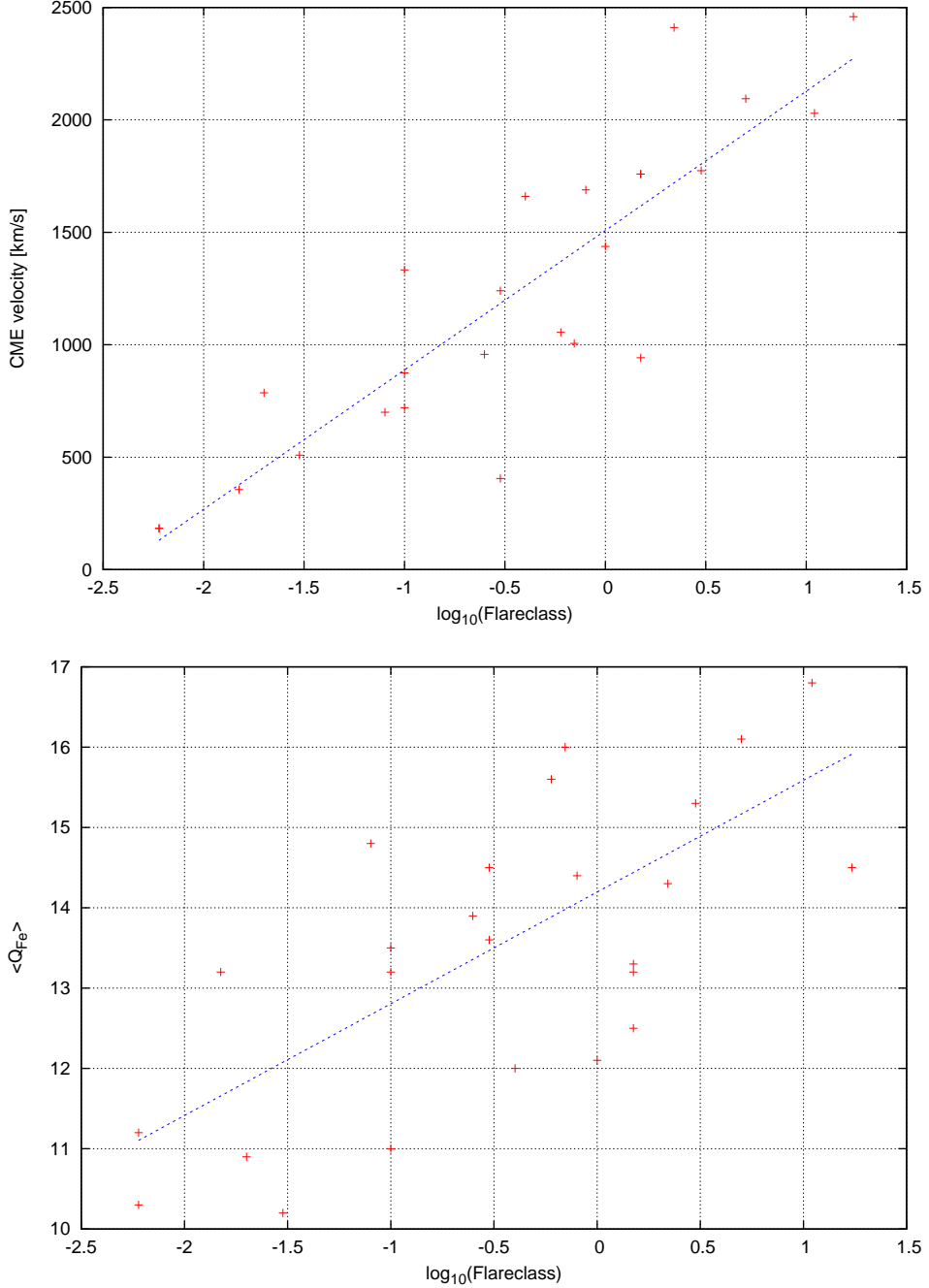


Figure 5.16.: The upper figure shows the dependence between the logarithm of the GOES X-ray flare class (0 is 1.0 X-class, -1 is 1.0 M-class, and -2 is 1.0 C-class) and the speed of the associated CME determined from LASCO images. The lower figure displays the dependence between the logarithm of the GOES X-ray flare class and the iron mean charge state. The blue lines were obtained by a linear regression. Limb flares (angular distance to solar disk centre $> 40^\circ$) were excluded in these plots.

5. Results

5.4.5. Energetics of flare related MCs

In this section we look for correlations between CME properties and the strength of the associated flare. The strength of a flare is represented by the peak flux in the 1-8 Å X-ray wavelength (GOES X-ray class, see section 1.5.1). A positive correlation indicates influence of the driving mechanism (for example reconnection) on both phenomena, the CME and the flare. Figure 5.16 reveals the dependence of the flare strength, the associated CME velocity determined from coronagraph observations, and the in-situ measured mean iron charge state. *Reinard* [2008] found that ICMEs associated with flares located far away from the centre of the solar disk (angular distance larger than 40°) show only weak charge-state enhancements independent of the flare strength. Therefore, four flare-associated MCs were excluded from this figure. The correlation coefficient for the flare strength and the CME velocity is 0.87 (significance level 98.5 %). From this we can deduce a correlation between the total CME energy and the associated flare strength. For CMEs with velocities larger than ≈ 600 km/s the total energy (sum of kinetic, magnetic, and potential energy) is dominated by the kinetic energy (see *Aschwanden* [2004]), and only four of the 23 shown CMEs have velocities lower than 600 km/s. The applied CME speeds are line of sight projected velocities. Nearly all of the CMEs are halo CMEs as they originate close to the centre of the solar disk. If all the CMEs would share the same true velocity, but would have a smaller cone angle when associated with a weak flare, we would also measure smaller projected velocities for the CMEs associated with weaker flares. Anyhow, the projected velocity is a lower limit of the actual velocity. The correlation coefficient for the flare strength and the mean iron charge state is 0.72 (significance level 96.2 %). Without exclusion of the limb events it would have been only 0.40. This correlation is higher as the one found by *Reinard* [2005]. The reason for this correlation could be primary accelerated electrons that partially heat the CME plasma and partially are included in the flare process, or evaporated chromospheric electrons that enter the CME plasma, or ionisation by the bremsstrahlung of the primary particles hitting the chromosphere.

5.5. Elemental Composition

The composition of the solar wind (determined in-situ) and of the photosphere (spectroscopic measurements) is different for many elements. E. g. Helium has an abundance of ≈ 9 % in the photosphere and an abundance of ≈ 3 % in the solar wind. As a rule elements with a low First Ionisation Potential (FIP) are enriched in the solar wind with respect to their photospheric abundances, while elements with high FIP are depleted. Low FIP elements are enriched by a factor of about 4-5 in the slow solar wind and by a factor of roughly 2 in the fast solar wind (see *Balogh et al.* [2001]). Deviations from normal solar wind conditions in the MC plasma would point to the presence of varied fractionation conditions. In the first part of this section we look for a dependence between elemental composition and coronal temperature conditions (quantified by the iron mean charge state) and in the second part we search for a solar cycle

5.5. Elemental Composition

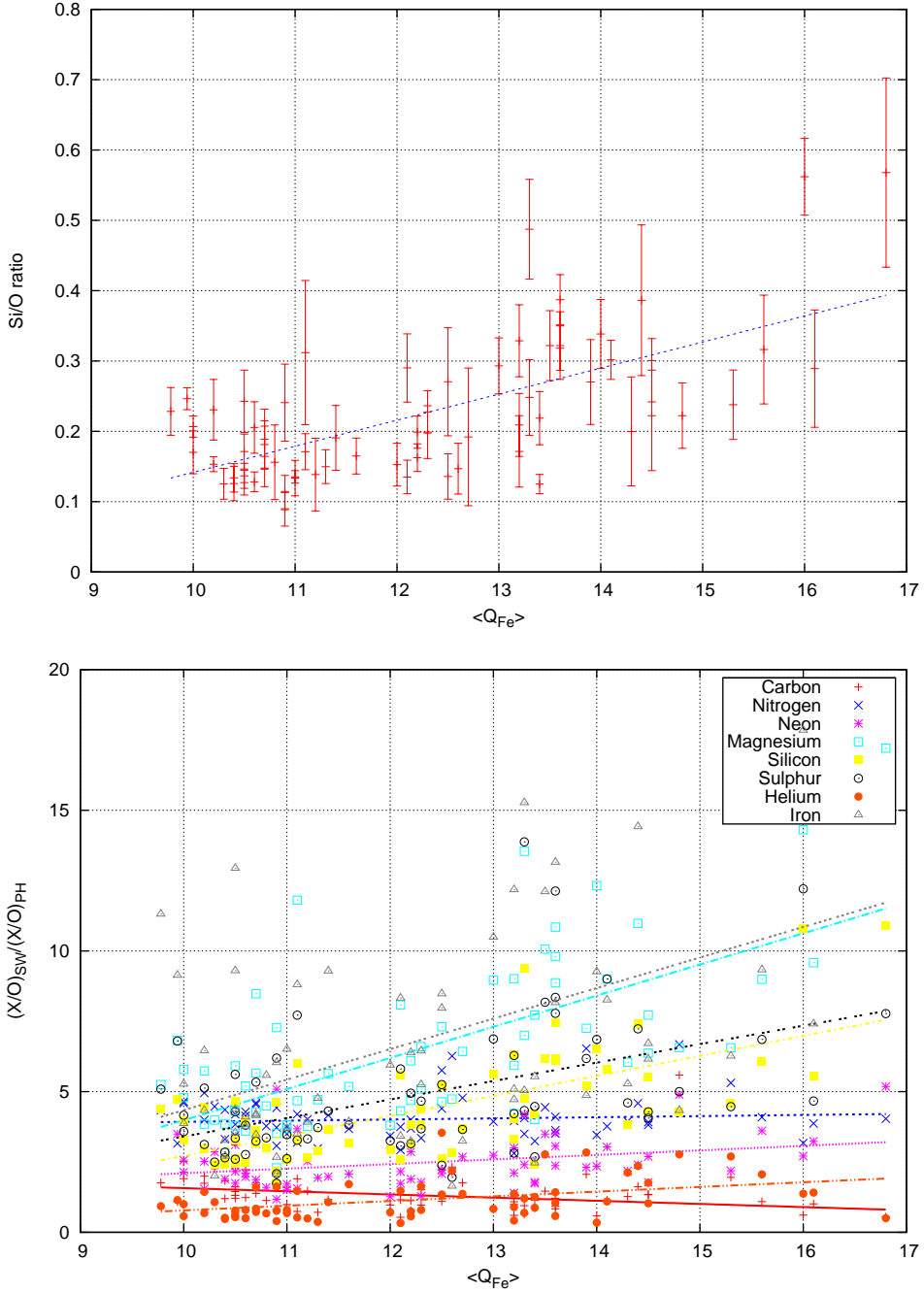


Figure 5.17.: The upper figures shows the dependence between the average Si/O ratio and the average iron mean charge state for all 66 MCs. Error-bars are calculated from the Si/O ratio variation in the 1-h data. The lower figure shows several elemental abundances in comparison to the oxygen abundance. The in-situ determined elemental ratios were divided by the photospheric elemental ratios taken from Aschwanden [2004]. For helium a theoretical stellar model abundance (also from Aschwanden [2004]) and for neon the abundance given by Widing [1997] have been employed. The straight lines show the linear regression for each elemental ratio.

5. Results

dependence in the MC elemental composition.

5.5.1. Connection between elemental abundances and iron mean charge state

Compositional anomalies of MCs with respect to normal solar wind have been known for years. *Richardson and Cane* [2004a] found an increasing enhancement in the Mg^{10+}/O and Ne^{8+}/O ratios in MCs with increasing solar wind speed with respect to normal solar wind. Ulysses measurements of fast and slow solar wind streams indicate a correlation between the freezing-in temperature of O^{7+}/O^{6+} and the Mg/O ratio. The larger the freezing-in temperature the larger the Mg/O ratio gets (see *Balogh et al.* [2001]). Now we look into the abundance of several elements with a different FIP and compare them to the oxygen abundance. We match these ratios with the iron mean charge state, which gives fundamental information about the coronal temperature (see section 5.4.4). In figure 5.17 these ratios are shown for the elements Fe, Mg, Si, S, C, N, Ne, and He. The in-situ measured ratio X/O was divided by the photospheric ratio $(X/O)_{ph}$. This arranges the low FIP elements above the high FIP elements. A linear regression was carried out for all element ratios. The results are shown as straight line in the figure. Interestingly elements with the lowest FIP and highest FIP show the largest dependence on the mean iron charge state. The higher or lower the FIP the larger is the slope of the straight line (see table 5.1). To make the slopes comparable we divide them by the average element ratio from all events. All elements show a positive slope except carbon. The probability that this slope results from a random distribution is 7.3 %. Comparing the enhancements at high charge states with the fractionation in the slow solar wind, the fractionation is up to a factor of 3 stronger, while it is comparable with normal solar wind at low charge states (see table 5.1).

To validate these results we examined the SWEPAM α /proton-ratio (hydrogen has the same FIP as oxygen) in dependence of the iron mean charge state and find the same tendency as for the He/O ratio. With this observation we can explain the results of *Richardson and Cane* [2004a] mentioned above. MCs with high iron mean charge state are flare-associated. The higher the charge state, the higher is the velocity (see figure 5.16). While normal solar wind shows decreasing fractionation with larger solar wind speeds, MCs show the different behaviour. Therefore, the difference in elemental composition increases with speed.

The obtained results are in agreement with the results of *Reinard* [2008]. They also found a strong enhancements in the Mg/O , Ne/O , and α /proton-ratios for ICMEs associated with flares appearing near the centre of the solar disk.

5.5.2. Solar cycle dependence of elemental composition

In this section we will look at the temporal behaviour of different elemental ratios. We compare the behaviour of 38 flare associated MCs, 28 MCs without flare association (see section 5.4.2), 21 slow solar wind periods, and 21 fast solar wind periods. The sun was near its activity maximum in 2001 and in its

Elem.	FIP	Av. X/O	Slope	Slope Av.X/O	Corr. Coeff.	X/O Photosph.	FIP enhancement
Fe	7.5	0.333	0.051	0.153	0.48	0.047	5.3
Mg	7.6	0.368	0.062	0.169	0.66	0.056	3.7
Si	8.1	0.226	0.037	0.164	0.66	0.052	4.3
S	10.3	0.177	0.021	0.119	0.47	0.032	2.5
C	11.3	0.682	-0.055	-0.081	-0.40	0.490	1.3
N	14.5	0.500	0.005	0.010	0.10	0.123	1.1
Ne	21.6	0.609	0.031	0.051	0.32	0.178	1.2
He	24.6	155	22.5	0.145	0.42	145	0.65

Table 5.1.: Dependence of several elemental abundances compared to O on the iron mean charge state. The FIP is given in eV, the slope was determined from the curve of linear regression, photospheric abundances are taken from *Aschwanden* [2004], except the Ne abundance, which is taken from *Widing* [1997]. The FIP enhancement factors are determined from in-situ measurements during periods of slow solar wind (taken from *Balogh et al.* [2001]).

activity minimum in 2007. Thus, the data covers roughly half of a solar cycle. Our principal interest is on the Mg/Ne ratio, because *Widing and Feldman* [2001] found a correlation between the age of magnetic field loops in AR and the Mg/Ne ratio. We will get back to this point in section 6.1. The Si/CNO (CNO is the combined carbon, nitrogen, and oxygen abundance) was chosen because Si has nearly the same FIP as Mg and C, N, and O are all highly abundant elements with a moderate FIP. The last ratio we look at is Mg/He, because He has a FIP similar to Ne.

Mg/Ne ratio

In figure 5.18 the average Mg/Ne ratio in each MC or solar wind period is shown together with yearly averages. The Mg/Ne ratio for the flare-associated MCs is always higher than the ratio for the MCs without flare association. The total average is 0.95 ± 0.03 for the flare-associated MCs and 0.66 ± 0.04 for the remaining MCs. The flare-associated MCs show no temporal variation of the Mg/Ne ratio while the Mg/Ne decreases with decreasing activity for the other MCs. Our Mg/Ne ratio for the flare-associated MCs is in good agreement with the results of *Reinard* [2008]. They plotted the Mg/O versus the Ne/O ratio and the data points are distributed around a straight line with slope 1. Fast and slow wind Mg/Ne ratios show no difference in their average and temporal trend. A small decrease from solar maximum to solar minimum is apparent.

5. Results

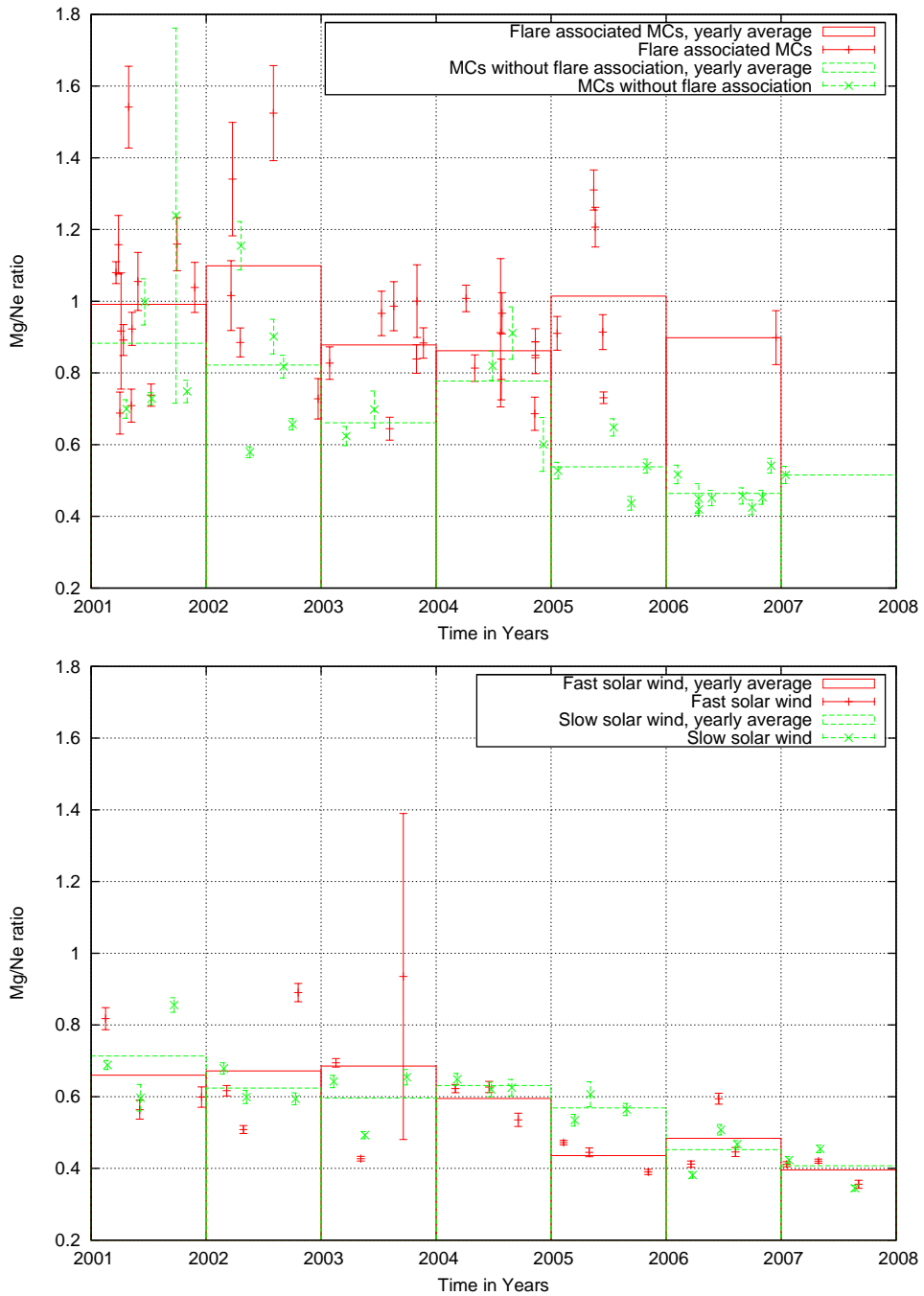


Figure 5.18.: The upper plot depicts the temporal development of the Mg/Ne ratio with the solar cycle for MCs with flare association and for MCs without flare association. Error-bars are calculated from the temporal variation of the 1h data. The yearly averages are drawn in the same colour. The lower figure depicts the development of the Mg/Ne ratio for three slow and fast solar wind periods in each year.

5.5. Elemental Composition

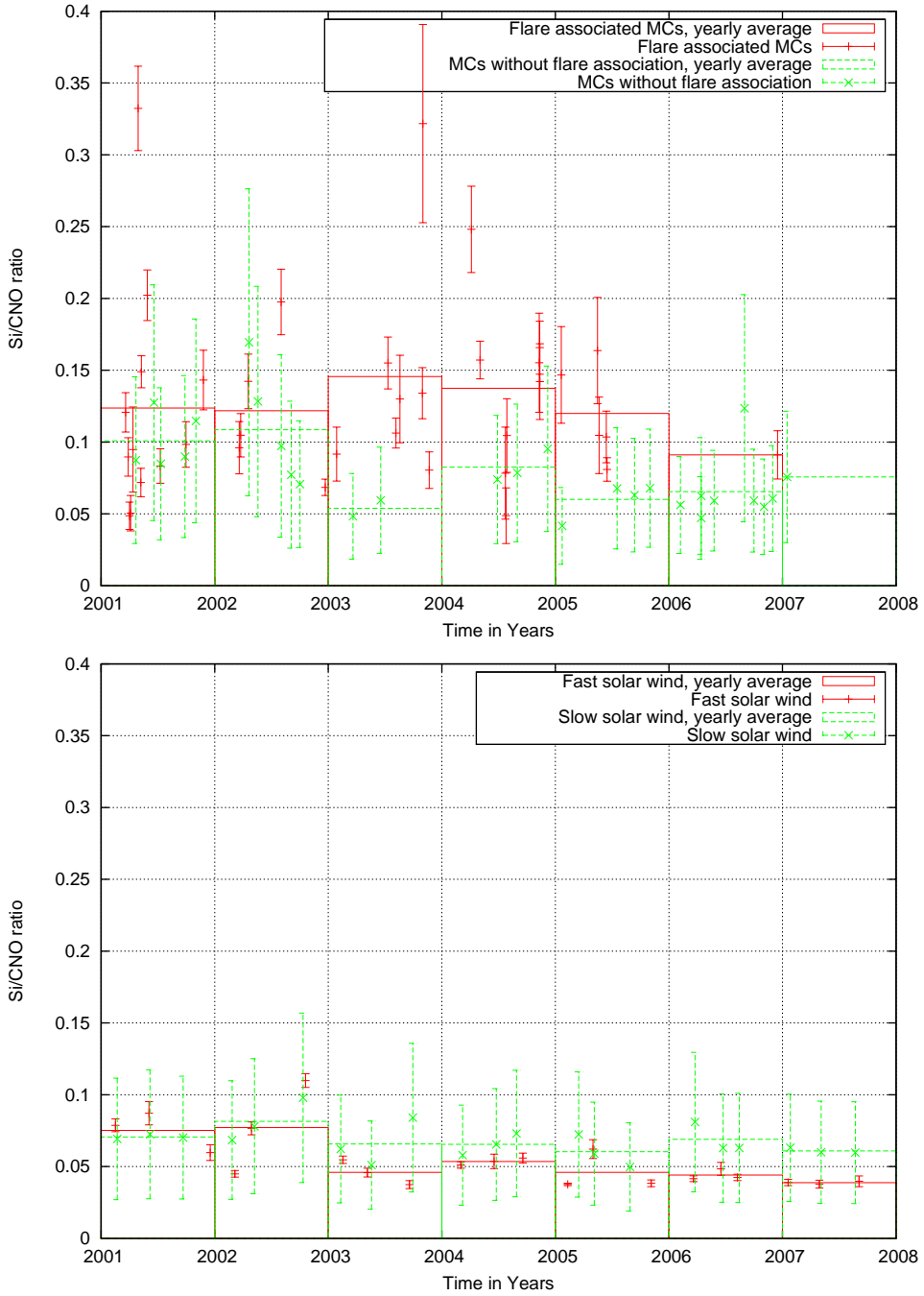


Figure 5.19.: The upper plot depicts the temporal development of the Si/CNO ratio with the solar cycle for MCs with flare association and for MCs without flare association. Error-bars are calculated from the temporal variation of the 1h data of each element by error propagation. The yearly averages are drawn in the same colour. The lower figure depicts the development of the Si/CNO ratio for three slow and fast solar wind periods in each year.

5. Results

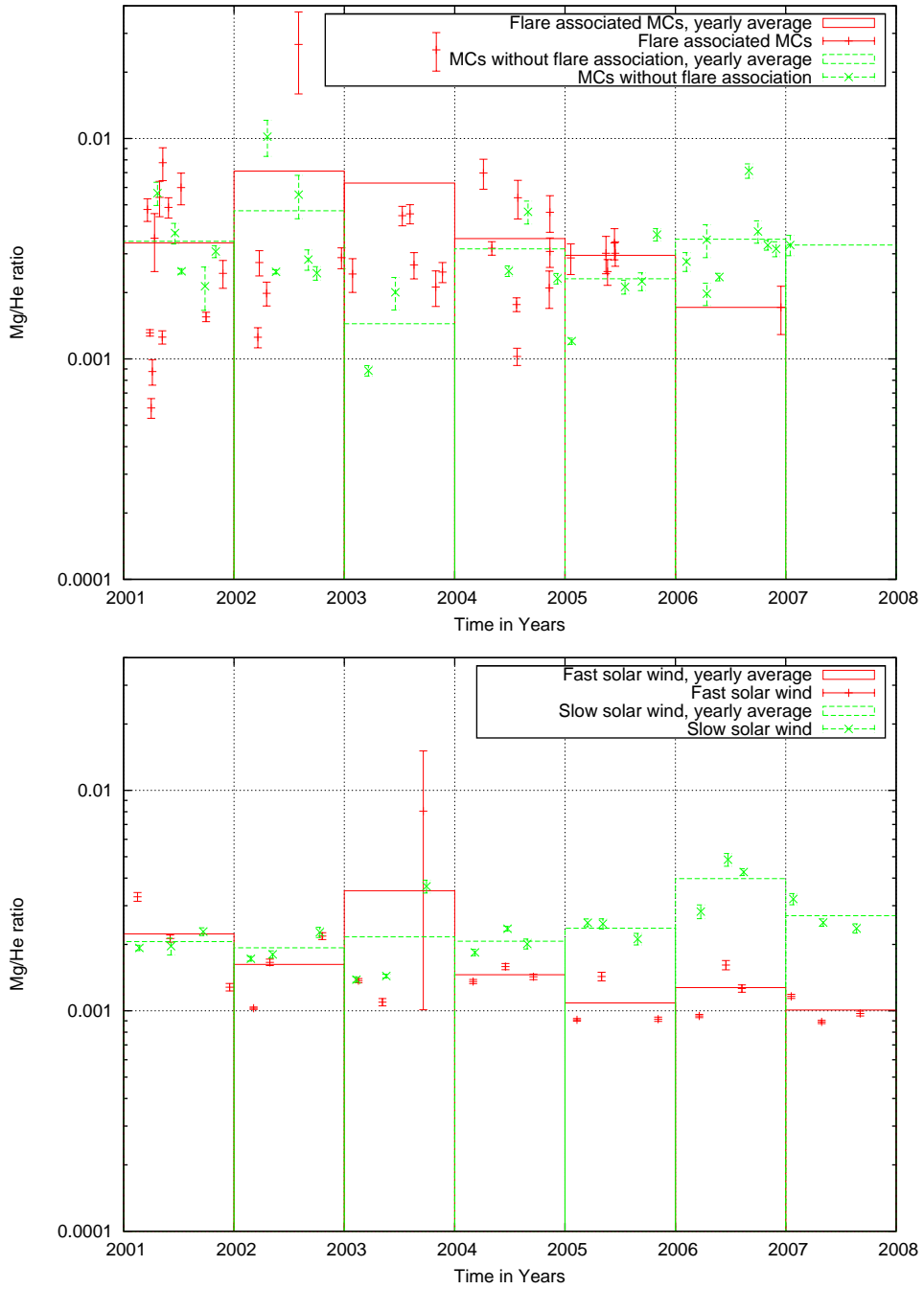


Figure 5.20.: The upper plot depicts the temporal development of the Mg/He ratio with the solar cycle for MCs with flare association and for MCs without flare association. Error bars are calculated from the temporal variation of the 1h data. The yearly averages are drawn in the same colour. The lower figure depicts the development of the Mg/He ratio for three slow and fast solar wind periods in each year.

Si/CNO ratio

In figure 5.19 the average Si/CNO ratio in each MC or solar wind period is shown together with yearly averages. As for the Mg/Ne ratio the Si/CNO ratio for the flare-associated MCs is higher than for the MCs without flare association. The same temporal trends are visible. The average Si/CNO ratio in the slow solar wind intervals is higher (0.068 ± 0.0024) than for the fast wind intervals (0.054 ± 0.004) and does not show a clear temporal trend. For the fast wind intervals a decrease from maximum to minimum solar activity is present.

Mg/He ratio

In figure 5.20 the average Mg/He ratio in each MC or solar wind period is shown together with yearly averages. If we exclude the two MCs with very large error-bars and a Mg/He ratio of ≈ 0.025 , no difference in the Mg/He ratio is visible between the flare-associated MCs and the MCs without flare association. We can understand this difference to the Mg/Ne ratio if we look into table 5.1. The Mg/O and He/O ratios show a similar dependence on the iron mean charge state while the Ne/O ratio has a much weaker dependence. Therefore, the Mg/He ratio is nearly independent of the iron mean charge state which is not the case for the Mg/Ne ratio. No variation of the Mg/Ne ratio with alternating solar activity is present in the data. The Mg/Ne ratio is larger for periods of slow solar wind, because the fractionation of Mg is about two times stronger for slow solar wind and the α/proton -ratio is only decreased by a factor of 1.25 (see *Balogh et al. [2001]*). A general trend of the Mg/Ne ratio with solar activity is not observed for the solar wind intervals.

5.6. Differential Streaming in MCs

Different ion species do not necessarily show the same bulk velocity. The disparity in the velocities is denoted as differential streaming. It can be explained by the formation of a core and beam component in the 3-d velocity distribution function. A possible reason for the beam formation is cyclotron resonant absorption of Alfvén waves. The beam is shifted with respect to the core along the magnetic field direction by about the Alfvén velocity v_A . The intensity of the beam/core-ratio depends on the considered ion and, therefore, different bulk velocities are observed. For details see *Berger [2008]*.

We concentrate on the differential streaming of He^{2+} in relation to protons. Proton bulk velocities are taken from SWEPAM data. We calculate the ratio $\frac{v_{\text{He}^{2+}} - v_p}{v_A}$ applying data with a time resolution of 1 h. The Alfvén velocity is determined from the mass density ρ and magnetic field strength B by $v_A = \frac{B}{(\mu_0 \rho)^{0.5}}$. As the beam components are shifted along the direction of the magnetic field we expect the strongest differential streaming to be present in the case of the magnetic field direction being parallel to the GSE x-axis. For an angle of $\pi/2$ between the magnetic field direction and the GSE x-axis the differential streaming cannot be resolved. The relation between the angle and the observed differential

5. Results

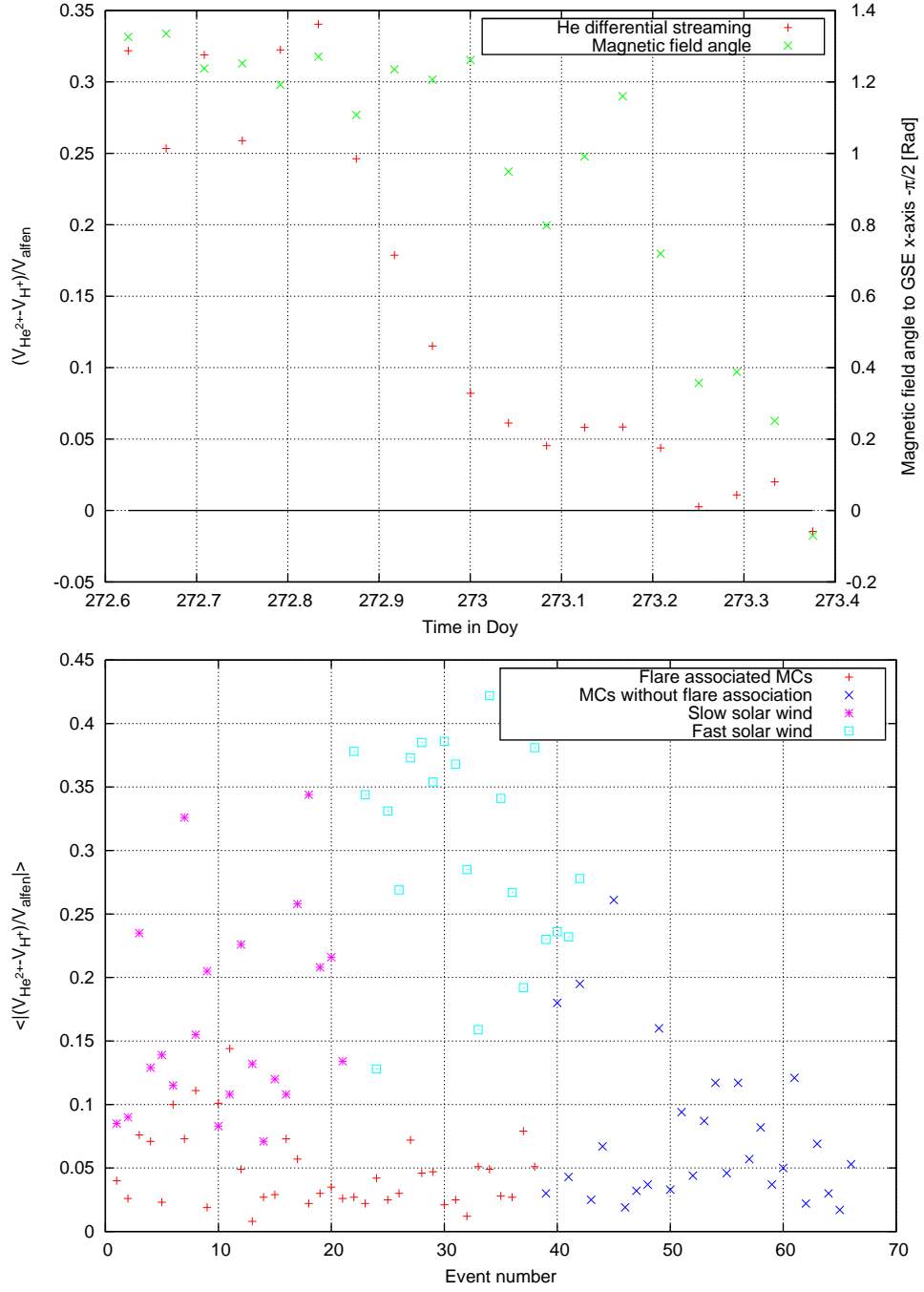


Figure 5.21.: The upper figure shows an example of He^{2+} differential streaming for the MC from DoY 272.62-273.43, 2001 in 1-h time resolution. This is one of the rare events were the differential streaming is strong and the correlation between the magnetic field angle and the intensity of the differential streaming is obvious. The lower figure depicts the absolute value of the differential streaming for each of the 66 MCs (divided in MCs with and without flare association) and the slow and fast solar wind reference intervals averaged from 1-h data.

5.6. Differential Streaming in MCs

streaming becomes blurred when using 1h data due to the magnetic field direction variations during this time. In MCs the variation of the magnetic field direction occurs slowly and 1 h data should be sufficient. In figure 5.21 an example of differential streaming during a MC passage is shown. The magnetic field direction and the strength of the differential streaming share the same trend. For many other MCs this is not the case.

We now calculate averages of the differential streaming for each MC and the solar wind intervals from the absolute values of the 1 h data. We use absolute values because otherwise negative and positive differential streaming could cancel out (negative differential streaming was observed frequently in the MCs). In figure 5.21 the results are shown separately for flare-associated MCs, MCs without flare association, slow solar wind periods, and fast solar wind periods. For the fast wind periods we get a total average of 0.302 ± 0.018 , 0.166 ± 0.0168 for the slow wind intervals, 0.047 ± 0.005 for the flare-associated MCs, and 0.076 ± 0.011 for the MCs without flare association. A stronger wave-particle interaction in fast solar wind streams can explain the higher in-situ temperatures compared to slow solar wind, although the fast wind emanates from cooler coronal regions (see *Schwenn and Marsch [1991]*). To rule out the possibility that the difference between the MC and solar wind differential streaming results from a different magnetic field direction distribution, we calculated the average from the absolute value of the 1h magnetic field angle. For the solar wind periods the average angle is 0.695 rad and 0.532 rad for the MC periods. The strength of the observed differential streaming has a nearly linear dependence on the magnetic field angle (see *Berger [2008]*). Thus, the observed MC differential streaming has to be multiplied by a factor of $\frac{0.695}{0.532} = 1.31$ to make it comparable to the solar wind differential streaming. We conclude that, wave-particle interactions play an even lesser role in MCs than in normal slow solar wind, as is to be expected.

6. Discussion

In this chapter we discuss some of the results from the last chapter. We compare the in-situ Mg/Ne ratio in MCs with spectroscopic investigations in emerging AR (section 6.1). The variation in elemental abundances with solar cycle is addressed in section 6.2. In section 6.3 we develop a simple analytical model describing the mixing of plasma inside MCs while they are travelling from the corona to Earth.

6.1. Formation of MCs

The AR associated with a MC is determined as described in section 5.4.2. With the help of SOHO MDI magnetograms the age of the AR at the time of CME release can be assigned¹. The magnetic field at the far side of the sun is calculated from MDI sound travel time analysis in these maps. The results of this analysis are very inaccurate when looking for AR emergence. Therefore, the ages of AR emerging at the far side of the sun have an uncertainty of several days. In figure 6.1 we examine the influence of AR age on the Mg/Ne ratio. The significance level for a correlation is 89 % (correlation coefficient 0.49, 25 data points).

We compare this result with spectroscopic Mg/Ne measurements in magnetic loops of young, emerging ARs performed by *Widing and Feldman* [2001]. They determined the Mg/Ne ratio by comparing the intensities of different Mg and Ne spectral lines in four ARs over 3-6 days. We will briefly summarise their key results. The Mg/Ne ratio in a newborn AR has photospheric composition ($Mg/Ne=0.296$). The ratio rises to 2 after ≈ 3 days and to 2.5 after ≈ 5 days. The increase with time is similar for the four ARs. The slowest increase in the Mg/Ne ratio (found in McMath Region 12684) is shown as the pink line in figure 6.1.

What are the reasons for this difference in temporal evolution? First, this could be an averaging effect by merging ambient coronal plasma and plasma from young and old loop systems as a consequence of CME initiation. CMEs have masses up to $\approx 10^{16}$ g (this are a few percent of the total coronal mass (see *Aschwanden* [2004])), while the mass in a single loop is much lower. Second, filaments could play a role (See section 1.5.2). Approximately 55 % of all CMEs are associated with erupting filaments and 94 % of all erupting filaments have an associated CME (see *Alexander* [2006]). A schematic view of a possible filament configuration with the stabilising overlying magnetic field arcade is shown in the lower part of figure 6.1. A magnetic fluxrope supports large amounts of cold, dense plasma against gravity. Its

¹Magnetograms can be found at http://soi.stanford.edu/data/full_farside/

6.1. Formation of MCs

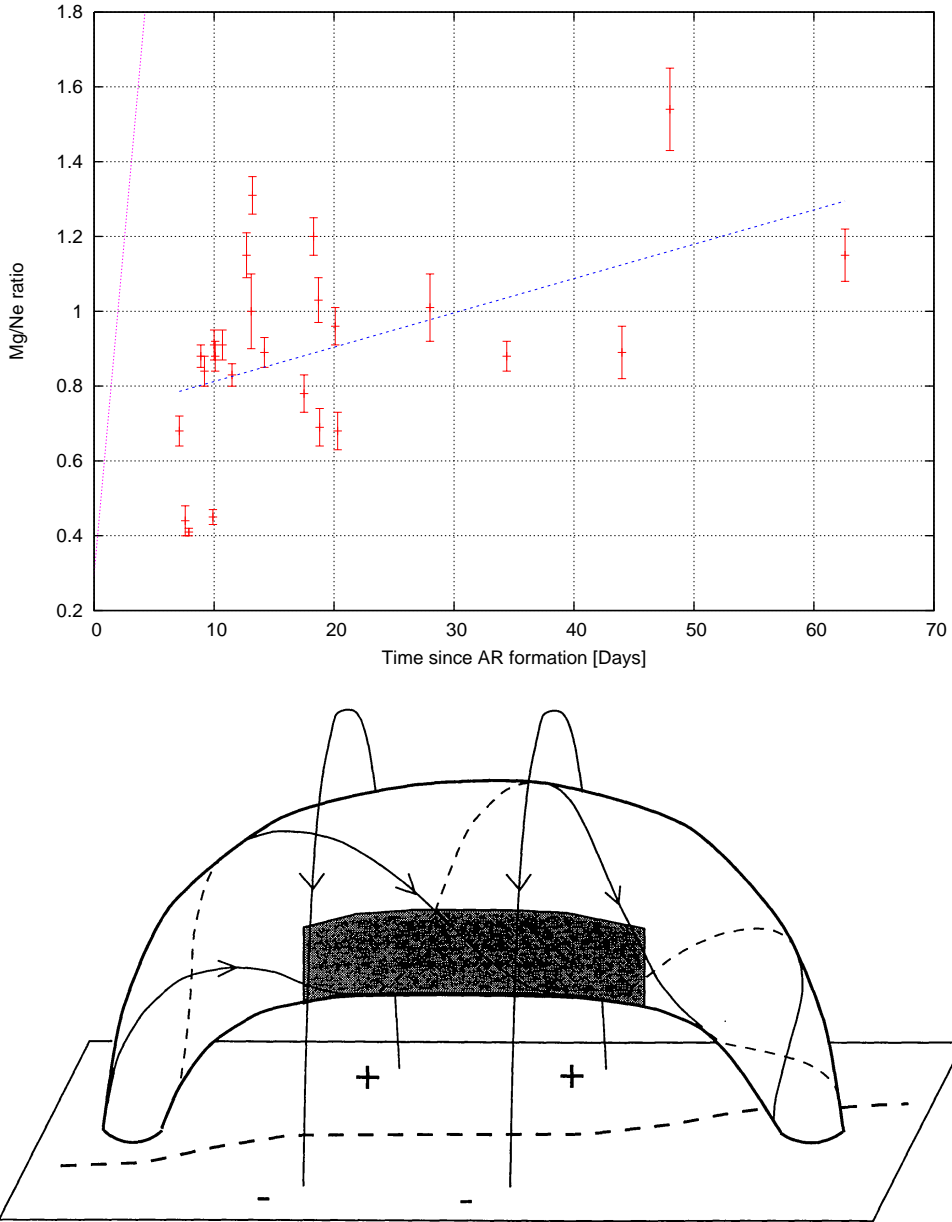


Figure 6.1.: The upper figure shows the average MC Mg/Ne ratio and the dependence on AR age. MCs having an association with a limb flare (angular distance to solar disk centre $>40^\circ$) are not taken into account. The error bars are calculated from the temporal variation over the MC duration. The blue line is obtained from linear regression. The pink line is the expected Mg/Ne ratio according to *Widing and Feldman [2001]*. The lower figure is a sketch of a magnetic fluxrope supporting a filament. Cold and dense filament plasma is shaded in black (figure taken from *van Ballegooijen [2001]*).

6. Discussion

magnetic field resembles the field observed in MCs at 1 AU. If this fluxrope emerges intact from below the chromosphere loaded with plasma of photospheric composition the flows from the footpoints of the magnetic field lines into the fluxrope might be too small to change the elemental composition during the short timescales observed in the simple magnetic field loops.

6.2. Elemental variation with solar cycle

The Mg/Ne ratio determined for the solar wind intervals is well below the coronal abundance value of 1.43 given by *Widing and Feldman* [2001]. To check our Mg/Ne ratios for consistency we calculated yearly averages for the Mg/O and Ne/O ratios from the data provided by the ACE science center². We divide these averages to obtain the yearly Mg/Ne ratio. The ratios from 2001 to 2007 are: 0.72, 0.71, 0.71, 0.57, 0.54, 0.37, 0.30. This is consistent with the solar wind ratios shown in figure 5.18. There is no difference in fractionation between slow and fast solar wind intervals. This is also true for the Si/CNO ratio and the Mg/He ratio at solar maximum (see figures 5.19 and 5.20). The large variation of the Mg/Ne ratio with solar cycle for the solar wind intervals indicates a connection to activity level. The amount of magnetic flux in closed fields is larger at solar maximum than at solar minimum. As we have seen in the last section fractionation is acting in magnetic field loops enhancing the Mg/Ne ratio with time. When the coronal fluxtubes dissipate they release the plasma to the corona and the solar wind. We do not know why this behaviour is not visible in the Si/CNO ratio and the Mg/He ratio. The FIP cannot be the reason, because it should affect these ratios in the same way. The flare-associated MCs are released from ARs, where the amount of magnetic flux in closed fields is particularly high. Therefore, they show the highest Mg/Ne ratio. The constant level of the ratio indicates that these MCs develop under similar conditions throughout the solar cycle. Only their number of occurrence depends on solar activity level. The Mg/Ne ratio for MCs without flare association follows the trend of the solar wind interval ratio. They show only a small enhancement in the Mg/Ne ratio. This indicates that most of the plasma they pick up has its origin in the corona.

6.3. Mixing of plasma inside MCs

A plasma parcel moving with the solar wind speed will slowly dissolve by the influence of the plasma temperature. Some particles are slower than the bulk velocity while others are faster. This leads to mixing with the adjacent plasma parcels, blurring differences between them. In this section we estimate on which spatial scales this effect is important. Additional mixing effects such as differential streaming (differential streaming plays a minor role in MCs, see section 5.6) between different ion species are not taken into account in this model. We will concentrate on protons because they are the lightest ions in

²<http://www.srl.caltech.edu/ACE/ASC/index.html>

6.3. Mixing of plasma inside MCs

the MC plasma resulting in the highest speeds at a given temperature. Observations in solar wind have shown that the in-situ temperatures of different ions i, j behave more like $T_i/T_j \approx m_i/m_j$ (see *Balogh et al.* [2001]). In this case all ions have the same thermal velocity.

First we assume a three-dimensional Maxwell-Boltzmann velocity distribution around the bulk speed,

$$F(v) = \sqrt{\frac{2}{\pi}} \left(\frac{m_M}{k_B T} \right)^{\frac{3}{2}} v^2 \exp \left(-\frac{m_M v^2}{2 k_B T} \right). \quad (6.1)$$

m_M is the proton mass, T the temperature, and v the absolute value of the velocity vector in this context. This distribution is only appropriate while plasma densities are high enough for thermalisation by Coulomb interactions. The temperature anisotropies frequently observed in normal solar wind (see *Schwenn and Marsch* [1991]) are not included in the model. But as we will see later in this section most of the mixing occurs near the sun. We can calculate the mean velocity v_m from the first moment of equation 6.1,

$$v_m = \int_0^\infty F(v) v \, dv = \sqrt{\frac{8 k_B T}{\pi m_M}}. \quad (6.2)$$

We assume that the mean velocity vectors are isotropically distributed in velocity phase space. Therefore, they form a spherical surface. Now we want to know the mean velocity along a certain direction (e. g. direction of magnetic field or the direction of MC movement). We are only interested in the particles that have a positive velocity along this direction (giving us a hemi-spherical surface in velocity phase space). If we know the average angle α of the velocity vector with respect to the considered direction, we can calculate the projected mean velocity v_d from $\cos \alpha = v_d/v_m$. α is calculated from surface integrals in spherical coordinates,

$$\int_0^{2\pi} \int_0^\alpha \sin(\vartheta) \, d\vartheta \, d\varphi = \int_0^{2\pi} \int_0^{\frac{\pi}{2}} \sin(\vartheta) \, d\vartheta \, d\varphi. \quad (6.3)$$

When this condition is fulfilled an equal amount of velocity vectors has a larger and lower angle with the considered direction. Solving equation 6.3 for α we obtain $\cos \alpha = 0.5$ leading to

$$v_d = 0.5 v_m. \quad (6.4)$$

If we assume that solar wind expansion is a polytropic process ($pV^\gamma = \text{const.}$, p is the pressure and V the volume) and make use of the ideal gas law ($pV = nk_B T$, n is the number of particles) we obtain,

$$\frac{T_1}{T_2} = \left(\frac{V_2}{V_1} \right)^{\gamma-1}. \quad (6.5)$$

If we know the expansional behaviour of MCs and the polytropic index γ we can calculate the proton temperatures (and projected velocities v_d) at different distances from the sun. For the adiabatic expansion

6. Discussion

of a monoatomic gas γ would be $\frac{5}{3}$. Observations of proton temperature and density in ICMEs at different distances from the sun indicate a non-adiabatic process. *Liu et al.* [2005] found a proton polytrope index of 1.15 from multi-spacecraft (Helios, WIND, ACE, and Ulysses) observations. They found no dependence of the polytropic index on distance and solar cycle, and additionally the inclusion of electron and magnetic pressure did not change it. *Forsyth et al.* [2006] list a value of 1.38 determined from Helios observations.

The dependence of the MC's radial size S from solar distance r was investigated by *Bothmer and Schwenn* [1998] with the help of Helios measurements. They found

$$S(r) = 0.24 \text{AU} \left(\frac{r}{\text{AU}} \right)^{0.78}. \quad (6.6)$$

Forsyth et al. [2006] give the radial dependencies for S found in other studies. The size at 1 AU varies from 0.19 AU to 0.31 AU while the exponent describing the radial dependence varies from 0.53 to 0.92. For the increase in the MC volume we assume a fluxrope structure (see sketch 5.8) with two-dimensional expansion according to equation 6.6 (cross section of the fluxrope) and a linear dependence on r in the third dimension (length of the fluxrope). SMEI observations (see *Webb et al.* [2006]; *Howard et al.* [2007]) have shown that the angular extent of ICMEs does not vary with increasing distance from the sun. This result is consistent with a linear size dependence. We derive

$$V(r) = crS(r)^2 = c0.24^2 \text{AU}^3 \left(\frac{r}{\text{AU}} \right)^{2.56}. \quad (6.7)$$

The proton density of course should roughly show an inverse behaviour. The exponents for the density given in *Forsyth et al.* [2006] range from -2.18 to -2.4 and are compatible with the applied value. Insertion of equation 6.7 into equation 6.5 gives us the proton temperature in dependence of the distance r

$$T(r) = T_0 \left(\frac{\text{AU}}{r} \right)^{2.56(\gamma-1)}. \quad (6.8)$$

T_0 is the proton temperature at the ACE spacecraft (1 AU). Almost all of the observed MCs have average proton temperatures of $10^4 - 10^5$ K at this distance (see appendix D). Now we calculate the average thermal speed along a specific direction (equation 6.4)

$$v_d(r) = \sqrt{\frac{2k_B}{\pi m_M}} \sqrt{T_0} \left(\frac{\text{AU}}{r} \right)^{1.28(\gamma-1)} \quad (6.9)$$

In figure 6.2 the proton temperatures and thermal velocities are shown for two different values of γ and T_0 . The coronal temperatures derived from iron freezing-in temperatures (up to 10 MK at 2-3 solar radii for flare associated MCs, 2-3 MK for MCs without flare association) (see section 5.4.4) are significantly larger than the temperatures calculated with a polytropic index of 1.2, indicating a larger value for the polytropic index. MCs with and without flare association show no difference in their proton temperatures (median 37000 K) at 1 AU. Possible explanations are the different expansion speeds (84 ± 17 km/s in

6.3. Mixing of plasma inside MCs

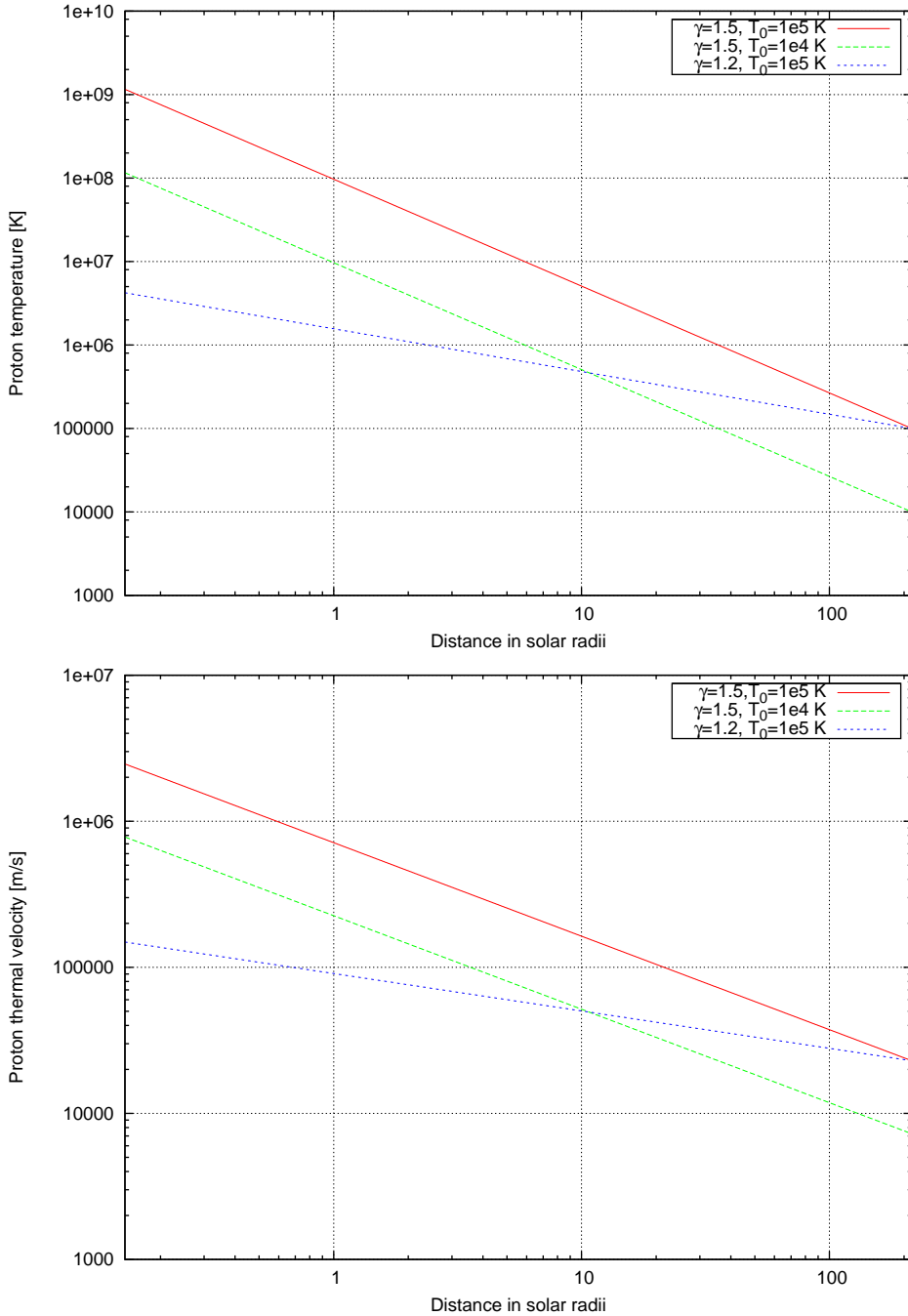


Figure 6.2.: The upper figure shows the proton temperature in dependence of distance to solar surface for three combinations of parameters. The lower plot shows the average thermal proton velocities calculated with the same sets of parameters.

6. Discussion

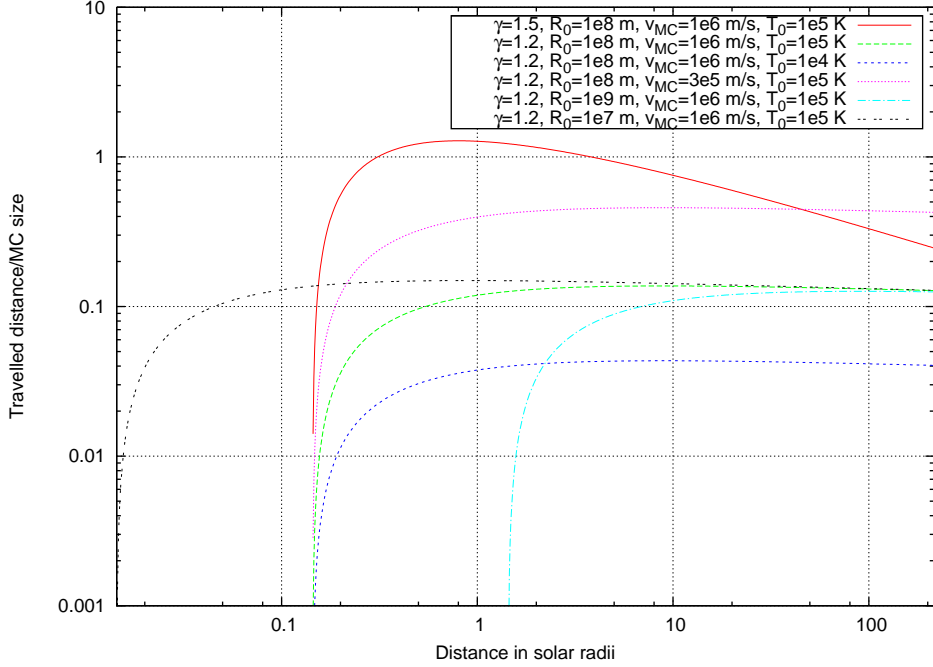


Figure 6.3.: Mixing of plasma inside a MC according to the model for different sets of parameters.

flare-associated MCs and 45 ± 14 km/s in MCs without flare association) or a difference in the polytropic index γ .

If we assume a constant speed v_{MC} of the MCs from initiation to 1 AU we can calculate the mixing at a distance r by dividing the integrated thermal velocity through the radial extent. Impulsive CMEs are accelerated to their final velocity in ≈ 20 - 30 minutes deep inside the corona (within 1 solar radii). Thus, the assumption of constant speed introduces only a small error for these CMEs. We obtain

$$\frac{\int_{R_0}^r v_d(r') dr'}{S(r)} = \frac{1}{v_{\text{MC}} (0.55 - 0.31\gamma)} \sqrt{\frac{2k_B}{\pi m_M}} \sqrt{T_0} \text{AU}^{1.28\gamma-1.5} \left(r^{1.5-1.28\gamma} - \frac{R_0^{2.28-1.28\gamma}}{r^{0.78}} \right) \quad (6.10)$$

The maximum of this curve provides the mixing. In figure 6.3 the expected mixing is shown for different sets of parameters. The final mixing depends on MC velocity, polytropic index, and proton temperature. For $\gamma = 1.2$, $T_0 = 4 \cdot 10^4$ K, and $v_{\text{MC}} = 1000$ km/s the mixing is below 0.1 times the MC dimension. Therefore, inhomogeneities formed in the corona before or during CME release will survive to 1 AU. The dependence of the iron mean charge state variability on velocity shown in figure 5.12 and the general asymmetries seen in the iron and oxygen mean charge state time series (see figure 5.14) qualitatively support the results from our model.

7. Summary and Conclusions

This thesis deals with the charge-state and elemental composition in MCs. First, we identified 67 MC intervals from 2001 to 2007. We applied data from the instruments MAG, SWEPAM, and EPAM on board ACE for this identification. The most important MC signatures were smooth rotation of the magnetic field vector, magnetic field strength enhancements, proton temperature decreases, and proton velocities. The MC boundaries indicated by these signatures are often contradictory. Therefore, the accuracy of the boundary times is ≈ 0.1 days for most of the MCs.

The spacecraft trajectory inside a MC is a one dimensional intersection of a three dimensional structure. We reconstruct this structure by modelling the magnetic field inside the MCs. Three different magnetic field models were applied. The first model assumes a force-free magnetic field inside a cylindric geometry. The second model shares the geometry but the applied field is non force-free. The third model again assumes a force-free field configuration with the cross section of the cylinder being no longer circular but elliptical. In the first two models the geometry is static during spacecraft intersection, while a self-similar expansion is included in the third model. The adaption of the models to the magnetic field data was carried out with a modified Levenberg-Marquardt algorithm, fitting the three components of the field at the same time. The final set of parameters for each MC was determined from a series of 75 fits. Elemental and charge-state composition was computed from ACE/SWICS data using an improved analysis technique by *Berger* [2008] and an efficiency model by *Kötén* [2009].

We compare the fit results for the parameters included in all of the three magnetic field models. The deviations between the two circular cross section parameter are small compared to the deviations with the elliptic cross section model. This questions the modelling of MCs as local cylindrical structures with circular cross sections. We calculated the expected progression of the proton velocity from the fit results of the elliptic cross section model and match them with the observed proton velocity. For most of the MCs the average difference in these velocities is smaller than 30 km/s.

Now we address the question, if the observed differences in the charge-state and elemental composition results from the spacecraft intersection through different parts of the MCs or from different conditions affecting MC initiation and release at the sun. The global model of the MC is a fluxrope with the footpoints of the magnetic field anchored at the sun. We use the fitted in-ecliptic angle of the MC's axis orientation to determine if one of the MC legs or the central part had been intersected by the spacecraft. The iron mean charge state does not show a dependence on the spacecraft position inside the MC obtained by this procedure. We now put our focus on the varying coronal conditions under which the MCs develop.

7. Summary and Conclusions

When looking into the iron charge-state composition two different classes of MCs can be identified. Some show a significant fraction of iron with charge state 16+ or higher, while others do not. For 60 % of the MCs the associated CME could be identified in LASCO coronagraph images. From comparing the time of first appearance in the LASCO field of view and the GOES soft X-ray flux flare associations of the MCs are determined. We find a striking correlation between MC flare association and the presence of highly ionised iron and divide the MCs in a group with and without flare association applying the iron charge-state distribution.

For a better characterisation of the mean charge state time profiles we calculated the variability and symmetry with respect to the middle of the time series with the help of the autocorrelation function for the oxygen and iron mean charge state. The variability shows a positive correlation with the MC velocity and the mean charge state time series tend to be asymmetric.

From the charge-state distributions we can derive coronal temperatures because ionisation and recombination stop when the electron densities become too low (freezing-in temperatures). For the flare associated MCs the plasma reaches temperatures of up to 10 MK and 2-3 MK for the MCs without flare association at a distance of 2-3 solar radii from the solar surface.

While the charge-state composition is formed during CME initiation and movement through the corona elemental composition develops before release. Yet we find a correlation between the charge-state and elemental composition. We calculated the ratios of several elements to oxygen and compared them to the iron mean charge state. Low and high FIP elements show a positive correlation with the mean iron charge state. The higher or lower the FIP, the stronger is this dependence. The reason for this behaviour is not known. We also addressed the variation of elemental composition in MCs with solar cycle. A dependence of the Mg/Ne ratio is present for the MCs without flare association similar to normal solar wind, while there is no dependence for the flare associated MCs. Strangely, the Mg/He ratio shows no solar cycle dependence.

For the MCs with flare associations we know the AR releasing the MC. We determined the AR age from magnetograms and relate it to the Mg/Ne ratio. There is only a small, if any, increase with AR age. In contrast, *Widing and Feldman* [2001] found a fast increase with time in magnetic field loops of emerging ARs. A possible explanation is the intact emergence of coronal fluxropes from the photosphere, loaded with large amounts of photospheric or chromospheric plasma.

We examined the presence of differential streaming between helium ions and protons in MCs. A possible mechanism explaining differential streaming is cyclotron resonant absorption of Alfvén waves. We find that the differential streaming is much lower in MCs than in normal solar wind intervals. This indicates a minor importance of wave-particle interactions in MCs.

Finally, we address the question if mixing of the plasma inside MCs destroys spatial inhomogeneities that are present or form during release while the MC travels to 1 AU. We assume a Maxwell-Boltzmann velocity distribution for the protons added to the MC speed. From this distribution we can calculate the

average velocity with which a plasma parcel drifts apart at a specific temperature. Taking into account observations of proton density and temperature at different distances from the sun we computed the temperatures assuming a polytropic process. We compare the MC radial dimension to the integrated thermal velocity and derive a mixing length of ≈ 0.1 times the MC dimension for typical MC parameters.

Finally, we can ask the question, what could be done to improve our knowledge about MCs? For further investigations of spatial charge-state and elemental composition we have to know the real three dimensional MC structure in interplanetary medium. Since the launch of the STEREO spacecraft in the end of 2006 CMEs can be observed with the SECCHI coronagraphs from two positions at the same time up to a solar distance of 1 AU. This allows stereoscopic reconstruction of the geometric structure from the images. Unfortunately, the sun has been very inactive since the launch.

For direct comparison of compositional or magnetic field data a multi spacecraft mission would be recommendable. Up to now only few ICMEs have been observed by more than one spacecraft at different positions. The spacecraft should be spatially well separated but the distances must be small enough to ensure an intersection of the MC with all spacecraft. The NASA Sentinel mission described in section A would be a mission of this type.

A. ICME detections with Solar Orbiter and Sentinels

A.1. Introduction

The Inner Heliospheric Sentinel (IHS) mission will be part of the Living With a Star Program (LWS¹). Its goal is to determine how solar variability affects humans and technology. The primary scientific goal is to understand the connection between solar phenomena and geospace disturbances. The most disrupting effects result from solar-heliospheric transients of ICMEs or interplanetary shocks. The understanding of CME initiation, ICME propagation and ICME evolution in the inner heliosphere will allow enhanced capabilities for space weather predictions. Therefore, the IHS will perform multi-point in situ measurements of magnetic fields and plasma parameters of ICMEs. The ESA Solar Orbiter mission additionally will observe the sun's polar regions and the equator from high latitudes.

The Sentinel mission is foreseen to launch in Sep 2015 and will continue to Dec 2022, while Solar Orbiter may be launched in May 2015 and would operate to August 2024.

The Sentinel satellites will travel around the sun in the ecliptic plane while the Solar Orbiter will leave the ecliptic plane by more than 0.3 AU. All satellites will have a final orbit roughly between 0.2 AU and 0.8 AU distance to the sun (see figure A.1).

The open topics for this work are:

- What are the detection efficiencies of ICMEs for different combinations of spacecraft?
- How large is the ratio of detected ICMEs to emitted ICMEs?
- How does the detection rate evolve with time in dependence on the solar cycle?
- What is the distance at which most encounters of satellites and ICMEs will take place?
- What is the effect of different model parameters to the results?

By calculating the number of ICME detections we get a first hint if the scientific goals needing multiple ICME encounters can be achieved. Thus, results from this study serve as input for the IHS Science and Technology Definition Team (STDT) report (NASA/TM-2006-214137).

¹<http://lws.gsfc.nasa.gov/index.htm>

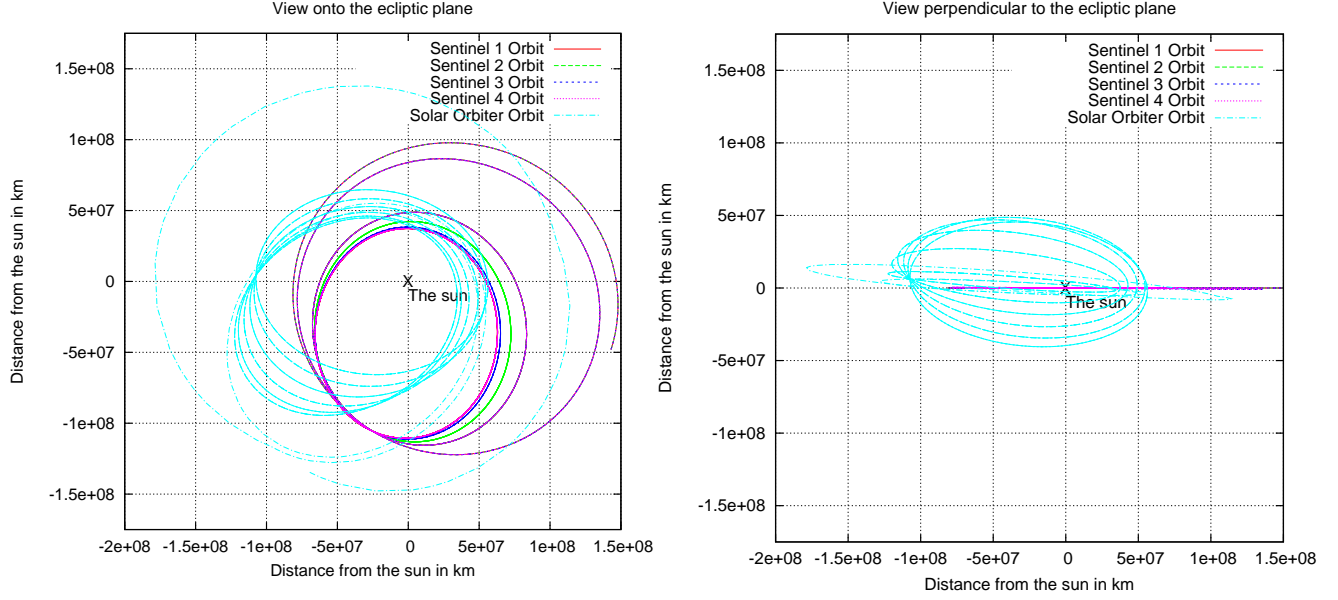


Figure A.1.: Solar Orbiter orbits for May 2015 to August 2024 and IHS orbits for Sep 2015 to Dec 2022.
Data source: Adam Szabo, NASA Goddard Space Flight Center and R. Marsden, ESTEC.

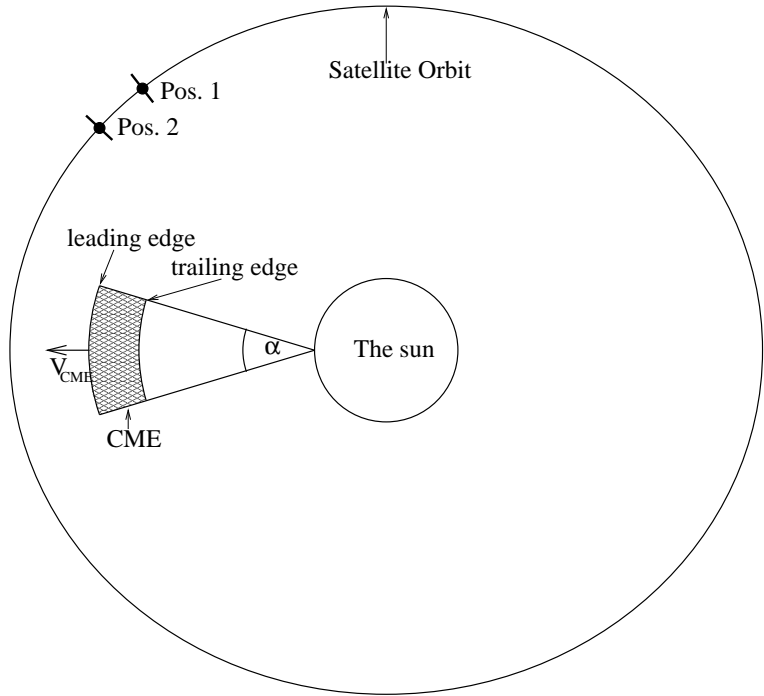


Figure A.2.: Schematic illustration of the applied model. See text for further information.

A. ICME detections with Solar Orbiter and Sentinels

A.2. The model

Satellite detection rates were determined by applying a simple model of ICME propagation in the inner heliosphere. CMEs were generated at the sun's surface with a cone-shaped geometry with a negligible spatial extent. The ICMEs move radially away from the sun with a constant speed. Different velocities for the leading edge and trailing edge result in expansion of the ICME. With the orbit data for the IHS and the Solar Orbiter the spacecraft are tracked and whenever one hits an ICME this ICME is treated as detected (see figure A.2 for a schematic illustration).

A.2.1. CME generation

The number of CME occurrences is strongly dependent on the solar cycle. It varies by a factor of 10 between about two per day at solar maximum and about one per week at solar minimum. So one can try to find a connection between CME occurrence and the smoothed monthly sunspot number (SSN). Using the SSN-curve from the Royal Observatory of Belgium² for the years 1749 to 2004 an averaged SSN cycle was constructed from 22 cycles (see figure A.3). The number of generated CMEs per day

was determined by the relation (see *Wimmer-Schweingruber [2002-04]*)

$$\text{CME/day} = 0.149 + 0.0146 * \text{SSN}. \quad (\text{A.1})$$

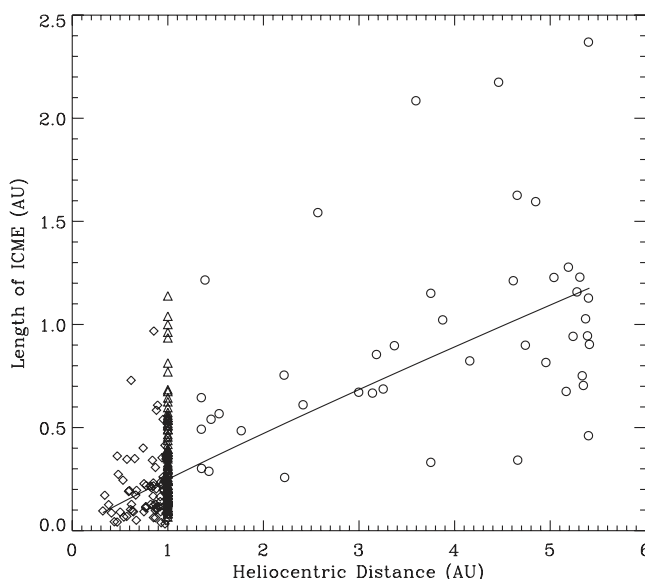


Figure A.4.: Radial widths of ICMEs observed with Helios 1 and Helios 2 (diamonds), WIND and ACE (triangles), and Ulysses (circles) (taken from *Liu et al. [2005]*)

From equation A.1 hourly CME generation probabilities were determined which lie in the range of zero to one. Uniformly distributed random numbers between zero and one were generated and compared with the CME generation probability.

The longitudinal and latitudinal distribution of the CME generation regions were determined according to the distribution of sunspots on the solar surface. The longitude was determined from a uniform distribution between 0 and 360 degrees. The latitude was determined from a polynomial fit of mean latitudes for sunspot

²Royal Observatory of Belgium, <http://www.astro.oma.be>

A.2. The model

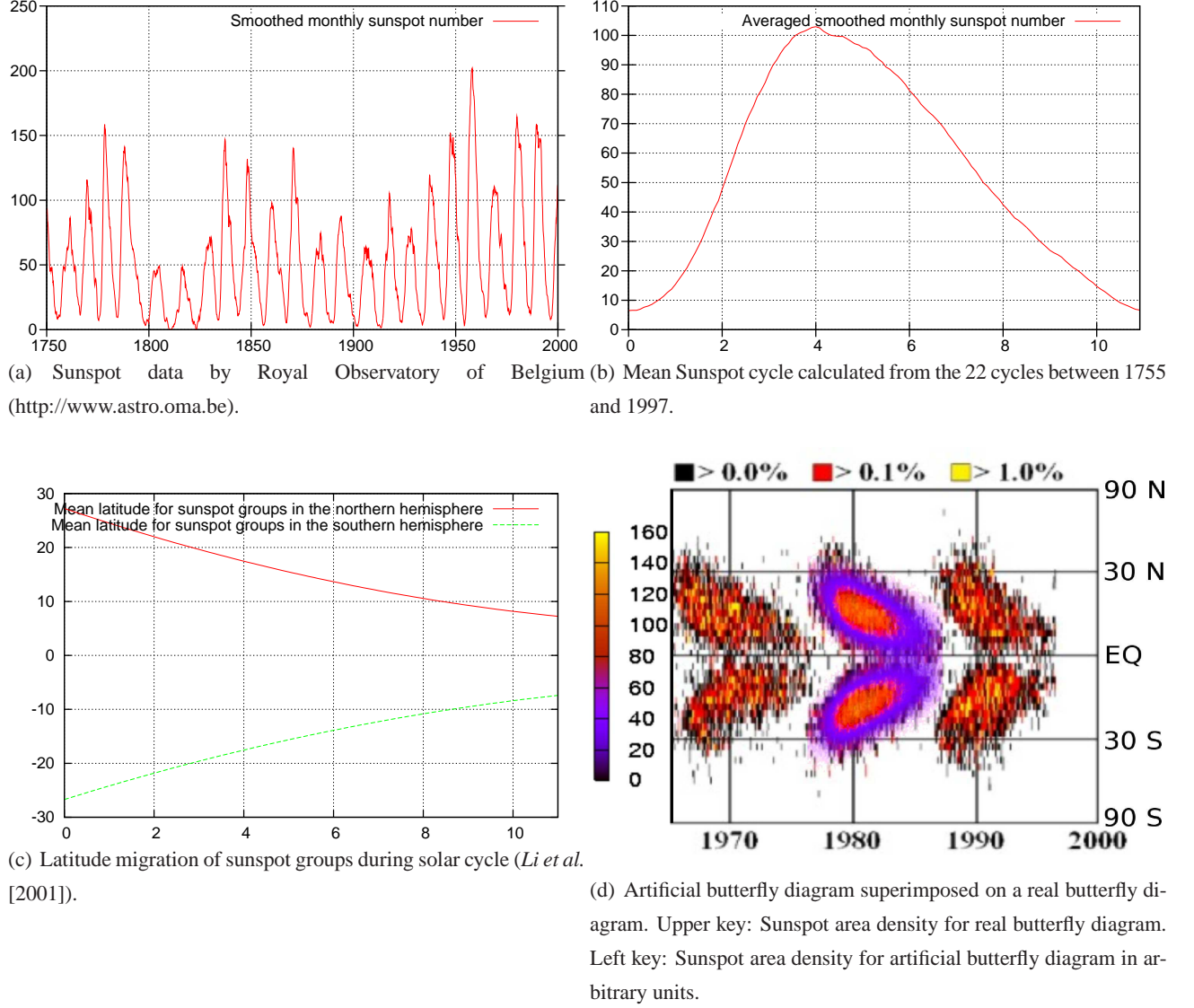


Figure A.3.: Determination of CME occurrence probability parameter and latitudinal distribution on solar surface

groups (see *Li et al.* [2001])

$$l = 0.0893t^2 - 2.8t + 27.24, \quad (\text{A.2})$$

$$l = -0.0767t^2 + 2.6t - 26.72, \quad (\text{A.3})$$

where t is the time in years and l is the latitude in degrees (see figure A.3 for resulting latitudes). On this time-dependent mean latitude random numbers from a Gaussian distribution with a standard deviation σ of six degrees were added to get the final latitude for the CME generation. Under these assumptions an artificial butterfly diagram was created (see figure A.3) by constructing a two dimensional histogram out of ~ 500000 data points with a time resolution of 1 month and an angular resolution of ~ 0.5 degrees.

A. ICME detections with Solar Orbiter and Sentinels

A.2.2. Evolution of ICMEs in the inner heliosphere

The magnitude of the cone angle α is determined from detections of limb CMEs observed with the Solar Maximum Mission (SMM) coronagraph in 1980 and 1984-1989 (see *Burkepile et al.* [2004]). They identified a CME to be a limb CME from spatial and temporal association with erupting prominences or H_{α} flares (see section 1.5). Altogether the cone angle distribution of 111 limb CMEs was taken into account (see figure A.5).

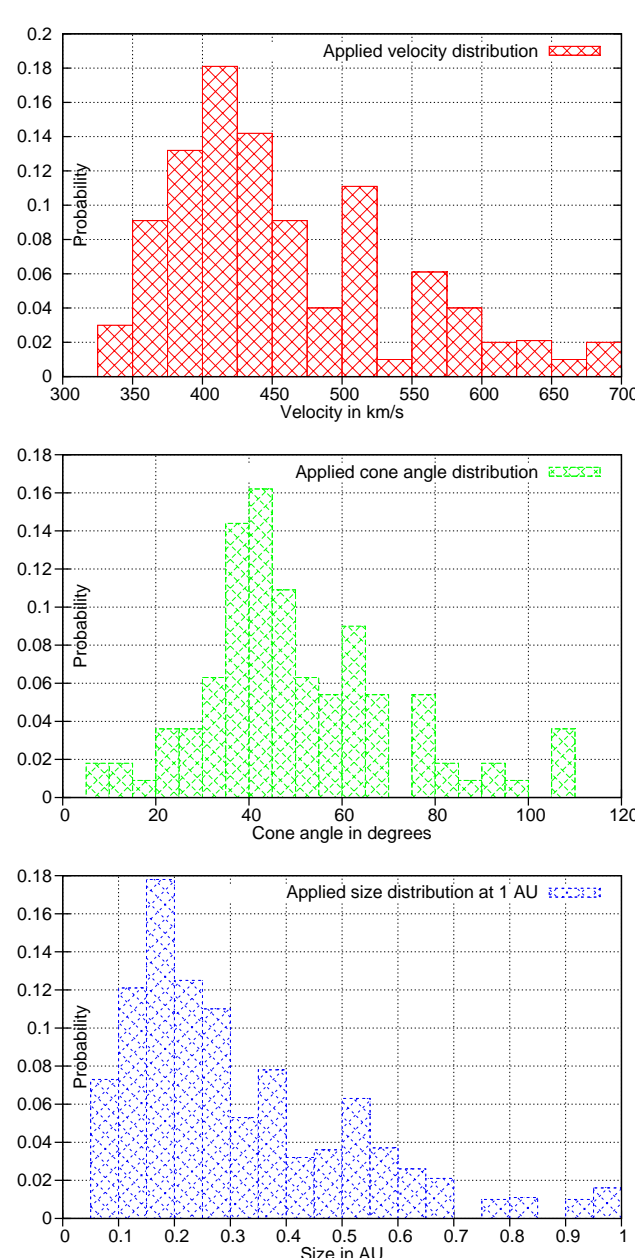


Figure A.5.: Utilised Distributions for important CME parameter

Velocity and size of the ICMEs were determined from ACE and WIND measurements. The ICMEs were identified by low proton temperatures and high α/proton density ratios (see *Liu et al.* [2005]). The velocity and size distribution is determined from 99 ICMEs that were observed from 1995 to 2002. The velocity was measured in-situ, while the size was determined from the duration of the event and the average velocity of the ICME (see figure A.5). This gives the distribution at ~ 1 AU radial distance from the sun. To determine the size and velocity at another distance from the sun we need observations of ICMEs at different distances from the sun. *Liu et al.* [2005] used observations from Helios 1, Helios 2, WIND, ACE and Ulysses which made measurements at distances between 0.3 and 5.4 AU from the sun with a focus on 1 AU (see figure A.4). Fitting a power law to the measurements, one obtains equation A.4 for the radial expansion of the ICME

$$S(R) = (0.25 \pm 0.01)R^{(0.92 \pm 0.07)} (\text{AU}) \quad (\text{A.4})$$

Doing the same for the velocity of the ICME results in

$$v(R) = (458.40 \pm 6.27)R^{(-0.002 \pm 0.02)} (\text{km s}^{-1}).$$

This fit result shows that there is hardly any dependence of ICME speed on the radial distance

	Sentinel 1	Sentinel 2	Sentinel 3	Sentinel 4	Solar Orbiter
time within 0.3 AU	0.08	0.05	0.06	0.07	0.05
time within 0.5 AU	0.29	0.28	0.26	0.26	0.25
time within 0.7 AU	0.66	0.63	0.62	0.63	0.48
time within 1.0 AU	1.00	1.00	1.00	1.00	0.94

Table A.1.: Probabilities of the spacecraft for being inside a given distance from the sun.

from the sun. Therefore the ICME speed is held constant through all model calculations. With this set of parameters a Monte Carlo simulation was performed, which covers the timeframe from Sep. 2015 to Dec. 2022. During this time the sun's activity will decrease toward solar minimum in 2018 and will then develop toward solar maximum, which will be reached at the supposed end of the missions.

A.3. Results

For each set of parameters 200 program runs with different seeds for the random numbers were conducted. The generated ICME trajectories were modelled with a time resolution of 1 h, while the time resolution for the spacecraft positions was 1 day. Positions for the Solar Orbiter were interpolated linearly, if the time resolution in the orbit data was smaller than 1 day. Multiple CME generation within one hour was not taken into account. For each generated ICME I determined which of the spacecraft encountered it while its centre was within 1 AU from the sun.

From this detection rate the number of ICMEs detected by at least one of the spacecraft, by at least one of the Sentinel spacecraft, by at least one of three Sentinel spacecraft, and by at least one of two Sentinels were determined. Another aspect is the number of ICMEs detected by more than one spacecraft. This helps to get an idea in which way parameters of the ICME develop in dependence on time, distance from the sun and at different locations. For this reason detection rates for ICMEs seen by at least two Sentinels, at least three Sentinels, all Sentinels and all spacecraft were determined. The detection rates for two and three Sentinel combinations were determined by calculating the average over all possible combinations.

Furthermore, the detection rate for different intervals 0-0.3 AU, 0-0.5 AU, and 0-0.7 AU distance from the sun were computed. These rates can be compared with the probabilities of the spacecraft being at these distance intervals (see table A.1).

In addition, the effect of different cone angle, velocity and size distributions were studied. The alternative cone angle distribution was determined from 5274 CMEs observed by LASCO from 1996 to 2004 and listed in the VSO Catalog³. Halo CMEs were not included. The alternative size was determined by

³Virtual Solar Observatory Catalog, <http://vso.nascom.nasa.gov/cgi-bin/vso/catalog.pl>

A. ICME detections with Solar Orbiter and Sentinels

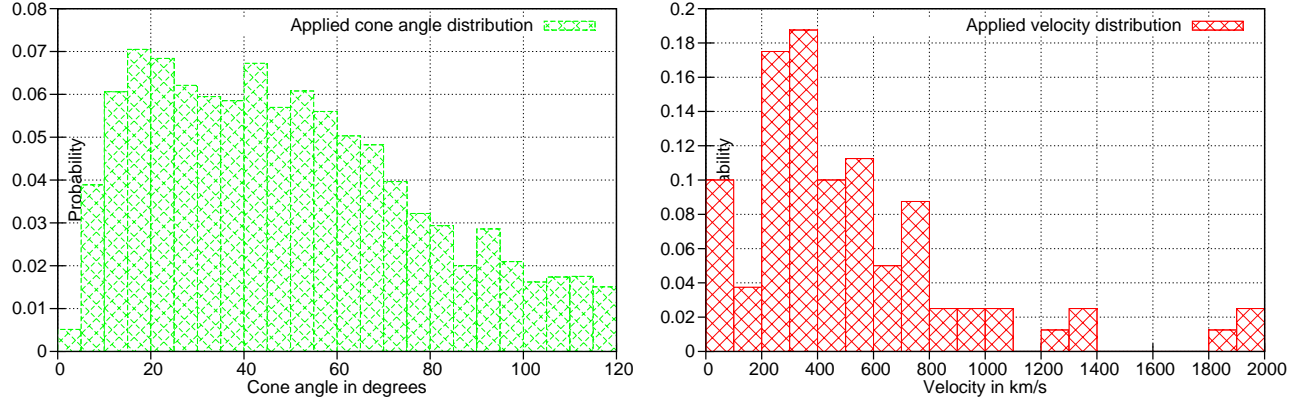


Figure A.6.: Alternative CME cone angle and velocity distribution

assuming a constant speed difference of 30 km/s between trailing edge and leading edge of the ICME. The initial size at the sun's surface was neglected. The alternative velocity distribution was taken from *Burkepile et al.* [2004]. They determined the velocities from 80 limb CMEs detected with the SMM coronagraph from 1980 and 1984-89 (see figure A.6).

From these data bar plots of the detection rates covering the whole Sentinel mission were made (see section A.3.1). The error bars drawn in this figures were determined from the 200 program runs. The 10th percentile and the 90th percentile from the distribution of the detection rate, resulting from the 200 program runs, were determined and plotted as lower error bar and as upper error bar respectively.

Furthermore, time series with a resolution of one month were plotted. During the whole mission time frame the Sentinel 1 spacecraft orbits the sun 19 times while the other Sentinel spacecraft orbit the sun 18 times. The Solar Orbiter will orbit the sun 17 times during this interval. The detection rate for the same set of spacecraft configurations, which previously had been used to calculate the histograms for the whole mission, was determined (see section A.3.2).

A.3.1. Histograms

On average a total number of 2016 ICMEs were generated at the sun's surface. In figure A.7 the ICME detection rates for different spacecraft combinations and different distance intervals are shown.

One can see that there is no difference in the detection efficiency between the Sentinel spacecraft. 9.3 % of all released ICMEs are seen by one Sentinel spacecraft alone. The Solar Orbiter alone has a detection efficiency of 8.6 %. Due to the fact that Solar Orbiter leaves the ecliptic plane the probability for detecting an ICME that is released at the opposite solar hemisphere is strongly decreased. In contrast, the Sentinels have quite a good chance of detecting ICMEs released from both hemispheres.

A two spacecraft Sentinel configuration would be able to detect 14.4 % of all released ICMEs, a three spacecraft Sentinel configuration would be able to detect 18.0 % and the four spacecraft configuration

A.3. Results

	Sentinel 1	Sentinel 2	Sentinel 3	Sentinel 4	Solar Orbiter
<u>ICMEs detected within 0.3 AU</u> time spent within 0.3 AU	211 (158-290)	217 (152-304)	227 (146-308)	215 (138-292)	97 (58-156)
<u>ICMEs detected within 0.5 AU</u> time spent within 0.5 AU	193 (162-228)	193 (164-229)	197 (158-236)	190 (155-228)	186 (151-226)
<u>ICMEs detected within 0.7 AU</u> time spent within 0.7 AU	190 (169-214)	191 (171-212)	193 (170-218)	190 (168-214)	191 (166-218)
<u>ICMEs detected within 1 AU</u> time spent within 1 AU	190 (172-208)	190 (174-208)	189 (171-208)	188 (170-206)	186 (169-204)

Table A.2.: Comparison of the ratio of detected ICMEs to the time spent at several distance intervals. The detection rate becomes independent from the time spent within a distance interval (see table A.1). The errors are given by the 10th percentile and 90th percentile of the distribution.

would be able to detect 20.6 % of all released ICMEs. Combined with the Solar Orbiter mission the detection rate can be increased to 26.6 %. From the increase in the detection rates it can be seen that saturation for detections in the ecliptic plane begin to play a role. On the other hand, this means that multiple spacecraft encounters with the same ICME become more likely. The reason for the strong increase in the whole spacecraft detection probability is that many ICMEs detected by Solar Orbiter cannot be seen from an orbit in the ecliptic plane.

Looking at the multiple ICME detections one can see that 4.2 % of the ICMEs will have an encounter with at least two Sentinel spacecraft, 2.8 % will have an encounter with at least three Sentinel spacecraft, while 2.3 % will have an encounter with all Sentinel spacecraft. Only 0.2 % of all released ICMEs will have an encounter with all five spacecraft. These probabilities are explained by the spacecraft orbits. There are several times when the four Sentinel spacecraft are at short distances from each other, especially in the beginning of the mission when the spacecraft move along one trajectory. If an ICME is released and is detected by one of the Sentinel spacecraft inside the ecliptic plane it has a probability of 45 % to be detected by at least a second Sentinel spacecraft. Detection of the same ICME with all five spacecrafts are rare because the orbits are too different.

Comparing the results from table A.1 with the number of ICMEs detected at several distance intervals (see table A.2) it can be seen, that the detection efficiencies are independent of the distance from the sun. On the one hand the spacecraft are moving faster close to the sun and therefore have a larger probability to hit an ICME moving in the spacecraft orbit. On the other hand the ICME size is smaller close to the sun (see equation A.4). The strong decay in the probability of multiple ICME detections inside the small distance intervals results from the small probability for two or more spacecraft being inside this distance interval at the same time.

A. ICME detections with Solar Orbiter and Sentinels

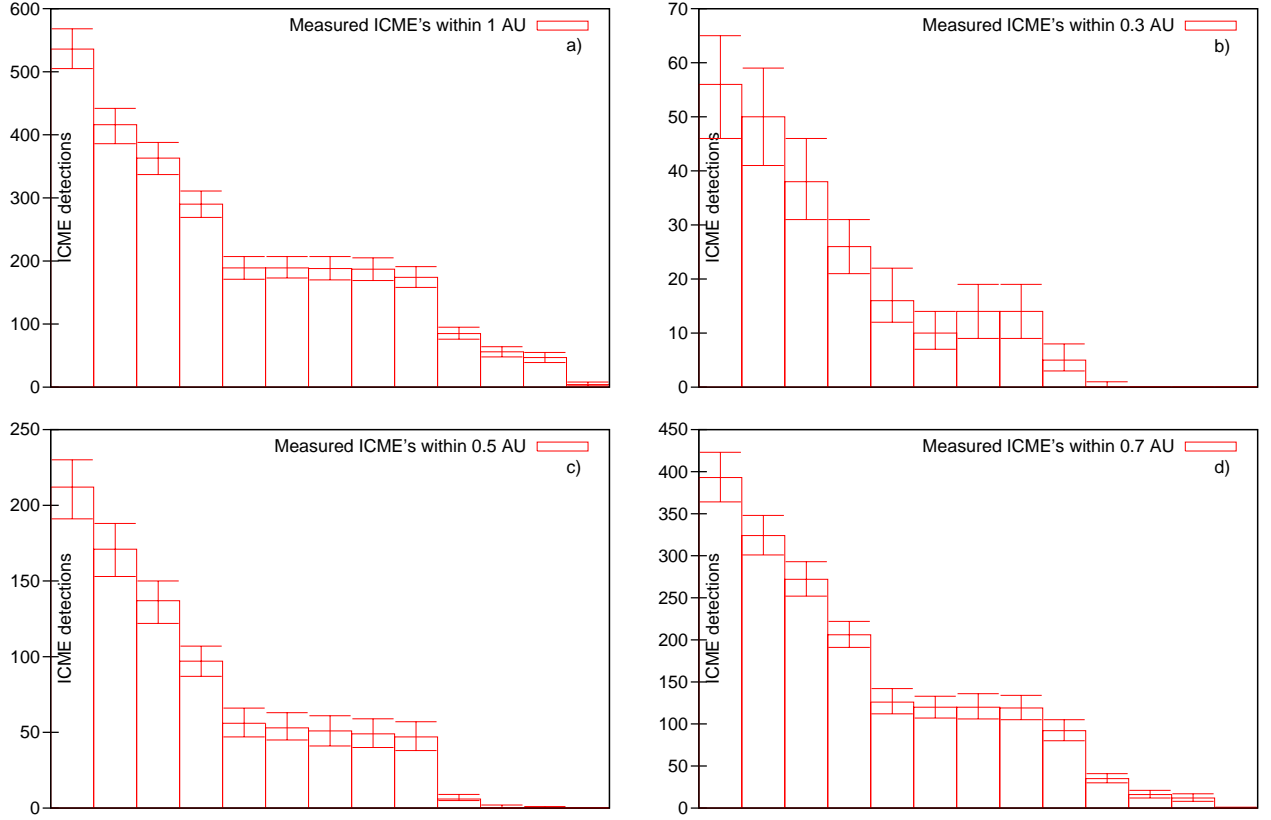


Figure A.7.: On average 2016 ICME were emitted during each program run. Shown are ICME detection rates for different spacecraft combinations and different distance intervals from the sun. From left to right: Detection by at least one spacecraft, detection by at least one of the Sentinels, detection by at least one of three Sentinels, detection by at least one of two Sentinels, detection by Sentinel 1, detection by Sentinel 2, detection by Sentinel 3, detection by Sentinel 4, detection by Solar Orbiter, detection by at least two Sentinels, detection by at least three Sentinels, detection by all Sentinels, detection by all spacecraft.

In figure A.8 the influence of different parameters on the detection rate is shown. Statistical properties of the compared distributions shown in figures A.5 and A.6 are listed in table A.3. Taking the difference between the mean and the 10th percentile (respectively the 90th percentile) as error of a single measurement the error in the mean value will be $\sqrt{200} = 14.14$ times smaller. Considering this, the statistical error in the detection rates is smaller than 2.3 counts.

Both compared velocity distributions show a similar mean value (see table A.3). Lower ICME velocities should lead to a higher detection rate. The higher detection rate occurring with the alternative velocity distribution can be explained by taking into account that the higher mean velocity in the alternative distribution results from few very fast CMEs. The difference in the detection rate for the compared size distributions is in the order of 4 %, although both distributions are very different. As expected a smaller

A.3. Results

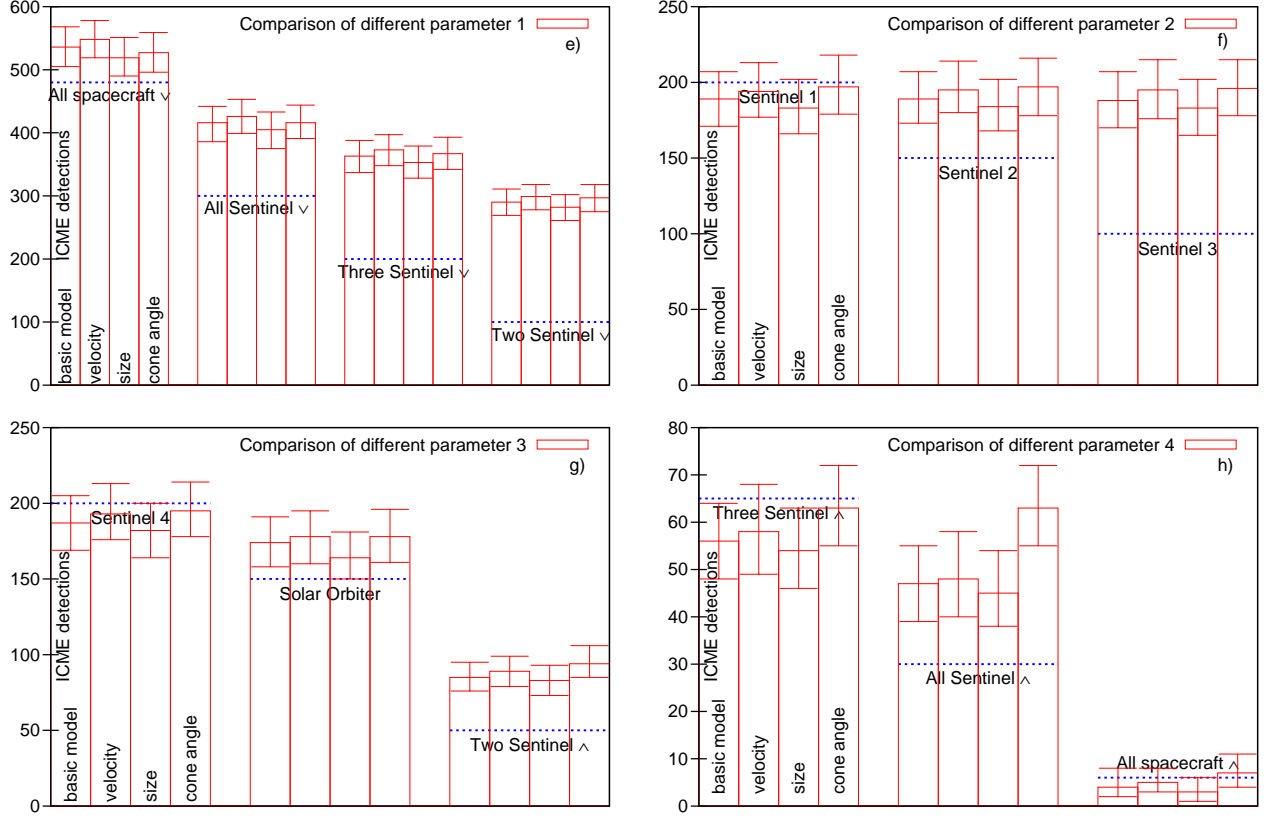


Figure A.8.: Influence of different sets of model parameters. Shown are the number of ICME detections within 1 AU distance from the sun. The first bar within one block shows the detection rates for the basic model, the second bar detection rates with alternative velocity distribution, the third bar for alternative size distribution and the fourth bar for the alternative cone angle distribution. The blocks are labelled with the considered spacecraft configuration. A \vee denotes a detection by at least one of the spacecraft, while a \wedge denotes a detection by all spacecraft.

	Basic model		Alternative distributions	
	Mean value	Standard deviation σ	Mean value	Standard deviation σ
Velocity in $\frac{\text{km}}{\text{s}}$	459	82	519	404
Size in AU	0.314	0.203	0.065	0.013
Cone angle in degree	50.38	21.03	49.5	28.7

Table A.3.: Statistical properties of applied parameter distributions. The standard deviation σ was determined from $\sigma = \sqrt{\frac{1}{N} \sum_{i=1}^n (x_i - \bar{x})^2}$.

A. ICME detections with Solar Orbiter and Sentinels

size leads to a lower detection rate. The two cone angle distributions have quite similar mean values and standard deviations σ . The difference in the detection rate arises from ICMEs with a very large cone angle. Because the detection probability is depending nonlinearly on the cone angle, large cone angle ICMEs have a strongly enhanced detection probability. In the basic model only 9 % of all ICMEs have cone angles larger than 80 degrees, while in the alternative distribution 17 % have cone angles larger than 80 degrees. Therefore, the distribution with the smaller mean value leads to higher detection rates.

A.3.2. Time series

In figures A.9, A.10, and A.11 time series are plotted for the different spacecraft configurations and several distance intervals. The effect of the solar cycle determining the number of released ICMEs is clearly visible (figure A.9 a). The detection rate for the individual spacecraft looks very similar. The decrease in the detection rates for the Solar Orbiter during month two to eight is caused by the orbit which is outside 1 AU during this time. Therefore, only the largest ICMEs are treated as detected because their centre is still inside 1 AU and the classification to the 1 AU distance interval is done from centre positions. For the first 15 months of the mission the Sentinel spacecraft have nearly the same positions and therefore the time series are identical. The same can be obtained from multiple observations of the same ICME. In the first 15 months a ICME is either detected by all Sentinels or by none of them.

The "spiky" structure from month 50 onwards seen in the combined spacecraft detections results from the positions of the Sentinel spacecraft. In some months the Sentinels are close together. This results in enhanced multiple detections of the same ICME. When the distances are big, more different ICMEs can be detected by the spacecraft combinations. Therefore, a maximum in the multiple detections of the same ICME is in-phase with a minimum in the overall ICME detection. The time from maximum to maximum corresponds to the time of the orbit period of the Sentinel spacecraft of ≈ 5 months.

From the detection rate in the different intervals one can see that it takes more than 30 months for the Sentinels to reach the 0-0.3 AU interval. When the Sentinel spacecraft are close to the sun their distance to each other is big, resulting in enhanced overall ICME detections.

The structure seen for the smaller distance intervals detection rate results from the orbits of the spacecraft. Having highly eccentric orbits the Sentinels will only spend short times close to the sun and longer times far away. This results in more or less short increases in the detection rates (depending on distance interval). Even for the 0-0.7 AU distance interval this structure is visible at all times. Thus, none of the final orbits is fully within this interval. The detection time series for a larger distance interval has to be the envelope for the shorter distance intervals time series. The strong decay of multiple detections of the same ICME in the smaller distance intervals is explained by the low probability of two or more spacecraft for being within the same distance interval.

A.3. Results

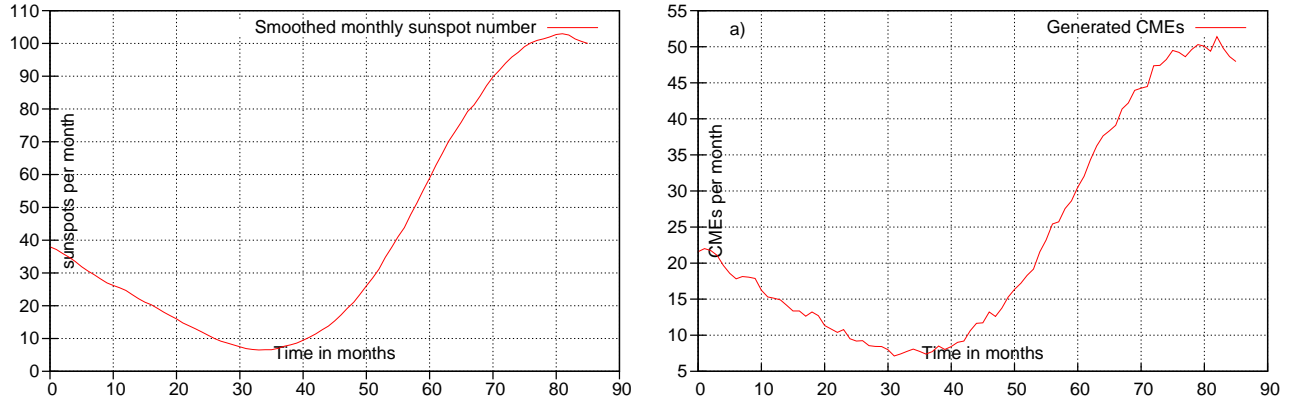


Figure A.9.: Smoothed number of monthly sunspots (SSN) and ejected ICMEs for the time frame Sep 2015 to Dec 2022.

A.3.3. Systematic errors

- **Dimension of ICME plasma cloud.**

Cane and Richardson [2003] found an average ICME size in radial direction of 0.33 ± 0.01 AU. This is in good agreement with the applied size distribution. Treating the plasma cloud of the ICME as a truncated cone is an oversimplification. The error of this assumption is hard to determine, because we do not know the correct structure of ICME plasma clouds. Assuming an expansion in the directions perpendicular to the sun-Earth line that is similar to the radial expansion one would expect quite a small error (see figure A.8).

- **Dependence of parameters on solar cycle.**

Ivanov and Obridko [2001] used data from the SMM and P78-1 mission to investigate the influence of solar cycle on CME angular width and velocity. The variation in the semiannual mean velocity is in the order of 300 km/s, while the variation in the semiannual mean angular width is in the order of 30 degrees. *Cane and Richardson* [2003] found variations of 100 km/s in the average ICME speed during solar cycle. Higher mean velocities would lower the detection efficiency while higher angular width would raise detection efficiency. Therefore, the number of detected ICMEs during times of maximum angular width (65° average) would be ~ 1.5 times higher while the number of detected ICMEs during times of minimum angular width (35° average) would be ~ 2 times smaller. The effect of ICME speed variation should be less than 10 %.

- **Correlations between different ICME parameters.**

Ivanov and Obridko [2001] found that CMEs with large angular width are more likely correlated with higher velocities. Unfortunately no correlation coefficient was given. Therefore large ICMEs would have lower detection probabilities, while the smaller ones would have higher detection efficiencies. Because the speed has no large impact on the detection probabilities, the error should

A. ICME detections with Solar Orbiter and Sentinels

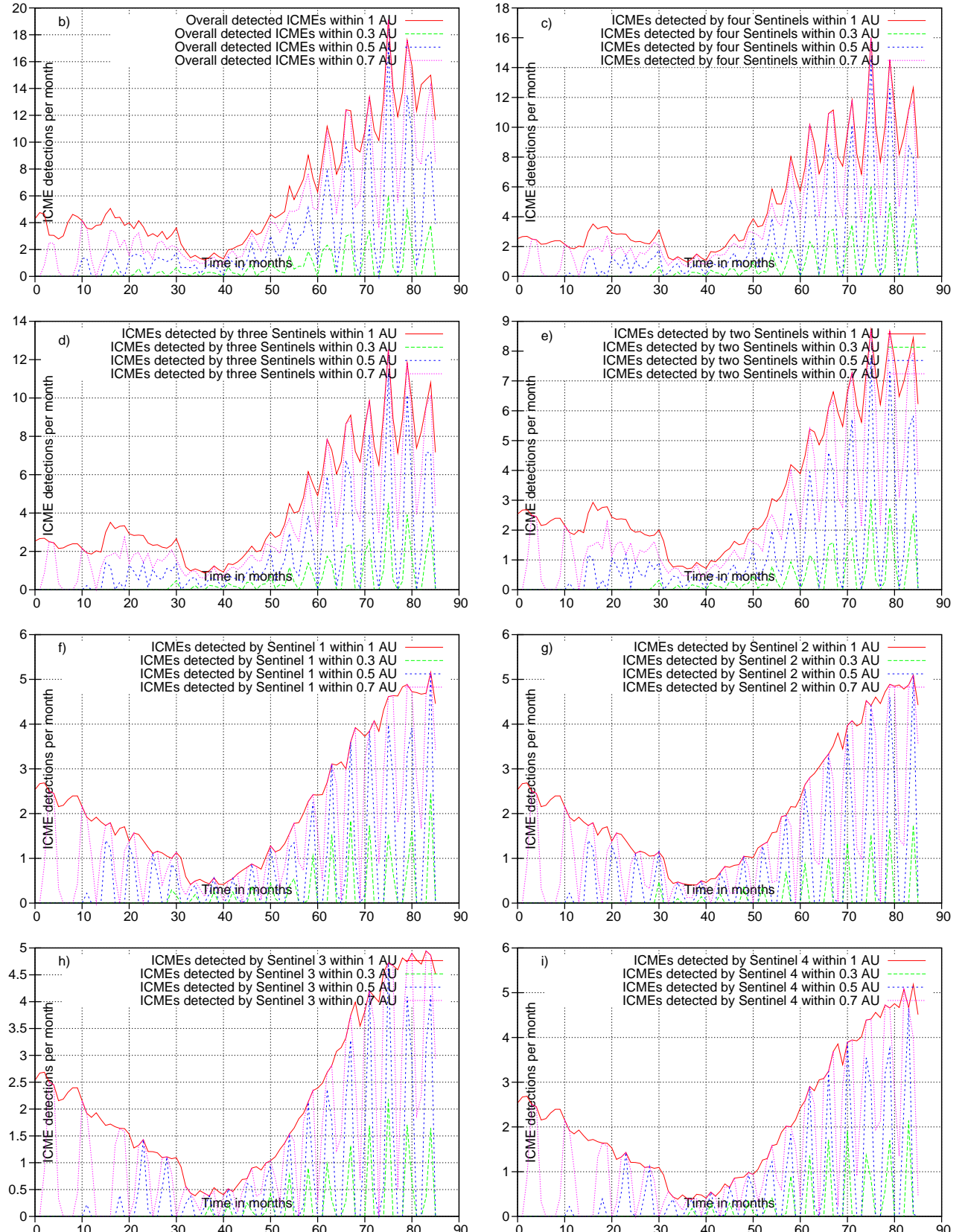


Figure A.10.: Time series of ICME detections from Sep 2015 to Dec 2022.

A.3. Results

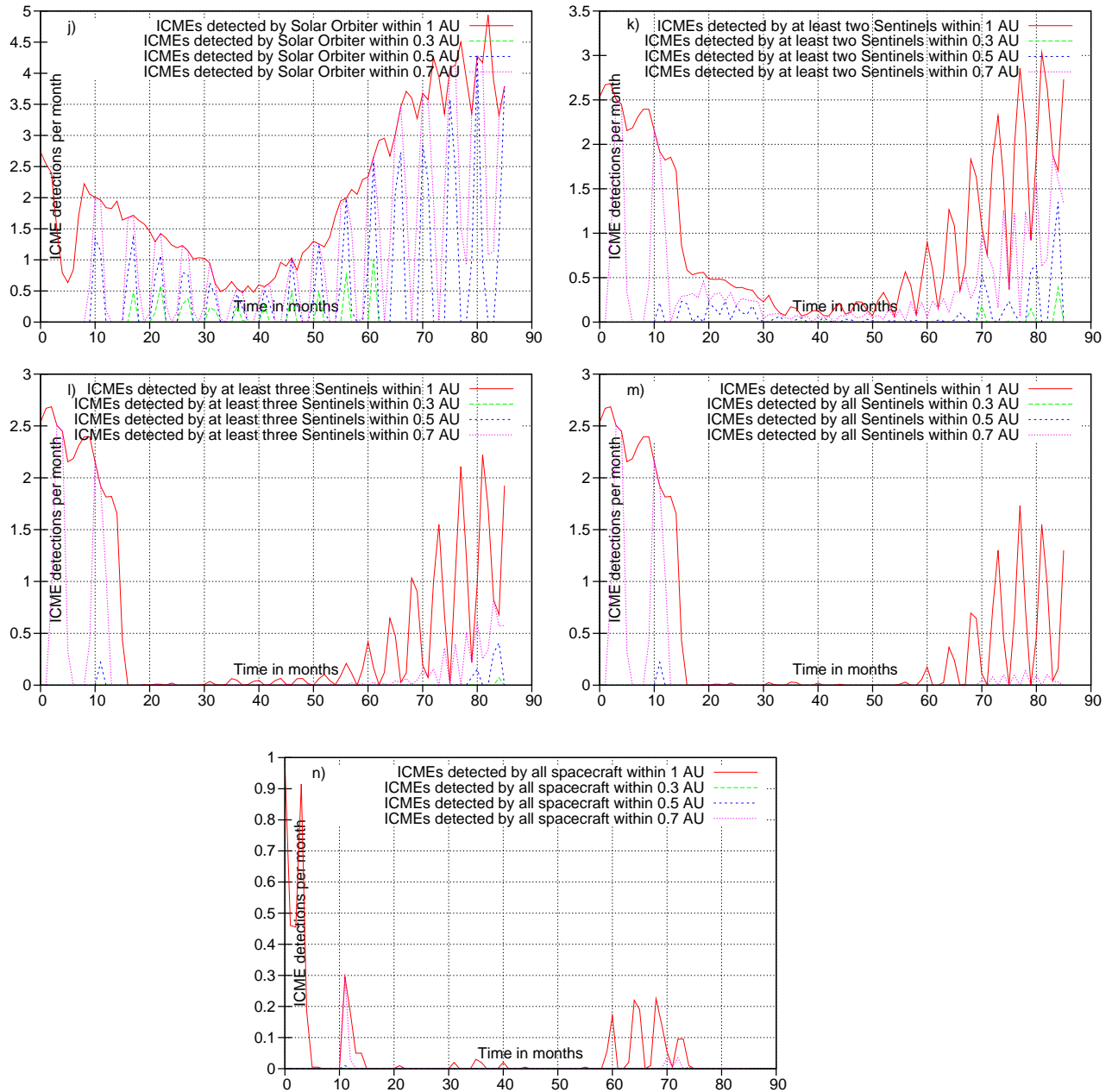


Figure A.11.: Continuation of figure A.10. Time series of ICME detections from Sep 2015 to Dec 2022.

A. ICME detections with Solar Orbiter and Sentinels

be smaller than 20 %.

- **Interactions with magnetic field and interplanetary medium.**

As seen from the velocity distributions in figures A.5 and A.6 slow ICMEs are on average accelerated while fast ICMEs are decelerated by interactions with surrounding solar wind plasma. Another effect of the interaction is deformation of the ICME plasma cloud. The interplanetary magnetic field can lead to reconnection with the primordial magnetic field of the ICME resulting in a changed expansion behaviour of the ICME plasma cloud.

- **Number of generated ICMEs and source location.**

Ivanov et al. [1999] compared the source locations of CME occurrence with the presence of the global field neutral line at different times of solar cycle 21 and 22. They found that the CMEs were mainly ejected at low apparent latitude during solar minimum and at a higher latitude interval during solar maximum. Projection effects were not taken into account. The same effect was found by *Yashiro et al.* [2003]. They worked with LASCO data of nearly 5000 CMEs detected from 1996 to 2001. This behaviour results in lower detection rates at solar maximum because the CME's generation locations are spread nearly over the whole solar surface. The abrupt change in the CME generation latitudes at the beginning of a new solar cycle using sunspot occurrence latitudes leads to lower ICME detection rates in the ecliptic plane as seen in figure A.10 from month 33 onward. Comparing the number of simulated CME ejections (~ 2000 within 7 years) with the number of observed LASCO CMEs during solar cycle 23 (~ 5000 within 6 years) a big difference in the CME number is obvious. Considering the difference in the sunspot number of the averaged sunspot cycle and solar cycle 23 as well as the different phases of solar cycle covered by the time intervals there is still a difference of factor two. This behaviour is explained by equation A.1. This equation is obtained from a fit to data older than 1994. Due to enhanced sensitivity of the LASCO coronagraph compared with older coronagraphs more smaller and weaker CMEs can be detected in white light. Assuming that these additional CMEs all have small cone angles (smaller than 45°) the determined detection rates would be underestimated by $\sim 30\%$. *Cane and Richardson* [2003] found typical rates of \sim three ICMEs per Carrington rotation at solar maximum and ~ 0.3 ICMEs per Carrington rotation at solar minimum. The scattering is much higher than in the simulated detection rates. There are variations of a factor of seven within one year. The measured ICME rate at ACE (at Lagrangian point 1 in the ecliptic plane) is in good agreement with the ICME detection rate determined for the Sentinel spacecraft. The higher scattering in the ACE detection rates results from multiple CME ejections from the same active region within short times. Another aspect is the averaging over 200 program runs which reduces the scattering in the simulated detection rate by a factor of 14.

- **Evolution of size and speed with distance from the sun.**

Cane and Richardson [2003] compared the maximum solar wind speed measured at ACE during an ICME with the transit speed of the ICME from sun to earth. The transit speed was determined from associated CME detections with LASCO. On average the transit speed was higher than the maximum solar wind speed indicating a deceleration process taking place. For faster ICMEs this deceleration was stronger than for slower ones. Assuming that the real velocity distribution lies between the distributions shown in figures A.5 and A.6 the error in the detection rate should be smaller than 10 %.

- **Detection probability for ICMEs during a spacecraft encounter.**

In *Cane and Richardson* [2003] ICMEs were identified by low proton temperatures ($T_p/T_{ex} < 0.5$) and by magnetic field observations (see table 3.1). Some additional signatures like the existence of shocks or the decrease in cosmic ray intensity were used to identify ICME periods. In *Richardson and Cane* [2004a] ICMEs were identified from plasma compositional anomalies. The ratio O⁷/O⁶, Mg/O, Ne/O and the ratio Fe^{≥16+} (Iron ionised at least 16 times) to Fe_{tot} were used to define periods of compositional anomalies. Comparing these two methods they found that 10 % of all ICMEs identified in *Cane and Richardson* [2003] did not show compositional anomalies. The amount of intervals showing compositional anomalies but were not classified as ICME in *Cane and Richardson* [2003] to the total number of detected ICMEs was in the order of 10 %. Assuming that 90 % of all engaged ICMEs can be detected the simulated detection rate is 10 % too high.

B. Neutron detections with Solar Orbiter

Neutrons are created in nuclear reactions as a consequence of solar flares. Flare-accelerated ions interact with ambient solar plasma and produce neutrons depending on the cross section of the individual nuclear reaction. Observing these neutrons helps to obtain total number, energy spectrum, time dependence and angular distribution of ion acceleration. Because free neutrons are unstable and decay after a mean life time of 886 seconds in the reaction $n \rightarrow p + e^- + \bar{\nu}_e + 0.78 \text{ MeV}$, neutrons with low energies are not able to reach Earth. With the help of the High Energy Telescope with neutron detection capabilities (HETn) onboard Solar Orbiter these low energy neutrons ($> 2 \text{ MeV}$) can be detected. The model for in-situ ICME detections was adapted to solar flare neutron detections to determine averaged spectra of solar neutrons and the maximum flux rate at Solar Orbiter.

B.1. Neutron production processes

Hua et al. [2002] determined angular and energy-dependent neutron emission from solar flare magnetic loops. In table B.1 the considered neutron production processes are shown. The most abundant isotopes are taken into account as target nuclei, while only helium ions and protons are included as projectiles. The threshold energy for each considered nuclear reaction is given. Different experimental results were used to obtain the inclusive cross sections for neutron production depending on the isotope and the energy of the projectile. In the next step differential cross sections $\frac{d^2\sigma}{dE_n d\Omega_n}$ were calculated for the different production processes. These differential cross sections allow the determination of energy and angular distribution of the produced neutrons. Pre-equilibrium processes and evaporation processes were examined separately.

Next an energy spectrum for the accelerated ions is assumed. The first analysed spectrum is a second-order Bessel function ($N(E) \approx K_2[(12p/mc\alpha T)^{\frac{1}{2}}]$) resulting from stochastic Fermi acceleration, the second analysed spectrum is a power-law spectrum ($N(E) \approx E^{-S}$) resulting from shock acceleration. Solar photospheric abundances were assumed for the accelerated ions and for the ambient medium. The influence of different heavy ion abundances and different spectral indices on the neutron production was examined.

For a power-law spectrum with $S=3.5$ the neutron spectrum from figure B.1 is obtained. This spectrum was used to model the energy distribution of the neutrons produced in solar flares. The spectrum was calculated using $Q_n(E) = E^{0.34} e^{-(\frac{E}{13})^{1.35}} \left(1 - e^{-(\frac{65}{E})^{1.35}}\right) + 1.41 \cdot 10^7 E^{-4.5} e^{-(\frac{65}{E})^{1.35}} \left(1 - e^{-(\frac{E}{13})^{1.35}}\right)$.

B.1. Neutron production processes

Isotope	Proton	α -particle	Isotope	Proton	α -particle
^1H	292.3	25.7	^3He	10.3	5.5
^4He	25.7	9.5	^{12}C	19.6	2.8
^{13}C	3.2	Exo	^{14}N	6.3	1.5
^{15}N	3.7	2.0	^{16}O	17.2	3.8
^{18}O	2.5	0.2	^{20}Ne	15.4	2.2
^{22}Ne	3.8	0.15	^{24}Mg	15.0	2.1
^{25}Mg	5.3	Exo	^{26}Mg	5.0	Exo
^{28}Si	15.6	2.3	^{29}Si	5.9	0.4
^{56}Fe	5.5	1.4	^{54}Fe	9.2	1.6

Table B.1.: Table of elements considered for neutron production processes. Given is the threshold energy in MeV/nucleon depending on target nucleus and projectile (taken from *Hua et al.* [2002]).

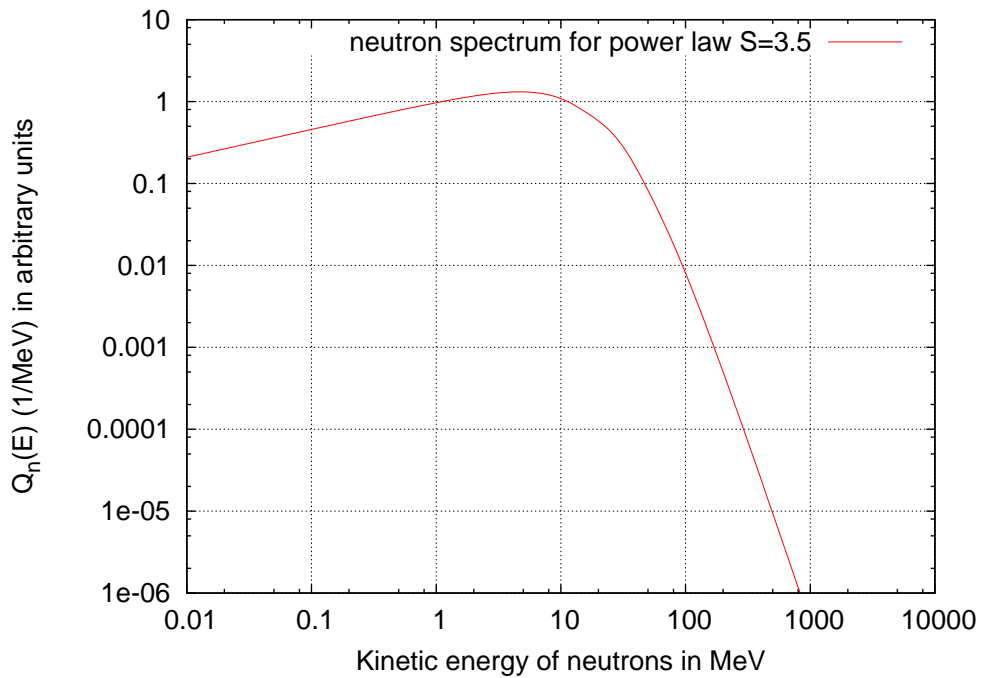


Figure B.1.: Obtained neutron spectrum from an accelerated ion spectrum $N(E) \approx E^{-3.5}$. Photospheric element abundances were used for the accelerated ions and the ambient medium. This spectrum models the neutron spectrum given by *Hua et al.* [2002].

B. Neutron detections with Solar Orbiter

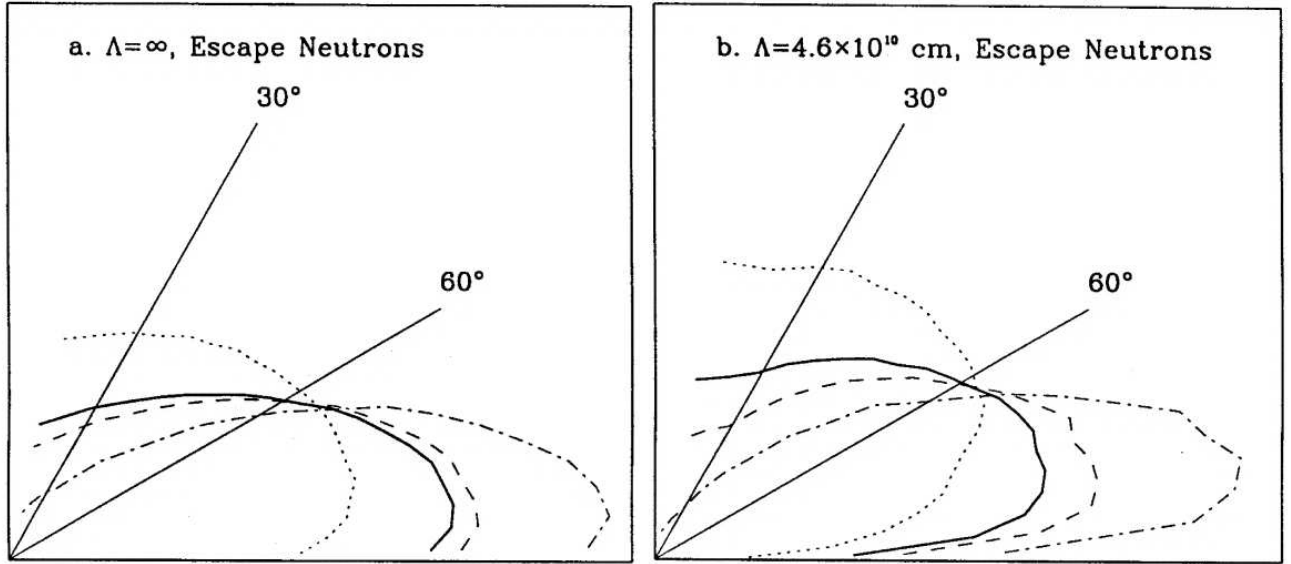


Figure B.2.: Angular distribution of escaping solar neutrons. The dotted line shows the angular distribution for 1-10 MeV neutrons, the dashed line for 10-100 MeV neutrons, the dashed-dotted line for 100-1000 MeV neutrons and the solid line the distribution for all neutrons. 0° denotes the direction normal to the solar surface and 90° the direction tangential to the solar surface. Figures taken from *Hua et al.* [2002].

B.2. Ion interactions with the magnetic field

The effect of the solar magnetic field on neutron emission outlined in this section is described in *Hua et al.* [2002]. To determine the angular dependence of neutron emission and the depth in the solar atmosphere where the neutrons are produced, one has to take into account the flare magnetic loops. The assumed magnetic field is described in (*Hua et al.* [1989]). The magnetic loop consists of two semicircular portions of length L_c in the corona and of two straight portions parallel to solar radius extending to chromosphere and photosphere. Magnetic field strength is constant in the corona and increased with a power law of the pressure δ in the chromosphere and photosphere ($B(h) = B_c(P(h)/P_c)^\delta$, where index c indicates coronal values). In the corona the gas is assumed to be fully ionised while it is neutral in the chromosphere and photosphere. The ions are accelerated in the corona and released instantaneously at the top of the magnetic loop with an isotropic angular distribution. L_c is chosen to be $1.15 \cdot 10^9$ cm and δ is 0.2.

The processes considered for the accelerated ions are:

- energy loss due to coulomb scattering
- destruction due to nuclear reactions

- mirroring of the ions in the converging magnetic field
- pitch-angle scattering due to MHD turbulence

Two cases of pitch-angle scattering were considered. In one case no pitch-angle scattering is assumed ($\Lambda = \infty$, Λ mean free path), in the other case nearly saturated pitch-angle scattering is assumed ($\Lambda = 4.6 \cdot 10^{10}$ cm). No pitch-angle scattering keeps the accelerated ions magnetically trapped in the low-density corona because the loss cone is not refilled. This leads to extended neutron production times and most of the neutrons are produced in the corona. In the case of high pitch-angle scattering the loss cone is constantly refilled and the accelerated ions reach the denser chromosphere and photosphere. Therefore, most neutrons are produced in these regions. Due to the enhanced density the periods of neutron production are much shorter. The angular distribution of the emitted neutrons is essentially tangential to the solar surface in the case of no pitch-angle scattering and essentially directed downward in the case of high pitch-angle scattering.

To get the number of neutrons escaping from the sun in dependence of the angle one has to take into account neutron decay and neutron capture from ^1H resulting in 2.223 MeV gamma ray emission. Figure B.2 shows the angular distribution of escaping neutrons. In the case of no pitch-angle scattering the neutrons are mainly produced in the corona and the attenuation for neutrons emitted tangential to solar surface is not as strong as for the case of high pitch-angle scattering.

B.3. Relativistic neutrons equations

The kinetic energy of the relativistic neutrons in dependence of the speed is determined by

$$E_{\text{kin}} = mc^2 \left(\frac{1}{\sqrt{1 - (\frac{v}{c})^2}} - 1 \right). \quad (\text{B.1})$$

This can be solved for the neutron speed

$$v(E_{\text{kin}}) = c \sqrt{1 - \frac{1}{\left(1 + \frac{E_{\text{kin}}}{mc^2}\right)^2}}. \quad (\text{B.2})$$

The length contraction for relativistic neutrons is

$$d'(v) = d \sqrt{1 - \left(\frac{v}{c}\right)^2} = v(E_{\text{kin}})t. \quad (\text{B.3})$$

To determine the number of neutrons arriving at a given distance from the sun one has to take into account the neutron mean life time of 886 seconds. The number of neutrons surviving a time t is determined by the decay law

$$N(t) = N_0 \exp\left(-\frac{t}{t_0}\right). \quad (\text{B.4})$$

B. Neutron detections with Solar Orbiter

Combining equations B.3 and B.4 leads to the number of solar neutrons that can be detected at a specific distance from the sun

$$N'(v, d) = N(v) \exp\left(-\frac{d'(v)}{t_0 v}\right). \quad (\text{B.5})$$

B.4. Number of neutrons produced in solar flares

Several neutron monitor measurements of solar neutron events were used to obtain the total number of neutrons that are emitted during a solar flare. The primary neutrons produce secondary nucleons in Earth's atmosphere. These secondary nucleons produce low energy neutrons inside the lead of the neutron monitor, which are detected by the counters of the neutron monitor. Because of atmospheric attenuation the detection efficiency for primary neutrons with kinetic energy smaller than 100 MeV decays very fast (*Chupp et al.* [1987]).

The data obtained from a neutron monitor is just a total count rate. To determine spectral information from count rate enhancement several effects have to be taken into account. In the case of time extended neutron production one can write (see *Debrunner et al.* [1997])

$$\Delta N_n(h, \theta, t) = R^{-2} \int_{t_{\min}}^{\infty} \mu(t - t_s) Q(E_n, t - t_s) \frac{dE_n}{dt_s} P(E_n) S_n(h, \theta, E_n) dt_s. \quad (\text{B.6})$$

$\Delta N_n(h, \theta, t)$ is the increase in the neutron monitor count rate in dependence of atmospheric height h , the zenith angle θ and time t . R is the Earth-sun distance, $\mu(t - t_s)$ is the intensity-time profile of neutron production, $Q(E_n, t - t_s)$ is the spectral distribution of produced neutrons, $\frac{dE_n}{dt_s}$ describes the energy-time dispersion caused by different neutron speeds and $P(E_n)$ is the neutron survival probability. The detection properties of the neutron monitor for primary neutrons are described by $S_n(h, \theta, E_n)$. t_{\min} is determined by the upper cutoff energy of the neutron spectrum.

Simple models assume a δ -function emission of neutrons at the sun (e. g. *Watanabe et al.* [2003b, 2006]). In this case the free parameters are the time of neutron production, the shape of the neutron spectrum and the total number of produced neutrons with kinetic energy greater than 100 MeV. The fundamentally applied spectral functional form is a power-law spectrum: $q(E_n) = N E_n^{-S}$. The high-energy cutoff implemented in most cases is in the range of a few GeV.

More sophisticated models assume time extended neutron production. *Watanabe et al.* [2003b, 2006] used the temporal behaviour of gamma ray production from carbon and oxygen nuclei deexcitation at energies of 4.4 and 6.1 MeV as tracers for the neutron production. *Chupp et al.* [1987] and *Debrunner et al.* [1997] used gamma rays from neutral pion decay as time history for neutron production. High energy protons (> 180 MeV) are needed to produce photons with mesonic origin (*Chupp et al.* [1987]). *Debrunner et al.* [1997] used the 79-109 MeV channel of the PHEBUS detector onboard the Granat spacecraft, while *Chupp et al.* [1987] used data from the SMM mission. As a last step temporal evolution of the spectral index S for different phases of the solar flare, like the extended and impulsive phase, can be assumed.

B.4. Number of neutrons produced in solar flares

Date	Location at sun	Power law index S	Flux at 100 MeV in 10^{28} neutrons $\text{MeV}^{-1} \text{sr}^{-1}$	X-ray class	Literature
1982 3 June	S09°E72°	-4.0	2.6	X8.0	1, 2, 3
1990 24 May	N36°W76°	-2.9	4.3	X9.3	1, 3, 4
1991 22 March	S26°E28°	-2.7	0.06	X9.4	1, 3
1991 June 4	N30°E70°	-7.3	1.8	X12.0	1
2000 November 24	N22°W07°	-4.9	0.18	X2.3	1
2001 August 25	S17°E34°	-3.9	0.11	X5.3	5
2003 October 28	S16°E08°	-3.5	0.33	X17.2	6
2003 November 4	S19°W83°	-3.9	2.1	X28.0	6

Table B.2.: Table of neutron detections with neutron monitors. The flux rate is obtained from neutron monitor count rate enhancements and model assumptions. The literature references are: 1=*Watanabe et al.* [2003b], 2=*Chupp et al.* [1987], 3=*Chupp et al.* [2003], 4=*Debrunner et al.* [1997], 5=*Watanabe et al.* [2003a], 6=*Watanabe et al.* [2006]

Fitting these free parameters to observed neutron monitor count rates, the total number of high energy neutrons (> 100 MeV) emitted from the sun can be obtained. Table B.2 shows a number of neutron producing solar flares which occurred in the last 25 years. Given is the date of flare, the location at sun's surface, the power law index S, which characterises the high energy neutron spectrum together with the flux at 100 MeV. The X-ray class given is determined from the flux in the wavelength band of 1-8 Å, which corresponds to a photon energy of 1.5 to 12.4 keV. The letters A, B, C, M, X denote the peak flux on a logarithmic scale and the number following gives the multiplicative factor. Therefore A5.1 means a solar flare with a soft X-ray flux of $5.1 \cdot 10^{-8} \text{ W m}^{-2}$ and X8.6 means a flare with a soft X-ray flux of $8.6 \cdot 10^{-4} \text{ W m}^{-2}$.

By plotting the X-ray class compared to the number of solar flare neutrons with kinetic energies higher than 100 MeV figure B.3 is obtained. The number of neutrons was corrected for angular dependencies in accordance to figure B.2. By assuming a linear correlation between these quantities and fitting the functions $f(x) = a \cdot x + b$ and $h(x) = c \cdot x$ to the data, f(x) is determined to $f(x) = 0.65 \cdot x + 27.79$ and h(x) is determined to $h(x) = 2.35 \cdot x$. The asymptotic standard error for c is ± 0.89 , ± 1.54 for a, and ± 21.06 for b. Just by eye one can see that the fit is rather poor and the correlation between X-ray flux and produced neutrons is weak. This is because the soft X-ray flux is basically caused by electron bremsstrahlung and by thermal emission of heated chromospheric plasma. The heating results from non-thermal electrons propagating through the chromosphere and loosing their energy (Neupert effect). It would have been better to use the neutron capture line at 2.2 MeV as tracer for neutron production because this radiation directly results from decelerated neutrons produced during the flare. Unfortunately no 2.2 MeV fluxes

B. Neutron detections with Solar Orbiter

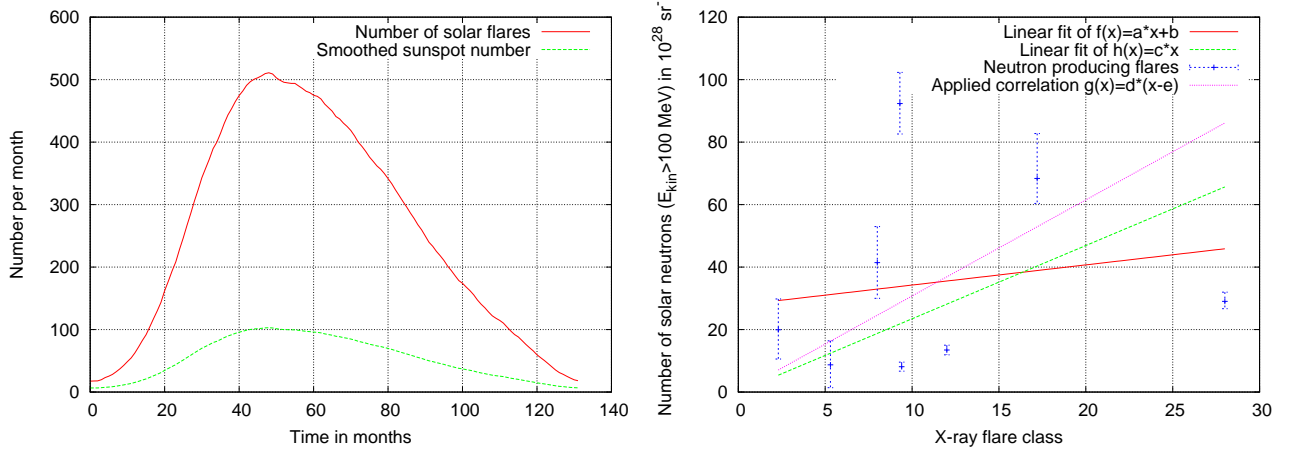


Figure B.3.: Shown are the numbers of solar flares with dependence on solar cycle and a plot of high energy neutrons ($E_{\text{kin}} > 100 \text{ MeV}$) compared with the X-ray flare class.

were available for most of the flare events listed in table B.2. Another aspect is that the flare statistics and temporal evolution with solar cycle is well known for soft X-ray solar flares. It was assumed that solar neutrons are only produced by flares with a soft X-ray flux of more than C1.0. The mean neutron number and the mean soft X-ray class for the flares from table B.2 was calculated and these two points were connected linearly (see figure B.3) leading to $g(x) = 3.08 \cdot (x - 0.01)$.

B.5. Number of solar flares

During the time from 1976 to 2000 a total number of 37851 solar flares with a soft X-ray flux larger than C1.0 were emitted from the sun and detected by the GOES (Geostationary Operational Environment Satellite) mission (See Veronig *et al.* [2002]). From these 37851 solar flares 32784 were of class C, 4708 of class M and 359 of class X. The number of C class flares might be underestimated because the sun's soft X-ray background can even reach M-level at solar maximum. To determine the number of flares in the soft X-ray sub-classes the frequency distribution for the solar flare fluence was used. Most frequency distributions can be described by a power-law of the form: $dN = Ax^{-\alpha}dx$, with x being the soft X-ray flux. Veronig *et al.* [2002] found $\alpha = 2.03 \pm 0.09$ for the fluence frequency distribution.

The second point is the temporal evolution of flare activity with solar cycle. We assume a variation of the monthly solar flare rate with a factor of 20 between solar minimum and solar maximum according to Aschwanden [2004]. Normally the flare rate shows large scattering within short timescales (up to a factor of ten). This scattering was neglected because it should cancel out over the 200 program runs made and does not affect the total number of flares. The total number of solar flares from 1976 to 2000 was compared with the total smoothed monthly sunspot number from the mean sunspot cycle shown in figure A.3. From this comparison the monthly number of solar flares was determined. A factor of two

results from the number of solar flares situated at the backside of the sun. The dependence of the number of solar flares from solar cycle is shown in figure B.3.

B.6. Modelling solar flare neutrons

Applying the solar flare rates determined in the previous section probabilities for flare occurrence with a time resolution of one hour were determined. Multiple flare occurrence within one hour was not taken into account. The time resolution for Solar Orbiter's orbit was one day. When a flare was taking place its longitude and latitude at solar surface was determined. These properties were determined from the longitude and latitude distribution of sunspots according to the chapter CME generation (see appendix A.2.1). If the flare occurs at the solar hemisphere looking toward Solar Orbiter the total number of emitted neutrons is determined. The spectrum from figure B.1 was scaled with the total number of neutrons. The cutoff energy in the neutron spectrum used was 2.8 GeV (there are no neutrons with energies exceeding 2.8 GeV). Using the angular dependencies from figure B.2 the spectrum in direction of Solar Orbiter was obtained. Taking into account neutron decay and the attenuation of neutron fluence with $\frac{1}{r^2}$ leads to the final differential neutron fluence at Solar Orbiter. 200 program runs with different random number seeds were performed. Each program run covers the time from Sep. 2015 to Dec. 2022.

B.7. Results for neutron detections with Solar Orbiter

On average Solar Orbiter will detect 8608 solar flares during the seven years of simulation. Altogether 1721688 solar flare detections were modelled during 200 program runs. The two different cases of pitch angle scattering $\Lambda = \infty$ and $\Lambda = 4.6 \cdot 10^{10}$ cm were treated separately. In figure B.4 the results of the simulation are shown. To compare the observations at Solar Orbiter the same results are shown for Earth's distance. In the first row of figures the time series for the first program run is shown. Time of flare observation is plotted versus the total neutron fluence at the position of Solar Orbiter. These figures were made using the neutron angular distribution without pitch-angle scattering. Clearly visible is the dependence of the number of detected neutrons from the orbit and from the solar activity cycle. The number of neutrons is enhanced by a factor of ~ 10 on average in comparison to Earth's distance.

The figures in the middle show histograms from all 200 program runs carried out. The frequency of occurrence for neutron producing flares of different strength is plotted. The fluence of neutrons at Solar Orbiter is compared with the fluence of neutrons at Earth's distance for the case of no pitch-angle scattering and nearly saturated pitch-angle scattering. Even though most neutron events are weak, the slope of decay is much stronger for the case of Earth's distance and the strongest neutron events at Solar Orbiter exceed the strongest events at Earth's distance by a factor of ≈ 100 .

The lower figures show some neutron spectra as seen at Solar Orbiter and at Earth's distance. The left one shows the average spectra for the case of no pitch-angle scattering and for nearly saturated pitch-

B. Neutron detections with Solar Orbiter

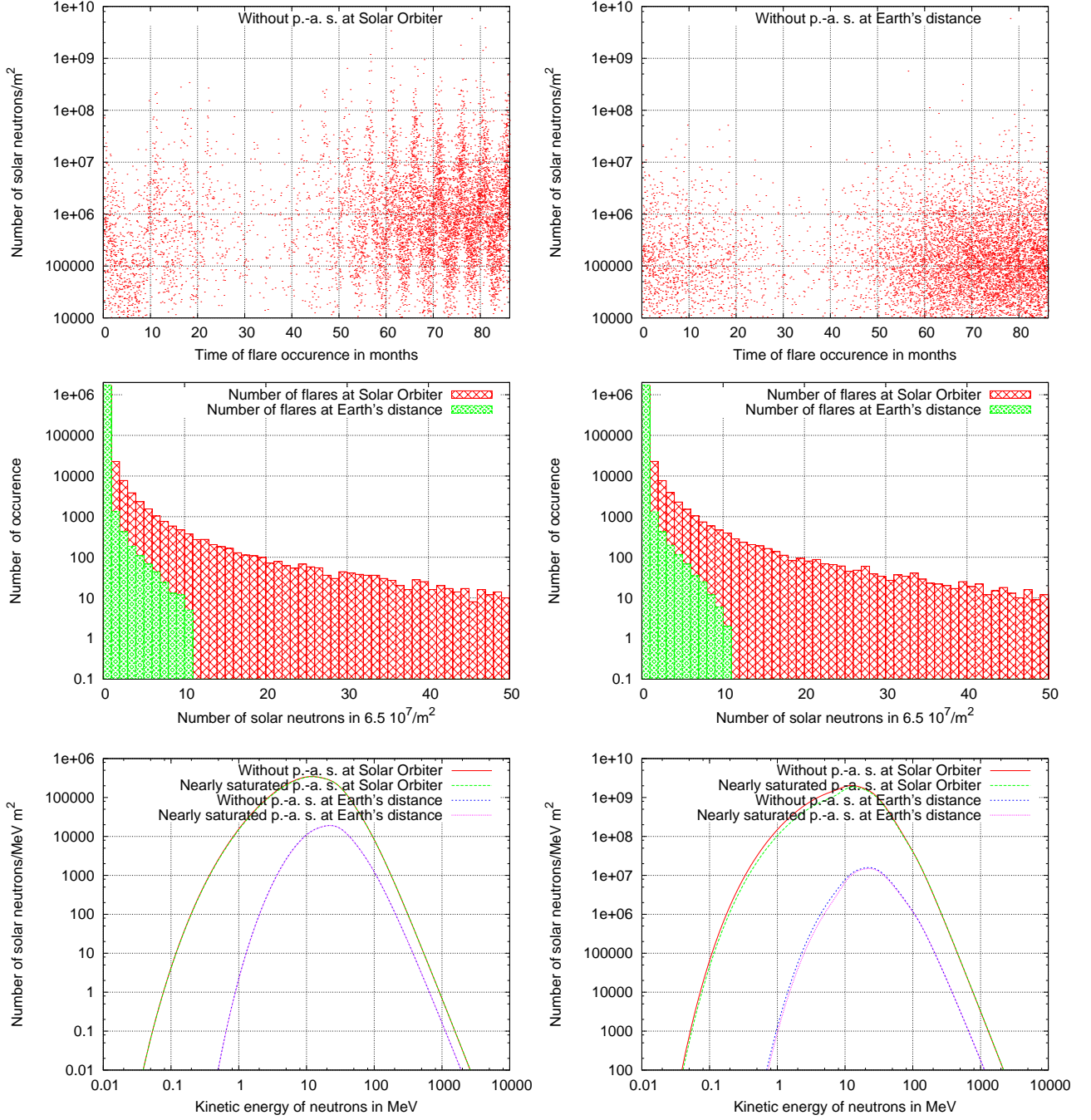


Figure B.4.: Top figures show the fluence of neutrons produced by solar flares during the first program run at Solar Orbiter and at Earth. Both figures are for the case of no pitch-angle scattering. The case of nearly saturated pitch-angle scattering looks very similar. The figures in the middle show histograms for 200 program runs. The left is without pitch-angle scattering, the right is with nearly saturated pitch-angle scattering. The left, lower figure shows the average spectra of all neutron producing flares at Solar Orbiter and at Earth. The right, lower figure shows the spectrum at Solar Orbiter and at Earth for the strongest neutron event generated during the 200 program runs (note the different scaling of the y-axes).

angle scattering. The average was determined from the spectra of all simulated neutron producing flares during the 200 program runs. As expected the intensity maximum in the spectrum is shifted towards lower energies in the case of Solar Orbiter and the fluence is higher in all energy ranges than for Earth's distance. At high neutron energies (> 200 MeV) the difference between the spectrum at Solar Orbiter and the spectrum at Earth's distance is just caused by the surface growth of the hemisphere ($\frac{1}{r^2}$). At lower neutron energies the neutron decay begins to play a role, leading to larger differences in the spectra. The right figure shows the spectrum for the strongest neutron event generated during the 200 program runs. The fluence at Solar Orbiter was $\approx 6.5 \cdot 10^{10}$ neutrons/m². Assuming a neutron production time of 30 min and a uniform neutron production the flux would be $\approx 3.6 \cdot 10^7$ neutrons/(m²s). From the comparison of the left and the right figure the ratio of the average number of produced neutrons to the maximum number of produced neutrons can be determined, leading to a ratio of ≈ 3000 .

B.8. Systematical error estimation

- **Latitude and longitude of flare generation**

According to *Shrivastava and Singh* [2005] solar flares associated with CMEs are located within a latitude interval of 0° - 30° with a maximum at 20° . The distribution is symmetric for the southern and northern hemisphere. Assuming that this latitude distribution is also true for flares not associated with a CME this is in good agreement with the applied latitude distribution from figure A.3. For the temporal evolution of solar flare generation latitude during solar cycle the same arguments as in the chapter about ICME detections should apply (see section A). An error of 20° in the angle can lead to an error of factor 2 in the total neutron number in worst case.

- **Number of flares generated**

The accuracy of the number of soft X- and M-class flares should be quite good because the sun's background radiation over the whole solar cycle is not exceeding this level. The number of C-class flares might be underestimated during the time of solar maximum. Taking the power-law index 2.11 of the peak flux frequency distribution found by *Veronig et al.* [2002] a number of 60000 C-class flares is expected from the number of the M-class flares and a number of 55000 C-class flares is expected from the number of X-class flares. This means that the number of C-class flares taking place at the sun might exceed the number of observed C-class flares by a factor of two.

- **Correlation between soft X-ray flare class and number of produced neutrons**

As seen in figure B.3 no linear correlation between soft X-ray flare class and the number of produced neutrons can be obtained by eye. Considering the error in the number of neutrons above 100 MeV resulting from the error in the spectral index and in the number of neutrons at 100 MeV the obtained reduced χ^2 is 17.1 for the case of two free parameters and 14.8 for the case of one free parameter. On the one hand this could mean that the data cannot be fitted by a linear function or on

B. Neutron detections with Solar Orbiter

the other hand that the errors are underestimated by a large amount. A reduced chi-square of one would be the result if the standard deviation in the data points were 32.6 for two free parameters or 34.3 for one free parameter. Assuming error bars as large as this, nearly every function could be fitted to the data. That a correlation between soft X-ray flux and number of emitted neutrons exists can be seen from observations. Up to now all neutron-producing solar flares detected by neutron monitors at Earth were of flare class X. With the measurements of the Solar Orbiter mission the correlation between different flare parameters will hopefully be better understood. Measurements of low energy neutrons (some MeV) will only be possible with the Solar Orbiter mission.

- **Influence of cutoff energy on the total neutron number**

Different values for the high-energy cutoff (there are no neutrons with energies exceeding the high-energy cutoff) will lead to different total neutron numbers because the number of high-energy neutrons varies though the same spectral index is applied. The lower the value for the spectral power-law index the stronger is the effect of different cutoff energies. Table B.3 shows the dependence of the total neutron number on these properties. The low energy part ($E_{\text{kin}} < 20$ MeV) of the spectrum remains the same. Since the neutrons with kinetic energies larger than 100 MeV are used to scale the whole spectrum (they are measured by the neutron monitors), different values in the spectral index have large influence on the total neutron number. Larger spectral indices lead to a larger ratio of the total neutron number to the high-energy neutron number (scaling the spectrum) and, therefore, to an enhanced total neutron number. According to table B.3 the effect of different cutoff energies on the total neutron number is negligible.

- **Influence of different spectral power-law indices**

As seen in table B.3 the total number of emitted neutrons is mainly determined by the spectral power-law index S . The total neutron number varies by a factor of ≈ 700 between a spectrum with a power-law index of 2 and a spectrum with a power-law index of 7, if one assumes the same number of high energy neutrons ($E_{\text{kin}} > 100$ MeV) in both cases.

- **Angular distribution of escaping neutrons**

The angular distribution of escaping neutrons is affected by the orientation and configuration of the magnetic field, the height of neutron production in the solar atmosphere and the strength of pitch-angle scattering. The influence of different cases of pitch-angle scattering on the height of neutron production is shown in *Hua et al.* [2002]. The dependence on different magnetic mirror ratios and different spectral indices for the primary particle spectra is presented in *Hua et al.* [1989] for the case of 4.438 MeV gamma ray line production. In general enlarged pitch-angle scattering and harder primary particle spectra lead to neutron production deeper in the solar atmosphere, while stronger magnetic mirroring leads to production higher in the solar atmosphere. The effect of asymmetric magnetic field strength for both legs of the loop (and therefore different magnetic

B.8. Systematical error estimation

Power-law index S	Cutoff energy in GeV									
	1	2	3	4	5	6	7	8	9	10
2	0.0369	0.0352	0.0347	0.0344	0.0343	0.0342	0.0341	0.0341	0.0340	0.0340
2.5	0.0672	0.0658	0.0654	0.0653	0.0652	0.0651	0.0651	0.0651	0.0651	0.065
3	0.131	0.130	0.129	0.129	0.129	0.129	0.129	0.129	0.129	0.129
3.5	0.258	0.257	0.257	0.257	0.257	0.257	0.257	0.257	0.257	0.257
4	0.510	0.509	0.509	0.509	0.509	0.509	0.509	0.509	0.509	0.509
4.5	1.00	1.00	1.00	1.00	1.00	1.00	1.00	1.00	1.00	1.00
5	1.95	1.95	1.95	1.95	1.95	1.95	1.95	1.95	1.95	1.95
5.5	3.78	3.78	3.78	3.78	3.78	3.78	3.78	3.78	3.78	3.78
6	7.28	7.28	7.28	7.28	7.28	7.28	7.28	7.28	7.28	7.28
6.5	13.9	13.9	13.9	13.9	13.9	13.9	13.9	13.9	13.9	13.9
7	26.6	26.6	26.6	26.6	26.6	26.6	26.6	26.6	26.6	26.6

Table B.3.: Ratio of the total solar neutron number resulting from spectra with different values for the cutoff energy and the spectral index S to the number of neutrons from a spectrum with power-law index $S = 4.5$ and a cutoff energy of 3 GeV.

mirroring) was not taken into account. The deeper in the solar atmosphere neutron production takes place the stronger is the change in the escaping neutron spectrum caused by neutron scattering leading to deceleration. Kocharov *et al.* [1997] investigated the effect of a tilted magnetic field on the anisotropy of escaping neutrons and suggest that large magnetic tilt angles will lead to a more isotropic emission.

- **Number of neutrons below 100 MeV**

The shape of the neutron spectra depends on the shape of the primary particle spectrum also at lower neutron energies (below 20 MeV). In Hua and Lingenfelter [1987] neutron spectra resulting from different primary ion spectra are shown. Harder primary particle spectra lead to a decreased number of low-energy neutrons. This adds to the behaviour shown in table B.3. Therefore, the neutron number in the low energy range ($E_{\text{kin}} < 20$ MeV) can deviate about a factor of 20 for different primary particle spectra.

C. MC modelling fit results

A total number of 67 MCs was fitted with the models described in section 4. For 14 of these MCs the sign of helicity was ambiguous. For the remaining 53 MCs the fit parameters are listed in tables C.1 to C.3. Table C.4 lists reference values from literature.

C.1. Force-free cylindrical model

θ is the angle of MC's z-axis out of the ecliptic plane (positive value \Rightarrow northern hemisphere), φ is the angle between the GSE x-axis and the MC's z-axis projected onto the ecliptic plane counted counter-clockwise. H is the sign of helicity and χ^2 was calculated according to equation 4.48. B_0 is the magnetic field strength at the centre of the MC. Angles are given in degrees, distances in AU, magnetic field strength in nT, and proton speed in km/s.

Table C.1.: Fit results from force-free cylindrical model (described in section 4.2.1)

Year	Start DoY	End DoY	Proton speed	θ	φ	D_0	Radius	B_0	H	χ^2
2001	78.80	80.67	378	-66	320	0.0	0.193	19.2	1	0.052
2001	91.32	91.82	747	62	64	-0.099	0.144	10.3	1	0.023
2001	94.80	95.31	687	28	113	0.095	0.133	16.5	1	0.042
2001	102.19	102.72	638	7	171	0.026	0.032	26.1	-1	0.010
2001	112.00	113.03	358	-58	121	-0.013	0.104	14.7	1	0.022
2001	119.02	119.57	626	7	294	-0.034	0.096	12.2	1	0.012
2001	127.77	128.35	361	8	230	-0.084	0.102	13.9	-1	0.025
2001	129.50	130.88	431	8	187	0.030	0.044	11.7	1	0.027
2001	148.48	149.4	452	-9	208	-0.039	0.071	13.4	1	0.029
2001	170.00	170.57	420	-8	24	0.091	0.095	29.1	-1	0.022
2001	190.08	190.56	443	39	80	-0.050	0.079	6.8	-1	0.056
2001	191.71	192.79	352	-23	100	0.069	0.128	10.3	-1	0.059
2001	304.87	306.37	335	1	252	0.0	0.137	13.0	1	0.052
2001	328.68	329.69	706	30	6	0.227	0.249	27.3	1	0.094
2002	78.95	79.54	374	12	325	-0.073	0.084	25.3	-1	0.004
2002	83.50	84.82	434	8	171	0.030	0.046	23.9	-1	0.034
2002	108.14	109.21	470	-6	161	0.058	0.076	19.8	-1	0.013

Table is continued on next page

C.1. Force-free cylindrical model

Year	Start DoY	End DoY	Proton speed	θ	φ	D_0	Radius	B_0	H	χ^2
2002	110.65	111.65	474	0	3	0.005	0.009	10.0	-1	0.034
2002	214.27	214.83	488	-14	135	-0.074	0.094	20.1	1	0.010
2002	246.00	246.70	350	23	16	-0.024	0.040	16.4	-1	0.057
2002	274.02	274.58	392	1	340	-0.013	0.025	30.8	-1	0.021
2003	27.07	27.65	517	-31	182	0.078	0.091	18.5	1	0.009
2003	79.53	79.94	650	-84	274	-0.074	0.106	17.1	1	0.013
2003	168.75	169.34	474	-11	27	0.038	0.055	19.3	1	0.024
2003	191.66	192.34	356	-17	212	0.039	0.056	14.3	-1	0.056
2003	217.41	218.00	430	14	71	0.058	0.090	14.8	1	0.020
2003	230.56	231.21	436	9	188	0.022	0.027	29.7	1	0.049
2003	302.46	303.07	1250	-40	18	-0.030	0.150	43.5	1	0.064
2003	304.07	304.5	1108	58	26	0.068	0.136	25.5	1	0.023
2003	324.44	325.10	580	-73	81	-0.005	0.109	41.9	-1	0.103
2004	95.08	96.66	424	81	97	0.088	0.212	21.3	1	0.068
2004	122.6	123.50	403	-37	210	0.088	0.113	14.2	1	0.052
2004	204.61	204.95	571	-21	231	0.023	0.049	22.7	-1	0.113
2004	206.54	207.51	555	-37	251	0.061	0.161	26.2	-1	0.023
2004	209.09	209.56	918	-10	328	-0.035	0.076	32.2	-1	0.030
2004	242.80	243.85	391	-19	287	-0.084	0.141	17.8	-1	0.018
2004	313.10	313.69	675	0	228	-0.020	0.087	24.0	1	0.011
2004	314.87	315.16	792	12	116	-0.023	0.063	45.1	1	0.034
2004	315.16	315.50	710	-39	213	-0.037	0.064	32.7	1	0.012
2005	135.24	136.17	826	61	16	-0.138	0.239	49.0	1	0.036
2005	140.31	141.22	452	58	84	0.021	0.119	14.9	1	0.122
2005	163.70	164.50	469	-8	353	0.030	0.036	23.2	1	0.015
2005	166.25	167.29	477	23	226	-0.030	0.113	10.6	1	0.125
2005	198.60	199.14	426	-23	243	-0.007	0.060	14.4	-1	0.031
2005	304.10	304.75	376	-1	352	-0.003	0.011	13.5	-1	0.039
2006	36.88	37.45	336	-11	343	-0.022	0.029	16.8	-1	0.028
2006	103.6	103.87	524	81	274	-0.007	0.040	19.7	1	0.042
2006	103.87	104.45	514	-12	50	0.051	0.083	24.9	1	0.016
2006	145.15	145.64	327	1	61	0.065	0.076	6.5	-1	0.060
2006	242.86	243.58	411	-2	39	0.034	0.063	10.8	1	0.024
2006	273.36	273.88	390	11	88	-0.005	0.058	19.3	1	0.165
2006	333.23	334.38	419	24	240	-0.017	0.124	14.8	-1	0.065
2007	14.59	15.29	360	6	66	0.071	0.097	19.5	1	0.031

C. MC modelling fit results

C.2. Non force-free cylindrical model

The parameters shown are the same as in the previous section. B_0 was calculated from parameter α .

Table C.2.: Fit results from non force-free cylindrical model (see section 4.2.2)

Year	Start DoY	End DoY	Proton speed	θ	φ	D_0	Radius	B_0	H	χ^2
2001	78.80	80.67	378	-66	304	-0.021	0.199	23.4	1	0.087
2001	91.32	91.82	747	60	98	-0.123	0.162		1	0.017
2001	94.80	95.31	687	30	84	0.128	0.161		1	0.037
2001	102.19	102.72	638	15	159	0.057	0.070	26.1	-1	0.010
2001	112.00	113.03	358	-62	93	-0.012	0.106	13.6	1	0.022
2001	119.02	119.57	626	5	310	-0.019	0.077	11.7	1	0.018
2001	127.77	128.35	361	5	215	-0.071	0.079		-1	0.030
2001	129.50	130.88	431	9	189	0.040	0.054		1	0.027
2001	148.48	149.4	452	-12	220	-0.047	0.092	12.5	1	0.031
2001	170.00	170.57	420	-7	21	0.071	0.075		-1	0.022
2001	190.08	190.56	443	36	152	-0.042	0.070		-1	0.060
2001	191.71	192.79	352	-24	35	0.072	0.130		-1	0.062
2001	304.87	306.37	335	3	250	0.009	0.136	14.6	1	0.068
2001	328.68	329.69	706	39	8	0.285	0.313		1	0.094
2002	78.95	79.54	374	16	311	-0.102	0.113		-1	0.011
2002	83.50	84.82	434	20	157	0.064	0.105		-1	0.033
2002	108.14	109.21	470	-9	151	0.084	0.110		-1	0.016
2002	110.65	111.65	474	3	21	0.071	0.087		-1	0.020
2002	214.27	214.83	488	-17	123	-0.081	0.105		1	0.016
2002	246.00	246.70	350	22	16	-0.023	0.039		-1	0.057
2002	274.02	274.58	392	1	326	-0.017	0.039	38.1	-1	0.025
2003	27.07	27.65	517	-13	181	0.036	0.041		1	0.017
2003	79.53	79.94	650	-83	310	-0.078	0.108		1	0.012
2003	168.75	169.34	474	-3	6	0.011	0.015		1	0.026
2003	191.66	192.34	356	-14	209	0.037	0.052		-1	0.057
2003	217.41	218.00	430	12	62	0.055	0.084		1	0.020
2003	230.56	231.21	436	2	182	0.005	0.006		1	0.050
2003	302.46	303.07	1250	-31	11	-0.027	0.121	47.4	1	0.077
2003	304.07	304.5	1108	39	11	0.061	0.107		1	0.023
2003	324.44	325.10	580	-79	59	-0.007	0.108	39.9	-1	0.116
2004	95.08	96.66	424	76	128	0.071	0.203	19.8	1	0.069
2004	122.6	123.50	403	-31	206	0.089	0.108		1	0.049
2004	204.61	204.95	571	-19	242	0.022	0.053	22.3	-1	0.130
Table is continued on next page										

C.3. Force-free elliptical model

Year	Start DoY	End DoY	Proton speed	θ	φ	D_0	Radius	B_0	H	χ^2
2004	206.54	207.51	555	-36	251	0.063	0.162	22.1	-1	0.025
2004	209.09	209.56	918	-14	315	-0.032	0.096	28.8	-1	0.027
2004	242.80	243.85	391	-20	275	-0.075	0.139		-1	0.021
2004	313.10	313.69	675	0	209	-0.003	0.022	13.8	1	0.029
2004	314.87	315.16	792	11	120	-0.025	0.062	37.4	1	0.035
2004	315.16	315.50	710	-35	209	-0.035	0.059		1	0.013
2005	135.24	136.17	826	65	7	-0.141	0.244		1	0.038
2005	140.31	141.22	452	57	88	0.021	0.119	16.6	1	0.144
2005	163.70	164.50	469	-13	348	0.051	0.061		1	0.018
2005	166.25	167.29	477	22	226	-0.023	0.111	8.5	1	0.123
2005	198.60	199.14	426	-20	239	-0.005	0.058	14.1	-1	0.039
2005	304.10	304.75	376	-2	341	-0.005	0.023	16.5	-1	0.052
2006	36.88	37.45	336	-16	333	-0.035	0.045		-1	0.032
2006	103.6	103.87	524	80	279	-0.006	0.040	18.1	1	0.041
2006	103.87	104.45	514	-19	73	0.042	0.092	23.4	1	0.023
2006	145.15	145.64	327	3	42	0.064	0.071		-1	0.050
2006	242.86	243.58	411	-4	58	0.035	0.079	10.1	1	0.024
2006	273.36	273.88	390	7	70	0.011	0.055	17.8	1	0.170
2006	333.23	334.38	419	21	238	-0.015	0.120	14.8	-1	0.090
2007	14.59	15.29	360	7	82	0.080	0.107		1	0.034

C.3. Force-free elliptical model

The parameters listed are as in the first section. t_0 is the constant of MC expansion (unit is seconds). In this model the MC radius is replaced by the length of the minor and major semi-axis.

Table C.3.: Fit results from force-free elliptical model (described in section 4.2.3).

Year	Start DoY	End DoY	Proton speed	θ	φ	D_0	Min. Axis	Maj. Axis	$\log t_0$	χ^2
2001	78.80	80.67	378	-82	10	-0.527	0.150	1.29	5.30	0.026
2001	91.32	91.82	747	73	71	-0.121	0.136	0.153	5.21	0.015
2001	94.80	95.31	687	31	99	0.139	0.136	0.212	9.77	0.041
2001	102.19	102.72	638	7	165	0.024	0.029	0.035	5.08	0.013
2001	112.00	113.03	358	-47	76	0.000	0.079	0.114	5.36	0.018
2001	119.02	119.57	626	1	299	-0.028	0.078	0.088	5.31	0.012
2001	127.77	128.35	361	-7	230	-0.074	0.080	0.081	5.33	0.016
2001	129.50	130.88	431	13	190	0.097	0.075	0.121	6.13	0.026
2001	148.48	149.4	452	-11	211	-0.067	0.080	0.114	10.28	0.026

Table is continued on next page

C. MC modelling fit results

Year	Start DoY	End DoY	Proton speed	θ	φ	D_0	Min. Axis	Maj. Axis	$\log t_0$	χ^2
2001	170.00	170.57	420	1	0	-0.049	0.041	0.098	4.89	0.010
2001	190.08	190.56	443	22	90	-0.042	0.053	0.061	4.80	0.055
2001	191.71	192.79	352	-24	114	0.093	0.098	0.159	5.76	0.048
2001	304.87	306.37	335	-10	235	0.000	0.101	0.310	5.66	0.047
2001	328.68	329.69	706	40	311	0.243	0.251	0.251	4.98	0.082
2002	78.95	79.54	374	15	326	-0.077	0.081	0.086	6.61	0.004
2002	83.50	84.82	434	1	178	0.004	0.003	0.006	6.03	0.034
2002	108.14	109.21	470	-8	166	0.071	0.064	0.084	5.99	0.013
2002	110.65	111.65	474	10	22	0.077	0.079	0.086	5.41	0.018
2002	214.27	214.83	488	-11	133	-0.079	0.092	0.097	7.21	0.010
2002	246.00	246.70	350	45	148	0.057	0.061	0.104	7.17	0.069
2002	274.02	274.58	392	2	340	-0.013	0.024	0.034	5.50	0.021
2003	27.07	27.65	517	-33	182	0.086	0.097	0.098	8.56	0.010
2003	79.53	79.94	650	-84	173	-0.085	0.107	0.109	5.71	0.016
2003	168.75	169.34	474	-7	19	0.075	0.043	0.096	5.74	0.020
2003	191.66	192.34	356	-6	344	-0.041	0.026	0.054	5.30	0.070
2003	217.41	218.00	430	16	70	0.068	0.089	0.099	6.16	0.022
2003	230.56	231.21	436	9	188	0.024	0.028	0.029	10.01	0.051
2003	302.46	303.07	1250	-53	18	-0.071	0.134	0.239	5.52	0.031
2003	304.07	304.5	1108	50	179	0.094	0.109	0.133	5.05	0.026
2003	324.44	325.10	580	-70	306	-0.010	0.069	0.077	4.77	0.130
2004	95.08	96.66	424	51	156	-0.001	0.094	0.261	6.98	0.033
2004	122.6	123.50	403	-35	209	0.068	0.089	0.104	9.11	0.053
2004	204.61	204.95	571	-25	286	0.000	0.035	0.197	5.12	0.077
2004	206.54	207.51	555	-34	258	0.072	0.155	0.205	6.26	0.021
2004	209.09	209.56	918	6	354	-0.053	0.021	0.082	4.92	0.023
2004	242.80	243.85	391	-19	291	-0.094	0.139	0.146	6.38	0.018
2004	313.10	313.69	675	-15	197	-0.036	0.030	0.058	4.80	0.019
2004	314.87	315.16	792	17	131	-0.061	0.056	0.098	5.10	0.032
2004	315.16	315.50	710	-29	239	0.000	0.035	0.065	5.23	0.016
2005	135.24	136.17	826	45	329	-0.055	0.107	0.122	4.84	0.072
2005	140.31	141.22	452	54	112	0.000	0.073	0.256	8.74	0.077
2005	163.70	164.50	469	-16	6	0.063	0.037	0.070	4.85	0.012
2005	166.25	167.29	477	23	271	0.047	0.080	0.310	5.19	0.074
2005	198.60	199.14	426	-13	257	0.000	0.051	0.087	5.20	0.027
2005	304.10	304.75	376	2	313	0.000	0.040	0.182	5.30	0.044
2006	36.88	37.45	336	25	320	-0.094	0.037	0.102	4.60	0.016
2006	103.6	103.87	524	83	238	-0.011	0.035	0.063	10.79	0.020

Table is continued on next page

C.4. Literature values from different models

Year	Start DoY	End DoY	Proton speed	θ	φ	D_0	Min. Axis	Maj. Axis	$\log t_0$	χ^2
2006	103.87	104.45	514	-7	55	0.050	0.075	0.077	5.26	0.016
2006	145.15	145.64	327	4	58	0.035	0.040	0.059	5.61	0.059
2006	242.86	243.58	411	-2	31	0.054	0.045	0.084	5.44	0.021
2006	273.36	273.88	390	17	105	-0.007	0.024	0.114	4.82	0.054
2006	333.23	334.38	419	27	235	-0.009	0.090	0.131	5.56	0.043
2007	14.59	15.29	360	11	66	0.053	0.050	0.102	5.21	0.020

C.4. Literature values from different models

Parameter are as in the first section.

Table C.4.: Published fit results determined from cylindrical and elliptical models.

Year	Start DoY	End DoY	θ	φ	D_0	Radius	B_0	H	Reference
2001	78.79	80.71	-63.5	319.0	0.002	0.183	19.2	1	Lynch et al. [2003]
2001	78.98	80.17	-64.0	337.0	0.001	0.125	19.4	1	Feng et al. [2007]
2001	94.88	95.33	11.0	314.0	0.039	-	-	1	Nieves-Chinchilla et al. [2005]
2001	94.75	95.35	28.0	257.0	0.170	0.205	17.5	1	Feng et al. [2007]
2001	94.88	95.35	8.0	281.0	-0.164	0.191	17.8	1	MFI
2001	102.17	102.79	49.0	103.0	0.000	0.106	17.8	-1	Lynch et al. [2003]
2001	101.96	102.67	-6.0	166.0	0.024	-	-	-1	Nieves-Chinchilla et al. [2005]
2001	102.31	102.75	23.0	335.0	0.053	0.068	21.8	-1	Feng et al. [2007]
2001	102.33	102.75	31.0	205.0	0.085	0.125	20.9	-1	MFI
2001	112.00	113.13	-47.2	141.1	0.047	0.105	14.9	1	Lynch et al. [2003]
2001	112.08	113.00	-1.0	359.0	0.015	-	-	1	Nieves-Chinchilla et al. [2005]
2001	112.01	113.05	-54.0	274.0	0.001	0.108	14.0	1	Feng et al. [2007]
2001	112.04	113.06	-78.0	293.0	0.007	0.133	13.9	1	MFI
2001	119.00	119.58	1.2	322.5	0.001	0.059	11.1	1	Lynch et al. [2003]
2001	119.08	119.63	-16.0	211.0	0.272	-	-	1	Nieves-Chinchilla et al. [2005]
2001	119.05	119.63	28.0	93.0	0.082	0.132	11.1	1	Feng et al. [2007]
2001	119.08	119.54	31.0	119.0	0.045	0.116	11.6	1	MFI
2001	127.75	128.38	0.0	170.0	0.011	0.015	12.3	1	Lynch et al. [2003]
2001	129.50	130.83	-28.4	138.0	0.000	0.121	9.1	-1	Lynch et al. [2003]
2001	148.46	149.42	-19.1	218.3	0.032	0.086	12.2	1	Lynch et al. [2003]
2001	148.50	149.29	-14.0	154.0	0.184	-	-	1	Nieves-Chinchilla et al. [2005]
2001	148.49	149.43	-15.0	131.0	0.035	0.102	12.3	1	Feng et al. [2007]
2001	148.50	149.44	-12.0	49.0	0.047	0.126	11.7	1	MFI
2001	170.03	170.60	-10.0	326.0	0.108	0.115	28.5	-1	Feng et al. [2007]

Table is continued on next page

C. MC modelling fit results

Year	Start DoY	End DoY	θ	φ	D_0	Radius	B_0	H	Reference
2001	190.08	190.67	57.5	96.7	0.056	0.089	6.3	-1	Lynch <i>et al.</i> [2003]
2001	191.42	192.42	-15.7	49.9	0.033	0.093	8.6	-1	Lynch <i>et al.</i> [2003]
2001	191.71	192.79	1.0	182.0	0.011	-	-	1	Nieves-Chinchilla <i>et al.</i> [2005]
2001	192.04	192.97	14.0	266.0	0.055	0.087	10.4	-1	Feng <i>et al.</i> [2007]
2001	191.72	193.37	9.0	251.0	-0.065	0.127	11.3	-1	MFI
2001	304.96	306.08	-3.0	5.0	0.011	-	-	1	Nieves-Chinchilla <i>et al.</i> [2005]
2001	304.89	306.43	-3.0	78.0	-0.013	0.141	13.1	1	MFI
2001	328.75	329.54	11.0	179.0	0.262	-	-	1	Nieves-Chinchilla <i>et al.</i> [2005]
2001	328.66	329.55	31.0	103.0	-0.225	0.281	27.5	1	MFI
2002	78.96	79.54	2.0	178.0	0.095	-	-	1	Nieves-Chinchilla <i>et al.</i> [2005]
2002	78.96	79.65	20.0	45.0	-0.019	0.104	16.0	-1	MFI
2002	83.16	84.95	35.0	288.0	0.017	0.216	17.6	-1	MFI
2002	108.18	109.09	-27.0	318.0	-0.084	0.159	16.2	-1	MFI
2002	110.58	111.58	1.0	313.0	0.001	-	-	-1	Nieves-Chinchilla <i>et al.</i> [2005]
2002	110.49	111.70	24.0	156.0	0.064	0.145	8.8	1	MFI
2002	214.33	214.92	5.0	160.0	0.106	-	-	1	Nieves-Chinchilla <i>et al.</i> [2005]
2002	214.31	214.88	-9.0	245.0	0.014	0.127	13.0	1	MFI
2002	246.01	246.78	39.0	207.0	0.026	0.073	14.4	-1	MFI
2002	273.94	274.50	-16.0	110.0	-0.007	0.067	27.7	-1	MFI
2003	79.54	79.92	-30.0	353.0	0.129	-	-	-1	Nieves-Chinchilla <i>et al.</i> [2005]
2003	79.50	79.94	-81.0	238.0	0.069	0.105	16.7	1	MFI
2003	168.74	169.34	-52.0	264.0	-0.022	0.130	15.1	1	MFI
2003	191.83	192.38	-45.0	30.0	-0.052	0.097	13.9	-1	MFI
2003	230.48	231.19	-49.0	301.0	-0.017	0.144	16.3	-1	MFI
2003	302.46	302.96	55.0	125.0	0.586	-	-	1	Nieves-Chinchilla <i>et al.</i> [2005]
2003	304.08	304.50	-48.0	140.0	0.053	-	-	1	Nieves-Chinchilla <i>et al.</i> [2005]
2003	324.45	325.09	-76.0	217.0	0.003	0.090	38.3	-1	MFI
2004	95.12	96.62	69.0	76.0	-0.095	0.197	22.6	1	MFI
2004	204.65	204.96	-26.0	67.0	-0.009	0.049	20.3	-1	MFI
2004	206.53	207.55	-21.0	86.0	-0.053	0.178	25.4	-1	MFI
2004	242.78	243.87	-8.0	54.0	0.007	0.120	13.4	-1	MFI
2004	313.15	313.69	-5.0	47.0	0.023	0.087	22.6	1	MFI
2004	314.88	315.15	35.0	290.0	0.027	0.072	45.1	1	MFI
2004	315.15	315.46	-59.0	37.0	0.031	0.075	30.0	1	MFI
2005	135.24	135.93	67.0	94.0	0.146	0.195	70.6	1	MFI
2005	140.30	141.22	59.0	221.0	-0.031	0.090	17.9	1	MFI
2005	163.65	164.29	-44.0	128.0	-0.037	0.131	15.9	1	MFI
2005	166.24	167.32	49.0	14.0	0.038	0.116	12.8	1	MFI

Table is continued on next page

C.4. Literature values from different models

Year	Start DoY	End DoY	θ	φ	D₀	Radius	B₀	H	Reference
2005	198.64	199.16	-41.0	79.0	0.033	0.074	14.6	-1	MFI
2005	304.13	304.85	-16.0	136.0	-0.007	0.053	12.9	-1	MFI
2006	36.79	37.54	-50.0	106.0	0.001	0.067	11.8	-1	MFI
2006	103.62	103.87	77.0	244.0	0.000	0.048	20.5	1	MFI
2006	103.86	104.42	-13.0	262.0	-0.026	0.113	20.1	1	MFI
2006	242.88	243.63	-8.0	223.0	-0.034	0.067	10.9	1	MFI
2006	273.36	273.90	-16.0	252.0	-0.017	0.049	21.8	1	MFI

D. List of MC and solar wind interval plasma properties

In this section elemental composition, plasma parameter, and mean charge states are tabulated for all MCs and the solar wind reference intervals. The solar wind intervals are divided in slow and fast wind intervals and the MCs are divided in MCs with and without flare association. All tabulated in-situ values (except Vexp) are averages calculated from 1h data.

- Start and stop times are given in DoY.
- Vsw is the SWEPAM in-situ measured proton speed in km/s.
- Vexp is the expansion speed between trailing and leading edge calculated from a 3h Vsw average in km/s.
- Dens is the SWEPAM in-situ determined proton density in cm⁻³.
- T_p is the SWEPAM in-situ measured proton temperature in K.
- B is the MAG in-situ determined magnetic field strength in nT.
- dB/B is the 1h variation of B calculated according to equation 3.3 from 16 s data in nT.
- The elemental abundances of Fe, O, He, Ne, Mg, C, N, Si, and S are given in 10⁻⁶ cm⁻³.
- Var Q_Fe and Var Q_O is the standard deviation of the mean charge state calculated from the whole MC or solar wind interval.
- |dStr| is calculated from the absolute values of $\frac{v_{\text{He}^{2+}} - v_p}{v_A}$.
- FlSt is the GOES 1-8 Å X-ray peak flux of the associated flare in 10⁻⁴ Watt/m².
- A AR is the age of the AR at the time of the CME release in days.
- V_CME is the LASCO plane of sky velocity of the associated CME in km/s.
- Pos1 is the latitudinal position of the associated flare in degrees (90 north pole, -90 south pole).
- Pos2 is the longitudinal position of the associated flare in degrees (90 western limb, -90 eastern limb).

D.1. MCs with flare association

D.1. MCs with flare association

#	Start	Stop	Year	Vsw	Vexp	Dens	T_p	B	dB/B	Fe	O	He	Ne	Mg
1	78.8	80.67	2001	378.1	161.7	7.32	10766.9	15.7	0.013	213.381	865.211	92416.8	294.548	319.713
2	86.86	87.27	2001	609.4	-12.7	8.04	120784.	13.7	0.052	526.778	1738.47	382106.	426.896	496.021
3	91.32	91.82	2001	745.4	147.4	1.18	77874.1	6.69	0.024	97.2650	259.747	124134.	103.396	67.4971
4	94.8	95.31	2001	685.4	75.34	2.83	485196.	10.7	0.061	15.3805	199.240	58742.2	81.4640	52.8176
5	102.19	102.72	2001	637.9	26.6	2.69	93984.9	15.5	0.039	40.3469	162.658	46567.2	67.6816	55.0822
6	119.02	119.57	2001	625.7	99.66	4.97	21397.2	9.43	0.026	125.264	149.347	27687.4	77.2129	119.686
7	127.77	128.35	2001	361.0	11.29	4.62	25499.6	7.87	0.026	55.2118	298.982	69168.7	118.473	86.7589
8	129.5	130.88	2001	430.9	38.02	5.83	17637.7	7.64	0.015	123.210	317.396	46826.4	183.767	159.983
9	148.48	149.4	2001	451.4	80.41	3.62	12020.1	9.42	0.018	85.8230	138.823	19539.7	81.1364	84.3423
10	190.08	190.56	2001	443.4	45.04	8.41	27614.5	4.71	0.052	115.038	716.218	32031.5	237.031	173.181
11	272.62	273.43	2001	579.5	149.9	6.54	155116.	12.4	0.023	320.468	1056.30	204767.	311.503	339.179
12	328.68	329.69	2001	712.3	244.8	2.30	57470.8	15.2	0.032	132.856	339.552	67584.1	139.850	153.618
13	78.95	79.54	2002	372.5	-41.1	0.85	54041.3	14.1	0.011	22.7930	99.6935	38233.8	43.9542	40.4764
14	83.5	84.82	2002	434.3	22.28	6.81	27851.8	15.6	0.018	183.229	704.552	119459.	234.338	304.482
15	108.14	109.21	2002	470.4	75.69	1.91	16164.3	12.2	0.021	49.3079	86.6320	32385.1	57.8274	48.8215
16	213.67	213.91	2002	441.7	13.48	11.7	22758.1	10.8	0.028	472.180	1084.67	50085.4	486.584	748.679
17	355.37	356.29	2002	421.0	84.61	7.50	19983.8	8.16	0.017	106.205	915.055	107530.	311.672	205.418
18	27.07	27.65	2003	516.3	92.79	2.09	31506.7	10.5	0.012	183.252	419.603	60729.6	158.820	132.512
19	191.66	192.34	2003	356.6	-13.5	12.8	21480.2	9.30	0.042	526.355	1067.29	120326.	557.489	535.763
20	217.41	218.0	2003	429.4	5.428	11.2	24012.9	9.96	0.030	286.957	955.428	72881.7	521.870	325.979
21	230.56	231.21	2003	435.5	10.59	3.89	30811.2	17.8	0.014	221.776	556.497	100943.	236.985	227.642
22	302.46	303.07	2003	1316.	461.2	1.55	471642.	34.8	0.039	107.937	342.198	81291.0	175.715	147.880
23	304.07	304.5	2003	1107.	189.0	1.88	174653.	19.2	0.068	222.774	210.838	14297.8	208.647	203.155
24	324.44	325.1	2003	580.3	166.6	13.6	100811.	35.1	0.057	606.019	2168.19	207432.	524.339	462.105
25	95.08	96.66	2004	424.1	121.8	8.42	18537.4	16.0	0.012	195.487	272.350	44107.6	218.218	206.596
26	122.66	123.5	2004	402.4	33.49	8.55	36639.4	8.63	0.023	88.1545	229.731	44198.3	155.152	126.032
27	204.61	204.95	2004	574.3	-186.	4.21	210334.	16.7	0.037	47.5796	312.102	57653.2	159.851	112.358
28	206.54	207.51	2004	555.0	0.946	3.23	137127.	20.3	0.015	23.9099	117.456	43890.6	109.741	43.1907
29	209.09	209.56	2004	917.2	165.9	2.59	108976.	23.9	0.022	384.250	1732.87	97959.0	462.063	409.572
30	313.1	313.69	2004	676.3	27.26	3.19	37254.0	20.4	0.037	47.6100	108.529	30141.9	74.8003	54.6719
31	314.87	315.16	2004	791.8	30.26	11.1	83459.5	35.6	0.022	287.215	501.665	92492.4	287.617	253.268
32	315.16	315.5	2004	708.6	81.73	5.36	22752.2	23.0	0.023	92.2494	389.461	36360.1	178.593	152.790
33	19.04	20.09	2005	802.6	267.4	1.70	40914.2	11.6	0.023	44.2647	127.176	24241.9	78.5090	68.2479
34	135.24	136.17	2005	827.2	195.1	3.45	81927.2	34.2	0.022	137.363	202.646	64454.9	92.9991	124.581
35	140.31	141.22	2005	451.6	58.48	6.42	25634.8	12.0	0.028	180.825	624.645	86774.0	211.808	222.774
36	163.7	164.5	2005	468.5	32.36	5.21	23631.0	13.5	0.022	276.604	1157.16	140200.	466.872	384.320
37	166.25	167.29	2005	477.6	40.42	5.22	41375.7	8.80	0.029	107.835	710.011	71251.3	256.671	186.479
38	348.98	349.58	2006	732.6	210.9	2.15	68629.8	12.4	0.033	58.0176	196.966	71595.7	82.2402	72.3541
#	C	N	Si	S	Q_Fe	Var_Q_Fe	Q_O	Var_Q_O	dStr	F1St	AAR	V_CME	Pos1	Pos2
1	410.170	356.167	196.961	129.115	12.3	0.78	6.59	0.17	0.040	nan	nan	nan	nan	nan
2	1289.21	830.781	345.860	204.721	12.3	0.40	6.70	0.19	0.026	nan	nan	nan	nan	nan
3	281.453	183.838	35.2850	19.8304	12.5	2.03	7.36	0.28	0.076	1.5	20.3	942.	20.	19.
4	226.526	153.511	29.2677	12.4423	12.6	1.43	6.49	0.32	0.071	20.	23.8	2505.	16.	67.
5	101.205	79.0145	32.5154	23.9450	14.3	1.06	6.63	0.15	0.023	2.2	14.2	2411.	-23.	9.
6	44.8426	58.3208	83.9234	58.3349	16.0	0.93	6.69	0.05	0.100	0.7	48.	1006.	17.	31.
7	251.292	135.272	49.2913	36.5317	11.6	0.73	6.41	0.06	0.073	nan	nan	nan	nan	nan
8	178.277	146.947	95.7365	91.4414	14.1	1.00	6.45	0.11	0.111	nan	nan	nan	nan	nan
9	56.8681	70.0649	53.7505	53.8844	13.6	1.50	6.58	0.10	0.019	nan	nan	nan	nan	nan
10	187.747	257.731	96.7925	70.5163	12.1	0.59	6.38	0.06	0.101	nan	nan	nan	nan	nan
11	902.258	518.701	243.684	173.288	10.2	0.95	6.38	0.21	0.144	0.03	62.6	509.	-20.	27.
12	191.774	156.457	98.5198	63.1035	12.1	1.21	6.69	0.24	0.049	1.0	18.7	1437.	-17.	24.
13	100.569	80.0806	26.9347	19.7053	13.9	1.43	6.82	0.24	0.008	0.25	28.	957.	-8.	3.
14	394.298	371.854	154.097	100.778	13.4	1.21	6.70	0.21	0.027	0.035	32.5	603.	-8.	68.
15	61.9970	47.3355	27.8833	22.6711	13.5	1.45	6.87	0.27	0.029	0.1	10.1	720.	-15.	1.
16	312.551	461.076	367.098	237.961	14.0	1.05	6.59	0.05	0.073	nan	nan	nan	nan	nan
17	390.653	364.677	114.405	78.4731	13.4	0.42	6.24	0.11	0.057	nan	nan	nan	nan	nan
18	239.030	214.700	80.0333	57.8700	11.4	0.36	6.64	0.07	0.022	nan	nan	nan	nan	nan

Elemental composition, average charge states, and plasma properties for 38 flare associated MCs. This table is continued in table D.1.

D. List of MC and solar wind interval plasma properties

#	C	N	Si	S	Q _{Fe}	Var Q _{Fe}	Q _O	Var Q _O	dStr	FIS	A AR	V _{CME}	Pos1	Pos2
19	432.795	517.238	312.806	234.697	13.0	1.34	6.45	0.07	0.030	nan	nan	nan	nan	nan
20	361.819	470.141	189.936	151.107	12.2	0.39	6.38	0.03	0.035	nan	nan	nan	nan	nan
21	299.903	301.290	150.509	93.4668	12.5	1.33	6.69	0.18	0.026	nan	nan	nan	nan	nan
22	225.510	164.859	98.1890	44.4593	14.5	2.47	6.58	0.18	0.027	17.2	11.5	2459.	-18.	-8.
23	56.6244	104.613	119.721	52.4400	16.8	0.87	6.75	0.11	0.022	11.	13.1	2029.	-15.	2.
24	1031.61	914.706	331.106	225.433	12.0	0.48	6.30	0.16	0.042	0.4	34.4	1660.	-2.	-18.
25	126.477	136.096	132.723	120.944	13.3	0.68	6.57	0.12	0.025	nan	nan	nan	nan	nan
26	136.438	99.0655	73.1120	61.3755	13.6	1.12	6.25	0.15	0.030	nan	nan	nan	nan	nan
27	269.435	183.325	59.9579	36.4839	12.7	2.43	6.50	0.27	0.072	0.9	15.6	710.	10.	-35.
28	321.558	96.4653	26.1112	18.7881	14.8	1.52	7.01	0.19	0.046	0.08	17.5	700.	5.	-14.
29	511.610	598.089	297.156	156.202	13.2	1.34	6.38	0.11	0.047	0.1	20.1	1333.	4.	30.
30	57.9903	54.5847	34.3267	23.8097	15.6	2.04	6.59	0.16	0.021	0.6	7.1	1055.	11.	-19.
31	243.100	250.258	164.902	100.905	13.2	1.00	6.49	0.19	0.025	1.5	8.9	1759.	9.	17.
32	123.256	167.504	96.6797	53.9191	13.3	0.98	6.46	0.05	0.012	1.5	9.2	1759.	9.	17.
33	62.9298	60.4939	36.7771	18.9947	16.1	1.86	6.96	0.28	0.051	5.	10.0	2094.	15.	25.
34	161.159	114.388	78.2943	46.8860	14.4	1.34	6.90	0.14	0.049	0.8	13.2	1689.	12.	-11.
35	408.709	293.234	138.881	85.5620	14.5	1.89	6.49	0.24	0.028	0.3	18.3	405.	-16.	-14.
36	614.242	563.788	241.931	156.125	13.2	0.98	6.41	0.12	0.027	0.015	10.7	356.	7.	-13.
37	392.428	322.493	115.391	71.5173	12.2	1.04	6.37	0.16	0.079	nan	nan	nan	nan	nan
38	188.605	128.641	46.8466	28.1512	15.3	2.32	6.91	0.21	0.051	3.	44.	1774.	-6.	23.

Table D.1.: Elemental composition, average charge states, and plasma properties for 38 flare associated MCs.

D.2. MCs without flare association

#	Start	Stop	Year	Vsw	Vexp	Dens	T_p	B	dB/B	Fe	O	He	Ne	Mg
1	112.0	113.03	2001	357.5	40.06	10.0	25478.5	11.7	0.022	225.966	1009.06	50671.9	373.356	266.406
2	170.0	170.57	2001	420.9	-59.2	1.58	133911.	15.6	0.009	18.4283	44.5456	8837.44	31.2830	29.4505
3	191.71	192.79	2001	352.2	48.29	4.84	32557.5	7.41	0.022	261.257	429.625	43445.2	142.936	104.128
4	269.41	269.79	2001	553.6	150.3	3.76	702340.	12.4	0.129	84.6580	520.064	112259.	313.514	246.934
5	304.87	306.37	2001	335.3	74.44	5.60	34097.2	10.8	0.029	167.644	383.570	39847.1	173.121	127.019
6	110.65	111.65	2002	474.2	79.08	3.69	13339.8	6.73	0.024	365.188	250.468	19568.7	113.371	124.367
7	139.15	140.1	2002	431.1	36.92	4.47	124282.	10.6	0.020	196.003	456.423	70475.9	304.534	174.302
8	214.27	214.83	2002	487.5	52.53	5.32	19694.4	12.0	0.012	150.593	914.892	65415.2	272.018	239.461
9	246.0	246.7	2002	350.1	1.631	22.2	37115.7	11.4	0.048	828.131	3159.00	286762.	963.629	793.950
10	274.02	274.58	2002	391.8	-48.9	14.5	45020.1	22.1	0.019	608.452	1987.84	182787.	650.383	425.443
11	79.53	79.94	2003	648.3	-0.48	2.01	150311.	11.0	0.016	34.1621	272.472	59828.5	87.8999	53.6805
12	168.75	169.34	2003	473.4	-31.3	5.13	57961.0	12.6	0.046	243.959	1407.64	149576.	405.881	289.830
13	178.91	179.63	2004	348.7	27.52	5.23	52417.2	5.91	0.011	28.0328	113.205	15233.0	46.2060	36.7099
14	242.8	243.85	2004	391.0	-4.49	8.47	17386.2	12.2	0.017	15.9030	82.5648	8833.46	33.1522	24.0455
15	340.34	340.7	2004	443.6	14.27	28.8	107070.	26.0	0.049	580.752	1092.44	136952.	10441.9	321.241
16	21.99	22.85	2005	771.6	162.5	3.16	132911.	14.1	0.028	189.396	1944.69	201172.	435.773	249.638
17	198.6	199.14	2005	425.9	46.13	13.8	52252.9	11.8	0.051	311.139	1595.18	180463.	568.900	381.162
18	254.25	255.25	2005	877.6	337.4	1.06	166051.	10.0	0.027	60.0200	390.407	27166.8	140.820	61.7829
19	304.1	304.75	2005	375.3	25.26	13.6	35586.1	10.7	0.041	88.0695	484.254	37724.2	237.405	129.933
20	36.88	37.45	2006	335.6	35.55	15.3	17131.2	10.3	0.025	79.3792	476.742	39295.0	196.767	101.047
21	103.6	103.87	2006	524.4	29.49	6.22	43684.0	16.1	0.029	75.1984	408.664	27154.4	197.380	86.2861
22	103.87	104.45	2006	514.5	-14.9	5.94	107241.	17.0	0.033	27.9464	295.996	42830.8	161.571	66.1316
23	145.15	145.64	2006	326.9	22.52	10.3	30009.8	3.78	0.070	94.1181	462.086	42435.7	222.203	99.5198
24	242.86	243.58	2006	410.3	64.16	10.3	15595.1	7.66	0.030	102.936	362.924	19645.0	352.527	147.946
25	273.36	273.88	2006	389.4	53.27	16.4	48620.4	16.1	0.025	147.969	719.805	52312.9	426.921	173.846
26	305.75	306.58	2006	379.9	47.08	5.30	14398.1	5.23	0.032	33.4060	262.740	16761.4	126.394	56.6646
27	333.23	334.38	2006	418.3	48.74	7.14	27095.8	12.0	0.022	379.608	2151.10	145271.	809.848	433.749
28	14.59	15.29	2007	360.2	25.62	5.70	14788.8	12.1	0.026	23.6143	119.592	11691.4	75.0381	37.8988
#	C	N	Si	S	Q_Fe	Var_Q_Fe	Q_O	Var_Q_O	dStr	FlSt	A_AR	V_CME	Pos1	Pos2
1	350.047	370.010	151.129	120.042	11.3	0.40	6.28	0.05	0.030	nan	nan	nan	nan	nan
2	41.4900	22.9896	13.8951	11.0013	11.1	0.62	6.29	0.10	0.180	nan	nan	nan	nan	nan
3	254.861	181.983	73.5550	58.9247	10.5	0.29	6.32	0.05	0.043	nan	nan	nan	nan	nan
4	352.209	220.290	98.2200	88.8634	10.7	0.48	6.37	0.20	0.195	nan	nan	nan	nan	nan
5	246.911	180.816	93.0982	68.9112	10.5	0.99	6.36	0.09	0.025	nan	nan	nan	nan	nan
6	113.434	111.728	80.6174	62.3895	13.6	1.46	6.56	0.19	0.067	0.3	12.7	1240.	-14.	34.
7	242.906	177.255	112.437	99.3425	9.94	0.16	6.09	0.05	0.261	nan	nan	nan	nan	nan
8	332.804	359.340	156.440	95.8286	11.1	0.42	6.36	0.04	0.019	nan	nan	nan	nan	nan
9	1750.30	1466.13	492.848	339.304	10.8	0.11	6.28	0.03	0.032	nan	nan	nan	nan	nan
10	960.799	855.517	268.990	220.833	11.0	0.29	6.27	0.03	0.037	nan	nan	nan	nan	nan
11	238.802	124.756	30.7629	18.1421	10.9	0.78	6.33	0.24	0.160	nan	nan	nan	nan	nan
12	1103.34	648.674	188.067	117.770	11.0	0.66	6.26	0.12	0.033	0.1	18.8	875.	-17.	15.
13	139.408	63.9231	23.4048	15.0664	10.0	0.49	6.30	0.07	0.094	nan	nan	nan	nan	nan
14	90.0544	43.4800	16.9650	10.0606	10.6	1.38	6.24	0.16	0.044	nan	nan	nan	nan	nan
15	943.482	582.298	249.563	177.828	9.78	0.12	6.34	0.03	0.087	nan	nan	nan	nan	nan
16	1518.29	735.112	174.858	108.202	10.9	0.49	6.09	0.07	0.117	8.	13.	882.	14.	61.
17	1382.29	891.832	262.248	165.232	10.7	0.30	6.25	0.04	0.046	nan	nan	nan	nan	nan
18	229.238	158.736	49.1062	33.0670	10.4	0.77	6.04	0.04	0.117	8.	24.3	2257.	-12.	-67.
19	452.427	276.687	82.4223	55.5132	10.0	0.69	6.22	0.05	0.057	nan	nan	nan	nan	nan
20	337.622	263.058	60.5745	39.6458	10.5	0.29	6.22	0.04	0.082	nan	nan	nan	nan	nan
21	294.629	201.892	56.6049	43.4297	11.2	1.10	6.16	0.11	0.037	0.006	7.6	183.	-12.	22.
22	328.177	162.727	37.1250	23.6575	10.3	0.47	6.14	0.15	0.050	0.006	7.9	183.	-12.	22.
23	452.082	281.609	70.8386	46.1391	10.2	0.17	6.16	0.02	0.121	nan	nan	nan	nan	nan
24	146.932	197.467	87.4079	71.9056	10.9	0.45	6.25	0.05	0.022	0.02	9.9	786.	-10.	-8.
25	570.193	371.423	98.4539	76.9924	10.5	0.53	6.07	0.10	0.069	nan	nan	nan	nan	nan
26	235.702	140.761	35.1754	23.9620	10.4	0.39	6.12	0.04	0.030	nan	nan	nan	nan	nan
27	1300.47	1094.38	275.919	190.290	10.6	0.23	6.23	0.04	0.017	nan	nan	nan	nan	nan
28	98.9623	67.6599	21.6795	172.167	10.7	0.64	6.14	0.08	0.053	nan	nan	nan	nan	nan

Table D.2.: Elemental composition, average charge states, and plasma properties for 28 MCs without flare association.

D. List of MC and solar wind interval plasma properties

D.3. Fast solar wind intervals

#	Start	Stop	Year	Vsw	Vexp	Dens	T_p	B	dB/B	Fe	O	He
1	46.0	47.99	2001	514.8	127.1	1.87	206814.	3.78	0.062	18.0825	146.770	11859.7
2	154.0	154.99	2001	506.9	39.43	2.69	136490.	5.24	0.031	30.8783	179.735	26813.8
3	350.5	352.5	2001	479.2	75.50	3.83	105281.	7.79	0.046	49.0409	333.351	64735.6
4	65.0	65.99	2002	641.4	31.87	3.19	156640.	5.75	0.038	128.720	1391.95	169004.
5	118.5	119.99	2002	499.6	-40.1	4.04	171918.	8.68	0.034	70.9511	366.143	64171.5
6	292.0	293.99	2002	647.8	12.06	1.86	235075.	7.04	0.031	51.3815	224.111	29556.8
7	47.0	48.5	2003	612.1	-50.8	4.71	170200.	7.47	0.045	176.332	1423.79	152831.
8	126.0	127.99	2003	694.1	-74.5	3.92	242977.	8.71	0.040	57.6005	536.448	73397.5
9	261.0	262.99	2003	735.7	97.65	2.31	250692.	6.16	0.039	38.3979	485.157	56806.5
10	61.0	62.99	2004	654.6	12.24	2.57	204798.	5.63	0.046	60.5975	532.228	58975.5
11	168.0	169.99	2004	521.8	67.97	2.42	132383.	5.10	0.045	40.0193	349.945	37860.2
12	260.5	261.99	2004	505.8	26.74	6.23	94846.3	6.01	0.060	101.762	609.599	77655.8
13	39.5	41.5	2005	701.9	-49.6	3.91	202757.	5.85	0.047	83.2508	984.641	120918.
14	121.0	121.99	2005	640.1	-62.2	2.71	286314.	6.61	0.076	25.3279	195.634	27414.0
15	308.0	309.99	2005	669.9	-15.0	2.95	205180.	5.15	0.057	35.6238	396.846	55503.2
16	79.0	80.99	2006	638.2	95.25	2.54	172910.	4.32	0.082	32.4488	308.277	48022.2
17	167.0	168.99	2006	577.1	6.225	2.17	187635.	4.64	0.053	29.9950	314.247	39195.4
18	220.0	220.99	2006	599.9	55.49	2.21	139306.	3.96	0.063	20.3812	232.162	27716.2
19	18.0	19.99	2007	631.5	2.262	2.85	150473.	4.39	0.065	37.8873	457.933	52851.8
20	118.5	120.5	2007	634.2	-28.8	3.33	153928.	4.71	0.068	72.6993	828.624	114293.
21	246.0	246.99	2007	623.8	-55.7	2.27	134355.	3.60	0.081	30.5448	335.613	49569.9
#	Ne	Mg	C	N	Si	S	Q_Fe	Var Q_Fe	Q_O	Var Q_O	dStr	
1	46.6965	36.9459	105.497	50.8910	23.8725	15.9499	9.35	0.53	6.07	0.03	0.378	
2	102.443	56.9925	106.326	71.8286	31.2043	21.8115	10.1	0.29	6.05	0.02	0.344	
3	137.896	79.1641	281.994	169.941	46.9482	34.3983	11.6	1.26	6.31	0.23	0.128	
4	284.470	174.038	1046.22	453.498	129.997	83.8813	11.1	0.29	6.01	0.00	0.331	
5	210.734	105.528	243.106	156.871	58.7204	46.0051	10.5	0.43	6.11	0.04	0.269	
6	71.4016	62.5367	180.544	75.9835	52.8018	30.8993	9.62	0.17	6.01	0.02	0.373	
7	300.972	207.824	1053.58	500.146	163.037	100.952	9.92	0.27	6.02	0.00	0.385	
8	181.833	77.1957	411.230	190.531	52.1525	36.8364	10.4	0.39	6.00	0.01	0.354	
9	127.526	52.6310	352.089	148.807	36.9474	23.5027	10.0	0.27	6.02	0.25	0.386	
10	127.203	78.6090	440.600	188.035	59.3520	35.2550	9.45	0.29	5.98	0.00	0.368	
11	90.2276	59.1813	275.362	133.563	40.6928	24.7107	9.45	0.34	6.00	0.03	0.285	
12	207.490	109.077	528.075	272.709	78.9322	51.9991	10.0	0.24	6.07	0.09	0.159	
13	233.760	110.162	786.786	333.528	79.1795	49.7827	9.58	0.17	5.97	0.00	0.422	
14	83.3309	36.2518	143.387	70.0772	25.4219	17.5201	9.42	0.28	5.96	0.02	0.341	
15	130.281	51.4159	329.712	153.660	33.7658	22.9694	9.76	0.26	5.97	0.01	0.267	
16	112.555	45.7874	259.866	122.419	28.7205	18.9192	9.61	0.26	5.97	0.03	0.192	
17	87.6879	50.0575	256.819	119.782	33.4678	20.6576	9.27	0.32	6.00	0.02	0.381	
18	78.3334	34.8959	181.039	89.2493	21.3117	13.5341	9.43	0.24	5.97	0.01	0.230	
19	147.445	60.9825	335.097	161.935	37.1606	23.1505	9.18	0.25	5.95	0.00	0.236	
20	239.910	101.457	672.338	280.490	67.3585	45.4889	9.43	0.13	5.96	0.10	0.232	
21	132.078	47.6068	276.895	133.430	29.6759	19.8941	9.59	0.24	5.95	0.01	0.278	

Table D.3.: Elemental composition, average charge states, and plasma properties for 21 fast solar wind intervals from 2001 to 2007.

D.4. Slow solar wind intervals

D.4. Slow solar wind intervals

#	Start	Stop	Year	Vsw	Vexp	Dens	T-p	B	dB/B	Fe	O	He
#	Ne	Mg	C	N	Si	S	Q-Fe	Var Q-Fe	Q-O	Var Q-O	dStr	
1	52.0	53.99	2001	353.2	-12.5	5.17	55489.7	4.98	0.056	327.318	1577.93	170364.
2	157.0	158.99	2001	385.1	-21.5	7.03	38063.0	7.22	0.041	68.9517	326.943	40792.8
3	263.5	265.5	2001	334.0	35.57	22.8	19692.0	4.91	0.078	390.130	1955.44	208929.
4	56.0	57.99	2002	331.5	-18.5	9.65	44335.5	6.66	0.032	516.263	2135.03	246341.
5	128.0	129.99	2002	365.2	-9.20	5.27	51516.8	8.15	0.032	78.4931	327.605	70238.0
6	284.0	285.99	2002	359.5	40.79	7.17	31813.7	5.61	0.054	93.9396	400.241	61174.2
7	40.0	41.99	2003	448.0	54.02	6.14	85799.1	7.51	0.029	235.788	1471.17	196335.
8	139.0	140.99	2003	425.5	22.56	7.36	91742.8	6.43	0.060	113.046	815.475	104540.
9	272.0	273.99	2003	306.2	61.89	10.8	18145.9	5.00	0.086	118.118	484.187	36772.7
10	67.0	68.99	2004	352.6	7.721	8.88	34163.9	6.23	0.033	96.7996	587.539	67207.5
11	175.0	176.99	2004	328.1	10.01	6.18	20995.6	5.06	0.036	83.8836	508.279	51938.5
12	240.0	241.99	2004	399.7	-10.1	3.94	87685.7	5.83	0.044	45.6773	221.317	33103.2
13	75.0	76.99	2005	394.3	-58.7	8.11	73140.1	7.95	0.073	86.0598	454.594	54266.6
14	125.0	126.99	2005	363.8	-45.7	10.2	46227.6	5.50	0.069	92.2916	640.410	67363.9
15	240.0	241.99	2005	394.1	13.74	4.55	58713.1	5.42	0.034	27.4159	207.312	27465.5
16	84.0	85.99	2006	357.0	-2.75	10.1	34796.0	4.71	0.116	116.007	375.568	50707.6
17	174.0	175.99	2006	302.7	11.39	11.7	19456.4	3.76	0.106	65.9186	475.050	31137.7
18	226.0	228.99	2006	301.0	19.59	9.43	21301.2	2.97	0.119	100.433	448.277	26561.2
19	25.0	27.99	2007	312.6	23.45	10.1	21632.4	3.60	0.099	52.6184	324.593	26511.1
20	124.0	126.5	2007	294.8	51.73	8.25	19283.5	3.04	0.073	88.1939	448.147	46063.0
21	234.0	235.99	2007	320.9	-1.40	7.72	32985.4	3.13	0.119	69.0341	488.911	46465.6

Table D.4.: Elemental composition, average charge states, and plasma properties for 21 slow solar wind intervals from 2001 to 2007.

E. List of MCs from 2001 to mid 2007 and their specific signatures

A total number of 67 MCs were identified and fitted with the models described in section 4. Identification of MC boundaries is based on SWEPAM plasma data (solar wind speed, α /proton-ratio, proton density, and proton temperature), MAG measurements (magnetic field rotation, magnetic field strength, and magnetic field variance), SWEPAM suprathermal electron pitch angle distributions (0.073-1.37 keV), EPAM electron intensities (38-315 keV), EPAM proton intensities (1.9-4.8 MeV), and a number of derived quantities (plasma β , proton specific entropy). For further details consult chapter 3.

Given are deviations from the typical MC signatures described in table 3.1. If various signatures indicate different start and end times for the MC, these signatures and the resulting start and end times are listed. The uncertainty in the start and stop times should be in the order of roughly one hour (0.05 days). Strongly deviating identifications by other authors are noted too. The occurrence of data gaps in the available data is described as well as the appearance of peculiarities. Furthermore, a quality flag is given, depending on magnetic field profile, variance in magnetic field data, and goodness of start and end time. 1 means clearly visible MC structure, 2 average profile, 3 means very poor profile.

The MCs are listed in the order of their occurrence and year.

2001

1. DoY 78.80-80.67

- a) Excellent magnetic field profile, slightly asymmetric (highest field strength shifted toward leading edge).
- b) Bidirectional suprathermal electrons only present at the leading edge of the MC (until DoY 79.3).
- c) Small decrease in EPAM electron and proton intensities (Factor < 2).
- d) SWEPAM data gap before DoY 78.4 and after DoY 80.2.
- e) Trailing edge not well determined because of SWEPAM data gap and lack of bidirectional electrons.
- f) Identified as 2 MCs in *Nieves-Chinchilla et al. [2005]*, *Hidalgo [2003]*, and MFI.

g) Quality 1

2. DoY 86.86-87.27

- a) No decrease in proton velocity.
- b) Large decrease in suprathermal electron intensities at the trailing edge of the MC.
- c) Proton temperature not lower than $0.5T_{\text{exp}}$.
- d) Depression in proton temperature and enhancement in the α/p -ratio continue after the end of the MC.
- e) Region of high proton density ($30 \text{ protons/cm}^{-3}$) near leading edge.
- f) Plasma β is between 0.1 and 1 (relatively high).
- g) Magnetic field strength profile shows much scattering and is very asymmetric.
- h) Quality 2

3. DoY 91.32-91.82

- a) Enhancement in the α/p -ratio starts near trailing edge of MC and continues after passage of the trailing edge.
- b) Depression in proton temperature continues for ≈ 2 days.
- c) Magnetic field strength decreases linearly from leading to trailing edge.
- d) Uncertainty in the end time ≈ 0.1 days.
- e) Quality 2

4. DoY 94.80-95.31

- a) Plasma β very high (in the range 0.3-3.0).
- b) Proton temperature exceeds T_{exp} up to a factor of 4.
- c) α/p -ratio is smaller than 0.04 for the whole time.
- d) Data gaps in the α/p -ratio from DoY 94.6 to 95.55.
- e) Magnetic field profile shows much scatter.
- f) Quality 3

5. DoY 102.19-102.72

- a) Proton temperature decrease from DoY 102.35 to 103.30.
- b) No decrease in proton velocity during MC passage.
- c) α/p -ratio enhancement ends at DoY 103.30.

E. List of MCs from 2001 to mid 2007 and their specific signatures

- d) Start and stop times are very uncertain (± 0.15 days).
- e) Quality 3

6. DoY 112.00-113.03

- a) No signs of bidirectional suprathermal electrons during MC.
- b) No enhancement in the α/p -ratio (≈ 0.04).
- c) Proton temperature not lower than $0.5T_{\text{exp}}$.
- d) SWEPAM data gap from DoY 113.25 to 113.9.
- e) Decreased intensity in low energy EPAM electrons from DoY 112.00 to 113.3.
- f) Quality 2

7. DoY 119.02-119.57

- a) Proton temperature depression starts at DoY 118.6 and lasts for more than 2 days.
- b) α/p -ratio remains high after MCs passage.
- c) Suprathermal electrons show beam profile parallel to magnetic field.
- d) Magnetic field strength relatively low (< 11 nT).
- e) EPAM electrons show no variation during MCs passage.
- f) Cane and Richardson [2003] give a much longer duration (DoY 118.58-120.08).
- g) Quality 2

8. DoY 127.77-128.35

- a) Very flat magnetic field strength profile with low magnetic field strength (< 9 nT)
- b) Data gap in the α/p -ratio from DoY 128.0 to 128.3 and from 128.6 onwards.
- c) Proton temperature only slightly lower than $0.5T_{\text{exp}}$.
- d) Large increase in 1.9-4.8 MeV proton intensities (factor of ≈ 100).
- e) Quality 2

9. DoY 129.50-130.88

- a) End time with large uncertainties (≈ 0.2 days).
- b) Only weak signatures of bidirectional suprathermal electrons.
- c) Magnetic field strength profile very asymmetric with linear decrease of field strength from leading to trailing edge.
- d) Start and end times mainly based on proton temperature depression.

- e) Simultaneous decrease in proton density, increase in α/p -ratio, and proton temperature at DoY 130.3 might indicate an object combined from two substructures.
- f) Quality 3

10. DoY 148.48-149.40

- a) Magnetic field strength profile very flat but symmetric ($|\vec{B}_{\text{center}}|/|\vec{B}_{\text{edge}}| = 1.25$).
- b) Bidirectional suprathermal electrons only during MCs beginning.
- c) Proton temperature is smaller than $0.5T_{\text{exp}}$ from DoY 148.2 to 149.9.
- d) α/p -ratio enhancement starts at DoY 149.1.
- e) *Cane and Richardson [2003]* give a much longer duration (148.13-149.88).
- f) Quality 3

11. DoY 170.00-170.57

- a) No signs of suprathermal bidirectional electrons.
- b) EPAM electron and proton intensities reduced by a factor of ≈ 2 after passage of MCs leading edge.
- c) Magnetic field strength profile nearly constant (16 nT).
- d) Some short data gaps (≈ 0.1 days) in the α/p -ratio.
- e) Proton speed profile shows no declining velocity, instead of that a slight increase in proton velocity is visible.
- f) Proton temperature higher than T_{exp} during the whole MC.
- g) Quality 2

12. DoY 190.08-190.56

- a) Large scattering in magnetic field direction near trailing edge of MC.
- b) Almost linear decay of magnetic field strength from leading to trailing edge.
- c) Bidirectional suprathermal electrons only present at the MCs trailing edge.
- d) Proton temperature lower than T_{exp} until DoY 192.2.
- e) α/p -ratio is very low (≈ 0.04) until DoY 190.4.
- f) Plasma β very high (0.3-2).
- g) Quality 3

13. DoY 191.71-192.79

E. List of MCs from 2001 to mid 2007 and their specific signatures

- a) Bidirectional suprathermal electron signature starts at DoY 191.6.
- b) Magnetic field direction shows large variance.
- c) Magnetic field strength is low near leading edge (6 nT) and rises toward the trailing edge (8 nT).
- d) SWEPAM data gap from DoY 192.3 to 192.6.
- e) Proton temperature exceeds T_{exp} from DoY 192.2 on.
- f) Low α/p -ratio (Average ≈ 0.04).
- g) Large uncertainty for start and end times (0.2 days).
- h) Quality 3

14. DoY 269.41-269.79

- a) SWEPAM data gap from DoY 268.8 to 269.7.
- b) Magnetic field strength profile is very flat (15 nT).
- c) Only short periods of bidirectional suprathermal electrons.
- d) Very high fluxes of EPAM electrons and protons indicate a SEP around DoY 268.8.
- e) SEP is not caused by this CME (travel speed would be 2850 km/s).
- f) Quality 3

15. DoY 272.62-273.43

- a) Very symmetric magnetic field strength profile.
- b) No enhancement in α/p -ratio (< 0.02 for first half of MC, ≈ 0.06 for second half).
- c) Proton temperature indicates a start and stop time of DoY 272.95-273.95.
- d) Plasma β very high near leading edge (≈ 2).
- e) This CME is not the cause for the SEP from DoY 268.8 (travel speed would be 450 km/s).
- f) Quality 2

16. DoY 304.87-306.37

- a) Bidirectional suprathermal electrons present until DoY 305.6.
- b) Magnetic field strength profile shows enhanced field near leading edge.
- c) SWEPAM data gap from DoY 305.7 to 306.45.
- d) On average the proton temperature is higher than T_{exp} .
- e) EPAM protons show a decrease of intensity near leading edge (by a factor of 3).
- f) Determination of end time uncertain (0.1 days).

- g) *Nieves-Chinchilla et al.* [2005] give a start and end time of DoY 304.96-306.08.
- h) Quality 2

17. DoY 328.68-329.69

- a) Magnetic field strength profile very asymmetric (highest field strength near leading edge).
- b) Large variance in magnetic field direction.
- c) SWEPAM data gap from DoY 328.2 to 328.75.
- d) Proton temperature indicates a duration until DoY 329.85.
- e) Enhancement in the α/p -ratio starts near trailing edge.
- f) EPAM electron and proton decrease denotes a start time of DOY 328.71.
- g) MC accompanied by a SEP that started at DoY 328.25.
- h) *Cane and Richardson* [2003] give start and stop times of DoY 328.58-330.46.
- i) Quality 3

2002

1. DoY 78.95-79.54

- a) No signature of bidirectional suprathermal electrons.
- b) Very small amount of variation in magnetic field strength (15 nT at maximum, 12 nT at minimum).
- c) Proton speed is at constant level with an increase near the trailing edge.
- d) Short gap in SWEPAM data from DoY 79.4 to 79.5.
- e) Proton temperature shows no reduction with respect to T_{exp} .
- f) EPAM electron intensity shows very low scattering during MCs passage.
- g) According to *Cane and Richardson* [2003] the start and end time are DoY 78.21 to 79.67.
- h) Quality 1

2. DoY 83.50-84.82

- a) First appearance of bidirectional suprathermal electrons at DoY 83.25.
- b) Background magnetic field strength very high (≈ 10 nT).
- c) Proton speed increase at DoY 84.05.
- d) Period of low α/p -ratio (0.04) from 83.8 to 84.4.
- e) Proton density increase near trailing edge (15 protons/cm $^{-3}$).

E. List of MCs from 2001 to mid 2007 and their specific signatures

- f) Boundary times very uncertain (0.2 days).
- g) *Cane and Richardson* [2003] give start and stop times of DoY 82.88-84.83, the MFI list¹ identified DoY 83.16-84.95, and *Nieves-Chinchilla et al.* [2005] list two MCs with the start and stop times DoY 83.17-83.92 and 84.25-84.96.
- h) Quality 3

3. DoY 108.14-109.21

- a) Signatures of bidirectional suprathermal electron start at DoY 107.95.
- b) Linear decrease in proton velocity starts at DoY 107.95.
- c) Proton temperature decrease start at DoY 107.9.
- d) Magnetic field strength shows almost linear decrease from leading to trailing edge.
- e) Quality 2

4. DoY 110.65-111.65

- a) Signatures of bidirectional suprathermal electrons last until DoY 111.2
- b) Magnetic field strength very low (<8 nT).
- c) Magnetic field strength profile shows almost linear decrease from leading to trailing edge.
- d) Data gap in the α/p -ratio starts at DoY 111.1.
- e) Reduction in proton temperature with respect to T_{exp} starts at DoY 110.5.
- f) SEP at DoY 111.05 indicates a magnetic connection of the MC to the sun.
- g) *Cane and Richardson* [2003] give DoY 110.00 and 111.75 as start and end times.
- h) Quality 2

5. DoY 139.15-140.10

- a) Magnetic field strength profile shows exponential decrease from leading to trailing edge.
- b) Some small data gaps in the α/p -ratio around DoY 139.
- c) Proton temperature is significantly higher than T_{exp} until DoY 139.9.
- d) Plasma β is relatively high (between 0.2 and 0.5).
- e) EPAM protons show an intensity decrease of factor 3 at MC's leading edge.
- f) Quality 2

6. DoY 143.88-145.75

¹Magnetic Clouds, http://lepmfi.gsfc.nasa.gov/mfi/mag_cloud_pub1.html

- a) Bidirectional suprathermal electrons only present for short time frames.
- b) Magnetic field strength almost constant at ≈ 10 nT.
- c) Data gap in the α/p -ratio from DoY 143.4 to 145.8.
- d) On average the proton temperature is higher than T_{exp} .
- e) Extremely low proton densities (< 0.3 protons/cm $^{-3}$).
- f) Large decrease in the EPAM electron and proton intensities on DoY 144.9.
- g) According to *Nieves-Chinchilla et al.* [2005] the start and end times are DoY 143.96-144.83, and MFI give start and end times of DoY 143.98-144.70.
- h) Quality 2

7. DoY 213.67-213.91

- a) Bidirectional suprathermal electrons present from DoY 213.85 to 213.95.
- b) Magnetic field strength profile shows linear decrease from leading to trailing edge.
- c) Enhancement in α/p -ratio ends at DoY 214.2.
- d) Determination of start time doubtful (0.15 days).
- e) Quality 3

8. DoY 214.27-214.83

- a) Only short periods of bidirectional suprathermal electrons.
- b) Magnetic field strength profile nearly constant (10.5 nT at trailing edge, 13 nT at maximum).
- c) α/p -ratio very low (≈ 0.05 or even lower).
- d) Proton temperature stays low ($< 0.5T_{\text{exp}}$) until DoY 215.4.
- e) EPAM proton intensity decrease by a factor of 5 at leading edge.
- f) Quality 2

9. DoY 246.00-246.70

- a) Signatures of bidirectional suprathermal electrons present from DoY 246.25 to 246.55.
- b) Magnetic field strength profile shows linear increase from leading (6 nT) to trailing (16 nT) edge.
- c) Large scatter in magnetic field direction.
- d) No decrease in proton velocity (constant speed of $v_p = 350$ km/s).
- e) Gap in SWEPAM data for the whole time except DoY 246.1-246.3.
- f) Start and end times very uncertain (0.15 days).

E. List of MCs from 2001 to mid 2007 and their specific signatures

g) Quality 3

10. DoY 274.02-274.58

- a) No signs of bidirectional suprathermal electrons present.
- b) Maximum of magnetic field strength shifted toward trailing edge.
- c) Increase in proton velocity from leading to trailing edge.
- d) α/p -ratio is very low (≈ 0.05).
- e) No decrease in proton temperature ($T_p \approx T_{exp}$).
- f) Quality 2

11. DoY 355.37-356.29

- a) Two very short periods (≈ 30 min) of bidirectional suprathermal electrons near leading edge.
- b) Magnetic field strength nearly constant at 8 nT.
- c) α/p -ratio increase starts at DoY 355.1 and ends at DoY 356.75.
- d) Decrease in proton temperature starts at DoY 354.8 and ends at DoY 356.75.
- e) Uncertainty in start time ≈ 0.1 days.
- f) Quality 2

2003

1. DoY 27.07-27.65

- a) Very nice signatures of bidirectional suprathermal electrons.
- b) Maximum of magnetic field strength is shifted toward trailing edge.
- c) Enhancement in α/p -ratio starts at trailing edge and continues until DoY 27.95.
- d) Proton temperature decrease starts at DoY 26.3 and ends at DoY 28.1.
- e) EPAM electron and proton intensities show a small decrease (\approx factor 2).
- f) Quality 2

2. DoY 79.53-79.94

- a) No signatures of bidirectional suprathermal electrons present.
- b) Magnetic field strength profile shows linear decrease from leading (12 nT) to trailing (9 nT) edge.
- c) Proton speed is constant at 650 km/s.

- d) α/p -ratio remains at a low level (<0.05).
- e) The proton temperature is higher than $0.5T_{\text{exp}}$.
- f) Large reduction in EPAM proton intensities at trailing edge (\approx factor of 5).
- g) Quality 2

3. DoY 168.75-169.34

- a) Only 4 hours with weak signatures of bidirectional suprathermal electrons.
- b) Magnetic field strength at 10 nT, sudden increase to 20 nT at DoY 169.2.
- c) Magnetic field direction shows much scattering.
- d) Proton velocity is constant ≈ 460 km/s with an increase to 500 km/s near the trailing edge.
- e) The decrease in proton temperature starts at DoY 168.35.
- f) EPAM proton and electron intensities show a reduction from DoY 168.80 to DoY 169.35.
- g) Quality 3

4. DoY 191.66-192.34

- a) Signatures of bidirectional suprathermal electrons continue until DoY 192.6.
- b) Magnetic field strength increases from leading edge (7 nT) to trailing edge (12 nT).
- c) SWEPAM data gap from DoY 191.55 to DoY 191.7.
- d) Proton speed is constant at ≈ 360 km/s.
- e) α/p -ratio is enhanced from DoY 191.95 to DoY 192.6.
- f) Start and end time uncertain (≈ 0.1 days).
- g) Quality 2

5. DoY 217.41-218.00

- a) First signatures of bidirectional suprathermal electrons occur at DoY 217.33.
- b) Magnetic field strength rises from 8 nT at leading edge to 13 nT at trailing edge.
- c) Proton temperature decrease below $0.5T_{\text{exp}}$ starts at DoY 216.25 and ends at DoY 218.05.
- d) Proton velocity nearly constant at 425 km/s.
- e) Quality 2

6. DoY 230.56-231.21

- a) Magnetic field strength profile shows linear increase from leading (17 nT) to trailing edge (19 nT).

E. List of MCs from 2001 to mid 2007 and their specific signatures

- b) Two enhancements in the α/p -ratio from DoY 230.1-230.6 and DoY 230.9-231.6.
- c) Proton temperature reduction below $0.5T_{\text{exp}}$ starts at DoY 230.2.
- d) Start and end times doubtful (0.1 days).
- e) Quality 2

7. DoY 302.46-303.07

- a) Suprathermal electron data only available from DoY 302.55 to 302.95. During this period the electrons are bidirectional.
- b) The magnetic field strength is higher at the leading edge than at the trailing edge. The maximum is shifted toward the leading edge.
- c) No SWEPAM measurements until DoY 304.05.
- d) One of the fastest ICMEs ever measured in the interplanetary medium (speed > 1000 km/s).
- e) Very high intensities of EPAM electrons and protons.
- f) *Skoug et al. [2004]* determined DoY 302.33-303.67 as the start and end time, *Malandraki et al. [2005]* specify DoY 302.46-303.38 based on EPAM particle observations.
- g) Quality 2

8. DoY 304.07-304.50

- a) Bidirectional suprathermal electrons present until \approx DoY 306.
- b) Magnetic field strength is 30 nT at leading edge and 10 nT at trailing edge.
- c) The angular direction of the magnetic field shows much scattering.
- d) No α/p -ratio and proton density available until DoY 304.45.
- e) Decrease in proton temperatures below $0.5T_{\text{exp}}$ continues until DoY 306.2.
- f) *Skoug et al. [2004]* give DoY 304.08-306.75 as start and end times, *Malandraki et al. [2005]* determined DoY 304.08-305.92, and Richardson² list DoY 304.08-306.00. According to this the MC might be a part of the whole ICME structure.
- g) Quality 3

9. DoY 324.44-325.10

- a) Signatures of suprathermal bidirectional electrons only present for short time slices.
- b) Magnetic field strength very high (55 nT). The maximum is shifted toward leading edge. Very large angle of rotation in magnetic field direction.

²Near-Earth Interplanetary Coronal Mass Ejections in 1996-2007, <http://www.ssg.sr.unh.edu/mag/ace/ACElists/ICMTable.html>

- c) Proton density is very high (up to 30 protons/cm⁻³).
- d) On average the proton temperature is not smaller than $0.5T_{\text{exp}}$.
- e) The α/p -ratio shows a lot of fluctuation (0.05-0.15).
- f) Richardson³ give an end time of DoY 325.33.
- g) Quality 2

2004

1. DoY 95.08-96.66

- a) Signatures of suprathermal bidirectional electrons start at DoY 94.85 and end at DoY 96.45.
- b) Magnetic field strength rises until DoY 95.6 and remains constant at ≈ 18 nT.
- c) Increase in the α/p -ratio starts at DoY 95.25 and ends at DoY 96.4.
- d) Richardson³ list a start time of DoY 94.58 and an end time of DoY 96.75.
- e) Quality 2

2. DoY 122.66-123.50

- a) Signatures of bidirectional suprathermal electrons are present from DoY 122.65-123.8.
- b) Magnetic field strength rises from 7 to 9 nT at leading edge and stays nearly constant.
- c) Plasma β is in the range 0.2-0.8.
- d) Proton temperature is smaller than $0.5T_{\text{exp}}$ from DoY 122.6-122.8.
- e) α/p -ratio is larger than 0.08 from DoY 122.7-122.9.
- f) Richardson³ determined an end time of DoY 123.88.
- g) Quality 3

3. DoY 178.91-179.63

- a) No evidence for the presence of bidirectional suprathermal electrons.
- b) Magnetic field strength linearly decreases from 6 nT at leading edge to 5 nT at trailing edge.
- c) No SWEPM data available (except proton speed).
- d) Large increase in the EPAM electron intensities at the trailing edge.
- e) Quality 2

4. DoY 204.61-204.95

³Near-Earth Interplanetary Coronal Mass Ejections in 1996-2007, <http://www.ssg.sr.unh.edu/mag/ace/ACElists/ICMTable.html>

E. List of MCs from 2001 to mid 2007 and their specific signatures

- a) Signatures of bidirectional suprathermal electrons start at DoY 204.75.
- b) The magnetic field direction shows a very irregular rotation pattern.
- c) Proton speed increases from 500 km/s to 670 km/s.
- d) Gaps in the α/p -ratio, the available data shows a very low ratio (<0.05).
- e) On average the proton temperature is higher than T_{exp} .
- f) Within the MC EPAM proton and electron intensities show a large increase.
- g) Richardson⁴ give start time of DoY 204.75 and an end time of DoY 206.33.
- h) Quality 2

5. DoY 206.54-207.51

- a) Signatures of bidirectional suprathermal electrons present until DoY 207.63.
- b) Magnetic field strength is almost constant at ≈ 20 nT.
- c) The magnetic field direction shows an abrupt change at DoY 207.25.
- d) α/p -ratio is very low (<0.05).
- e) Proton temperature is smaller than $0.5T_{exp}$ during some short periods.
- f) Quality 3

6. DoY 209.09-209.56

- a) Maximum of magnetic field strength shifted toward leading edge.
- b) Gap in the proton density and the α/p -ratio from DoY 209.1 to DoY 209.3.
- c) α/p -ratio is very low (<0.06) for the time data is available.
- d) Large decrease in the EPAM proton intensities at the leading edge.
- e) Richardson⁴ determined an end time of DoY 209.92.
- f) Quality 2

7. DoY 242.80-243.85

- a) Only weak signals of bidirectional suprathermal electrons near leading edge.
- b) Magnetic field strength increases abruptly from 10 nT at the leading edge to 12.5 nT and to 15 nT at the trailing edge.
- c) Data gap in the α/p -ratio from DoY 243.25 to 243.6.
- d) α/p -ratio is extremely low (≈ 0.01).

⁴Near-Earth Interplanetary Coronal Mass Ejections in 1996-2007, <http://www.ssg.sr.unh.edu/mag/ace/ACElists/ICMTable.html>

e) Quality 2

8. DoY 313.10-313.69

- a) No signatures of bidirectional suprathermal electrons present.
- b) Linear decrease in the magnetic field strength from leading (45 nT) to trailing edge (8 nT), with a steep decrease at DoY 313.2 (48 nT-27 nT).
- c) Proton velocity shows an increase at DoY 313.2 from 650 km/s to 730 km/s.
- d) EPAM proton and electron intensities show a minimum at trailing edge.
- e) Richardson⁵ listed DoY 312.92 and DoY 314.42 as start and end times.
- f) Quality 2

9. DoY 314.87-315.16

- a) Short occurrence of suprathermal bidirectional electrons around DoY 314.85.
- b) Linear decrease of magnetic field strength from 40 nT at leading edge to 31 nT at trailing edge.
- c) α/p -ratio is very low (≈ 0.04).
- d) Decrease in proton temperature continues until DoY 316.8.
- e) EPAM proton intensities show a decrease at the leading edge, while electron intensities show an increase.
- f) First component of double fluxrope structure.
- g) Quality 2

10. DoY 315.16-315.50

- a) No signatures of bidirectional suprathermal electrons present.
- b) Linear decrease in magnetic field strength from 31 nT at leading edge to 15 nT at trailing edge.
- c) Change in magnetic field direction is large near leading edge.
- d) α/p -ratio is very low (≈ 0.05).
- e) Determination of end time is uncertain (≈ 0.15 days).
- f) Second component of a double fluxrope structure.
- g) Richardson⁵ give an end time of DoY 316.96.
- h) Quality 2

11. DoY 340.34-340.70

⁵Near-Earth Interplanetary Coronal Mass Ejections in 1996-2007, <http://www.ssg.sr.unh.edu/mag/ace/ACElists/ICMTable.html>

E. List of MCs from 2001 to mid 2007 and their specific signatures

- a) Linear decrease of the magnetic field strength from leading (36 nT) to trailing edge (18 nT).
- b) SWEPAM data gap before DoY 340.3.
- c) No α/p -ratio available for the whole time period.
- d) Proton temperature is higher than T_{exp} .
- e) Proton density is very high (20-40 protons/cm³).
- f) Plasma β is large (0.2-0.7).
- g) Quality 2

2005

1. DoY 19.04-20.09

- a) Weak signatures of suprathermal bidirectional electrons start at DoY 19.25.
- b) Magnetic field strength shows almost linear decrease from leading (15 nT) to trailing edge (7 nT).
- c) SWEPAM data gap before DoY 18.95.
- d) α/p -ratio exceeds 0.08 from DoY 19.85 onwards.
- e) Quality 2

2. DoY 21.99-22.85

- a) Signatures of suprathermal bidirectional electrons start at DoY 21.75 and continue until DoY 22.9.
- b) Almost linear decrease in of magnetic field strength from leading (22 nT) to trailing edge (6 nT) with an additional maximum near leading edge (27 nT).
- c) α/p -ratio is very low (smaller than 0.06).
- d) Proton temperature becomes smaller than $0.5T_{\text{exp}}$ at DoY 22.15.
- e) End time is uncertain (0.15 days).
- f) Richardson⁶ determined a start and end times of DoY 21.79 to 22.71.
- g) Quality 2

3. DoY 135.24-136.17

- a) Signatures of bidirectional suprathermal electrons present until DoY 136.55.
- b) α/p -ratio is low (≈ 0.04) except near the trailing edge (after DoY 136.05).
- c) Proton temperature decrease starts at DoY 135.35 and ends at DoY 137.5.

⁶Near-Earth Interplanetary Coronal Mass Ejections in 1996-2007, <http://www.ssg.sr.unh.edu/mag/ace/ACElists/ICMTable.html>

- d) EPAM electron and proton intensities show a decrease of factor 100 at leading edge.
- e) Determination of end time is doubtful (0.15 days).
- f) The MFI⁷ list gives an end time of DoY 135.93, Richardson⁸ determined an end time of DoY 139.00.
- g) Quality 2

4. DoY 140.31-141.22

- a) No signatures of bidirectional suprathermal electrons present.
- b) Magnetic field strength profile distorted until DoY 140.7.
- c) Magnetic field directions show much scattering.
- d) Proton temperature decrease starts at DoY 139.15 and ends at DoY 141.95.
- e) Richardson⁸ give DoY 140.13 as start time and DoY 142.08 as end time.
- f) Quality 3

5. DoY 163.70-164.50

- a) No signatures of bidirectional suprathermal electrons present.
- b) Magnetic field strength shows linear decrease from leading (18 nT) to trailing edge (8 nT).
- c) Steep increase in the EPAM electron intensities at leading edge.
- d) The MFI list⁷ gives an end time of DoY 164.30.
- e) Quality 2

6. DoY 166.25-167.29

- a) Intervals with and without bidirectional suprathermal electrons, signatures end at DoY 167.35.
- b) Magnetic field strength profile shows a minimum near MCs center.
- c) Rotation of magnetic field direction is irregular.
- d) Decrease in proton temperature indicates a start time of DoY 166.45 and stop time of DoY 167.35.
- e) Quality 2

7. DoY 198.60-199.14

- a) Some intervals show weak signatures of bidirectional suprathermal electrons.
- b) Magnetic field strength profile shows a lot of scattering.

⁷Magnetic Clouds, http://lepmfi.gsfc.nasa.gov/mfi/mag_cloud_pub1.html

⁸Near-Earth Interplanetary Coronal Mass Ejections in 1996-2007, <http://www.ssg.sr.unh.edu/mag/ace/ACElists/ICMTable.html>

E. List of MCs from 2001 to mid 2007 and their specific signatures

- c) α/p -ratio is very low (≈ 0.02).
- d) Proton temperature is lower than T_{exp} from DoY 198.65 to 198.9.
- e) Proton density is very high (average value of 15 protons/cm $^{-3}$).
- f) Plasma β is very high (0.05-1.0).
- g) Richardson⁹ list an end time of DoY 199.96.
- h) Quality 2

8. DoY 254.25-255.25

- a) Signatures of bidirectional suprathermal electrons present from DoY 254.2 to DoY 255.25.
- b) Maximum of magnetic field strength near leading edge (18 nT).
- c) Variance in the magnetic field direction is high.
- d) SWEPAM data gap before DoY 254.45.
- e) α/p -ratio is low (≈ 0.04).
- f) Quality 2

9. DoY 304.10-304.75

- a) Bidirectional suprathermal electrons present from DoY 304.3-304.4.
- b) Magnetic field strength shows a lot of variance.
- c) α/p -ratio is very low (≈ 0.01).
- d) Proton temperature is lower than T_{exp} from DoY 304.05 to DoY 304.3.
- e) Proton density is high (in the range of 10-20 protons/cm $^{-3}$).
- f) Plasma β is high (0.1-0.8).
- g) Quality 2

2006

1. DoY 36.88-37.45

- a) Bidirectional suprathermal electrons are present, except for a short period around DoY 37.05.
- b) Magnetic field strength shows increase from leading (8 nT) to trailing edge (10 nT).
- c) SWEPAM data gap starts at DoY 37.0.
- d) α/p -ratio is smaller than 0.04 before DoY 37.0.

⁹Near-Earth Interplanetary Coronal Mass Ejections in 1996-2007, <http://www.ssg.sr.unh.edu/mag/ace/ACElists/ICMTable.html>

e) There are no signs of proton temperature decrease before DoY 37.0.

f) Quality 2

2. DoY 103.60-103.87

a) Signatures of bidirectional suprathermal electrons start at DoY 103.55.

b) Steep increase of the magnetic field strength near leading edge, followed by a small linear increase toward trailing edge.

c) α/p -ratio is very low (≈ 0.02).

d) Decrease in EPAM proton intensities at leading edge.

e) First component of a double fluxrope structure.

f) Quality 3

3. DoY 103.87-104.45

a) Signatures of bidirectional suprathermal electrons end at DoY 104.3.

b) Maximum of magnetic field strength is shifted toward leading edge, field strength at leading edge is much higher than at trailing edge.

c) No decrease in proton velocity visible.

d) α/p -ratio is very low (0.01) until DoY 104.25.

e) Proton temperature increase indicates an end time of DoY 104.25.

f) Second component of a double fluxrope structure.

g) Quality 2

4. DoY 145.15-145.64

a) Weak signatures of bidirectional suprathermal electrons present around DoY 145.5.

b) Magnetic field strength is very weak (<4.5 nT).

c) SWEPPAM data gap starts at DoY 144.5.

d) Identification as MC very uncertain.

e) Identification of end time is doubtful (≈ 0.1 days).

f) Quality 3

5. DoY 242.86-243.58

a) Transition between periods with and without occurrence of bidirectional suprathermal electrons.

E. List of MCs from 2001 to mid 2007 and their specific signatures

- b) Magnetic field strength profile shows much scattering and the maximum field strength is small (<10 nT).
- c) α/p -ratio is small (≈ 0.03).
- d) Proton density is very high (≈ 20 protons/cm 3) around DoY 243.15.
- e) Plasma β is high (0.3-1), except for DoY 243.3-243.55.
- f) Identification as MC is doubtful.
- g) Richardson¹⁰ give start and end times of DoY 242.83-244.29.
- h) Quality 3

6. DoY 273.36-273.88

- a) Signatures of bidirectional suprathermal electrons are present except from DoY 273.55 to 273.7.
- b) Maximum of magnetic field strength is shifted toward leading edge.
- c) α/p -ratio is very low (≈ 0.01 on average).
- d) Proton temperature is not lower than $0.5T_{exp}$ and indicates an end time of DoY 273.8.
- e) Proton density is very high (≈ 30 protons/cm 3 at the MC center).
- f) EPAM electron intensities show an increase near the trailing edge.
- g) Quality 2

7. DoY 305.75-306.58

- a) Boundary times are in good agreement with the occurrence of bidirectional suprathermal electrons.
- b) Magnetic field strength is very low (< 6 nT).
- c) SWEPAM data gap occurs from DoY 306.35 onward.
- d) α/p -ratio is very low (≈ 0.02 on average).
- e) Plasma β is very high near leading edge (0.6-3).
- f) Richardson¹⁰ do not list this ICME as MC.
- g) Quality 2

8. DoY 333.23-334.38

- a) Bidirectional suprathermal electrons near leading and trailing edge.
- b) Maximum of magnetic field strength shifted toward leading edge.
- c) α/p -ratio is enhanced with respect to the ratio measured before DoY 333.23 but below 0.08.

¹⁰Near-Earth Interplanetary Coronal Mass Ejections in 1996-2007, <http://www.ssg.sr.unh.edu/mag/ace/ACElists/ICMTable.html>

- d) Decrease in proton temperature starts at DoY 332.75.
- e) Quality 2

9. **DoY 348.98-349.58**

- a) Signatures of bidirectional suprathermal electrons start at DoY 348.75 and end at DoY 349.8.
- b) Magnetic field strength shows linear decrease from leading (18 nT) to trailing (5 nT) edge.
- c) Proton temperature decrease starts at DoY 348.8 and ends at DoY 349.55.
- d) Plasma β is high near trailing edge (0.6-2).
- e) EPAM proton intensities show a decrease near leading edge, while electrons show an increase.
- f) Quality 2

2007

1. **DoY 14.59-15.29**

- a) No signatures of bidirectional suprathermal electrons visible.
- b) Variance in the magnetic field strength profile is high, and the maximum is shifted toward trailing edge.
- c) SWEPAM data gap before DoY 14.55.
- d) Proton speed is nearly constant at 350-380 km/s.
- e) α/p -ratio is low (≈ 0.03 on average).
- f) Quality 2

Bibliography

Magnetic clouds, http://lepmfi.gsfc.nasa.gov/mfi/mag_cloud_pub1.html.

Aellig, M., et al., Solar Wind Minor Ion Charge States Observed with High Time Resolution with SOHO/CELIAS/CTOF, in *Correlated Phenomena at the Sun, in the Heliosphere and in Geospace*, 1997.

Alexander, D., An Introduction to the Pre-CME Corona, *Space Science Reviews*, 123, 81–92, 2006.

Antonucci, E., M. A. Dodero, S. Giordano, V. Krishnakumar, and G. Noci, Spectroscopic measurement of the plasma electron density and outflow velocity in a polar coronal hole, *A&A*, 416, 749–758, 2004.

Arnaud, M., and R. Rothenflug, An updated evaluation of recombination and ionization rates, *Astronomy and Astrophysics Supplement Series*, 60, 425–457, 1985.

Aschwanden, M., *Physics of the Solar Corona*, Springer-Verlag Berlin Heidelberg New York, 2004.

Aschwanden, M., et al., Theoretical modeling for the stereo mission, *Space Science Reviews*, 136, 565–604, 2008.

Balogh, A., R. G. Marsden, and E. J. Smith, *The Heliosphere Near Solar Minimum, The Ulysses perspective*, Springer, 2001.

Berger, L., Velocity Distribution Functions of Heavy Ions in the Solar Wind at 1 AU, Ph.D. thesis, IEAP, CAU-Kiel, Germany, 2008.

Bothmer, V., and R. Schwenn, The structure and origin of magnetic clouds in the solar wind, *Annales Geophysicae*, 16, 1–24, 1998.

Bronstein, I. N., K. A. Semendjajew, G. Musiol, and H. Mühlig, *Taschenbuch der Mathematik*, 5 ed., Verlag Harri Deutsch, 2001.

Burkepile, J. T., A. J. Hundhausen, A. L. Stanger, O. C. St. Cyr, and J. A. Seiden, Role of projection effects on solar coronal mass ejection properties: 1. A study of CMEs associated with limb activity, *Journal of Geophysical Research*, 109, 3103–+, 2004.

Bibliography

- Cane, H. V., and I. G. Richardson, Interplanetary coronal mass ejections in the near-Earth solar wind during 1996–2002, *Journal of Geophysical Research*, 108, SSH6–(1–13), 2003.
- Charbonneau, P., Dynamo Models of the Solar Cycle, *Living Reviews in Solar Physics*, 2, 2–+, 2005.
- Chupp, E. L., H. Debrunner, E. Flückiger, D. J. Forrest, F. Golliez, G. Kanbach, W. T. Vestrand, J. Cooper, and G. Share, Solar neutron emissivity during the large flare on 1982 June 3, *The Astrophysical Journal*, 318, 913–925, 1987.
- Chupp, E. L., G. Trottet, P. Dunphy, and E. Rieger, What we know and do not know about high energy neutral emissions from solar flares (A challenge for future missions), in *28th International Cosmic Ray Conference*, 2003.
- Cid, C., M. A. Hidalgo, T. Nieves-Chinchilla, J. Sequeiros, and A. F. Viñas, Plasma and magnetic field inside magnetic clouds: A global study, *Solar Physics*, 207, 187–198, 2002.
- Debrunner, H., et al., Energetic neutrons, protons, and gamma rays during the 1990 May 24 solar cosmic-ray event, *The Astrophysical Journal*, 479, 997–1011, 1997.
- Demtröder, W., *Experimentalphysik 2, Elektrizität und Optik*, 5 ed., Springer Berlin Heidelberg, 2009.
- Feng, H. Q., D. J. Wu, and J. K. Chao, Size and energy distributions of interplanetary magnetic flux ropes, *Journal of Geophysical Research*, 112, 2102–+, 2007.
- Forbes, T., et al., CME Theory and Models, *Space Science Reviews*, 123, 251–302, 2006.
- Forsyth, R., et al., ICMEs in the Inner Heliosphere: Origin, Evolution and Propagation Effects. Report of Working Group G, *Space Science Reviews*, 123, 383–416, 2006.
- Gazis, P., et al., ICMEs at High Latitudes and in the Outer Heliosphere, *Space Science Reviews*, 123, 417–451, 2006.
- Gloeckler, G., et al., Investigation of the composition of solar and interstellar matter using solar wind and pickup ion measurements with SWICS and SWIMS on the ACE spacecraft, *Space Science Reviews*, 86, 497–539, 1998.
- Gold, R. E., S. M. Krimigis, S. E. Hawkins, D. K. Haggerty, D. A. Lohr, E. Fiore, T. P. Armstrong, G. Holland, and L. J. Lanzerotti, Electron, Proton, and Alpha Monitor on the Advanced Composition Explorer spacecraft, *Space Science Reviews*, 86, 541–562, 1998.
- Hidalgo, M. A., A study of the expansion and distortion of the cross section of magnetic clouds in the interplanetary medium, *Journal of Geophysical Research*, 108, (SSH4–)1–6, 2003.

Bibliography

- Hidalgo, M. A., T. Nieves-Chinchilla, and C. Cid, Elliptical cross-section model for the magnetic topology of magnetic clouds, *Geophysical Research Letters*, 29, 15–(1–4), 2002.
- Howard, T., C. Fry, J. Johnston, and D. Webb, On the Evolution of Coronal Mass Ejections in the Interplanetary Medium, *The Astrophysical Journal*, 667, 610–625, 2007.
- Hua, X.-M., and R. E. Lingenfelter, Solar flare neutron production and the angular dependence of the capture gamma-ray emission, *Solar Physics*, 107, 351–383, 1987.
- Hua, X.-M., R. Ramaty, and R. E. Lingenfelter, Deexcitation gamma-ray line emission from solar flare magnetic loops, *The Astrophysical Journal*, 341, 516–532, 1989.
- Hua, X.-M., B. Kozlovsky, R. E. Lingenfelter, R. Ramaty, and A. Stupp, Angular and energy-dependent neutron emission from solar flare magnetic loops, *The Astrophysical Journal Supplement Series*, 140, 563–579, 2002.
- Hudson, H., J.-L. Bougeret, and J. Burkepile, Coronal Mass Ejections: Overview of Observations, *Space Science Reviews*, 123, 13–30, 2006.
- Ivanov, E. V., and V. N. Obridko, Cyclic variations of CME velocity, *Solar Physics*, 198, 179–196, 2001.
- Ivanov, E. V., V. N. Obridko, E. V. Nepomnyashchaya, and N. V. Kutilina, Relevance of CME to the structure of large-scale solar magnetic fields, *Solar Physics*, 184, 369–384, 1999.
- Ivanov, K. G., A. F. Harshiladze, E. G. Eroshenko, and V. A. Stiazhkin, Configuration, structure, and dynamics of magnetic clouds from solar flares in light of measurements on board VEGA 1 and VEGA 2 in January–February 1986, *Solar Physics*, 120, 407–419, 1989.
- Kocharov, L., J. Torsti, F. Tang, H. Zirin, G. A. Kovaltsov, and I. G. Usoskin, Impact of magnetic environment on the generation of high-energy neutrons at the sun, *Solar Physics*, 172, 271–278, 1997.
- Kötén, M., An improved efficiency model for ACE/SWICS - Determination of the carbon isotopic ratio $^{13}\text{C}/^{12}\text{C}$ in the solar wind from ACE/SWICS measurements, Ph.D. thesis, Christian Albrechts Universität, Kiel, 2009.
- Lepping, R. P., J. A. Jones, and L. F. Burlaga, Magnetic Field Structure of Interplanetary Magnetic Clouds at 1 AU, *Journal of Geophysical Research*, 95, 11,957–11,965, 1990.
- Lepping, R. P., D. B. Berdichevsky, and T. J. Ferguson, Estimated errors in magnetic cloud model fit parameters with force-free cylindrically symmetric assumptions, *Journal of Geophysical Research*, 108, 1356–+, 2003.

Bibliography

- Lepping, R. P., D. B. Berdichevsky, and T. J. Ferguson, Correction to “Estimated errors in magnetic cloud model fit parameters with force-free cylindrically symmetric assumptions”, *Journal of Geophysical Research*, 109, 7101–+, 2004.
- Li, K. J., H. S. Yun, and X. M. Gu, Latitude migration of sunspot groups, *The Astrophysical Journal*, 122, 2115–2117, 2001.
- Liu, Y., J. D. Richardson, and J. W. Belcher, A statistical study of the properties of interplanetary coronal mass ejections from 0.3 to 5.4 AU, *Planetary and Space Science*, 53, 3–17, 2005.
- Lundquist, S., Magnetohydrostatic fields, *Ark. Phys.*, 2, 361–365, 1950.
- Lynch, B. J., T. H. Zurbuchen, and L. A. Fisk, Internal structure of magnetic clouds: Plasma and composition, *Journal of Geophysical Research*, 108, (SSH6–)1–14, 2003.
- Malandraki, O. E., D. Lario, L. J. Lanzerotti, E. T. Sarris, A. Geranios, and G. Tsiropoula, October/November 2003 interplanetary coronal mass ejections: ACE/EPAM solar energetic particle observations, *Journal of Geophysical Research*, 110, 9–+, 2005.
- McComas, D. J., S. J. Bame, P. Barker, W. C. Feldman, J. L. Phillips, P. Riley, and J. W. Griffee, Solar Wind Electron Proton Alpha Monitor (SWEPAM) for the Advanced Composition Explorer, *Space Science Reviews*, 86, 563–612, 1998.
- Nieves-Chinchilla, T., M. Espinosa, C. Cid, M. A. Hidalgo, and J. Sequeiros, A new model for the magnetic topology of magnetic clouds, in *Solar Variability: From Core to Outer Frontiers*, 2002.
- Nieves-Chinchilla, T., M. A. Hidalgo, and J. Sequeiros, Magnetic Clouds observed at 1 AU during the period 2000–2003, *Solar Physics*, 232, 105–126, 2005.
- Odstrcil, D., J. A. Linker, R. Lionello, Z. Mikic, P. Riley, V. J. Pizzo, and J. G. Luhmann, Merging of coronal and heliospheric numerical two-dimensional MHD models, *Journal of Geophysical Research*, 107, 1493–+, 2002.
- Owens, M. J., V. G. Merkin, and P. Riley, A kinematically distorted flux rope model for magnetic clouds, *Journal of Geophysical Research*, 111, 3104–+, 2006.
- Pagel, A. C., N. U. Crooker, T. H. Zurbuchen, and J. T. Gosling, Correlation of solar wind entropy and oxygen ion charge state ratio, *Journal of Geophysical Research*, 109, 1113–+, 2004.
- Pick, M., et al., Multi-Wavelength Observations of CMEs and Associated Phenomena. Report of Working Group F, *Space Science Reviews*, 123, 341–382, 2006.
- Press, W. H., S. A. Teukolsky, W. T. Vetterling, and B. P. Flannery, *Numerical Recipes in C - The Art of Scientific Computing*, second ed., Cambridge University Press, 1992.

Bibliography

- Rakowski, C., J. Laming, and S. Lepri, Ion Charge States in Halo Coronal Mass Ejections: What Can We Learn about the Explosion?, *The Astrophysical Journal*, 667, 602–609, 2007.
- Reinard, A., Comparison of Interplanetary CME Charge State Composition with CME-associated Flare Magnitude, *APJ*, 620, 501–505, 2005.
- Reinard, A., Analysis of Interplanetary Coronal Mass Ejection Parameters as a Function of Energetics, Source Location, and Magnetic Structure, *The Astrophysical Journal*, 682, 1289–1305, 2008.
- Reinard, A., T. Zurbuchen, L. Fisk, S. Lepri, R. Skoug, and G. Gloeckler, Comparison between Average Charge States and Abundances of Ions in CMEs and the Slow Solar Wind, in *Joint SOHO/ACE workshop "Solar and Galactic Composition"*, 2001.
- Richardson, I. G., and H. V. Cane, Regions of abnormally low proton temperature in the solar wind (1965–1991) and their association with ejecta, *Journal of Geophysical Research*, 100, 23,397–23,412, 1995.
- Richardson, I. G., and H. V. Cane, Identification of interplanetary coronal mass ejections at 1 AU using multiple solar wind plasma composition anomalies, *Journal of Geophysical Research*, 109, 9104–+, 2004a.
- Richardson, I. G., and H. V. Cane, The fraction of interplanetary coronal mass ejections that are magnetic clouds: Evidence for a solar cycle variation, *Geophysical Research Letters*, 31, 18,804–+, 2004b.
- Riley, P., and N. U. Crooker, Kinematic treatment of coronal mass ejection evolution in the solar wind, *The Astrophysical Journal*, 600, 1035–1042, 2004.
- Romashets, E. P., and M. Vandas, Force-free magnetic fields with not constant alpha, in *Solar Variability: From Core to Outer Frontiers*, pp. 17–20, 2002.
- Romashets, E. P., and M. Vandas, Asymmetric magnetic field inside a cylindrical flux rope, *Advances in Space Research*, 35, 2167–2171, 2005.
- Schwenn, R., and E. Marsch, *Physics of the Inner Heliosphere 1 Large-Scale Phenomena*, Springer, 1990.
- Schwenn, R., and E. Marsch, *Physics of the Inner Heliosphere 2 Particles, Waves and Turbulence*, Springer, 1991.
- Schwenn, R., et al., Coronal Observations of CMEs. Report of Working Group A, *Space Science Reviews*, 123, 127–176, 2006.
- Shrivastava, P. K., and N. Singh, Latitudinal Distribution of Solar Flares and Their Association with Coronal Mass Ejections, *Chinese Journal of Astronomy and Astrophysics*, 5, 198–202, 2005.

Bibliography

- Skoug, R. M., J. T. Gosling, J. T. Steinberg, D. J. McComas, C. W. Smith, N. F. Ness, Q. Hu, and L. F. Burlaga, Extremely high speed solar wind: 29–30 October 2003, *Journal of Geophysical Research*, 109, 9102–+, 2004.
- Smith, C. W., J. L’Heureux, N. F. Ness, M. H. Acuña, L. F. Burlaga, and J. Scheifele, The ACE Magnetic Fields Experiment, *Space Science Reviews*, 86, 613–632, 1998.
- Sonnerup, B. U. Ö., and L. J. Cahill, Magnetopause Structure and Attitude from Explorer 12 Observations, *Journal of Geophysical Research*, 72, 171–183, 1967.
- Sonnerup, B. U. Ö., H. Hasegawa, W.-L. Teh, and L.-N. Hau, Grad-Shafranov reconstruction: An overview, *Journal of Geophysical Research*, 111, 9204–+, 2006.
- Stone, E. C., A. M. Frandsen, R. A. Mewaldt, E. R. Christian, D. Margolies, J. F. Ormes, and F. Snow, The Advanced Composition Explorer, *SSR*, 86, 1–22, 1998.
- Stroth, U., *Einführung in die Plasmaphysik*, 2002.
- The Group “Numerical Analysis” at Delft University of Technology, On the computation of Mathieu functions, *Journal of Engineering Mathematics*, 7, 39–61, 1973.
- van Ballegooijen, A., Three-Dimensional Modeling of Coronal Magnetic Fields, in *Advanced Solar Polarimetry – Theory, Observation, and Instrumentation*, 2001.
- Vandas, M., and E. P. Romashets, Magnetic field in an elliptic flux rope: A generalization of the Lundquist solution, in *Solar Variability: From Core to Outer Frontiers*, 2002.
- Vandas, M., and E. P. Romashets, A force-free field with constant alpha in an oblate cylinder: A generalization of the Lundquist solution, *Astronomy & Astrophysics*, 398, 801–807, 2003.
- Vandas, M., S. Fischer, P. Pelant, and A. Geranios, Spheroidal models of magnetic clouds and their comparison with spacecraft measurements, *Journal of Geophysical Research*, 98, 11,467–+, 1993.
- Vandas, M., D. Odstrcil, and S. Watari, Three-dimensional MHD simulation of a loop-like magnetic cloud in the solar wind, *Journal of Geophysical Research*, 107, 1236–+, 2002.
- Vandas, M., E. P. Romashets, and S. Watari, Magnetic clouds of oblate shapes, *Planetary and Space Science*, 53, 19–24, 2005.
- Vandas, M., E. P. Romashets, S. Watari, A. Geranios, E. Antoniadou, and O. Zacharopoulou, Comparison of force-free flux rope models with observations of magnetic clouds, *Advances in Space Research*, 38, 441–446, 2006.

Bibliography

- Veronig, A., M. Temmer, A. Hanslmeier, W. Otruba, and M. Messerotti, Temporal aspects and frequency distributions of solar soft X-ray flares, *Astronomy & Astrophysics*, 382, 1070–1080, 2002.
- Watanabe, K., et al., Solar Neutron Event in Association with a Large Solar Flare on August 25, 2001, in *28th International Cosmic Ray Conference*, 2003a.
- Watanabe, K., et al., Solar Neutron Event in Association with a Large Solar Flare on 2000 November 24, *The Astrophysical Journal*, 592, 590–596, 2003b.
- Watanabe, K., et al., Solar neutron events of 2003 October-November, *The Astrophysical Journal*, 636, 1135–1144, 2006.
- Webb, D., et al., Solar Mass Ejection Imager (SMEI) observations of coronal mass ejections (CMEs) in the heliosphere, *Journal of Geophysical Research*, 111, 12,101–+, 2006.
- Widing, K., Emerging Active Regions on the Sun and the Photospheric Abundance of Neon, *The Astrophysical Journal*, 480, 400–+, 1997.
- Widing, K., and U. Feldman, On the Rate of Abundance Modifications versus Time in Active Region Plasmas, *The Astrophysical Journal*, 555, 426–434, 2001.
- Wimmer-Schweingruber, R., et al., Understanding Interplanetary Coronal Mass Ejection Signatures. Report of Working Group B, *Space Science Reviews*, 123, 177–216, 2006.
- Wimmer-Schweingruber, R. F., Einführung in die extraterrestrische Physik, 2002-04.
- Yashiro, S., N. Gopalswamy, G. Michalek, and R. A. Howard, Properties of narrow coronal mass ejections observed with LASCO, *Advances in Space Research*, 32, 2631–2635, 2003.
- Zurbuchen, T., and I. Richardson, In-Situ Solar Wind and Magnetic Field Signatures of Interplanetary Coronal Mass Ejections, *Space Science Reviews*, 123, 31–43, 2006.

List of Acronyms

ACE	Advanced Composition Explorer
ACF	Auto Correlation Function
AR	Active Region
CIR	Corotating Interaction Region
CME	Coronal Mass Ejection
DoY	Day of Year
EIT	Extreme ultraviolet Imaging Telescope
EPAM	Electron, Proton and Alpha Monitor
FIP	First ionisation potential
FWHM	Full Width Half Maximum
GOES	Geostationary Operational Environmental Satellites
GSE	Geocentric Solar Ecliptic
ICME	Interplanetary Coronal Mass Ejection
LASCO	Large Angle and Spectrometric Coronagraph
MAG	Magnetometer
MC	Magnetic Cloud
MVA	Minimum Variance Analysis
PHA	Pulse Height Analysis
RMS	Root Mean Square

List of Acronyms

SEP	Solar Energetic Particle Event
SO	Solar Orbiter
SOHO	Solar and Heliospheric Observatory
STEA	Suprathermal Electron Angle Scan
SWEPAM	Solar Wind Electron Proton Alpha Monitor
SWICS	Solar Wind Ion Composition Spectrometer
ToF	Time of Flight
TRACE	Transition Region and Coronal Explorer
VDF	Velocity Distribution Function

Danksagung

Mein Dank gilt zuerst Herrn Prof. Dr. Robert F. Wimmer-Schweingruber für die Vergabe dieser Arbeit und die sehr gute Betreuung. Er hatte stets ein offenes Ohr bei auftretenden Problemen und gab viele wertvolle Denkanstöße.

Weiterhin gilt mein Dank Herrn Dr. Lars Berger, Herrn Dipl. phys. Bent Ehresmann, Herrn Dipl. phys. Onno Kortmann und Herrn Dipl. phys. Muharrem Köten für die vielen wissenschaftlichen und nichtwissenschaftlichen Diskussionen und Betätigungen der letzten Jahre.

Den oben Genannten und den restlichen Mitgliedern der Arbeitsgruppen Wimmer-Schweingruber und Heber gilt mein Dank für das angenehme Arbeitsklima. Zu vielen der Kollegen hat sich neben dem beruflichen Kontakt auch eine private Verbindung aufgebaut.

Ich danke ebenfalls der Deutschen Forschungs-Gemeinschaft und dem Land Schleswig-Holstein, die diese Arbeit finanziell unterstützt haben.

Nicht zuletzt danke ich meiner Familie. Ohne die Unterstützung meiner Eltern wäre diese Arbeit nicht beendet worden.

Lebenslauf

Name: Roland Rodde
Wohnort: Alter Markt 10, 24103 Kiel
Geboren: 14.2.1979 in Neumünster
Familienstand: Ledig
Staatsangehörigkeit: Deutsch

Schulbildung : 1985 - 1989 Grundschule, Brügge
1989 - 1998 Alexander-von-Humboldt-Schule, Neumünster
Abschluß: Abitur

Wehrdienst : 1998 - 1999 Wehrdienst bei der Marine

Studium : 1999 - 2005 Studium der Physik an der Christian-Albrechts Universität zu Kiel,
Diplomnote : gut
Diplomarbeit mit dem Titel
“Lithiumhäufigkeiten in schnell rotierenden
F- und G-Hauptreihensternen”,
Betreuer: PD. Dr. M. Hünsch

Berufstätigkeit : Seit April 2005 Wissenschaftlicher Mitarbeiter der
Arbeitsgruppe Wimmer am Institut
für Experimentelle und Angewandte
Physik der Christian-Albrechts-
Universität zu Kiel

Eidesstattliche Versicherung

Hiermit versichere ich an Eides Statt, dass ich die vorliegende Arbeit abgesehen vom Rat meiner akademischen Lehrer ohne fremde Hilfe und lediglich unter der Verwendung der angegebenen Literatur sowie den bekannten Nachschlagewerken der Naturwissenschaften angefertigt habe, und sie nach Inhalt und Form meine eigene ist. Diese Arbeit ist unter Einhaltung der Regeln guter wissenschaftlicher Praxis entstanden.

Des weiteren versichere ich, dass diese Arbeit weder ganz noch teilweise an anderer Stelle zur Prüfung vorlag. Frühere Promotionsversuche wurden von mir nicht vorgenommen.

Kiel, den

Roland Rodde